Project Title: Development of a High-Efficiency Hot Gas Turbo-expander and Low-Cost Heat Exchangers for Optimized CSP Supercritical CO_2 Operation

Project Period: 09/01/12 – 12/31/18

Budget Period: Phase 3: 9/01/17 – 12/31/18

Budget Period Budget: $9,747,973

Recipient: Southwest Research Institute®

Address: 6220 Culebra Road
San Antonio, TX 78238-5166

Award Number: DE-EE0005804

Project Team: General Electric
Thar Energy, LLC
Knolls Atomic Power Laboratory

Principal Investigator: Jeff Moore, Ph.D.
Institute Engineer
Phone: 210-522-5812
Fax: 210-522-4506
Email: jeff.moore@swri.org

Business Contact: Robin Rutledge
Senior Contract Specialist
Phone: 210-522-3179
Email: robin.rutledge@swri.org

DOE Project Officer: Thomas Rueckert

DOE Tech Manager: Mark Lausten

Executive Summary

Southwest Research Institute® (SwRI®) has developed a novel, high-efficiency, supercritical carbon dioxide (sCO_2), hot gas turbo-expander optimized for the highly-transient, solar-power-plant, duty-cycle profile. This MW-scale sCO_2 turbo-expander design advances the state-of-the-art of sCO_2 turbo-expanders from a current Technology Readiness Level (TRL) of three (initial, small-scale, laboratory, size testing) to a full TRL6 (MW-scale prototype demonstration). A secondary objective of this project was to optimize novel compact heat exchangers for sCO_2 applications to drastically reduce their manufacturing costs. Significant learning was achieved on how to design and fabricate a more cost effective, high performance recuperator, at the MWt capacity. The sCO_2 turbo-expander and novel sCO_2 heat exchanger have been tested in a 1-MWe sCO_2 test loop, fabricated to demonstrate component performance and the performance of the optimized sCO_2 Brayton cycle over a wide range of part load conditions and during transient operations representative of a typical Concentrating Solar Power (CSP) duty cycle.

The scalable sCO_2 expander design and improved heat exchanger address and close two critical technology gaps required for an optimized CSP sCO_2 power plant and provide a major stepping stone on the pathway to achieving CSP power at $0.06/kW-hr Levelized Cost of Electricity (LCOE), increasing energy conversion efficiency to greater than 50% and reducing total power block cost to below $1,200/kW installed.

Construction of the facility and testing has been completed. Test targets of 1,320°F, 27,000 rpm, and 3,500 psi were reached during separate tests. Overall, the turbine saw 37.5 hours of operation with many other hours of testing and troubleshooting all of the loop components. All the test data and troubleshooting is useful and applicable for future tests and operations with not only this loop but in any sCO_2 application.

Table of Contents

List of Figures

List of Tables

Introduction

The proposed CSP power cycle uses sCO_2 as both the heat transfer fluid in the solar receiver and the working fluid in the power cycle. The lower thermal mass and increased power density of the sCO_2 power cycle, as compared to steam-based systems, enables the development of compact, high-efficiency power blocks that are compatible with sensible-heat thermal energy storage and can respond quickly to transient environmental changes and frequent start-up/shutdown operations. These smaller, integrated power blocks are ideal for modular tower-mounted CSP solutions in the 5-10 MW range.

The team of SwRI, General Electric (GE), Fluor Marine Propulsion Corporation, operator of Knolls Atomic Power Lab (KAPL), and Thar Energy LLC (Thar) has developed a novel, high-efficiency sCO_2 hot gas turbo-expander, optimized for the highly-transient, solar-power-plant, duty-cycle profile. In Phase 2, Aramco Services Company provided additional cost share. Finally, in Phase 3 the Electric Power Research Institute (EPRI) provided cost share during the demonstration phase This MW-scale sCO_2 turbo-expander design advances state-of-the-art sCO_2 turbo-expanders from a current TRL3, initial small-scale, laboratory-size testing to a full TRL6 (MW-scale prototype demonstration). A secondary objective of this project was to optimize novel compact heat exchangers for sCO_2 applications to drastically reduce their manufacturing costs. The sCO_2 turbo-expander and novel sCO_2 heat exchanger have been tested in a 1 MWe sCO_2 test loop, fabricated to demonstrate component performance and the performance of the optimized sCO_2 Brayton cycle over a wide range of part load conditions and during transient operations representative of a typical CSP duty cycle.

The scalable sCO_2 expander design and improved heat exchanger address and close two critical technology gaps required for an optimized CSP sCO_2 power plant and provide a major stepping stone on the pathway to achieving CSP power at $0.06/kW-hr LCOE, increasing energy conversion efficiency to greater than 50% and reducing total power block cost to below $1,200/kW installed.

This is the first MWe-scale, $sCO_{2,}$ power-cycle demonstration and is currently the highest temperature sCO_2 loop in the world. The turbo-expander developed for this demonstration was optimized for the unique characteristics of CSP; quick start-up/shutdown and transient thermal inputs. The unique turbo-expander operating requirements, high pressure, high temperature, and supercritical working fluid were well beyond the current state of the art in turbo-machinery design.

During the course of development of the expander, to support testing, additional components were developed, built and tested, such as high temperature heater using Inconel 740h and printed circuit heat exchanger recuperator. These two components were the highest temperature examples of the tested components.

Phase Breakdown

Phase 1. Turbomachinery and Heat Exchanger Design

The objectives for Phase 1 are to develop the sCO_2 turbo-expander and recuperator designs to move into Phase 2 and Phase 3 of the project for a recuperated recompression cycle.

Task 1.1. Heat Exchanger Design and Bench Testing

Subtask 1.1.1. Define Test Loop Heat Exchanger Requirements

Define the requirements for the heat exchanger: Perform heat exchanger and cycle analysis to define the detailed design requirements of the high- and low-temperature heat exchangers in the proposed cycle. (Recuperator must facilitate over 75% of energy into expander in the proposed cycle.) Two manufacturing technologies will be considered for micro-channel heat exchanger fabrication: (1) Additive manufacturing using metallic powder, and (2) Fabrication of printed circuit heat exchangers using diffusion brazing.

Subtask 1.1.2. Bench Testing of Heat Exchanger Concept

Perform bench scale testing of heat exchanger concepts in conjunction with commercial feasibility studies to down-select the advanced heat exchanger from several competing technologies to meet requirements defined in Task 1.1.1.

Subtask 1.1.3. Design of Test Loop Recuperator Heat Exchanger

Develop a design that will increase heat transfer area per unit volume, while from a manufacturing point of view, reduce the capital cost, labor, and time required relative to diffusion bonding and other fabrication processes. Several novel recuperator designs and manufacturing technologies will be studied that have the potential to reduce manufacturing costs by up to 40% while maintaining performance and life for a 5 MWt recuperator design. This design will utilize Finite Element Analysis (FEA), thermal analysis, and a commercial feasibility study.

Task 1.2. Turbomachinery Design

Complete detailed design of the 1 MWe turbo-expander and associated turbo-machinery. Detailed design includes mechanical design, package integration, and impeller blade path design. Design turbo-machinery package, including skid, utility, ancillary, and controls subsystems. Prepare detailed engineering specifications for mechanical installation, controls logic, process, and electrical for all turbo-machinery on-skid components.

Perform design of the 1 MWe turbo-expander and associated turbo-machinery package. Design includes aero-thermo design of the hot-gas-expander, mechanical design of the rotor and pressure casing, gas seal and bearing integration, rotor dynamic analysis, materials selection, generator integration, and design for thermal management.

Perform full design review of the turbo-machinery package and its integration into the test loop. Develop detailed manufacturing, mechanical installation, P&ID, controls logic block, and electrical drawings for the turbo-machinery package.

Subtask 1.2.1. Steady and Transient Aerodynamic 1-D Flow (Mean-Streamline) Design

Subtask 1.2.2. Machinery Component General Layout (Impeller, Seals, Bearings, Rotor, Vanes)

Subtask 1.2.3. Lateral and Torsional Rotordynamic Stability Analysis

Subtask 1.2.4. Impeller and Blade Structural Dynamic, Stress, and Thermal Fatigue Life FEA

Subtask 1.2.5. Radial/ Thrust Bearing, (Axial/ Radial) Clearances and Seal Design

Subtask 1.2.6. Thermal Management, Load, and Load Swing Analysis for Creep and Thermal Machine Fatigue

Subtask 1.2.7. Transient Start-up and Shut-down Analysis and Load Response Analysis

Subtask 1.2.8. Key Components Material Selections

Task 1.3. Test Loop Design

SwRI will finalize the test loop design incorporating final turbo-expander and recuperator designs. Final test loop design will include transient process simulation, thermal simulation, and final P&ID definition.

Define the 1 MWe scale test loop requirements and establish initial test loop layout for demonstration of the sCO_2 power cycle. Test loop design will utilize transient process simulation and thermal analysis to assist with defining P&ID for the test loop and initiate the major component specification.

Subtask 1.3.1. Define Operating Requirements for all Major Components of the Cycle

Subtask 1.3.2. Design P&ID for Turbo-Expander Test Loop

Subtask 1.3.3. Design Test Loop Layout and Identify Integration into Existing Infrastructure

Sub-subtask 1.3.3.1. Thermo-economic Cycle Analysis and Commercial Product Evaluation

Perform thermo-economic analysis of CSP cycle using sCO_2 recompression Brayton cycle and identify component vendors to cost the components required in addition to the power cycle.

Subtask 1.3.4. Identify CSP Power Plant System Layout and Component Vendors for a Commercial CSP Product

Subtask 1.3.5. Identify the Component Performance and Cost Targets to Achieve the Competitive CSP Product

Subtask 1.3.6. Demonstrate Agreement between the Technical Targets of Task 1.1. and Task 1.2. and the CSP Power Plant System Commercial Performance and Cost Targets from Tasks 1.4.1 and 1.4.2

Phase 2. Component Fabrication and Test Loop Commissioning

Objectives for Phase 2 are fabrication, installation, and commissioning of the sCO_2 turbo-expander, recuperator, and test loop.

Task 2.1. Heat Exchanger Fabrication

Fabricate the 5 MWt recuperator.

Task 2.2. Turbo-Machinery Fabrication

SwRI will fabricate and assemble the complete turbo-machinery package, including skid, ancillary systems, and control system using in-house machine shops and contractors, as necessary.

Task 2.3. Test Loop Hardware Acquisition and Installation Start-up and Commissioning

SwRI has acquired long lead time critical components required for the test loop and cycle demonstration. Start-up and commissioning of individual components were completed, culminating in the commissioning and start-up of the test loop with sCO_2 turbo expander and recuperator.

Subtask 2.3.1. Identify and Acquire Long-Lead Critical Components Required for Test Loop Fabrication and Commissioning

Subtask 2.3.2. Install and Commission Subsystems and Components into sCO_2 Expander Test Loop

Task 2.4. Thermo-Economic Cycle Model and Concentrated Solar Power Conversion Plant Specs

Perform sensitivity analysis on the CSP thermo-economic model to develop LCOE and cost metrics for a CSP plant at a typical location in the U.S. (e.g., Dagget, California). Determine the optimal system efficiency and design point to optimize for lowest LCOE.

Subtask 2.4.1. Develop the LCOE Model and Perform Sensitivity Analysis to Determine Overall System Efficiency and Design Point

Subtask 2.4.2. Determine Specifications of a Commercial CSP Power Plant Using the Developed Power Cycle

Phase 3. Performance Testing

Task 3.1. Performance Testing

The objectives for Phase 3 are testing of the sCO_2 test loop, documentation of the turbo-expander performance, documentation of the recuperator performance, and demonstrating critical component endurance. Turbo-expander performance (power, efficiency) will be performed per ASME PTC-6, 10, and 18. Recuperator efficiency testing will be performed per ASME PTC-12.

Tune the sCO_2 test loop to optimize turbo-expander performance. Document the performance of the sCO_2 turbo-expander and recuperator across their full operating range and cyclic transient conditions representative of the unsteady solar duty cycle.

Demonstrate sustained operation and reliability of the turbo expander and recuperators. Determine thermo-mechanical fatigue and creep of critical components.

Task 3.2. Design Optimization

Update and refine the design of key components including but not limited to the turbo-expander, recuperator, and compressor based on performance and endurance test data and scaled to a commercial size as identified in Subtask 2.4.2.

Task 3.3. Go/No-Go Decision Points

Phase 1 efforts, detail design and fabrication of sCO_2 turbo-expander and recuperator, and construction of the test loop meet:

- Scaled demonstration of an advanced compact heat exchanger for sCO_2 applications meeting duty requirements, system operating condition requirements, and efficiency targets, as stated above in Task 1.1.
- Full scale design and supporting analysis and modeling of a sCO_2 turbo-expander and related turbo-machinery (meeting duty requirements, system operating condition requirements, and efficiency targets, as defined above in Tasks 1.2.) The predicted turbine-expander isentropic efficiencies to exceed 86%. Seals and bearings were designed for continuous operation with low maintenance requirements at intervals above 24,000 hours.
- Full scale design and supporting analysis and modeling of a sCO_2 test loop (meeting duty requirements, system operating condition requirements, and efficiency targets as stated above in Tasks 1.1., 1.2., and 1.3.). Design of this pilot scale loop and prototype turbo-expander testing demonstrated that the proposed cycle, expander, and recuperator can reliably exceeded DOE's goal of a 50% efficient thermal power conversion cycle with dry cooling.
- Attainment of these goals, along with establishment of appropriate reliability standards for the resulting equipment, additional component vendors, and satisfaction of other competitive requirements substantiated that the product has sufficient potential to warrant commercialization. Specific markets for commercial application were sought out. Steps in the commercial process included, but were not limited to, identification of the specific markets, the externalities that impact the optimum size for installations, and the capacity factors that are needed to affect a competitive LCOE. The commercialization plan incorporating the above aspects is reported to the DOE.

Task 3.4. Briefings/Technical Presentations

A kick-off meeting took place at SwRI on October 8-9, 2012. This meeting was attended by the technical teams of SwRI, GE, Thar, and KAPL. During this meeting, the program objectives and work breakdown were reviewed, and the overall project schedule was also defined. Each team discussed their approach to their assigned tasks, and brainstorming sessions took place to discuss concepts for the expander, heat exchanger, and test loop. Additional meetings were also scheduled.

FOCUS Thermal Seal Testing

The goal of the FOCUS project is to reconfigure the existing sCO_2 test loop at SwRI to facilitate FOCUS-specific testing of a new thermal seal developed by GE GRC. This scope includes rotor shaft test instrumentation & ability to install and run the sCO_2 turbine with new thermal seal stator components. Part of this solution includes applying a thermal barrier coating (TBC) to the existing Sunshot shaft adjacent to the thermal seal to provide shielding of the heat flux from affecting the thermal gradient in the shaft. The measured stator temperatures will be directly compared to the measurements from the original Sunshot thermal seal design.

Phase 1. Component Design and Development

Task 1.1. Heat Exchanger Design and Bench Testing

Subtask 1.1.1 Define the Requirements for the Heat Exchanger

A cycle analysis of the entire system was conducted in Aspen to determine the requirements for each component; they are listed in Table 1.

Table 1: Test Loop Operating Conditions

Component	$T_{downstream}$ (°C [°F])	$P_{downstream}$ (bar [psi])	Flow (kg/s [lb/s])
Pump	61.76 [143.17]	255 [3698]	8.5 [18.7]
Low-temperature heater	180.5 [356.9]	254.9 [3697]	
Recuperator: hot	531 [988]	252.9 [3668]	
High-temperature heater	715 [1320]	251.9 [3654]	
Expander	643.3 [1190]	87 [1262]	
Recuperator: cool	185.6 [366.1]	84 [1217]	
Cooler	30 [86]	83 [1204]	

Design calculations performed in Task 1.1.1 confirmed the milestone goals of the detailed design of the recuperator. Preliminary design drawings and specifications are presented below. Prototype testing was completed on the first of two prototypes built [using Direct Metal Laser Sintering (DMLS)]. This concept was rejected because of cost and scale-up difficulty. A second prototype was built but then damaged due to exposure to hydrochloric acid, by the welding subcontractor, before testing could begin. While manufacturing feasibility was proven, we had not yet confirmed design calculations for heat transfer efficiency. A replacement prototype was to be completed and assembled by January 17, 2014, and immediately tested for efficiency at both Thar and Knolls Atomic Research Laboratory.

Conceptual Design: The path for conceptual design followed a route that first reviewed several forming techniques, choosing two of them for experimental machining to assess manufacturability. Both were prototyped. The first of these prototypes proved too costly for scale-up; consequently, performance tests were purposely kept to a minimum. The second prototype was the subject of ongoing testing in support of detailed design. These designs are DMLS and laser welding, respectively (Table 2).

The Microtube recuperator is a shell and tube HX that uses horizontal separators versus vertical baffles to direct flow in a counter-current direction. Figure 1 shows a tube bundle cross section where lower temperature, higher pressure sCO_2 flows inside the microtubes. The higher temperature, lower pressure sCO_2 flows in annular hour-glass space formed by the separator sheets and microtube outside diameter. The microtubes and separator sheets are brazed together for mechanical support and to enhance heat transfer. Figure 2 shows the tube sheets that are joined to the microtubes.

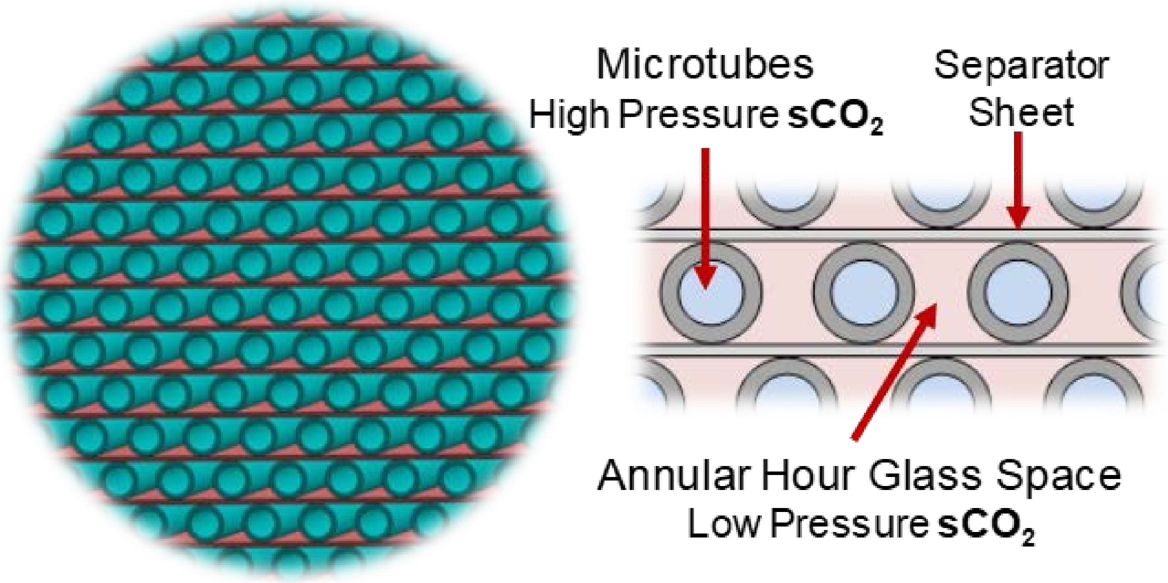

Figure 1: Recuperator Microtube Bundle Cross Section

Both FEA and CFD were performed to assure that project thermo-mechanical and hydraulic requirements would be met. Figure 2 is an example of a recuperator tube-sheet FEA.

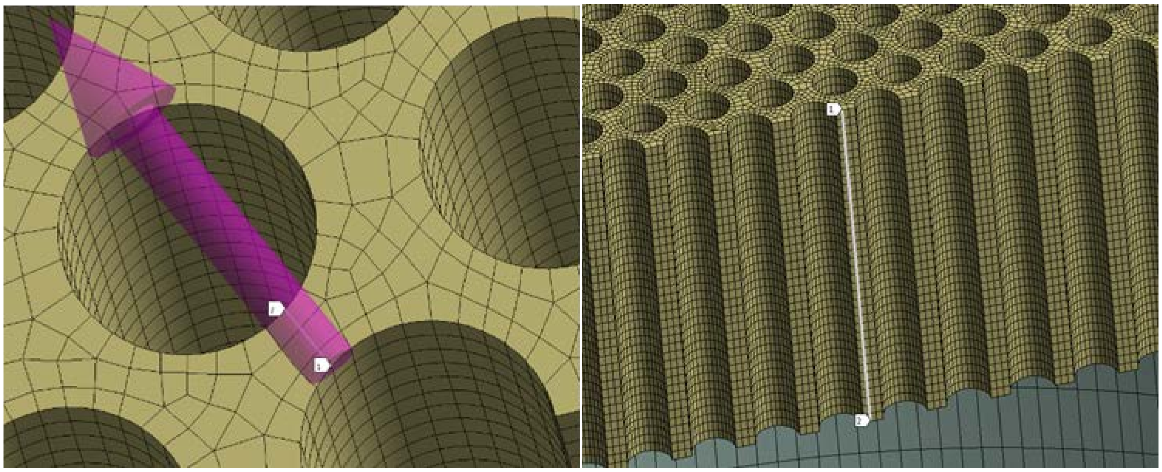

Figure 2: Tube Sheets Showing Location of Blaze Joint with Tubes

<u>Concept Review</u>: Several design intentions guided this review. One was to minimize “opacity,” defined as the ratio of the cross-sectional areas of solid metal to open channels. Another was to minimize fabrication time. A metric of 200 hours was arbitrarily chosen as the time limit for making the core heat-exchanger bundle. A cost limit of $50/kWt was a given, imposed by project milestone goals. This limit was unlikely to be met specifically in this high-risk project but should have been demonstrable on the basis of commercial-scale cost estimates. Table 2 summarizes the various fabrication methods taken under review.

The two methods chosen for prototyping were DMLS and laser welding. DMLS processing was recognized from the start as costly and not very scalable, but there were strong indications that larger production machinery would soon become available. Nonetheless, the prototype – while well-made and leak-free – demonstrated that the high cost of production machines together with slow build rates made the process unsuitable to large heat exchangers. The concept was better suited to small-scale applications as one might find in medical equipment.

It should be noted that this is a first of a kind prototype. The recuperator was 3D printing with IN718 and successfully performed at 600°F @ 2,500 psi. At the time, Thar was only able to identify and partner with one company with the capacity to achieve this milestone. However, at that time, costs were limiting for consideration of using DMLS to fabricate a large scale prototype.

Thar has worked in a parallel program to advance recuperator performance/cost metrics (DOE Project DE- FE0026273). In that program, Thar has documented that DMLS like many fabrication technologies have since greatly improved with regards to the performance/cost ratio. Thar could now work with more than a dozen vendors, with the capacity to fabricate this recuperator, on a more cost competitive basis.

Laser welding is already in wide use in the medical equipment industry. The challenge here was to demonstrate that the technique could be parlayed to the large scale. Edison Welding Institute (Columbus, Ohio) was contracted to aid in this development. The prototype experience was highly positive. The main benefits of laser welding include:

- Fast processing. Even though thousands of tubes would have to be welded, the speed is about one meter per second for welds made along the axis of tubes; butt welds between tube ends and the tube sheet can be performed at a rate of about a half-dozen such circular welds per second.

Table 2: Trade-off Study of Manufacturing Concepts for the Heat Exchanger

Design Concept	Pro Arguments	Con Arguments
Direct metal laser sintering (DMLS)	• True counter-current flow patterns in a "checkerboard" array are possible. • Bundle and manifolds can be formed as one piece. • Works well for high-nickel alloys. • Totally automated.	• Work pieces must be enclosed in argon atmosphere. • Chamber size limited by optics. • Process takes a long time to build up to a length of 7 inches. • Size limit would require multiple heat exchangers in series. • Costly.
Electrochemical machining	• Materials costs minimized by starting with solid metal. • The cathode is intricate, but could be formed by DMLS.	• Requires extensive electrolyte handling, clean-up and recycling. • Channel depth limited to 9 inches. • No cathodes have been made with more than 1,000 electrodes in it • Opacity is high.
Laser welding	• Lowest opacity of any method. • Fast, accurate welding is highly automated. • Compact manufacturing takes place inside automated welding enclosure. • Allows for thermal expansion.	• Assembly of the tube-and-separator sheet bundle in tube sheets is tedious; requires accurate alignment of tubes during laser welding. • Initial prototype required high degree of hand work between steps, which can be ameliorated with robots/automation. • Real-time weld quality monitoring required to ensure reliability.
Printed circuit board	• Channel patterns are easily formed by lithography. • Channel patterns can be varied in numerous ways.	• Opacity is high. • Diffusion bonding requires a large vacuum furnace plus an extremely heavy press. Diffusion brazing relieves the press requirement but requires surface treatments. • Furnace conditions need tight control over long periods. • Manifolding of inlet/outlet streams requires excessive amount of cross-flow configuring of the channels.
	Process is amenable to bonding large areas without excessive pressure.	• Opacity is also high. • Process can be slow. • Not sufficiently tested on Inconel.
Saw milling	• Channels of trapezoidal cross-section can be formed. • Low opacity. • Brazing surface can applied by electroless coating.	• Milling is too slow. • Messy process required a lot of cleaning.
	Method as all the advantages of milling and brazing, but with the added advantage of not having to prepare surfaces for brazing.	• Process is still slow due to milling step. • Cleaning is also a major requirement in order to ensure good weld contact.

- Automated operation. Overall production time was dominated more by hand work between welding runs, but this could be minimized by robotic automation. Individually, automated workstations could be deployed for large-scale production. No enclosed atmosphere was required.
- Pre-fabrication of tubes. The tubes handle the higher pressure. They are manufactured separately and can be inspected during production for defects (typically eddy-current monitoring). This lowered the risk of defects.
- Low cost. Time-study estimates for production of the 5 MW test-loop recuperator came very close to 200 hours, which was arbitrarily set as a goal. This included laser work and intermediate handling for parts to be welded. As a result, labor costs were expected to account for less than 10% of overall costs (Table 3). Material costs were based on real quotations.

A common concern was defect control. The test loop recuperator had 20,000 tubes, each of which was butt welded to tubes sheets at each end as well as stitch welded longitudinally to the length of each one on two sides to adjacent separator sheets. The tube sheet welds were of particular concern because they had to hold a pressure differential of approximately 2,500 psi. What was needed was a way to ensure the integrity of welds as they are formed, so that long term reliability is assured. There were, fortunately, a couple of techniques newly available, one of which was included in the optics for the laser workstation that was built for this project. The goal was to attain the defect rate of less than one in ten thousand, with a stretch goal of one in a hundred thousand. Calculations showed that staying under these defect rates ensure efficient operation of the recuperator.

The laser welds under discussion were quite small (~ 0.2 mm deep x 0.05 mm wide). They emitted very little sound or “plume” light. This was quite different than the majority of applications for laser welding today, which typically require much higher power and for which plume (and even plasma) light emission can be pronounced and highly useful for process monitoring.

Commercially available, real-time, laser-welding process monitors have exhibited varying degrees of success in real-world manufacturing environments. These devices have been primarily devoted to high-power laser welding applications, such as automotive transmission welding and tailored blank welding. The monitored process outputs in such systems include plasma light intensity, acoustic emission and weld surface temperature. The Edison Welding Institute has also investigated light intensity, optical spectrum and sound data. These techniques have not yielded reliable solutions for monitoring the weld quality of the small, fast, “dim and quiet” welds of interest here.

A promising new arrival to laser-welding inspection is an optical interferometer with feedback control that can be employed to determine whether penetration is adequate and to watch out for trends that indicate potential performance degradation. In one commercial application of the technique – marketed by Laser Depth Dynamics Inc. (Kingston, ON, Canada) – the device connects to a laser-welding head assembly through a port occupied normally by a camera, through which a measurement beam of a specific wavelength is projected coaxially with the weld beam. Interferometry of the reflected measurement beam determines the depth of penetration. This takes place concurrently with the welding operation and has the potential for feedback control to the material processing beam. A method of processing interferograms based on homodyne filtering provides a degree of precision heretofore unavailable in commercial measurement devices, such that real-time process control during laser welding of 1-mm-dia. tubes is now feasible.

Subtask 1.1.2 Perform Bench Scale Testing of Heat Exchanger Concepts

Table 3: Cost Estimate – Laser Welding

Size: 5,000 kW			**Quoted**		**Required**		
Item	**Specification**	**Metric**	**Unit**	**$/unit**	**Units**	**Cost**	**$/kW**
Tubing	Inconel 625 tubing,	ft	100	30.52	2,174	$66,357	$13.27
Sheets	Inconel 625, estimated*	sq in	1	0.277	165,557	$45,859	$9.17
Containment	TBD, est. half of bundle material cost					$56,108	$11.22
Labor - welding	2 operators at all times	hrs	1	35	409.9	$14,345	$2.87
Labor - assembly		hrs	1	35	100.0	$3,500	$0.70
Other	Not estimated						
Total							**$37.23**
Target							*$50.00*

* Estimate based on quotes for sizes of 48x36 and 36x36-in sizes, respectively.

Another emerging method of laser-welding process monitoring uses high-speed camera-based image analysis. Cameras with specific optical filtering (with or without additional illumination) can provide high resolution images of the weld pool and seam, which can be digitally analyzed for specific traits that coincide with weld defects. Until recently, the speed of these cameras as well as the speed of affordable, computer-based image analysis has not been sufficient for use in high-speed laser welding, considering that the image capture and analysis time for these high speed welds needs to be in the range of 1 kHz in order to acquire a sufficient amount of information about the entire weld length. Fortunately, imaging technology has advanced so much so that 1 kHz frame rates and analyses are viable today.

Prototyping. The first DMLS prototype was tested at KAPL and confirmed high heat transfer capability, although pressure drop was very high because of under-designed manifold depths. The unit held pressure to 5,000 psi in tests at Thar.

Laser-welded Prototype 2 was completed in September 2013 and assembled to the pressure containment vessel, as shown in Figure 3. The completed unit was then sent out for code stamping for 2500 psi and 600°F, the conditions that KAPL expected to test. The unit was then returned to Thar for internal leak testing. Several pinhole leaks were discovered. In discussions with the welding subcontractor, it was learned that the entire bundle had been exposed to hydrochloric acid after all welding had been completed, so as to remove spacers that had been inserted between the tube ends in order to facilitate insertion into tube sheets. The tube bundle was declared a loss, and the subcontractor agreed to a re-build. Only the tube bundle was affected. The code-stamped containment vessel was fine.

A rebuild was executed on a fast track despite year-end 2013 holidays and was expected to be completed by January 17, 2014, with testing beginning immediately. Minor modifications were being made to the tube bundle to ensure easier insertion into tube sheets. Difficulties in this step led the laser machinist to apply acid (without prior authorization) to remove aluminum wires that helped align the tubes for insertion.

Figure 3: Laser-Welded Prototype 2: Pressure Container, Left, Shown Without End Caps so as to Expose the Side-stream Manifold. Tube Bundle, Right, Inserts through Center Hole. 640 Tubes Fill the Rectangular Opening in the Tube Sheet

Design Requirements: With regard to detailed design, which was underway, a couple of assumptions deserved special attention. One was the application of a 75% factor to the heat transfer coefficients for both hot and cold streams (Table 4). This was included as a conservative hedge against under-design. Another was the “area factor”. This factor attempted to account for the extra contribution to heat transfer efficiency by conductive effects of the unique hourglass configuration of the channels (value of 1.19 used). Note also, there was no effect from turbulence promoters, as indicated by a Nusselt No. enhancement value of 1.0. This was something that could have been added later in the form of flow turbulators in the hourglass channels, if necessary. The substantiation of these assumptions was a key objective of prototype testing.

An interesting outcome of this modeling was that the design length was surprisingly insensitive to tube count because the flow regime occurred near the transition zone of turbulence. Adding more tubes decreased flow velocity, resulting in lower Reynolds and Nusselt numbers, and ultimately lower heat transfer coefficients. Required length changed very little. This condition provided a great deal of flexibility in design and cost containment.

Table 4: Heat Exchanger Parameters

	Inlet Temp (C)	Inlet Press (bar)	Outlet Temp (C)	Outlet Press (bar)	Mass Flow (kg/s)
Hot CO_2	580	87	186	84	10.73
Cold CO_2	181	255	531	253	10.73

	Loss dP (bar)	Inlet Loss Coef	Outlet Loss Coef	HTC Eff (%)	UA	NTU
Hot CO_2	1.7	0.5	1	75	141,070	11.27
Cold CO_2	0.37	0.5	1	75	141,070	11.27

	Pitch (mm)	Tube Center (mm)	Hyd Diam (mm)	HX Length (m)	No. Tubes	No. Sheets
Hour Glass	1.6	1.6	0.526	1.504	40,000	260

	OD (mm)	ID (mm)	Diam (mm)	HX Length (m)	No. Tubes	No. Sheets
Tube Side	1.067	0.813	0.526	1.657	40,000	260

Subtask 1.1.3 Design for a 5 MWt sCO_2 Recuperator Detailed Design

The objectives of the prototype were to (1) prove the manufacturing method and (2) confirm calculations for heat transfer coefficients. No accommodation was made for thermal cycling, which was a major concern of the test loop recuperator. To that end, Thar relied on past experience with supercritical extraction systems and deployed sealing systems that have proved reliable in the past. This is explained in Figure 4, which calls out the differences between manifold designs at the hot and cold ends of the heat exchanger. (This drawing is not to scale and is for illustrative purposes only. In the full-scale model, the tube bundle is much larger in diameter. The relative thickness of the pressure containment vessel to the tube bundle is exaggerated.)

On the hot side, a sleeve enveloped the tube sheet and was welded to it. The sleeve was also welded to a casing that surrounded the tube bundle. A dam that was integral to the sleeve prevented short-circuiting of hot flow to the cold side. Metallic ring seals prevented leakage between inlet/outlet ports of the opposing streams. The hot end was fixed. On the cold end, the installation of a spring seal allowed for thermal expansion. This was an important benefit from a design point of view because it allowed for expansion of the tube bundle, especially during transients.

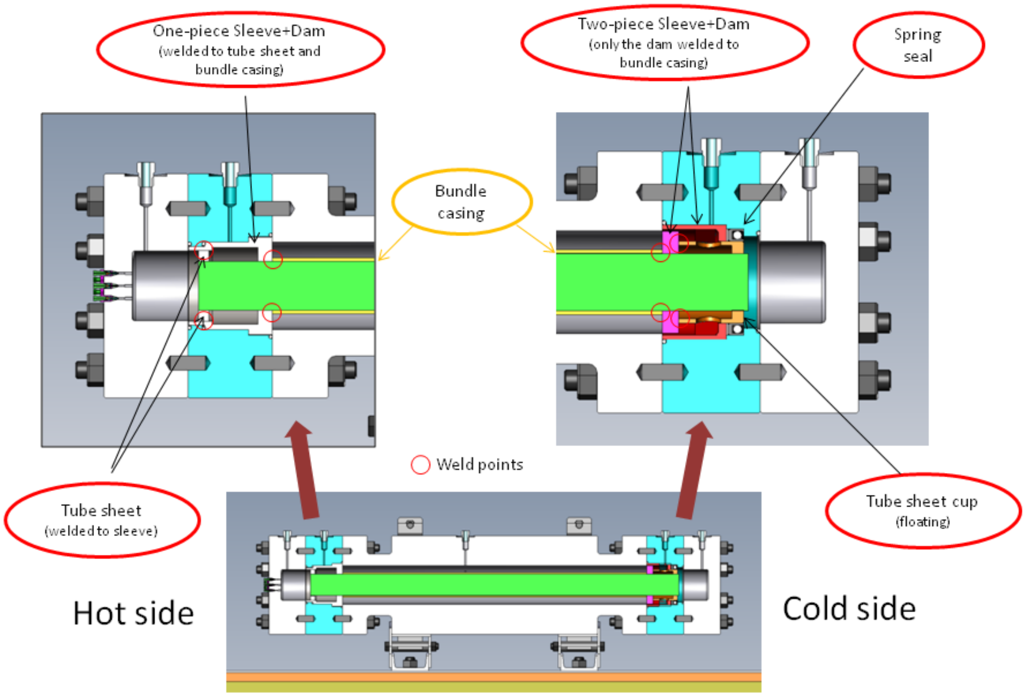

Figure 4: Manifolding for Thermal Expansion

On the cold side, the tube sheet was cupped and connected to the dam but not the sleeve. The tube sheet, dam, and bundle casing were welded together and moved axially inside the sleeve as temperatures change. The movement took place under the spring seal. The spring seal prevented leakage back to the inlet/outlet port of the manifold. Fluid could flow around the dam, which floated with the cupped tube sheet, but short-circuiting of fluid between hot and cold sides was prevented at the hot-side dam.

Detailed design was still taking place and was completed by the end of Phase 1. The solid model was large due to the high tube count, and software limitations in both mechanical design and simulations were being experienced. To cope with this problem, details in the tube bundle were limited. This was of little consequence because a CNC machine was not programed for the crucial laser welding operation. As for simulation, the team was concentrating detail on the manifold areas so as to optimize flow distribution. FEA was extensive throughout.

Once Phase 2 was underway, additional effort was put into the design of the fixtures that hold components down during welding. The basic tools and procedures for this have all been worked out in Phase 1 during building of Prototype 2. Furthermore, the difficulties that caused the re-building of Prototype 2 led to new designs and procedures for assembling the completed tube bundle to tube sheets. There is by now a great deal of know-how invested in this procedure.

Detailed design milestones: All of the design milestones, summarized in Table 5, were met. There are different definitions for the capacity of the recuperator, specifically whether the case is included in the volume calculation. Therefore, four different versions are shown in Table 5. The capacity of the bundle only meets the goal of 35,000 kW/m3. The test-loop recuperator was outfitted with extra pressure containment that would likely be avoided in a commercial design.

Table 5: Detailed Design Milestones

		Measure	Milestone Goal	Status	Comment
Detailed design of 5 MWt recuperator					
	Heat transfer area/volume*	m2/m3	> 1,000	1,588	Tube * area factor method
	Capacity**	kW/m3	35,000	41,500 25,500 23,500 10,500	Bundle only Bundle + internal manifolds Add axial inlet flow distributor Expand dia x1.5 for test loop pressure containment
	Pressure drop (hot side)	bar	1	0.77	
	Pinch temperature (cold side)	°C	5	5	
	Manufacturing cost	$/kWt	$50.00	$37.23	Labor and materials only

* Tube bundle alone

** Capacity components not defined in SOPO

Sizing milestones are discussed in Table 6. Opacity was not an official project milestone but was monitored nonetheless, so as to compare with state-of-the-art PCB heat exchangers. The tube bundle number of 30% compared very favorably to the typical 50% factor for PCB designs. The area density was also better. The design team applied a compactness factor of 1.19 to the minimum ID area so as to account for extra conductive heat transfer effects of the unique hourglass geometry. Thus, this design beat the milestone target by more than half. In order to better describe capacity, four different versions were tabulated. Also, the test-loop recuperator was being outfitted with extra pressure containment that would likely be avoided in a commercial design. The pressure container was based on the allowable stress for Inconel at the high temperature and the low pressure of the turbine exhaust. The high pressure was contained within tubes, which were sized with sufficient wall thickness. There was pressure relief on the container to guard against tube failure that could have increased the pressure within the containment enclosure.

Table 6: Compactness and Opacity

Parameters:

Tube count:	40,000		Low pressure:	1,300	psi
			Allowable stress:	20,000	psi
			Containment factor		
			Calc'd:	1.07	
Bundle length:	1.504	meter	Used here:	1.30	
Bundle diameter:	0.3125	meter	Heat duty:	5,000	kW

Milestone measure		Single	Total		Result	Target
Opacity		**m2**	**m2**		**Percent**	
	Opacity				30.2%	None
Areal density		**m2**	**m2**	**m3**	**m2/m3**	
	Eff. areal density, m2/m3				1,585	1,000
		Bundle Length	**Cross-section**			
Compactness		**m**	**m2**	**m3**	**kW/m3**	
	Bundle only	1.504	0.0767	0.1154	43,344	35,000**
	Add inlet/outlet manifolds	2.44	0.0767	0.1871	26,717	
	Add 2-ft conical inlet dist.	3.05		0.2034	24,582	
	Add pressure containment			0.3426	14,593	

* Single-sheet cross-sectional area based on average sheet chord width

** Capacity components not defined in SOPO

Workstation: During Phase 1, discussions were held and non-disclosure agreements were entered into with three systems integrators of laser-welding workstations. The best estimate of cost that could be made at that time for one of these stations was $0.5 million. The concept presented by Lincoln Electric is shown in the following figures. Figure 5 presents a schematic of the workstation along with a list of recommended equipment. The workstation is in two parts, each of which is serviced by the same laser generator. On the left is the area where the tube bundle would be welded and stacked. The optics are simplified in this station because only longitudinal welding was performed. A nice feature of this station is the turntable, which rotates in and out of the protected area (worker protection against accidental exposure to a laser beam). Because there is a lot of hand work involved in assembling tubes and sheets into the hold-down fixture, we placed two such fixtures on the turntable, one of which was under the laser beam in the protected area, while the other was outside being outfitted with fresh material by hand. This turntable eventually supported the entire tube bundle. Lincoln Electric had assured us of its ability to construct turntables strong enough to handle the load.

On the right side of Figure 5 is the station for laser welding of the tube sheets. It was expected that the completed bundle will be brought into this station by crane or fork-lift through the wide door provided and then fixed in place for welding. The optics for this operation required scanning equipment that was not needed in the other station, so as to complete circular butt welds. Because the two stations were not in service at the same time, a single laser generator sufficed.

Actual examples of the workstations depicted in Figure 5 are shown in Figure 6. The nameplate “Wayne Trail” on these stations refers to the integration unit of Lincoln Electric (Cleveland, Ohio).

Lead Times*:* There were significant lead times that could have affected the delivery of the recuperator in Phase 2. Once Phase 2 was green-lighted, orders needed to be place immediately for tubes and the workstation. Both had delivery lead times in the range of 16 to 18 weeks.

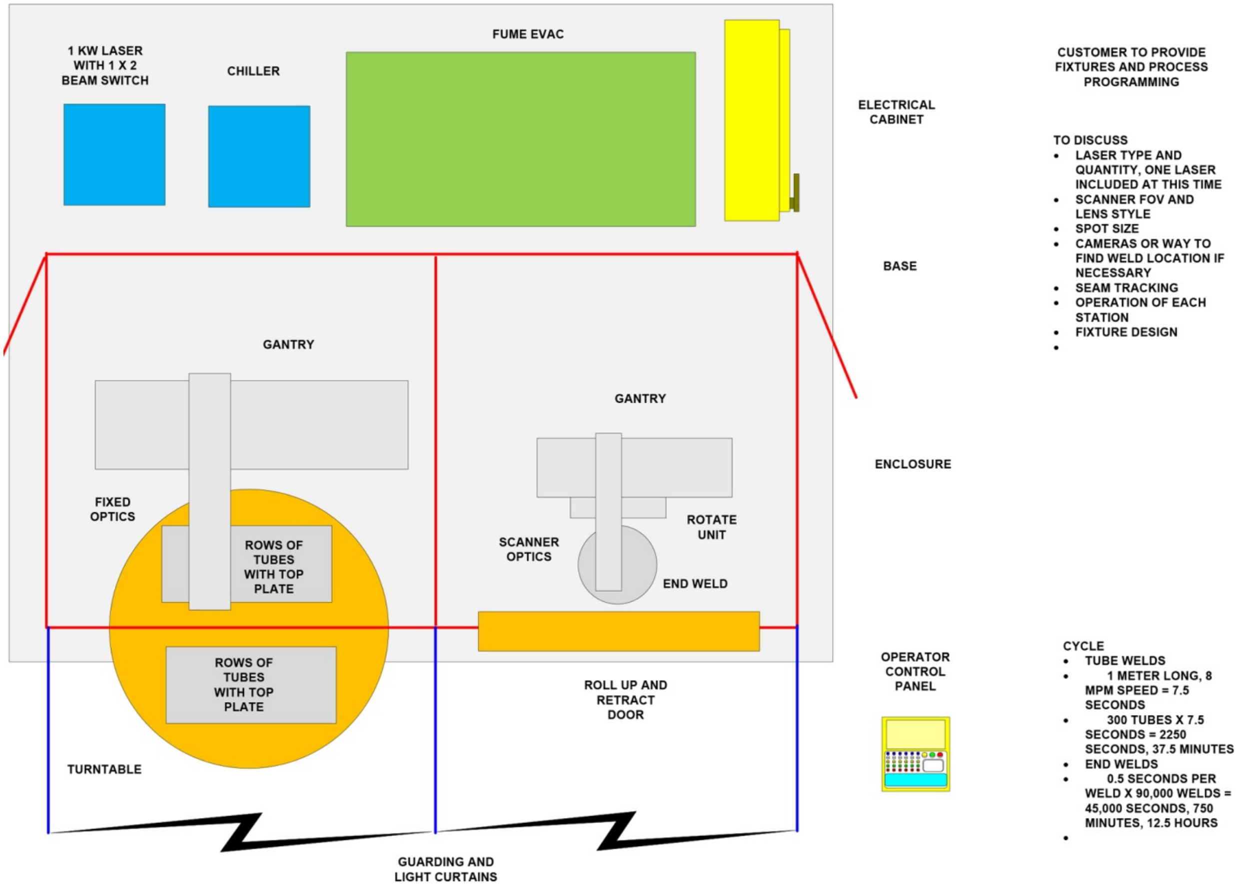

Figure 5: Laser Workstation Concept

Figure 6: Turntable Station for Bundle Assembly (Left) and Open-door Robot Station for Tube Sheet Welding (Right)

Laser welding was the first fabrication technique used to construct the prototype recuperator. A number of fabrication limitations developed based on the precision of the completed tube/separator sheet stack and the holes drilled in the tube-sheet. To address these limitations, aluminum wire was weaved to evenly space the tubes, see Figure 7, to better allow the tubes to mate with the holes of the tube sheet.

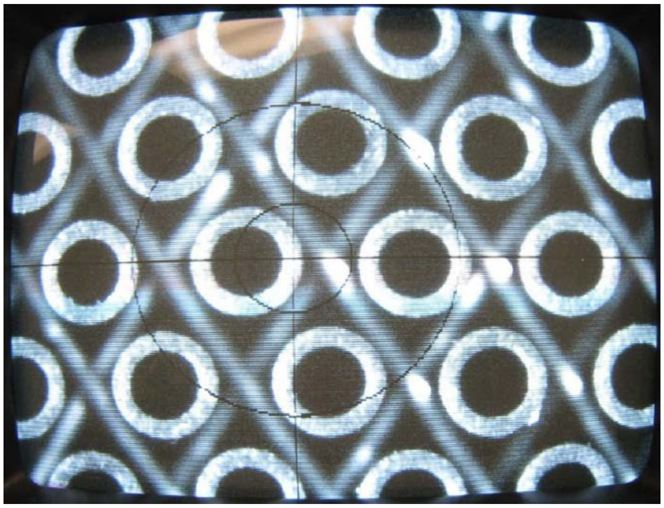

Figure 7: Photo of Microtubes Aligned with Aluminum Wire Weave

After the microtubes were laser welded to the tube sheet, the aluminum wire was dissolved in acid. Unfortunately, the vendor selected an acid that also damaged the stainless steel tubing.

To repair the damage done by exposure to acid, a method for brazing the damaged parts was developed.

The laser welded/braze repair prototype was tested at KAPL at 2,500 psi at 600˚F. The test results indicated that the recuperator capacity to transfer heat meat or exceeded design conditions.

The braze repair method worked so well, a program to implement the braze joining of the microtubes to the tube-sheet as a preferred fabrication method was pursued.

A series of brazing qualification tests were performed, using mechanical tests and metallurgical evaluations. Additionally, thermal cycling tests were conducted at ~6,500 psi. The brazed joints were cycled >200 times from room temperature to 550˚C (1,022˚F) with no sign of damage identified.

With the braze-joining method qualified, it was selected as the fabrication technique to join the microtubes to the tube-sheet.

Task 1.2. Turbo-Machinery Design

The turbo-machinery design task under this program was to deliver a turbine design for subsequent manufacturing and testing in Phase 2 and 3 that meets the DOE SunShot target of delivering 50% thermal conversion efficiency at 43°C ambient conditions with air cooling. Under this program, the team was targeting to achieve the required power block conversion efficiency using a supercritical CO_2 re-compression Brayton cycle in the 10MWe range. The power block size was decided based on the feasibility of a tower mounted re-compression power cycle for CSP applications as discussed by Turchi et al. and in the proposal. Block diagram of the recompression cycle for this application is shown in Figure 8. This power cycle is highly recuperated with moderate expansion ratio on the order of 2-4 across the expander. A re-compression loop was employed by splitting the recuperator and transferring fraction of the flow (~20%) before the pre-cooler into a second compressor (re-compressor in the block diagram below) to achieve higher recuperation rates by matching the heat transfer curves in the recuperator and thus achieving higher thermodynamic conversion efficiencies.

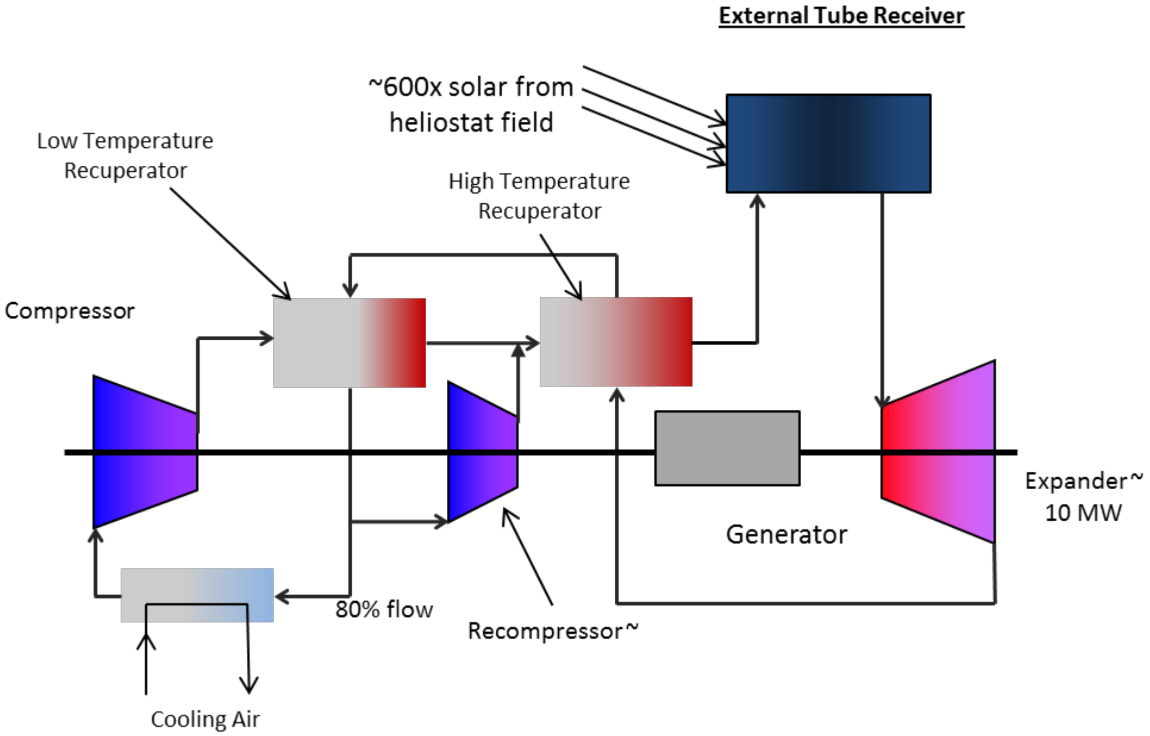

Figure 8: Proposed Re-Compression CO_2 Brayton Cycle Layout for CSP Application

Subtask 1.2.1 Steady and Transient Aerodynamic 1-D Flow Design

In this task, the power cycle operating conditions were optimized for a CSP plant operation in Dagget, California, as a reference location. For Dagget, California, the variation of ambient temperature over the year is shown in Figure 9 (a). For most relevant operation of a CSP power plant, the design point performance was optimized for Direct Normal Irradiance (DNI) weighted ambient temperature. This resulted in highest power block efficiency at most probably ambient conditions. The optimal turbine pressure ratio for given turbine inlet conditions is a strong function of the ambient temperature, therefore, the selection of design point ambient conditions was critical for turbine design activity. This is shown in Figure 9 (b). For Dagget, California, the DNI weighted ambient temperature was 24°C, and the optimal turbine pressure ratio was ~3.5. The turbine operating conditions: inlet temperature, pressure and pressure ratio were selected to meet the DOE SunShot target (50% efficiency at 43°C ambient). Keeping this as a constant, the operating conditions were then optimized for DNI weighted ambient temperature resulting in design point pressure ratio and turbine inlet conditions. The calculated power block overall efficiency was 54% at DNI weighted ambient temperature.

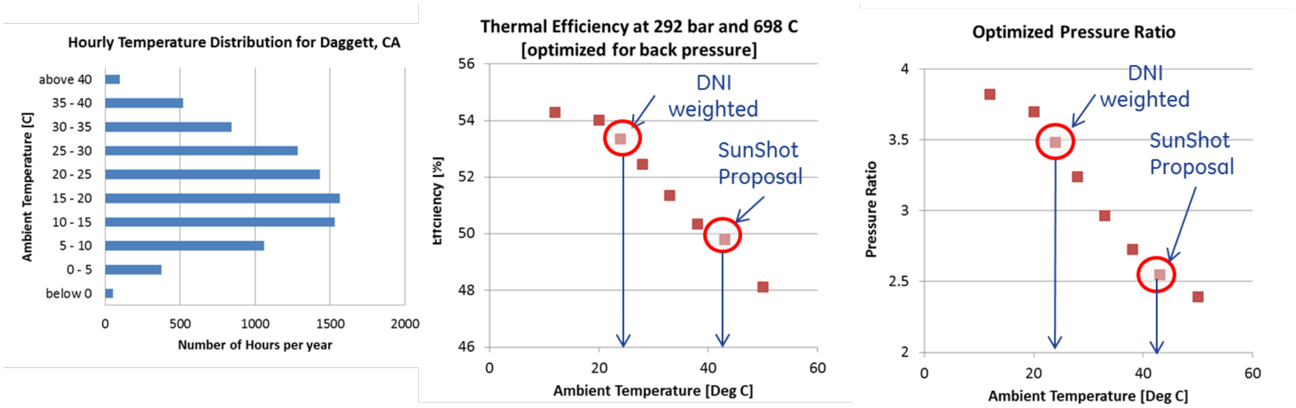

Figure 9: (a) Ambient Temperature Variation at Dagget, CA (Source: Solar Advisory Model (SAM) from NREL); (b) Variation of Power Block Thermal Efficiency as a Function of Ambient Temperature at Constant Turbine Inlet Pressure (292 bar) and Temperature (698°C); (c) Optimal Turbine Pressure Ratio for a Given Ambient Temperature Corresponding to Efficiency Curve in (b)

As the pressure ratio increased for optimal operation of the power block from 3.0 to 3.55, at a relevant location in western US (Dagget, California), the turbine aero design got more challenging. The volumetric flow rate at the inlet was low enough such that the radial clearances at impeller blades were a significant fraction of the impeller height. This resulted in achieving high aerodynamic efficiency on the order of 90% difficult to achieve in a reasonable number of turbine stages. Similar consideration existed for compressor designs. The two compressors employed in this power cycle were within the industrial experience and capability range. To mitigate some of the turbo-machinery design challenges, with the help of aero design iterations and material temperature capability studies presented later, the turbine operated conditions were modified as shown in Table 7, while keeping the thermal conversion efficiency constant.

Table 7: Modified Turbine Inlet Conditions from the Proposal to Enable Feasible Aero Design and Efficiency

Parameter	Original Cycle (Proposal)	New Cycle (Turbine design point)	Comment
Inlet Pressure (bar)	292.6	250.6	Reduced by 40 bar
Inlet Temperature (C)	698	715	Moderate Increase
Inlet Volume Flow Rate (m3/s)	0.51	0.64	Increased by 26%
Recuperator Duty (MW)	39.5	47	15% increase
Pressure Ratio	3.55	3	Lower

The increased volumetric flow rate and reduced inlet pressure helped achieve higher turbine aero efficiency due to lower seal leakages while maintaining thermal conversion efficiency by a moderate increase in turbine inlet temperature and recuperator duty. The turbine thermodynamic boundary conditions discussed above along with the performance and life targets presented in the proposal define the product (turbine) requirements documented in Table 8 that would meet the overall program goals. The turbine speed spec in the table is derived directly from the FOA, the fault torque requirement is derived from the generator selection, similarly, the thermal transient requirements from the FOA, and are presented later in this report. Also, the turbine boundary conditions were primarily selected based on the SunShot target (50% power block efficiency), the impact of this selection on the LCOE and sensitivity of various component specs is presented in detail under Task 1.4. The turbine speeds presented are approximate to yield high efficiencies and will be refined later in the detail aerodynamic and mechanical design.

Table 8: Product (Turbine) Requirements

Spec	Unit	LSL	Target	USL
Expander isentropic efficiency	%	87	89	91
Expander inlet temperature	C	705	715	725
Expander inlet pressure	bar		250.6	
Expander outlet pressure	bar		83	
Expander inlet total mass flow rate	kg/s	83	85.9	87
Expander speed	rpm	25,200	28,000	30,800
Expander leakage flow rate	kg/s	1.5	3.0	4.5
Compressor exit – turbine inlet: pressure drop	bar	5.0	6.4	7.5
Expander design point shaft power	MW	13.65	13.85	14.0
Operating hours per year	hour/yr		3000	
Full thermal cycles per year	#/yr		360	
Allowable time to reach operating temperature	min		20	
Receiver/expander thermal ramp rate	C/min		35	
Max temperature ramp down rate (cloud event)	C/min		40	
Expander O&M interval	Hours		24,000	
Expander service life	years		30	
Expander service life	hours		90,000	
Total start-up cycles	#		10,000	

Sub-subtask 3.4.1.1 Aerodynamic Flow Design (Cycle Deck)

This section documents the aero design of a nominal 10 MW expander for a sCO_2 power cycle designed for use in a concentrated solar plant. The intent is to capture the final design configuration only and not the many iterations that were made on the path to the final design.

Design Tools: Initial design concepts were explored using a spreadsheet based tool due to the ease in accommodating the sCO_2 properties via NIST Refprop. Once a candidate design was selected, models were built in the traditional GE design system using TP3, CAFD, and BBP with equivalent perfect gas properties. To verify the design, a TACOMA (CFD) simulation was run using both perfect gas properties and tabular properties for sCO_2 developed for this project using Refprop.

Requirements: Overall thermal design requirements were established by the thermodynamic cycle for the concentrated solar power plant and are summarized in Table 8. Note that the turbine flow rate is the difference between the overall expander primary flow rate and the secondary (leakage) flow rate. In this case the turbine design flow is 82.9 kg/s. In addition to the cycle requirements, mechanical design analysis was performed on intermediate aero designs providing feedback on the levels of static stress due to rotation. This resulted in the need to minimize the blade heights and tip diameters resulting in an aero design with flow coefficient increasing from inlet to exit. Additionally, the bending stress on the airfoils due to the gas load from the dense high pressure CO_2 resulted in the need for high solidity, low Zwiefel number blade rows. Aeromechanics analysis on an intermediate turbine design resulted in the airfoil counts documented in Table 9 to maximize margins on the interference diagram.

Table 9: Nozzle and Blade Counts

Stage	Nozzle Count	Blade Count
1	30	40
2	28	40
3	26	36
4	26	30

Flowpath Selection: Several flowpath layouts were considered throughout the conceptual design phase of the turbine. Once the design configuration was down-selected to a multi-stage axial, directly coupled to a centrifugal compressor (sized but not designed by GE Oil and Gas) a study of several three stage and four stage designs was made. To reduce mechanical stresses and improve efficiency, a four stage design at 27,000 RPM was chosen, over three stage designs at higher speed. A summary of these designs is shown in Figure 10. Further refinement of both the cycle and the mechanical design led to a four stage design with a decreased root diameter of 4.25 inches, shown pictorially in Figure 11.

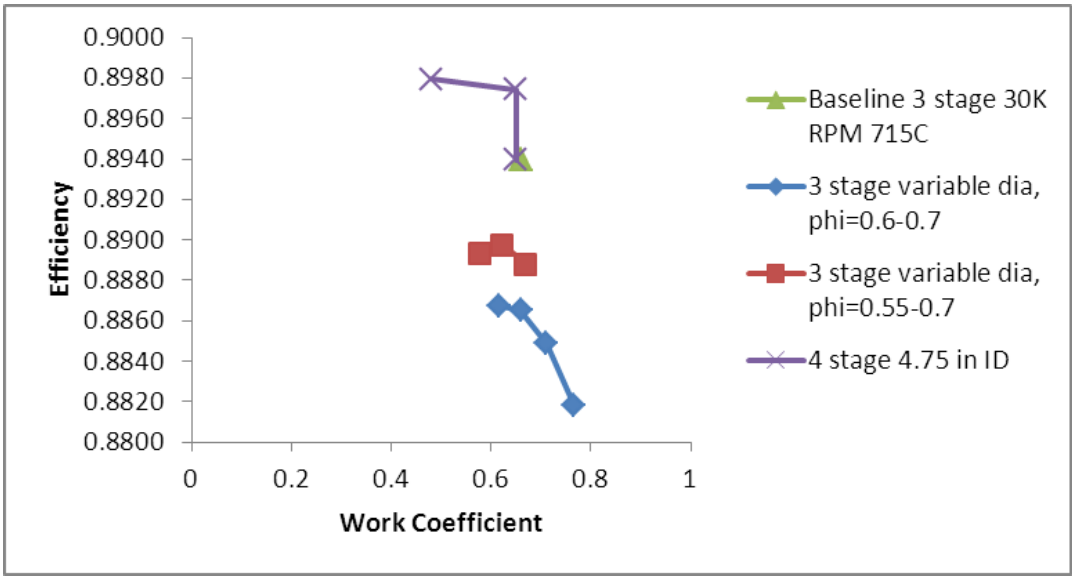

Figure 10: Flowpath Design Space Study

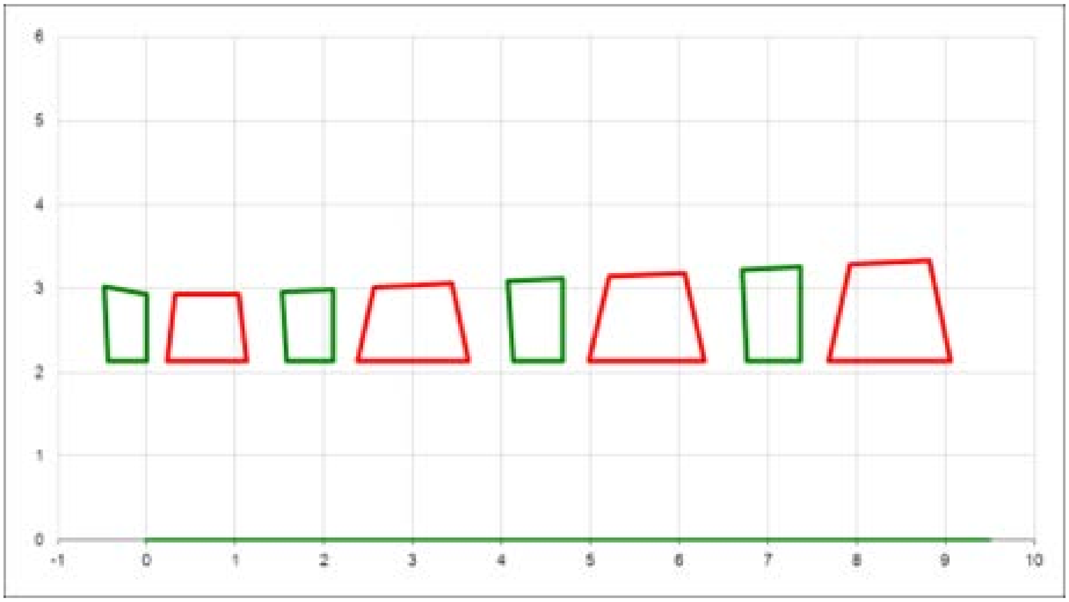

Figure 11: Preliminary Flowpath Layout

Flowpath Design: The chosen flowpath was recreated using the design mode in TP3. For this step, the working fluid was assumed to be a perfect gas with gamma=1.215 and R=35.125 ft*lbf/R*lbm. Predicted performance for the 4 stage turbine was 91.24 on a total to total basis and 87.90 on a total to static basis. This efficiency does not include the impact of leakage flow through the nozzle seals on Stages 2 – 4 which was estimated to be 2 points resulting in corrected efficiencies of 89.24 total-to-total and 85.90 total-to-static. While the exhaust diffuser has not been designed yet, a diffuser sufficient to recover 40% of the difference between the total to total and total to static efficiencies will result in a total to flange efficiency of 87.24 which meets the lower spec limit on turbine efficiency. A free vortex meridional design of the turbine was done in CAFD to set the throat dimensions and inlet angles for each of the blade rows. A view of the flowpath showing the station numbering is shown in Figure 11. This analysis was done with the same perfect gas fluid properties used for the TP3 analysis. Note that the flowpath was designed with an increasing flow coefficient (VZ2/U2) to minimize the increase in blade height in the later stages of the turbine. The blade rows were also designed with high solidity to maximize the available cross sectional area for carrying the stress in this very power dense turbine. Because the hub/tip diameter ratio for this turbine is around 0.7, there is a significant change in the vector diagrams between the root and tip of the rotating blades due to the difference in peripheral speed. This change in vector diagrams resulted in a large change in inlet relative flow angle for the rotating blades, a corresponding change in stagger angle, and the significant taper in axial width evident for the rotor blades in Figure 12. The computed flow properties from CAFD were used to set the boundary conditions for 2D airfoil section designs at 5 radial locations for each of the 8 airfoils. Representative plots for rotor 1 are shown in Figure 12 where Station 1.6 is the rotor leading edge and Station 1.9 is the rotor trailing edge. For all blade rows a trailing edge thickness of 0.020 inches (0.5 mm) was used. Airfoil design was done using BBP and Novak blade to blade solver. The resulting airfoils are shown in Figure 13.

CFD Analysis: To confirm the quality of the design, a 3D CFD analysis using TACOMA was performed. This analysis was done with two different fluid models, first with the perfect gas assumptions used for the design and second with a tabular CO_2 equation of state generated from the RefProp database specifically for this project. Computational meshes were generated for each blade row containing about a million grid points with an average y+ between 30 and 45. Figure 14 shows a representative mesh from the pitch section of the first vane.

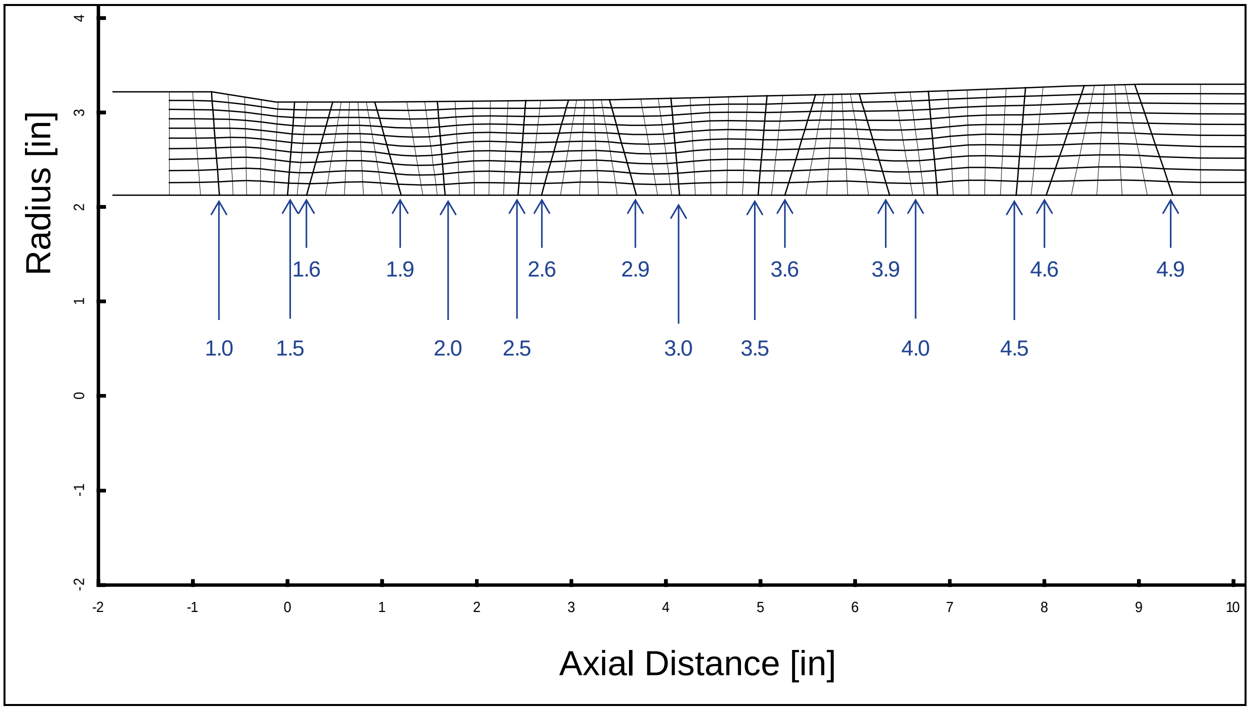

Figure 12: CAFD Turbine Layout

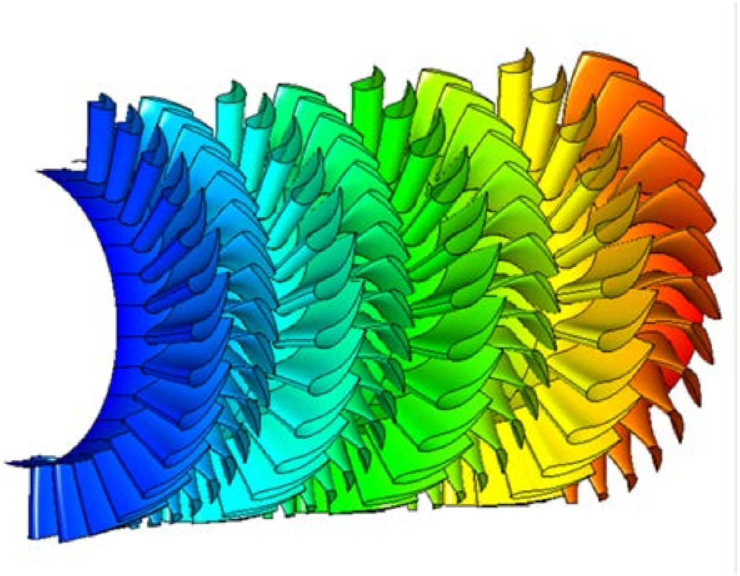

Figure 13: Airfoil Design

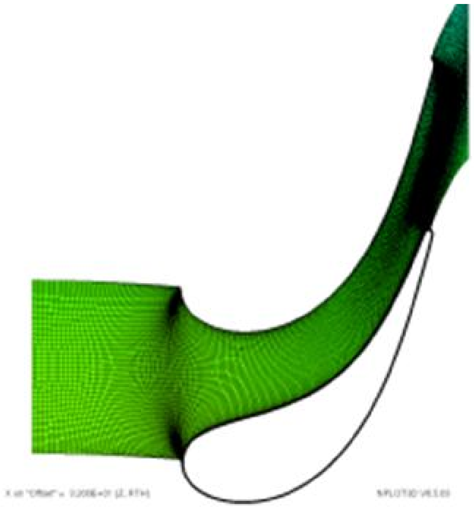

Figure 14: Vane 1 Mesh

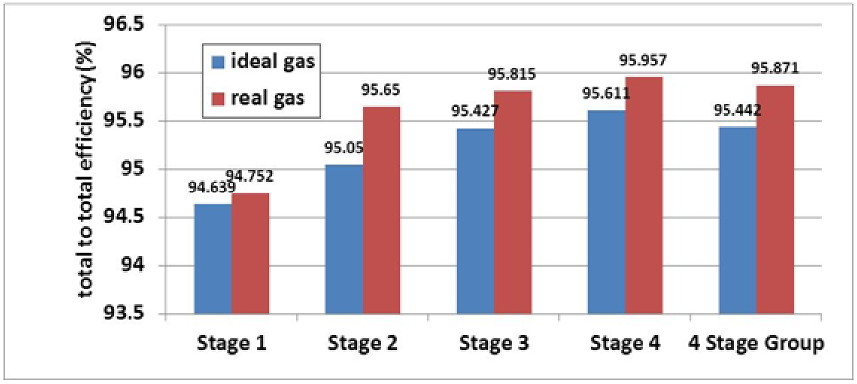

Figure 15: Comparison of Ideal and Real Gas CFD Efficiencies

Comparisons of the blade row efficiency and overall turbine group efficiency between the perfect gas CFD computation and the tabular CO_2 CFD computation using the same boundary conditions and meshes show a slightly higher efficiency for the tabular CO_2 case as can be seen in Figure 15. Note that the efficiencies shown in this plot do not include the effects of any leakages either over the rotor tips or under the nozzle hubs so are significantly higher than those calculated by TP3. Because of the omission of leakages from the CFD calculations, the TP3 values are more representative and should be used when evaluating cycle performance. Comparing between the perfect gas case and the CO_2 case, the efficiencies are generally within 0.5 points indicating that executing the design process using ideal gas properties was a reasonable compromise although there may be some potential for optimization using the tabular CO_2 CFD results to guide design iteration.

Conclusions: Due to the extreme power density associated with a supercritical CO_2 turbine and the high temperatures needed to meet the SunShot cycle efficiency goals, the mechanical design of the turbine was extremely challenging. Meeting the mechanical design requirements required compromises in the aero design of which two are significant. The most significant is the high solidity and low Zwiefel blade row designs needed to meet the bending stress requirement. The high solidity increased the wetted area of the blade surface and thus increased the losses due to wall friction. The second significant factor was the need to keep the tip speed low to minimize the static stresses due to the centrifugal loading. This requirement resulted in a large through flow velocity in the last stage to minimize the blade height and a greater than optimal exit velocity. This exit velocity was the reason for the relatively large difference between the total-to-total and total-to-static efficiencies. Some of this kinetic energy leaving the last stage can be recovered with an exhaust diffuser but a longer blade with lower exit velocity would result in a higher realized efficiency. Improved material capability and better understanding of the mechanical design requirements for the power turbine in a concentrated solar power cycle should offer opportunities to re-optimize the design and improve the aerodynamic performance of the flow path. The data and experience coming from the SunShot program were key steps to improving understanding of these requirements.

Subtask 1.2.2 Machinery Component General Layout

The overall power block for CSP installation using recompression CO_2 cycle has the following rotating machinery: expander, main compressor, re-compressor, and generator. These components can be organized in various different layouts and rotational speeds, and the system configuration would provide different overall thermal conversion efficiencies for the same primary component designs. The layout options for recompression cycle turbomachinery are listed in Table 10.

Table 10: Turbo-Machine Layout Options (IC: Inductively Coupled, PM: Permanent Magnet, 3,600 rpm Synchronous Generator)

Option	Generator	Compressor	Turbine	RPM
High speed, Optimal	A. IC B. PM	A. Single stage centrifugal B. Multi stage pump	A. Radial B. Axial	Optimized for compressor
High speed, expander only	A. IC B. PM	None	A. Radial B. Axial	Optimized for expander
High speed, Geared	A. IC B. PM C. 3600 rpm	A. Single stage centrifugal B. Multi stage pump	A. Radial B. Axial	Both expander and compressor run at optimal speed
3600 rpm integrated	3600 rpm	Multi stage pump or compressor	Multi stage Axial at 3600 rpm	3600 rpm
3600 rpm – expander only	3600 rpm	None	Multi stage Axial at 3600 rpm	3600 rpm

In Table 10, all the possible configurations of the turbomachinery layout that can be used in a modular CSP power plant have been included. Using this table, the common components from each layout were selected for preliminary design to feed into rotor-dynamics analysis and initial down-selection.

1. Turbine wheels
    a. Axial turbine designs
    b. Radial turbine designs
2. Compressor wheels
    a. Centrifugal compressors
    b. Dense flow pumps
3. Generator
    a. Synchronous generators (low speed)
    b. Induction generators
    c. Permanent magnet generators
4. Generator cooling analysis
5. Pressure containment / casing design
6. Sealing system design
7. Bearing and rotor dynamics analysis

Using this analysis and component designs, a more detailed study of the four feasible designs was performed, and the impact of layout was quantified on the overall system performance. The block diagram schematic of four feasible designs is shown in Figure 16. Down-selection activity required that the designs needed to be mature enough to understand the system level impacts of each layout included detailed aero-design, generator selection, gearbox selection, compressor wheel selection (off-the-shelf), sealing system designs, rotor-dynamics, and bearing designs for each design. These details are not presented here.

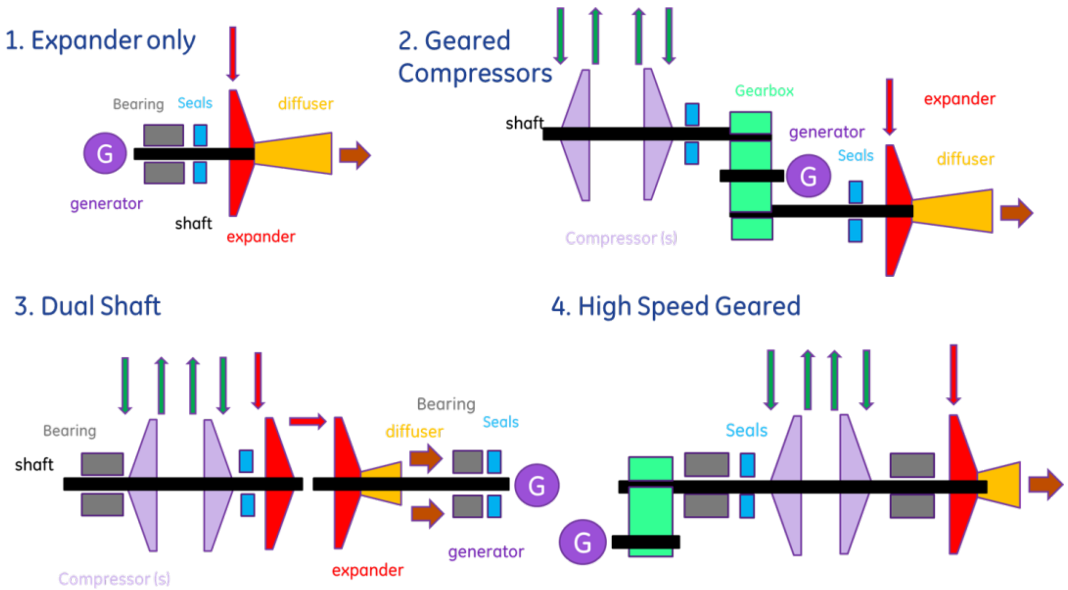

Figure 16: Block Schematic of the Four Feasible Layouts for Recompression CO_2

Brayton cycle based modular CSP power blocks. (1) Direct drive or geared turbo-generator with undefined motor driven compressor, (2) Geared compressor train with direct drive or pinion geared generator, (3) a dual shaft concept with a single expander stage driving the compressors, while a second shaft with turbo-generator – direct drive or geared, and (4) a single shaft concept with both expander and compressor train running at same speed with a geared generator.

The down-selection of this turbomachinery architecture was based on trade-off analysis using performance and cost comparison divided into the following four (4) categories:

1. Annual energy production (AEP)
2. Cost of the machine and system cost
3. Operation and maintenance (O&M) cost
4. Commercialization criteria

The weighting of each criterion was derived from its weight going into the LCOE calculation. For commercialization activity, the weights were derived directly from Task 3.2 of this program (commercialization activity). This resulted in clear identification of the best design to be pursed in this program. In addition to the best design, a second option with significantly lower technical risk but also lower scores on the criteria list has been selected a back-up. The down-selected design is shown in the layout Option 4 in Figure 16.

The turbo-machinery layout finalized for the system design and commercialization activity under Task 1.4. This task primarily focused only on the turbine design with shaft speed, mass flow rate, leakage requirements, and efficiency targets that are boundary conditions. The aero-design meeting these design requirements has been presented in Subtask 1.2.1. With this aero design the rotor mechanical design and assembly methods are evaluated and presented in the next section.

Subtask 1.2.2.1 Rotor Mechanical Design

For the turbine rotor, three potential configurations were considered for manufacturing and assembly:

a. A conventional dovetail attachment of airfoils to a rotor disc for each turbine stage, with each stage then coupled to the rotor shaft using attachment/torque transmission methods such as a center tie bolt or Hirth couplings

b. An integral Bladed Rotor, also referred to as a bladed disk or ‘blisk’ where the airfoil and rotor disc are machined as a single integral piece from a one piece solid forging and then attached to the rotor shaft using attachment/torque transmission methods such as a center tie bolt or Hirth couplings

c. A fully integrated concept with the rotor shaft, disc and airfoils machined from a single billet as a monolithic component

In each of the above cases, based on the aero efficiency requirements, a design decision was made to use shrouded airfoils in order to reduce leakage flows. Based on the calculated airfoil sizes and counts, it was determined that the option of inserting airfoils into a rotor disc with dovetails would be infeasible due to:

a. Very small dovetail geometries to carry the centrifugal loads at acceptable stress levels to enable the rotor to have a useful service life

b. Limitations in manufacturing capabilities to broach the required dovetail slot dimensions.

Manufacturing Feasibility of a Fully Integrated Concept: Manufacturing of the turbine rotor with integral blades and shroud was evaluated to prove feasibility of this design. The closed passages between blade rows can be manufactured using Electrical Discharge Machining (EDM) or Electro-Chemical Machining (ECM). This is challenging for the current turbine design due to small blade height on the order of 1 inch, highly twisted blade airfoils to achieve high efficiency, and high surface finish and tolerance requirements. Various manufacturing processes were evaluated for this shaft and EDM for machining followed by Abrasive Flow Machining (AFM) for high quality surface finish were selected. EDM of the airfoils for machining was most challenging for the Stages 2 and 3, where accesses to the airfoils for machining was limited from both sides due to adjacent stages on the shaft. This problem was resolved by using L-shaped electrodes from either side for airfoil machining and appropriate inter-stage spacing between the stages for appropriate access. The second problem concerning with the highly twisted airfoil in the radial direction was resolved partially by the use of access from both sides and also by splitting the machining electrodes in the radial directions. Manufacturing simulations were used to optimize the number of electrodes required for fabrication without tool interference. This method of machining for 2nd stage airfoils is shown in Figure 17 along with the electrode design.

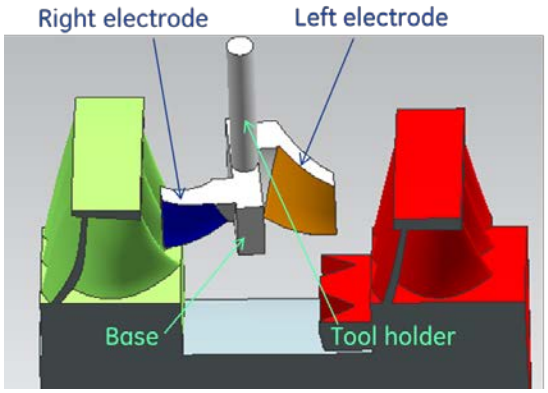

2nd stage electrode design:

- Need 4 electrodes
- Electrodes can assess the gap between blade rows
- Left and right electrodes are assembled on a base and that eliminates secondary fixtures

Figure 17: EDM Electrode Design for Manufacturing of the Second Stage Airfoils on an Integral Turbine Shaft

Subtask 1.2.3 Lateral and Torsional Rotor-Dynamic Stability Analysis

Figure 18 shows the basic layout of the expander rotor. The middle section is the core consisting of four axial stages and nozzles as per the aero design from Section 1.2.1. On the left side, the inlet plenum is a provision for the inlet ducting and the first nozzle. Upstream of the inlet is the balance piston and a 4’’ cooling management length to cool down the flow by injecting a cold flow bringing down the temperature to a level that can be withstood by the state-of-the-art Dry Gas Seal (DGS). Three-fourth (¾) inch axial space separates the DGS from the radial bearings, and one (1) inch separates the radial bearing from the generator-side coupling end on the left. The sections downstream of the core are similar to the sections upstream, starting with a cooling and diffuser section, followed by a DGS, and a radial bearing. Thrust bearing section sits between two 1’’ axial spaces on either side to provide for casing support and separate the bearing from the compressor-side coupling. A summary of the main rotor structure facts is compiled in Table 11.

The rotor material is Nimonic 105 and details of material selection are presented in a later section. The stiffness of the material is temperature dependent. The Young’s modulus for the length of the rotor between the middle of the two cooling management sections is taken at 700°C. Young’s modulus at 200°C is used for the reminder of the rotor.

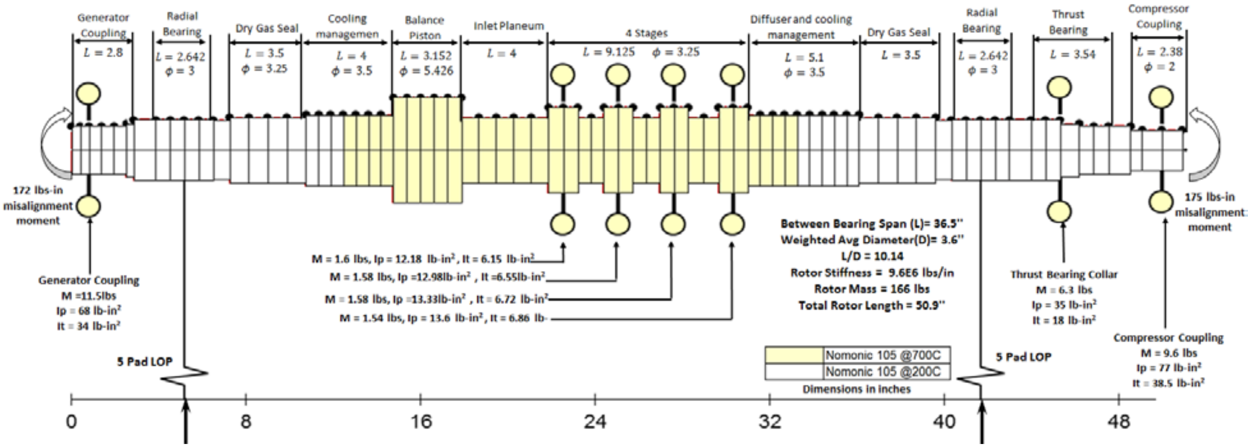

Figure 18: Rotor Layout with Axial Lengths and Diameters Noted in Inches

Table 11: Rotor Structural Properties

Between-Bearing Span	36.5''	0.92 meter
Total Rotor Length	50.9''	1.3 meter
Average Between-Bearing Diameter	3.59''	0.091 meter
L/D	10.14	
Rotor Weight	133 lbm	60.3 Kg
Total Weight (rotor +stages + Couplings)	166.5 lbm	75 Kg
Rotor stiffness	9.6E6 lb/in	1.68E9 N/m
Compressor-end Bearing Static Load	78.5 lbf	349 N
Generator-end Bearing Static Load	87.9 lbf	391 N

The main destabilizing forces acting on the rotor are annular gas seal forces and Alford aerodynamic forces. Because radial bearings are tilting pad type, they are not considered as a source of destabilization. Also the dry gas seals do not contribute towards lateral destabilizing forces.

Rotor-dynamic Coefficients for Balance Piston Seal are Frequency Dependent: The predictions of the variation of the hole pattern seal on balance piston effective stiffness and damping are shown in Figure 19. The acoustic effects of the holes create a dependency of the seal reaction forces on the frequency of the vibrations. This effect is critical to the stability of the machine since the forces of the hole pattern seal are considerable and can have pronounced effect on the stability and dynamics of the machine.

The variation of the effective damping of hole pattern seals show a transition from negative to positive damping with a sharp negative damping at low frequencies. The frequency where the effective damping crosses from negative to positive is referred to as cross over frequency. For stability, it is important that the cross over frequency be below the first sub-synchronous vibration mode of the rotor, otherwise the machine will suffer a significant destabilizing effects from the hole pattern seal. Because hole pattern seals are frequency dependent, the process of evaluating the stability of the sub-synchronous modes becomes iterative.

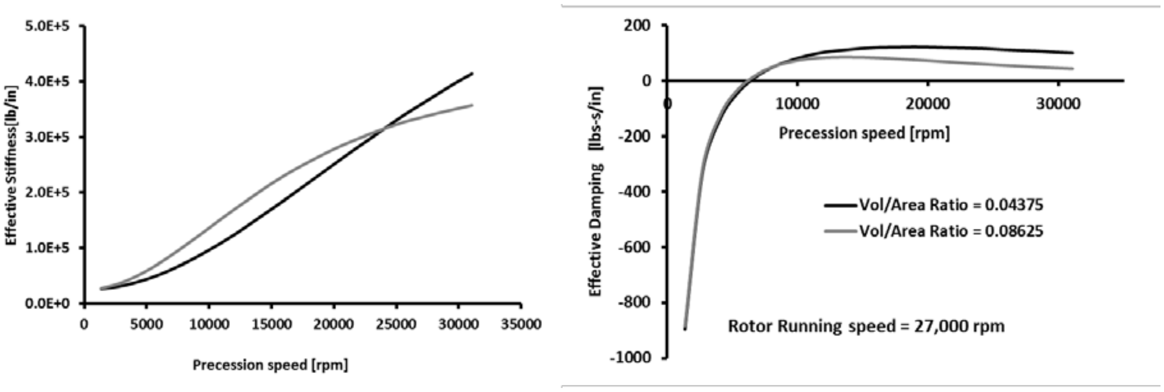

Figure 19: (a) Variation of the Balance Piston Hole Pattern Seal Effective Stiffness with Precession Frequency and (b) Effective Damping Variation with Precession Frequency

In addition to the force coefficients frequency dependency, hole pattern seals are sensitive to changes in the taper angle. The taper angle is the conning of the seal creating either a divergent clearance (where the clearance of the seal exit is larger than the clearance at the inlet), or a convergent clearance (where the clearance of the seal inlet is larger than the clearance at the exit). The rotor-dynamic stability and effective stiffness for the balance piston hole pattern seal with ±30% taper angle is shown in Figure 20. For the same precession frequency; effective damping of a divergent seal is larger than a convergent seal, and effective stiffness of a divergent seal is less than a convergent seal. The combined effect of the effective damping and stiffness is that divergence increases damping but reduces the first critical speed of the rotor closer to the cross over frequency. While convergence increases the critical speed of the rotor (due to higher stiffness), but pushes crossover frequency up.

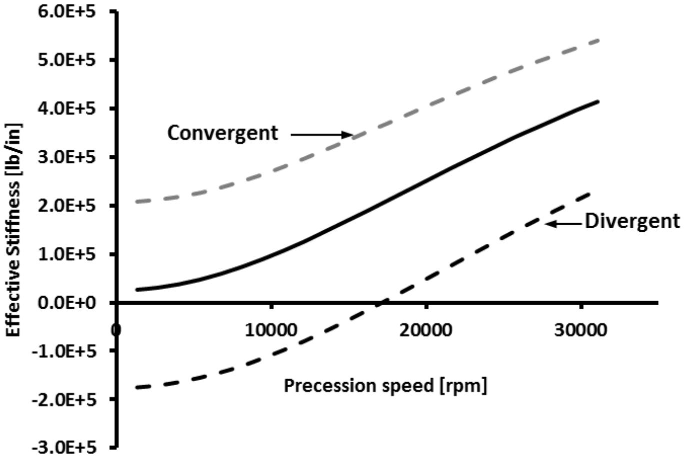

Figure 20: Effects of Taper Angle on the Effective Stiffness of Hole Pattern Balance Piston Seal

The rotor-dynamic predictions of the inter-stage labyrinth seals direct stiffness and damping are calculated similarly for the four turbine stages. The seals have a negligible effect in terms of forces. However, labyrinth seals are known to develop strong cross-coupled stiffness and significant negative effective damping. The cross-coupled stiffness of the first and fourth stages are shown in Figure 21. The effective damping of the seals will be compared to the destabilizing Alford forces in the next section.

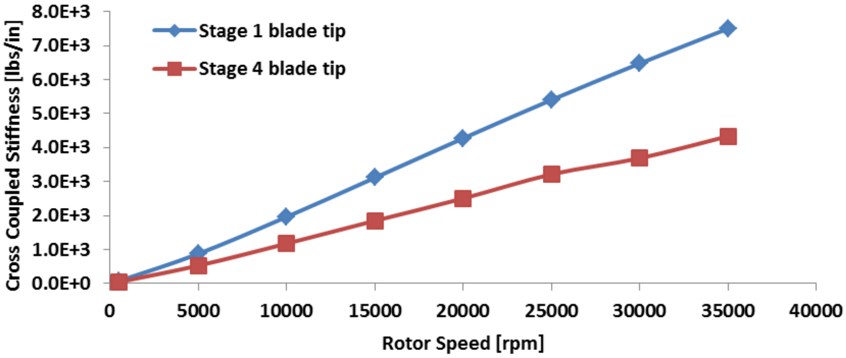

Figure 21: Inter-Stage Labyrinth Seal Kxy

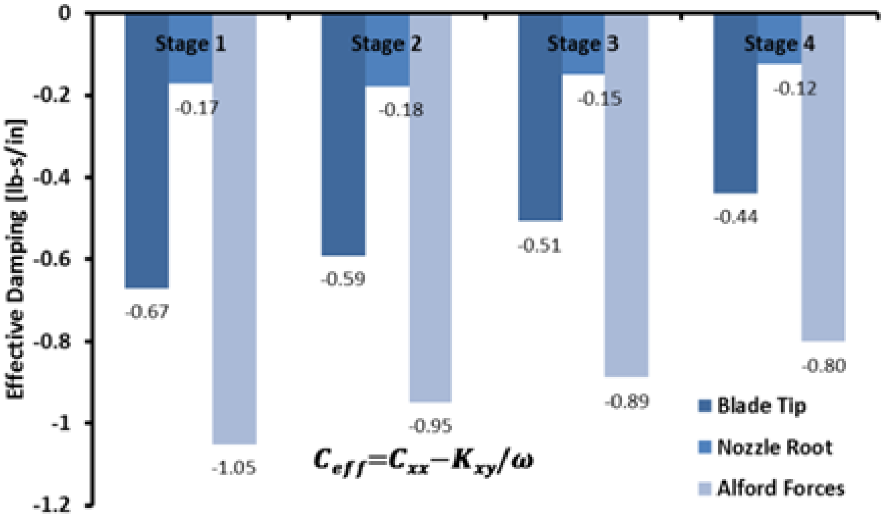

Figure 22: Effective Damping

Alfords forces are the result of changes in the local efficiency of the stage due to the vibration excursion. These changes in the local efficiency create follower forces that tend to destabilize the forward modes. The amount of cross-coupled stiffness resulting from the Alford's phenomena is dependent on the torque generated from the stage, and the blade height and given by:

$$K_{xy} = \frac{\beta P}{\omega D H}$$

β is a factor that depends on the shape of the blade (shrouded or unshrouded). P is the power generated from the stage, ω is the running speed, D is the blade diameter, H is the blade height. The effective damping of the blade tip and nozzle root labyrinth seals compared to the Alford's forces is shown in Figure 22.

Two Types of Bearings Were Identified for this Application: 5 pad rocker pivot Load On Pad (LOP) bearing, and four pad flexure pivot Load Between Pad (LBP) bearing. The design space of the bearings was explored by considering two clearance to radius ratios for each bearing type (1.5 and 2 mil/inch), and three pad axial length [characterized by L/D ratio (active axial pad length to pad diameter ratio) 0.4, 0.6 and 0.8]. To cover the full range of available stiffness provided by the different configurations of the two bearing types, five configurations were down-selected.

Rotor Support Configurations: Two main support configurations were considered. A hard mounted support is the traditional bearing support and a soft mounted support where the bearing is carried on an integral squeeze film damper. An example Integral Squeeze Film Damper (ISFD) installed on a flexure pivot bearing is shown in Figure 23(a). Internal squeeze film dampers are devices that can provide additional damping to the system. The stiffness of ISFD is derived from the S-shape spring. Both stiffness and damping can be controlled and designed with accuracy. For each rotor configuration, different bearing designs are considered. The down-selection of the "best" bearing design is decided through the undamped critical speed map and sub-synchronous stability of the different bearing designs. The undamped critical speed map for the soft mounted configuration is shown in Figure 23(b). Table 12 summarizes the results of the rotor-dynamic analysis for the two configurations. Both the configurations meet API and GE stability criteria. The soft mounted configuration is selected for this turbine due to higher margins and tolerance on casing taper under transient operation.

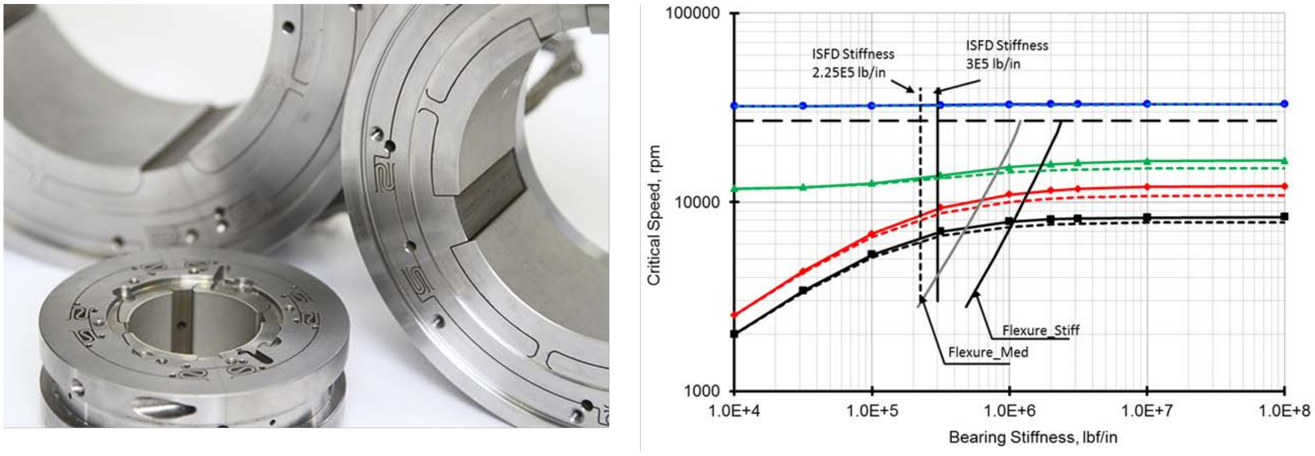

Figure 23: (a) Photo-Image if the Flexure Pivot Bearing and Integral Squeeze Damper and (b) Undamped Critical Speed Map for the Soft Mounted Configuration

Table 12: Results Summary and Applicable Standards for the two Configurations

Category	Standard	Criteria	Limit	Hard Mounted		Soft Mounted
				Rocker Soft Bearing	Flexure Soft Bearing	Flexure Med. Bearing
Stability	API Level I	Q0/QA	>2	2.5	4.4	22.1213279
		log dec (A)	>0.1	0.066	0.178	1.786
		Fulton Region		Region B		Region B
				Level II Required		No level II
	API Level II	log dec (final)	>0.1	0.744	0.918	2.353
Synchronous Resp.	API	Separation Margin	Actual>Req.	Yes	Yes	Yes
		D. Seal Clr	< 75%	Yes	Yes	Yes
		Amplification Fact.		10.15	1.34	2.72

Subtask 1.2.4 Impeller and Blade Structural Dynamics, Stress, and Thermal Fatigue Life Analysis

Blade Mechanical Design: The airfoil design went through a number of iterations to meet geometric design criteria in terms of shape and form factor of the buckets. These were based on extensive turbine design experience at GE and are not discussed in detail here. The bucket concentrated and average stress numbers were then evaluated and compared to selected material properties at temperature. The methods to calculate the representative stress numbers in the airfoils and the material allowable stress for > 90,000 hour (30 years) rotor life are proprietary but a comparison is shown in Table 13.

Table 13: Stress Analysis of the Turbine Buckets

	STG - 1		STG - 2		STG - 3		STG - 4	
Max Temp (F)	1,278		1,210		1,140		1,068	
	Factor of Allowable Stress (%)	Calc Temp Allowable (F)	Factor of Allowable Stress (%)	Calc Temp Allowable (F)	Factor of Allowable Stress (%)	Calc Temp Allowable (F)	Factor of Allowable Stress (%)	Calc Temp Allowable (F)
GE Criter1	48.7%	1,375	37.3%	1,362	30.6%	1,361	28.8%	1,352
GE Criter2	77.6%	1,305	64.0%	1,284	56.7%	1,274	49.7%	1,278

Structural Dynamics: In traditional axial turbine applications, blade structural vibrations are damped using frictional forces at the dove tails (location of blade assembly to the rotor). In this application due to high power density in the working fluid (CO_2), an integral shaft design is being pursued. Various options to introduce frictional damping to mitigate the vibrations were evaluated including z-locks machined into the shrouds. These were not feasible due manufacturing limitations and extremely small gap requirements between adjacent shrouds. As a result, the structural dynamics of this design are similar to a blisk with no frictional forces to dampen the structural vibrations. The only damping available for the structure is in the form of material damping. It is therefore critical to evaluate the structure natural frequencies and establish that excitation sources within the turbine have enough margin to avoid resonance. This can be achieved by carefully selecting the stage nozzle counts such that natural structural frequencies are far from resonance with the nozzle passing frequencies.

Interference Diagrams were used to evaluate the aeromechanic performance of the four continuous integral shrouded blisk stages. An interference diagram calculates the effect of nodal disc vibrations on blade vibrations. It is a plot showing blisk natural frequencies with nodal diameter on the horizontal axis and frequency on the vertical axis. It also plots the first and the second nozzle passing frequencies. Nozzle passing frequency is considered the vibratory force on the turbine blades. It is caused by the working fluid flowing through a nozzle. This force is cyclic given the design of the nozzles. The cyclic force may excite the blisk at its natural frequency and lead to resonance. The interference diagram corresponding to a nozzle count shows the nodal diameter excited for that nozzle count (marked by vertical lines on the diagram), the blisk mode shapes at nodal diameters (zero to half the nozzle count) as well as the first and second nozzle passing frequency. For each of the four stages of the SunShot turbine, a desired percent margin is required for the natural frequencies of the first six modes with respect to the first nozzle passing frequency (NPF) at design speed based on extensive turbine design experience at GE. The selection of nozzle count was based on the bucket count, efficiency requirements (all obtained via the aero design process) and the interference diagrams to meet the margin requirement between blisk natural frequency and first NPF. Only the upstream nozzle counts were considered for each stage as a dominant forcing function.

Blisk natural frequency analysis: The first six modes for nodal diameters (ND) zero to Number of Bucket (NB)/2 were calculated by modal analysis using cyclic symmetry in ANSYS. A single sector model of the blisk was created in Uni-Graphics-NX (UG-NX) and imported in ANSYS. A 4- node brick element (ANSYS element SOLID45) was used to mesh the blisk.

Boundary Conditions: Constraint equations were used to connect the dissimilar meshes on the blade, the shroud and the disk. Cyclic constraint equations are applied to the specified cyclically symmetric faces on the shroud and the disk. The axial constraints on the two side faces are to prevent any axial movement in the blisk as in reality the shaft is long and any axial movement is negligible. Tangential constraint is applied at the selected nodes (these are nodes at a distance of one-third the height of the hub from the center of the disk) to prevent rigid rotation for ND =0 analysis. Material properties used for the analysis are modulus of elasticity (E), 2.5e7 lbs/inch2, Poisson’s ratio (η), 0.3, reference temperature 70°F, friction coefficient, 0.4. The nozzle passing frequency was corrected for the right temperature.

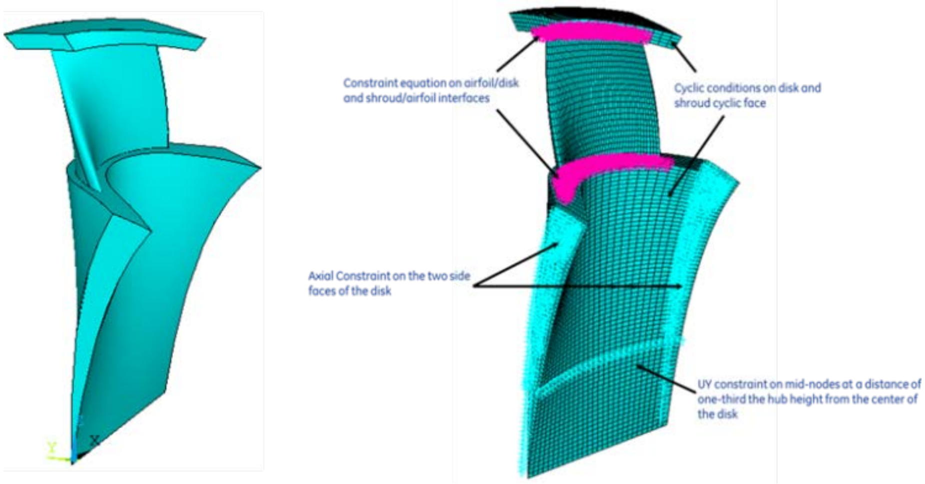

Figure 24: Single Sector Blisk Model: (a) UG-NX Sector Model, and (b) Ansys Mesh and Moundary Conditions for Cyclic Modal Analysis

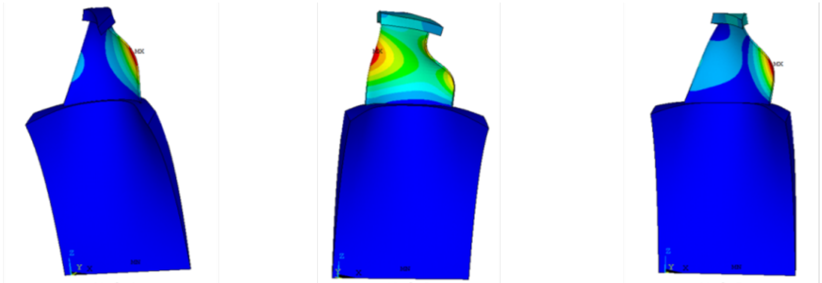

Mode 1
(Torsional and Trailing edge flapping)

Mode 2
(Torsional and Trailing edge flapping)

Mode 3
(Axial and Trailing edge flapping)

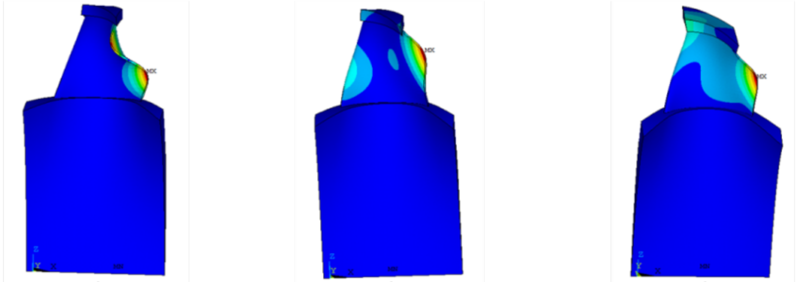

Mode 4
(Trailing edge flapping)

Mode 5
(Torsional and Trailing edge flapping)

Mode 6
(Axial and Trailing edge flapping)

Figure 25: Turbine Stage 1 Mode Shapes 1 to 6 for Nodal Diameter 10

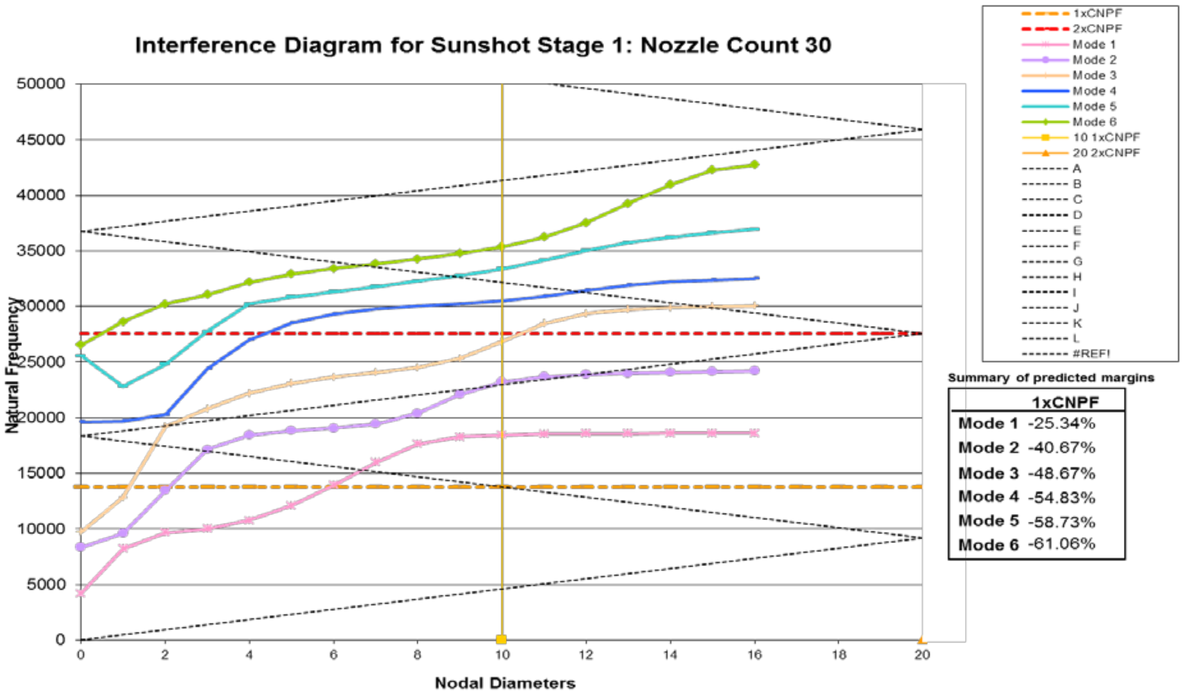

	1xCNPF
Mode 1	-25.34%
Mode 2	-40.67%
Mode 3	-48.67%
Mode 4	-54.83%
Mode 5	-58.73%
Mode 6	-61.06%

Figure 26: Turbine Stage 1 Interference Diagram (Bucket Airfoil Count = 40; Nozzle Count = 30)

Figure 25 shows the mode Shapes 1 to 6 for turbine Stage 1 and are labeled as identified. The frequency margins at operating speed are shown in the interference diagram Figure 26. The intersection between the horizontal and vertical yellow lines shows the stage operating point and the natural frequency margins to this operating point are shown in the table in the right inset. As noted in this table, the margins to the natural vibration frequency are high (higher than GE criteria) to establish stable operation and infinite fatigue life. The operating point can be optimized by changing the nozzle count (thus moving the vertical yellow line) without changing the airfoil designs. This optimization was done for all 4 stages and desired margins were established by using the nozzle counts shown in Table 14

Table 14: Final Nozzle and Bucket Counts to Establish Desired Margin to Resonance for Stable Aero-Mechanics Operation

Stage	1	2	3	4
Bucket Count	40	40	36	30
Nozzle Count	28	28	26	26

Subtask 1.2.5 Radial/ Thrust Bearing, Clearances and Seal Design

<u>Balance Piston Seal Design</u>: The sealing system for balance piston is a hole pattern seal similar to the example seal shown in Figure 27(a). Unlike labyrinth seals, hole pattern seals achieve their sealing action by the friction to the axial flow due to the textured surface marked by the holes. The balance piston hole pattern seal boundary conditions and layout is shown in Figure 27(b). The upstream section before the shunt injection is intended to balance the exhaust of the first stage.

Hole pattern balance piston seal geometry:

Diameter = 5.255’’

Seal Length = 2.5’’ (L/D = 0.475)

Radial Clearance = 9.2 mil (3.5 mil/inch)

Preswirl = 0.2

Hole Diameter = 0.125’’

Hole Depth = 0.125’’

A hole pattern seal is selected for the high pressure drop balance piston seal due to its superior rotor-dynamic damping properties, ease of construction and high temperature operation feasibility.

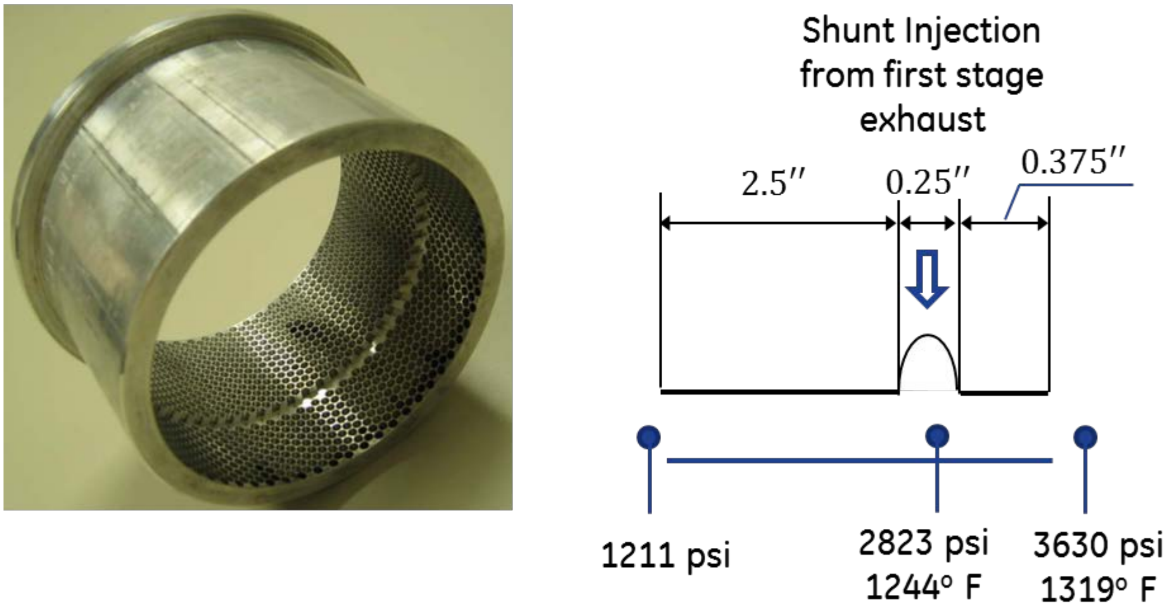

Figure 27: (a) Example of Hole Pattern Seal Casing and (b) Balance Piston Seal Boundary Conditions

Inter Stage and Bucket Tip Labyrinth Seal Designs: The basic geometrical properties of the blade tip and nozzle root labyrinth seals are listed below:

Radial clearances 3mil/in

Number of teeth = 2

Tooth pitch = 0.2

Tooth height = 0.2

Blade tip L/D = 0.06

The temperature and pressure boundary conditions of the stages’ blade tip and nozzle roots are shown in Figure 28(a), and the seal leakages are presented in Figure 28(b). With the above presented geometric criteria the inter-stage and blade tip laby seals meet the rotor-dynamic and leakage rate requirements for turbine and system efficiency. A seal packaging solid model and dimensions are shown in Figure 29.

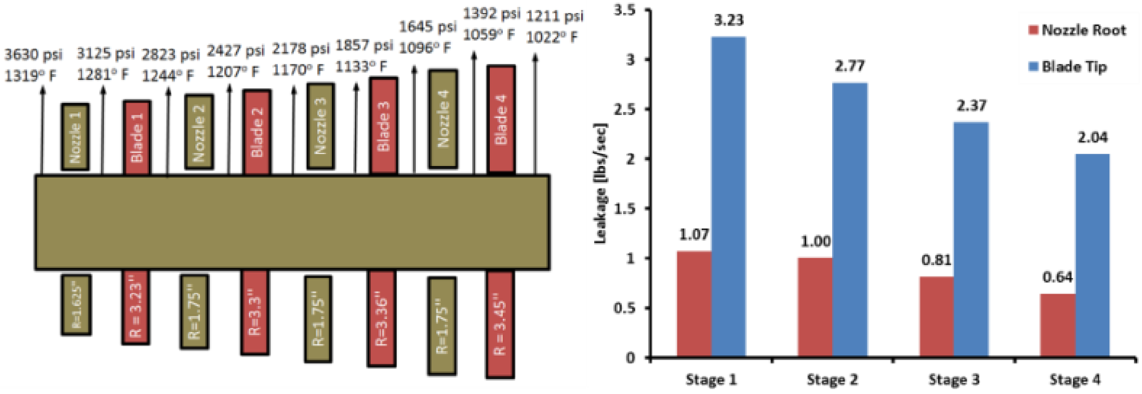

Figure 28: (a) Blade Tip and Nozzle Root Labyrinth Seal Boundary Conditions and (b) Seal Leakage in Pounds per Second as Predicted by the XLTRC2 Real Gas Properties

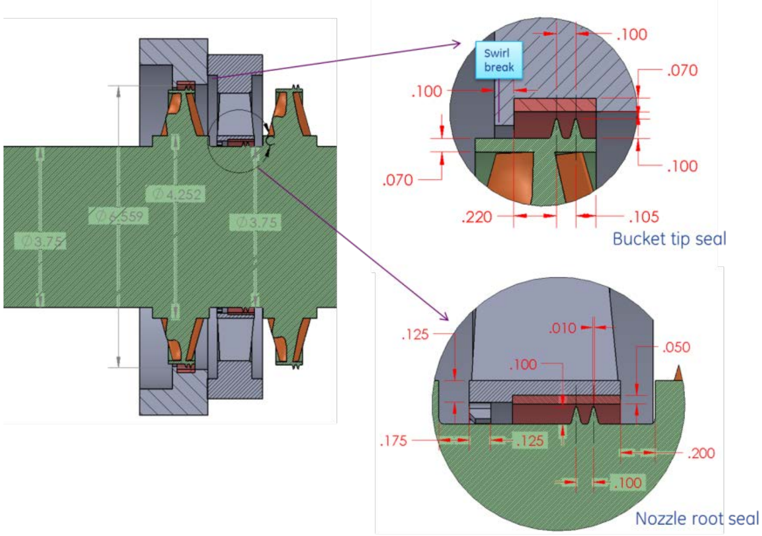

Figure 29: Model for Bucket Tip and Nozzle Root Labyrinth Seals Meeting the Turbine Design Requirements

Finally a Dry Gas Seal (DGS) is used to separate the high pressure CO_2 environment inside the turbine region from ambient air and oil lubricated bearings. DGS is a known technology available from various vendors and primarily applied to high pressure compressor to minimize the loss of working fluid to the ambient. In certain situations the fluid leaking out of the DGS can be captured and recompressed using an external compressor. A DGS, suitable for this turbine operating speed and shaft diameter was designed by a vendor, John Crane. The solid model and performance numbers for this seal were provided by John Crane and CO_2 leakage from the seal is expected to be on the order of 0.01 lb/s which meets the turbine design requirements as presented here. A schematic of the DGS cross-section is shown in Figure 30 with leakage flows from the seal operation shown in red. The off-shelf designs of DGS are however limited by the highest operating temperature of the shaft and fluid. The current designs are flooded with high pressure cold flow (usually below 150°C) to avoid damage to the seal components. To achieve this cooling of the shaft from turbine inlet temperatures of 700°C or higher a thermal management solution is implemented before the DGS to ensure safe and reliable operation of the turbine. The details of this thermal management solution are presented in the next section.

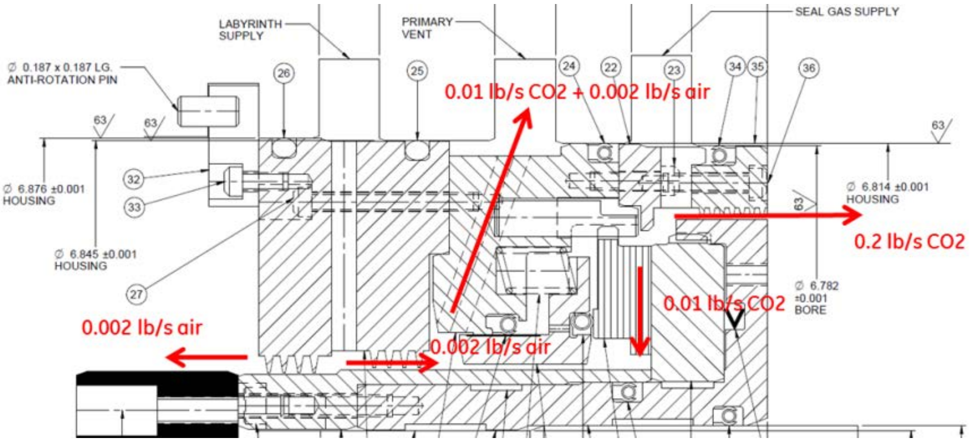

Figure 30: Schematic of the DGS Designed by John Crane for Application to the SunShot sCO_2 Turbine

Subtask 1.2.6. Thermal Management System

The SunShot expander is being designed for turbine inlet conditions of 250 bar and 715°C. These conditions have been flowed down from the product requirements from Task 1.2.1, to meet the DOE target of 50% thermal conversion efficiency from the re-compression supercritical CO_2 cycle. Currently available off-the-shelf sealing solutions for this high pressure (80 bar) casing, DGS, have a temperature limit of 150°C on the shaft. The heat transfer coefficient and shaft management scheme post balance piston, in the low pressure region determines the thermal gradient in the shaft and thermal stress levels.

The convective heat transfer coefficients in high pressure CO_2 are computed using standard Gazley Correlation Equations as shown below:

$$Nu = 0.0369\,\mathrm{Re}^{0.77}; \quad Nu = \frac{hL}{k}; \quad \mathrm{Re} = \frac{\rho VL}{\mu};$$

where Nu and Re are the non-dimensional parameters associated with heat transfer and flow, respectively. For supercritical CO_2, the high gas density coupled with high shaft rotational speeds results in high heat transfer coefficients as demonstrated in the chart below. This chart compares relative figure of merit (FOM) or fluid heat transfer effectiveness (convective) for CO_2 and air as a function of pressure, where the figure of merit is defined as:

$$\mathrm{FOM} = \rho 0{\cdot}8 k 0{\cdot}6 C_p 0{\cdot}4 \mu^{-} 0{\cdot}4$$

where:

ρ is density; k is the thermal conductivity; Cp: specific heat; and μ is viscosity.

A comparison of this heat transfer FOM for CO_2 with air is shown in Figure 31. As CO_2 passes through the critical point, the fluid density increases significantly resulting in very high heat transfer coefficients. This high heat transfer coefficient when compared with the thermal conductivity of the high nickel super alloys being used to manufacture the rotor results in very high Biot numbers between 10 and 40. Due to the high Biot numbers in this application, traditional cooling schemes using counter-flow of cold CO_2 stream in the thermal management region results in very rapid shaft surface cooling while the core of the shaft is still at a very high temperature. This sets up high radial thermal gradients resulting in high thermal stress in the shaft.

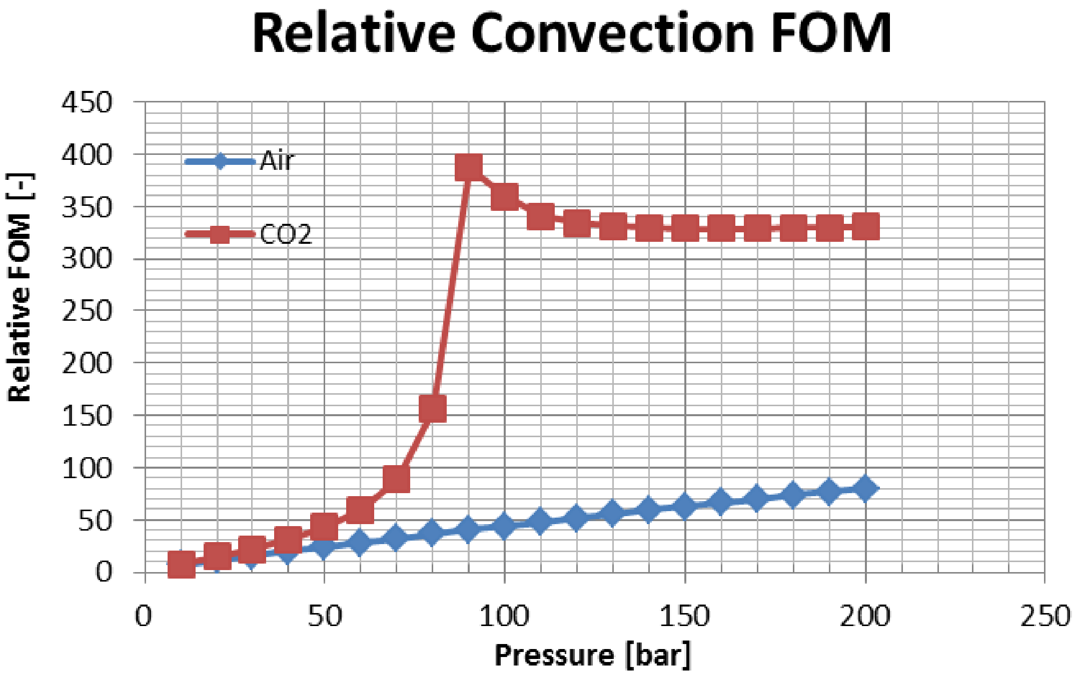

Figure 31: The Comparison of Relative Figure of Merit (Convection) Between Air and CO_2 as a Function of Pressure

Since the use of any flow over the shaft surface results in very high heat transfer and control of the surface flow temperature cannot be robust enough to guarantee reliable performance, the use of no flow region is proposed here. Due to these flows, a gradient is established on the stator piece similar to the rotor but this gradient is essentially axial. Additionally on either side of this stator, the shaft is in contact with the cooling and heating flows as well, setting up the convection boundary conditions as shown below. The fluid in the cavity is simulated as a quasi-solid (zero stiffness) with enhanced thermal conductivity to account for recirculation. Windage heating in the cavity is simulated via volumetric heat generation in the FEA model.

Assumptions in this model:

1. There is no pressure drop across the cavity → no mass flow rate.
2. There is no mixing at the ends of cavity → sudden change in boundary conditions.
3. The axial thermal conductivity in the fluid zone (cavity) due to natural convection results in enhancement of up to 2 orders of magnitude.
4. The calculated values for HTC and windage are correct.

Typical temperature and equivalent stress profiles for this solution are plotted in Figure 32. Note the linear drop in temperature along the shaft in the thermal management region resulting in moderate thermal stress in the shaft.

Temperature (F):

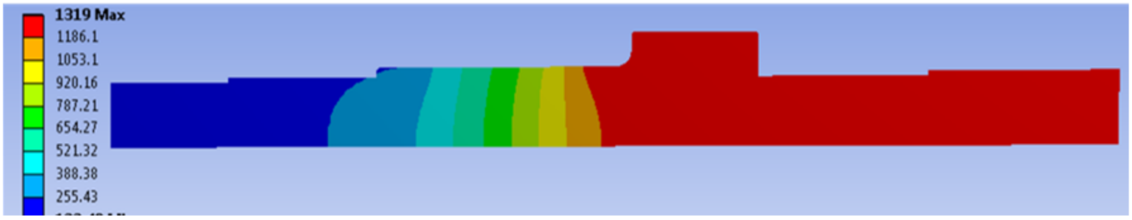

Equivalent Stress (PSI):

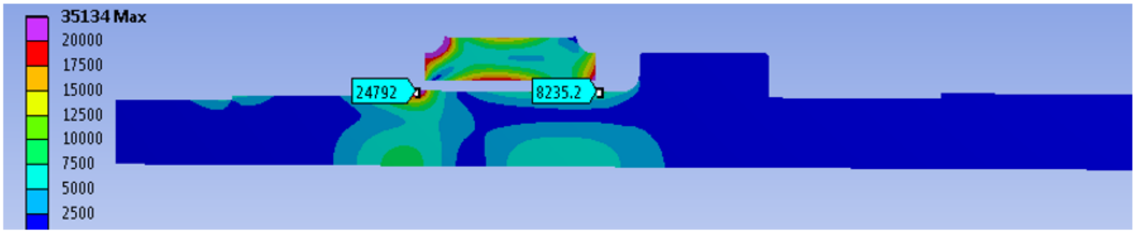

Figure 32: Temperature and Equivalent Stress Profile in the Shaft and Stator Piece in the Thermal Management Region

Subtask 1.2.7. Transient Start-up and Shut-down Analysis

The required thermal ramp rates can be different for warmup and cooldown. For warmup, the solar heat flux can be controlled to match the thermal ramp rate capability of the system hardware. At 2MWt incident receiver power, it will take about 50 minutes to heat up 70 tons of metal (two recuperators plus receiver) from a cold condition to the operating temperature. However, a cold morning start should be a rare occurrence. With sufficient insulation for a 140°F external temperature, 7.5m2 of external area each, and an external heat transfer coefficient of 10 W/m2-C, the two recuperators should only lose about 3kW each to convective cooling. At 30 tons each, they will then cool down by about 10°C overnight. In contrast, the receiver will cool down very quickly (less than an hour) unless the cavity is well insulated and provided with a damper. Assuming the receiver completely cools down overnight but the recuperators remain warm, it will take about 15 minutes to reach operating temperature using 2MWt of sunlight. The capability requirement is then dictated by the project economics and the revenue lost during warmup. An analysis of the site solar data indicated that approximately 3.3% of the annual DNI is in the first hour of the morning. Loss of this AEP would raise the LCOE by 0.3 c/kWh. A target turbomachinery cold start time of 15 minutes and a maximum limit of 30 minutes is therefore specified. Electrical heaters may be used to pre-warm the turbomachinery casing, as morning start times will be predictable.

The cool-down is dictated by one of two events: Rapid cloud transients or emergency off-point. An analysis of typical cloud events at the Sierra site indicate that typical cumulus and high cirrus cloud events result in a DNI decline rate of 200 W/m2-min, or about a 25% decrease from full power in one minute. For the eSolar SCS3 heliostat system, the maximum heliostat removal rate during an emergency off-point event is 2% per second, or about 50 seconds from full power to zero. The resulting change in expander inlet temperature is estimated from a simple transient model that assumes the recuperator mass is infinite, an 11-ton receiver and hot piping, constant CO_2 flow rate, and constant receiver specific heat and thermal losses during the event. The results are shown in Figure 33(a). Based on this analysis, the turbine inlet temperature changes by 0.9°C/s during a cloud event and 2.9°C/s during an emergency off-point event. In the worst thermal scenario, the casing is assumed to remain at 715°C, and the rotor is at the receiver exit temperature of 520°C.

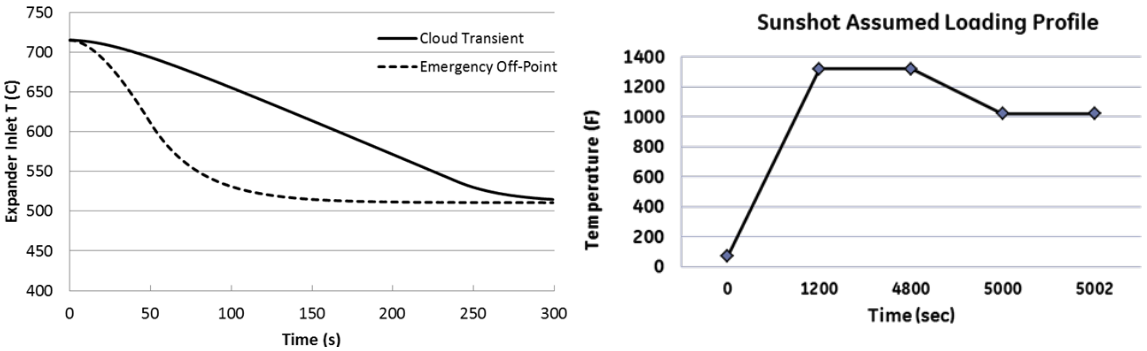

Figure 33: (a) Transient Analysis of Turbine Inlet Temperature during Cloud and Emergency Off-point Events, (b) Thermal Load Profile for the Turbine

With the thermal loading profile established, the most limiting turbine rotor components in terms of thermal cycling and LCF life is the turbine stage shroud. In order to allay these concerns, a FEA was performed considering both these loads to evaluate the resultant stresses. The temperature loading profile assumed for this analysis based on CSP power plant startup and shut down analysis above is shown in Figure 33(b). Based on the evaluation of this transient thermal loading profile, the blisk concept was determined to be viable in terms of primary low cycle fatigue criteria evaluated using FEA. The resultant stress profile in the turbine blade row and the shroud are shown in Figure 34, and the concentrated stress numbers at different points in time are tabulated in Table 15. This assessment where the peak concentrated stress is below the 0.2% yield stress values for the material at temperature confirms the LCF life of this machine and could be designed >10,000 start up and shut down cycles as required. A detailed assessment of this process is currently in progress.

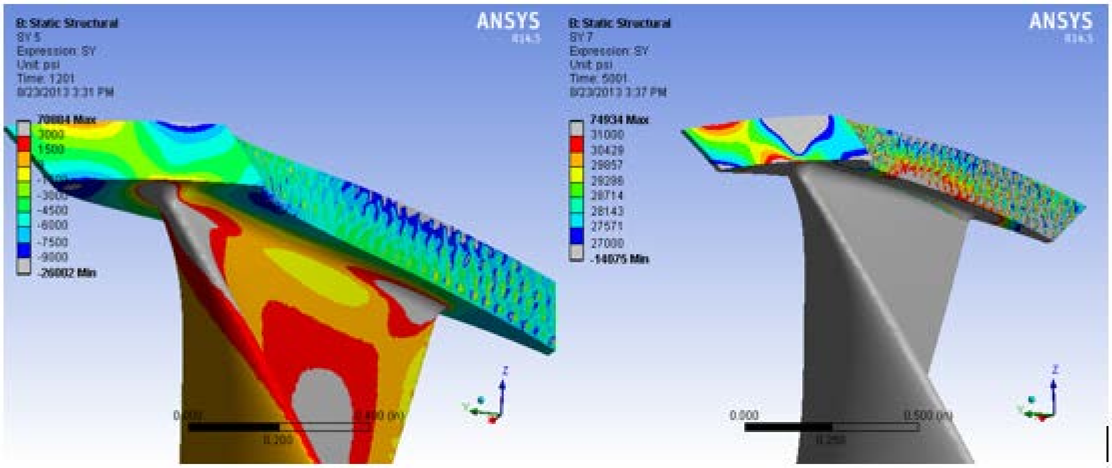

Figure 34: Peak Equivalent Stress Profile in the Turbine Blade and Shroud for (a) After 20 Minutes Transient to Full Rated Conditions (Centrifugal + Thermal) and (b) After 200 Sec Cool Down Due to Cloud Transient (Centrifugal + Thermal)

Table 15: Resultant Concentrated Stresses on the Turbine Blades from LCF Hoop Stress Study (Peak Stress of 75 KSI < 100 KSI (0.2% Yield at 700°C for Nimonic 105)

	Root Fillet		**Tip Fillet**	
Time [s]	**Min. [psi]**	**Max. [psi]**	**Min. [psi]**	**Max. [psi]**
1	-417.65	25464	-371.19	37720
1201	-26002	6206.7	-13008	19717
4801	-431.2	25411	-369.74	37789
5001	-756.05	74934	-510.66	69476
5003	-529.27	49868	-2811.9	37455

Subtask 1.2.8 Key Component Design

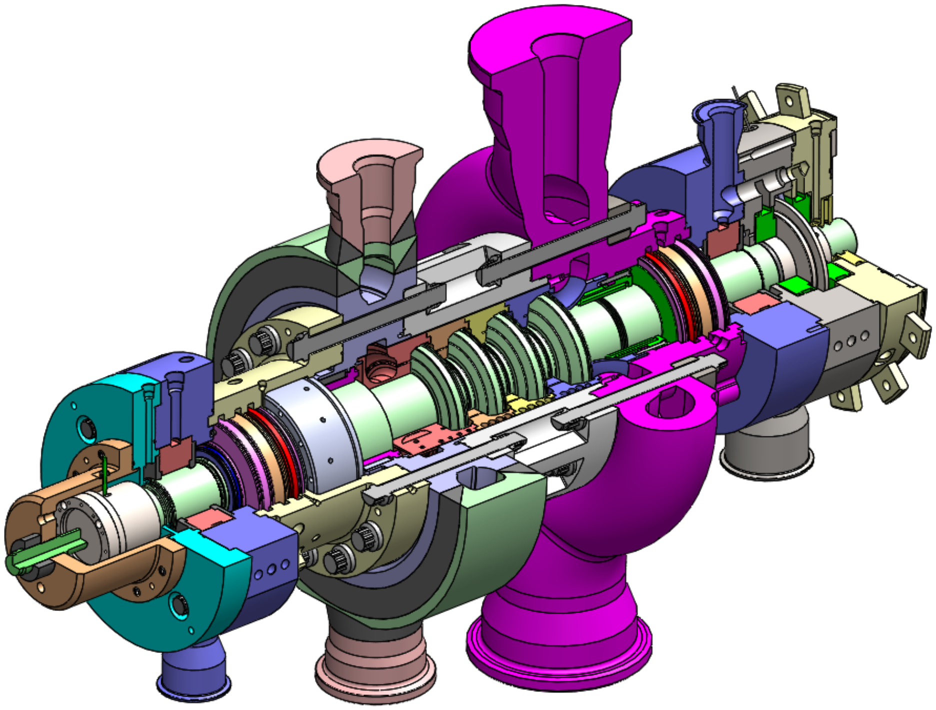

Figure 35: Final SunShot Turbine Model with Fabricated Casing and Focus Thermal Seal

Design of the turbine was a joint effort between GE and SwRI. The turbine was designed with the intent of the ASME Boiler and Pressure Vessel (BPVC) Section VIII Division 2 for pressure containment and API 684 for rotordynamics. Before production, the design and analysis were reviewed by chief engineers from SwRI and GE. It went through a Conceptual Design Review (CDR), preliminary design review (PDR), and a final detailed design review (DDR). The following is a summary of the detailed design review which was broken out as follows:

All pressure containing components went through two main analysis: static structure with pressure loads and a transient analysis with thermal loads. All original casing components were designed to meet 20,000 hour allowable creep rupture properties for cast Haynes 282. Haynes 282 was selected based on a casting study under the final technical report, “Materials for Advanced Ultrasupercritical Steam Turbines.” Bolt and rotor material were also selected from this report. While Nimonic 105 was chosen for both, it was only used for the bolts since a readily available Waspaloy barstock was easier to obtain to maintain project schedule. The rotor was designed to meet creep rupture and creep rate requirements, while the bolts were designed to meet creep relaxation requirements. As will be discussed later in this report, the Haynes 282 castings were eventually scrapped, and the pressure containing case had to be redesigned from cast CF8M (316 SS) for the exit plenum and forged and fabricated Inconel 625 for the other pieces.

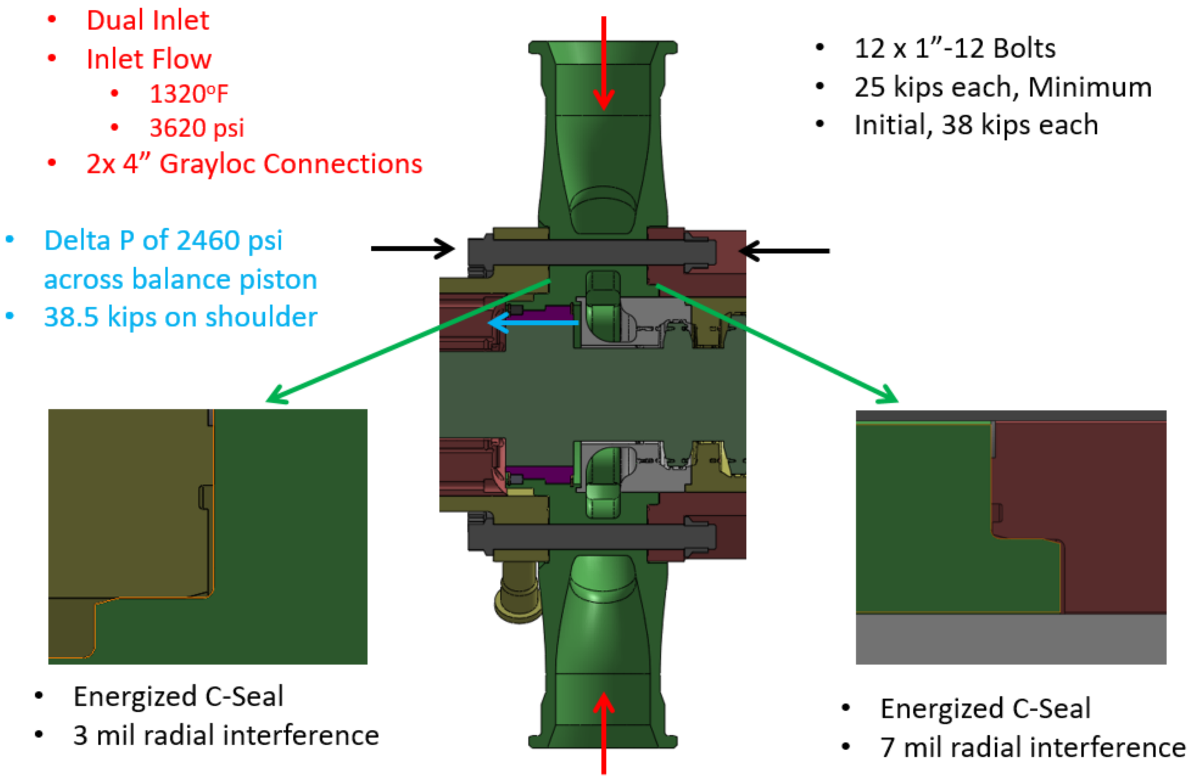

Figure 36: Inlet Plenum Boundary Conditions

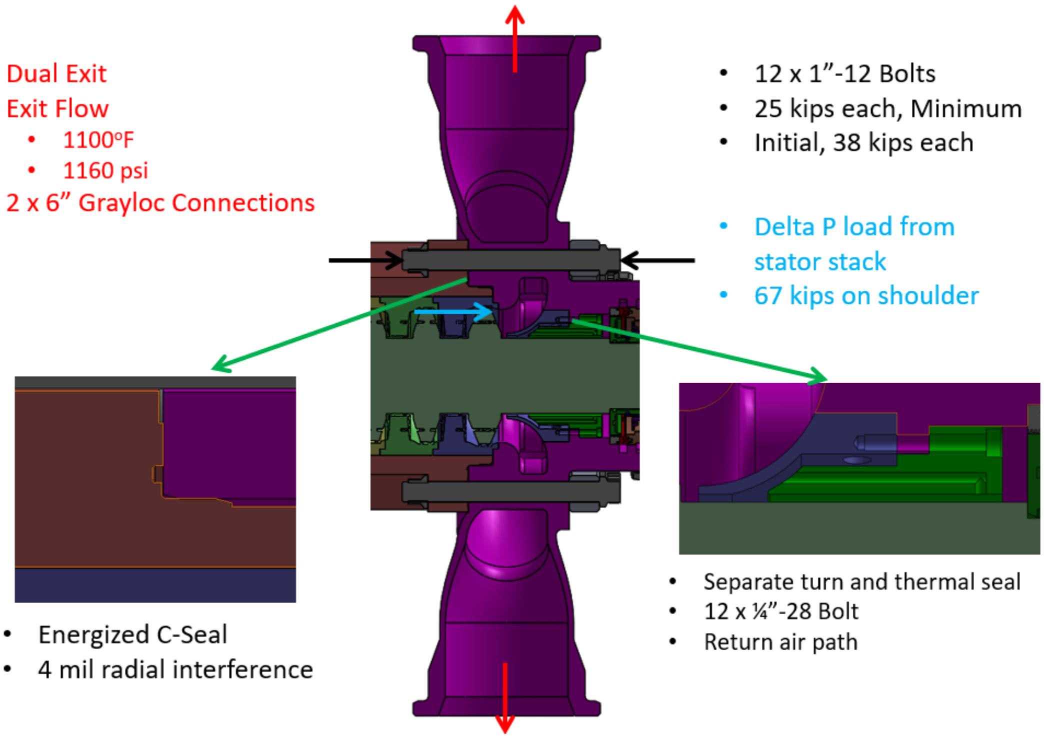

- Dual Exit
- Exit Flow
  - 1100°F
  - 1160 psi
- 2 x 6” Grayloc Connections

- 12 x 1”-12 Bolts
- 25 kips each, Minimum
- Initial, 38 kips each

- Delta P load from stator stack
- 67 kips on shoulder

- Energized C-Seal
- 4 mil radial interference

- Separate turn and thermal seal
- 12 x ¼”-28 Bolt
- Return air path

Figure 37: Exit Plenum Boundary Conditions

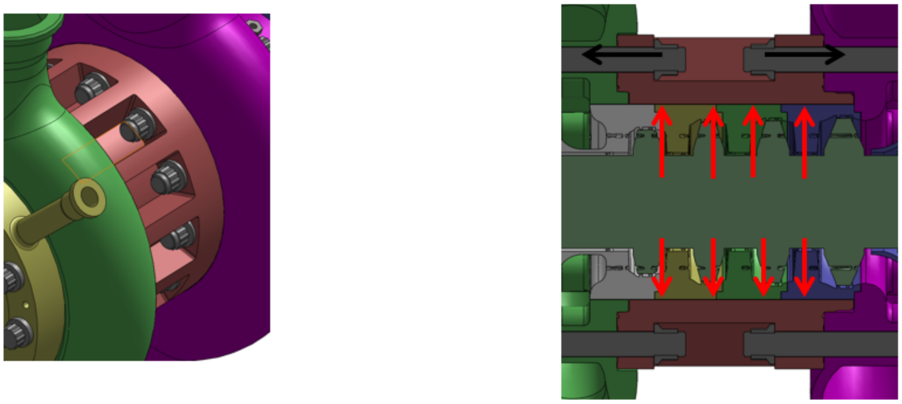

- 12 x 1” Bolts – each side
- 25 kips each, Minimum
- Initial, 38 kips each

- Internal Pressure
  - 1320°F
  - 3620 psi
- Minimum Wall Thickness – 0.95”
- Required Thickness based on ASME Pressure Vessel Calculation – t = PR(S-.6*P)
  - P: Pressure; R: Radius; S: Allowable Stress
  - t = 0.60”

Figure 38: Nozzle Casing Boundary Conditions

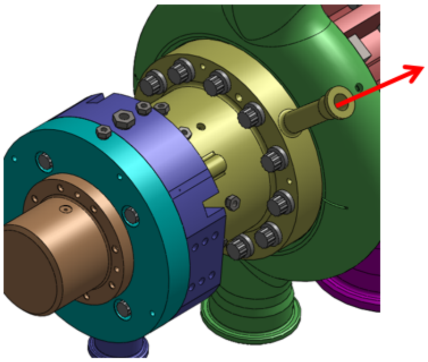

- Inlet Buffer Air
- Exit CO2 and Air
- Inlet Buffer CO2
  - 1160 psi
  - 200°F
- Mixed Balance Air
  - 1160 psi; 1100°F
- Minimum Wall Thickness: 0.625”
  - Meets ASME Pressure Vessel Code at 3260 psi and 1100°F

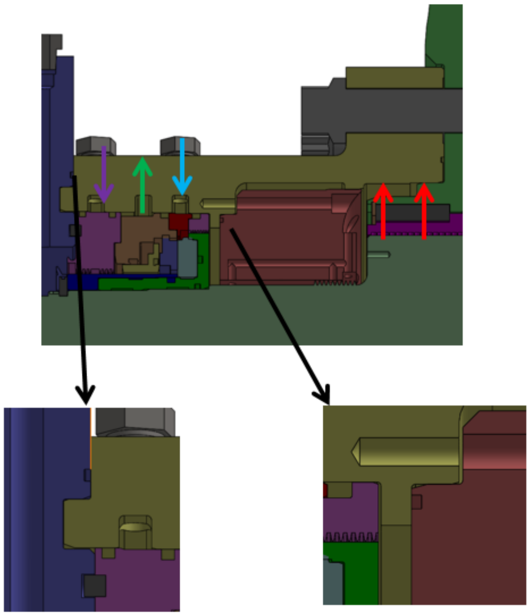

- Elastomer O-ring Face seal
- Seals off buffer air and oil
- Zero Interference Radial Fit

- C-ring Face Seal
- Separate hot and cold C02

Figure 39: Dry Gas Seal Housing Boundary Conditions

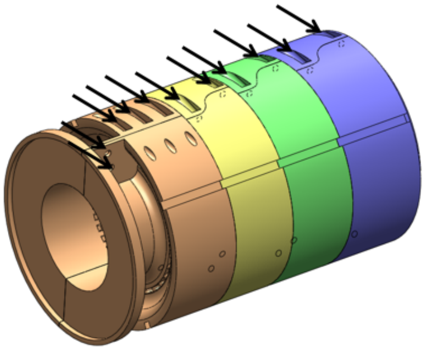

- 4 x ¼”-28 Bolts holding each stator pair together
  - 10 for Stator 1
- 1400 lbs / Bolt

- Inlet Flow
  - 3620 psi
  - 1320°F

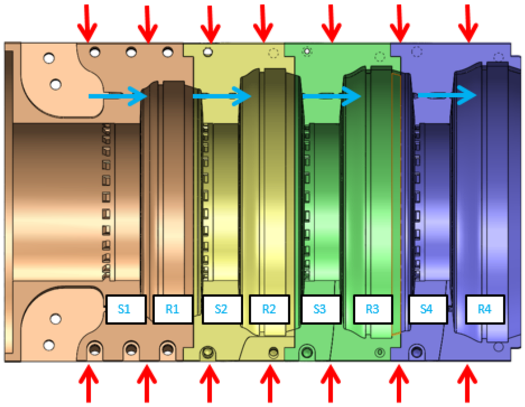

Stage	Inlet		Outlet	
	Pressure	Temp	Pressure	Temp
S1	3620	1320	3125	1320
R1	3125	1320	2824	1254
S2	2824	1254	2425	1254
R2	2425	1254	2178	1187
S3	2178	1187	1854	1187
R3	1854	1187	1645	1118
S4	1645	1118	1389	1118
R4	1389	1118	1211	1034

Figure 40: Stator Nozzle Boundary Conditions

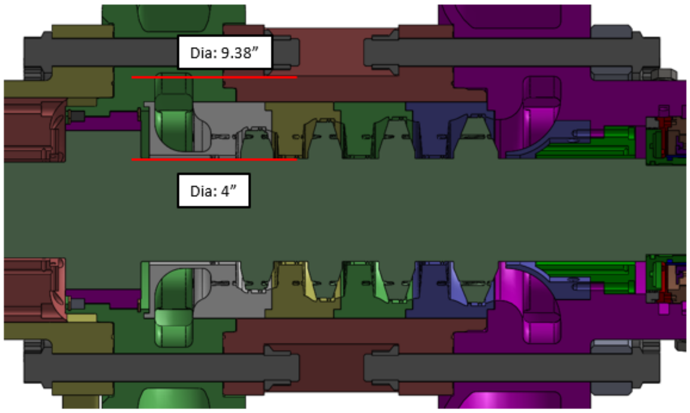

- Blowout Load. Full 3620 psi
  - 205 kips
- 12 Bolts, Initial Load, 60 ksi (38 kips)
  - Safety Factor of 2.23
- 1000 hour relaxed, 40 ksi (25 kips) each
  - Minimum Safety Factor of 1.5

- 24 x 1”-12; 12 Point Bolts and Nuts
- Inlet Side
  - Length: 7.75”
- Exit Side
  - Length: 8.50”
- Provide support to structural struts in bolt plenums

Figure 41: Main Case Bolts Boundary Conditions

- 4 Key inserts
- Allow separate thermal growth for hole pattern seal
- Maintain concentricity
- Minimal Torque

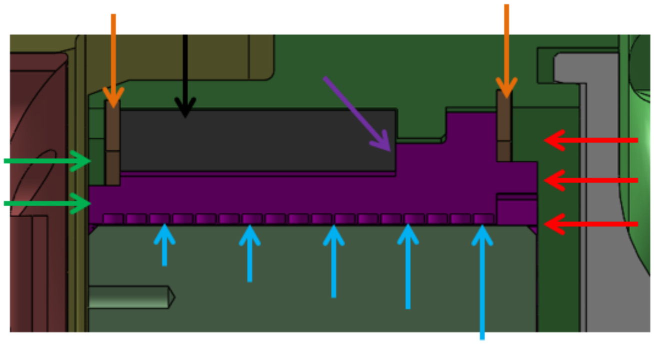

- 2 Retaining Rings
  - Hold Keys
  - Restrain axially during assembly

- Balance Return Flow
  - 1160 psi
  - 1100°F
    - Mixing with DGS CO2
- Shoulder Load
  - 38.5 kips
  - Shear Area: 21.33 in^2
  - Shear Stress: 1800 psi

- Balance Return Flow
  - 3260 – 1160 psi
  - 1320°F

- Balance Return Flow
  - 3260 psi
  - 1320°F

Figure 42: Balance Piston Seal Boundary Conditions

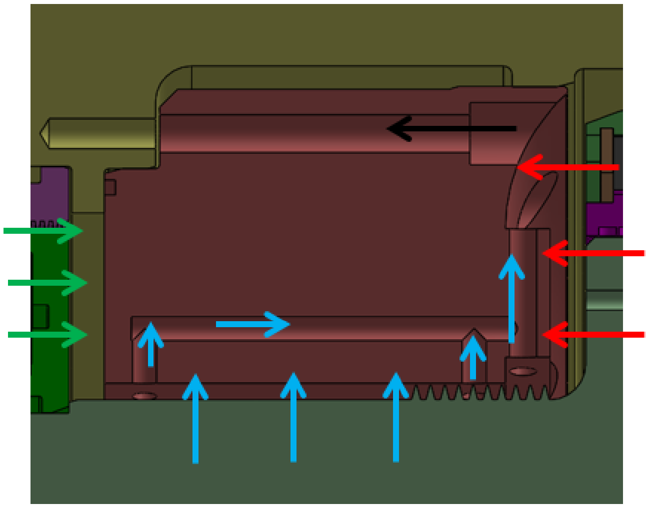

- 12 x ¼”-28 bolts
  - Holds thermal seal to DGS Housing

- Mixed Balance Air
  - 1160 psi
  - 1100°F

- DGS CO2 Buffer Air
  - 1160 psi
  - 200°F

- CO2 Mixing
  - 1160 psi
  - 200 – 1100°F

Figure 43: Thermal Seal Boundary Conditions

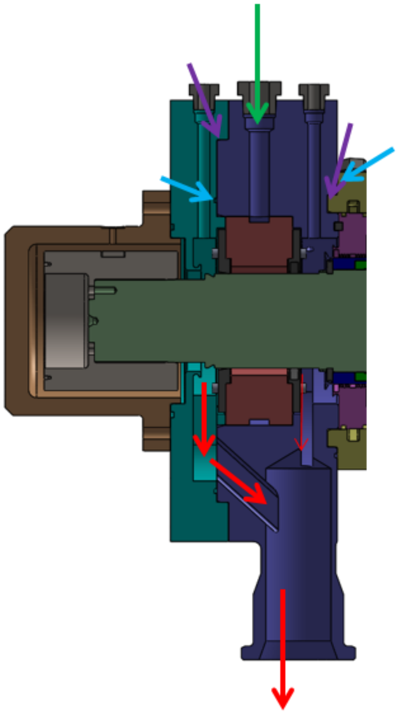

Oil Inlet and Exit Requirements

- Each bearing (thrust and radial) requires 10 gpm
- Inlet – Max: 10 ft/s
- Inlet Diameter – Min: 0.64”
- Exit (gravity drain) – Max: 2 ft/s
- Exit Diameter – Min: 1.43”
- Majority of radial bearing flow is outboard

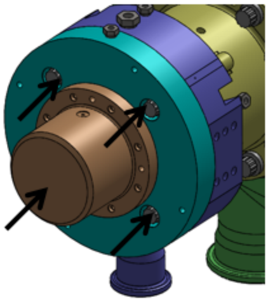

- 4 x 7/8”-14 Bolts
- 25 kips each
- Connect End Cap, Bearing Housing, and DGS Housing
- Elastomer O-rings seal off buffer air and oil from the bearing
- Zero to slight interference fits

Figure 44: Inlet Side (Generator End) Bearing Housing Boundary Conditions

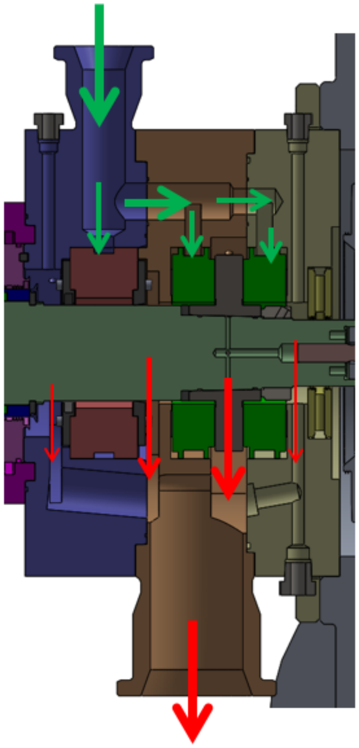

Oil Inlet and Exit Requirements

- Total Oil Flow: 42 gpm
    - Radial Bearing: 10 gpm
    - Thrust Bearing: 16 gpm each
- Inlet – Max: 10 ft/s
- Inlet Diameter – Min: 1.30”
- Exit (gravity drain) – Max: 2 ft/s
- Exit Diameter – Min: 2.92”
- Majority of radial bearing flow is outboard
- Majority of thrust bearing flow is around the thrust collar

Figure 45: Exit Side (Compressor End) Bearing Housing Boundary Conditions

Figure 41 through Figure 49 summarize the main operating boundary conditions of all the major components that were designed for the SunShot turbine. It is important to note that the designs for the inlet and exit plenum were changed significantly to account for reduced material strengths of the replacement materials after the cast Haynes 282 models were scrapped.

Some of the main challenges were in the design of the two plenums and the sealing joints between all of the main pressure containing components. With the combination of pressure, temperature, and axial span, packaging of all the necessary features was the biggest challenge. The high power density of supercritical CO_2 leads to small machinery which leads to an overall smaller package to fit all of the necessary features. Thermal transitions regions are short (300°F/inch), and the available room for necessary features for bearings and dry gas seals is very limited. The goal of this design was to design a full frame model with readily available bearings and seals that would be used for a 10 MWe future design to prove out the containment, mechanical performance, and packing of all the necessary features.

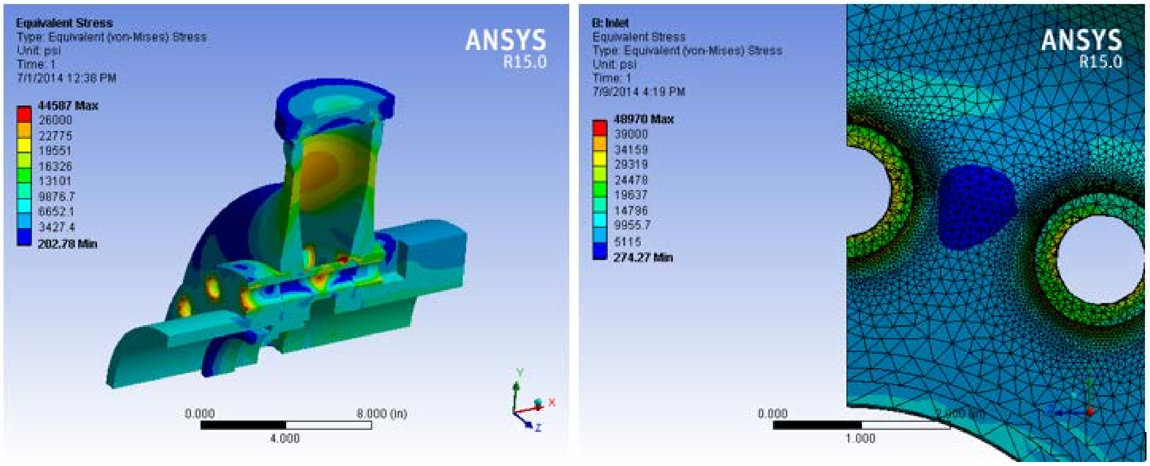

Figure 46: Static FEA Results - Inlet Plenum

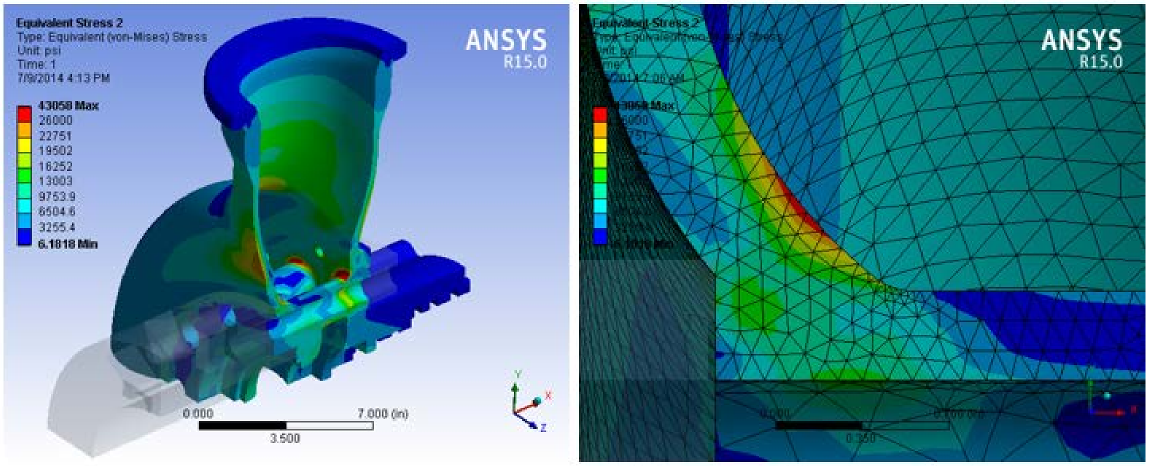

Figure 47: Static FEA Results - Exit Plenum

From a pressure containment perspective, the inlet and exit plenum proved to be the biggest challenge due to their complicated geometry and high temperatures. To provide proper sealing and reduce stresses in the part, struts were required on both parts. These struts were a challenge to manufacture and were also a negative impact on plenum performance, but were necessary to keep the plenums from opening up. While the bolts provided loads for the axial face seal, they also provided a compression force on the struts that lowered the peak tensile stresses in the plenum. Due to lower performance of the reduced aero flowpath, both plenums were designed for 1320°F (26 ksi allowable stress for Haynes 282). However, the inlet plenum was designed for 3950 psi while the exit plenum was designed for 1650 psi (predicted settle out pressure of the loop). Both plenums met von mises stress requirements over a majority of part, while peak stress locations were greater than 26 ksi. Through a more detailed linearized stress breakdown, the membrane and bending stresses were below the allowable. The nozzle casing and dry gas seal housing wall thickness were sized by hand calculations due to more simple shapes.

During thermal transients, certain criteria had to be met to ensure proper operation and life of the machine:

- Contact pressure between axial faces to ensure proper sealing between joints

  - Ensure the seal face is in contact at all times to prevent any leakage
  - Contact pressure that is 2x operating pressure will provide a backup metal to metal seal past the spring energized C-seal.
- Contact pressure between radial faces to ensure case alignment will be maintained
  - Ensure there is always contact between the pilot faces
  - Too much contact can lead to over stressing of the joint but not contact will lead to radial misalignment across the machine
- Peak stresses in the casing to determine fatigue life from thermal loads
  - Limit peak thermal stress in the case to meet fatigue life requirements. For this case, a minimum of 11,000 cycles was set
  - High stresses will occur at pilot joints due to mating parts heating up or cooling down faster than the other part
- Stress in the bolts to ensure they do not yield or unload
  - With casings heating up quicker, bolts can be overstretched and yield, meaning they will lose preload when all the joints reach the same temperature
  - With casing cooling down quicker, bolts can become unloaded leading to possible leaks in the joint
  - Bolted joint analysis leads to a max temperature difference of 150°F between bolts and case

First transient runs were analyzed with 60 minute start up times, 60 minute steady state hold, 60 minutes shut down, and then time for the model to reach steady state during cool down. If the criteria above were not met, the start up and shut down times needed to be increased. If all the criteria were met, then the times could be reduced.

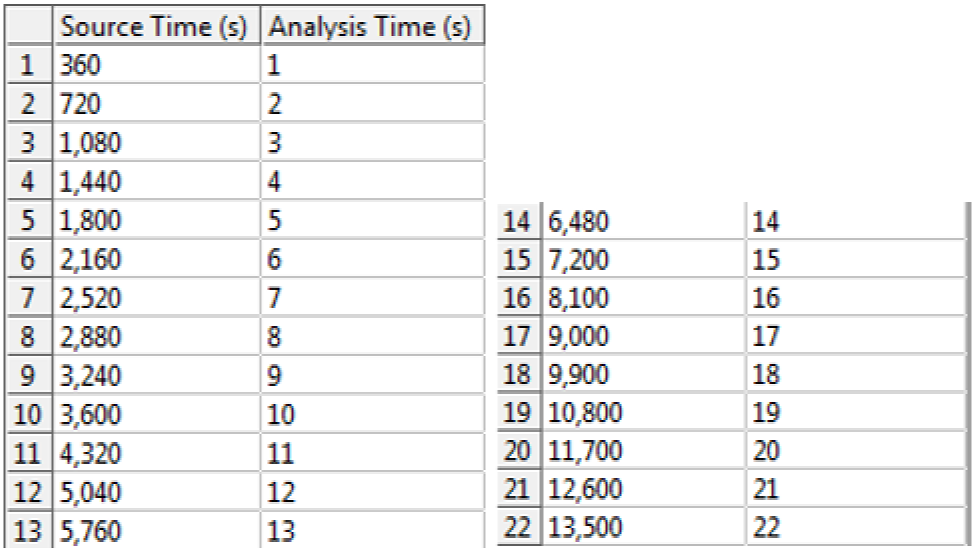

	Source Time (s)	Analysis Time (s)
1	360	1
2	720	2
3	1,080	3
4	1,440	4
5	1,800	5
6	2,160	6
7	2,520	7
8	2,880	8
9	3,240	9
10	3,600	10
11	4,320	11
12	5,040	12
13	5,760	13
14	6,480	14
15	7,200	15
16	8,100	16
17	9,000	17
18	9,900	18
19	10,800	19
20	11,700	20
21	12,600	21
22	13,500	22

Figure 48: Transient Times for Inlet Plenum, Dry Gas Seal Housing, and Nozzle Casing Joints

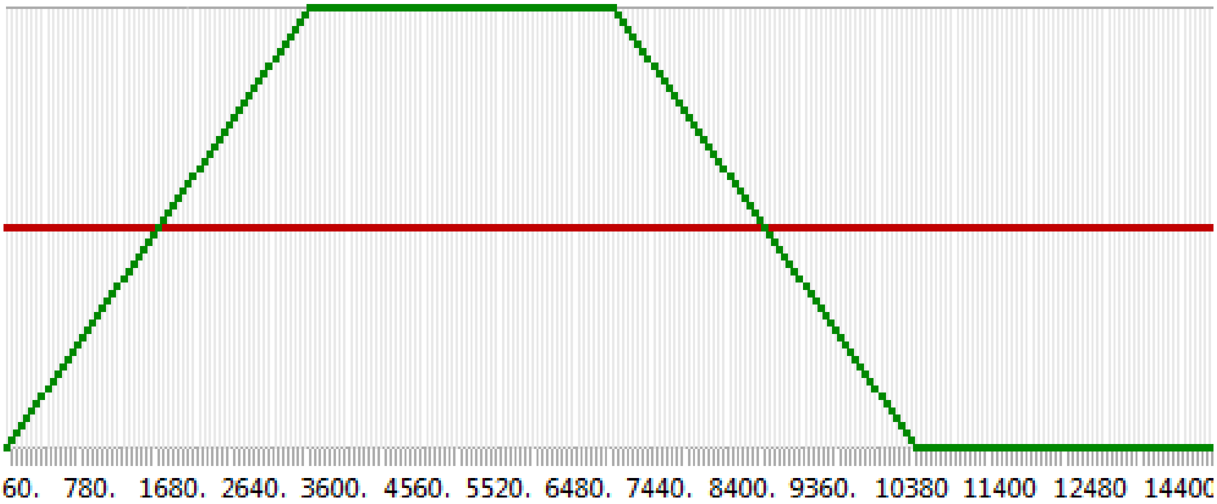

Figure 49: Transient Times for Nozzle Casing to Exit Plenum – Temperature (Green) & HTC (Red)

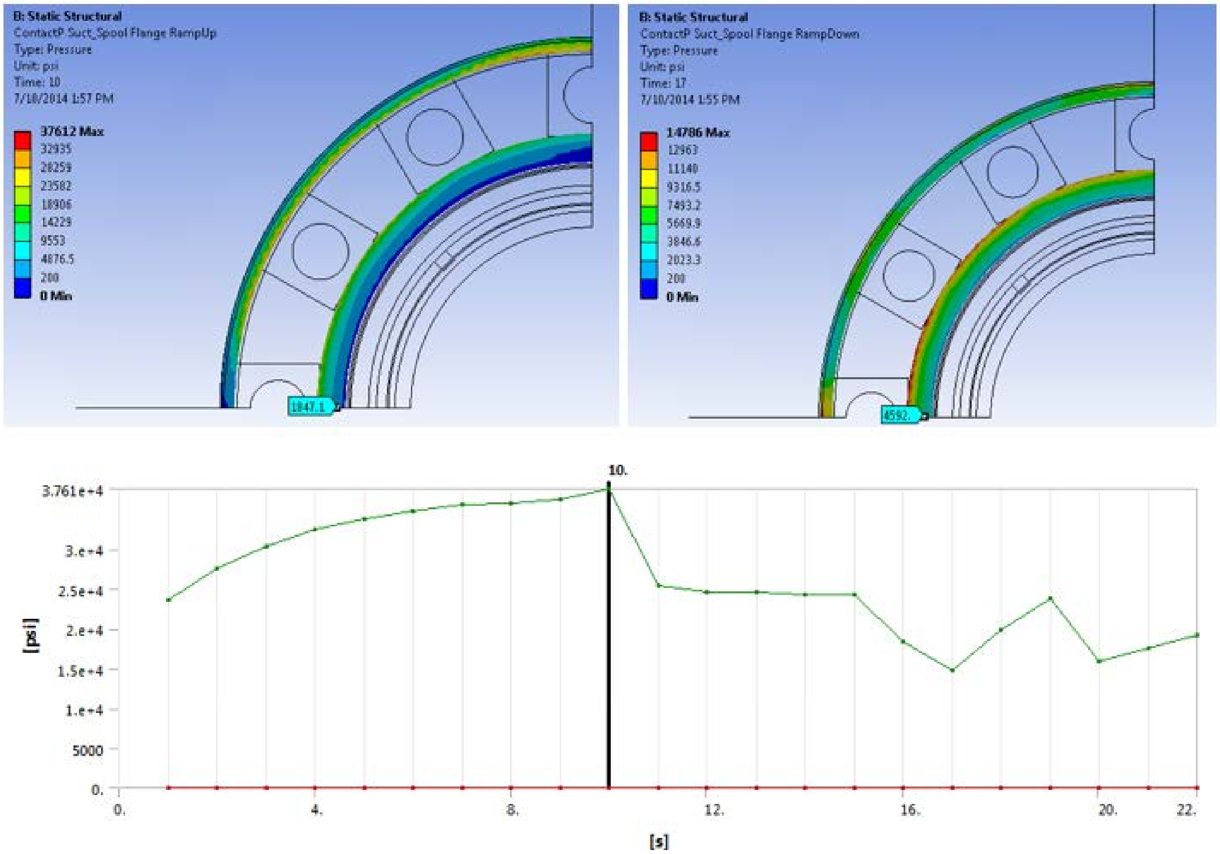

Figure 50: DGS Housing to Inlet Plenum Axial Face Contact Pressure - Start up and Shut Down – Max Contact Stress (green) & Minimum Contact Stress (red)

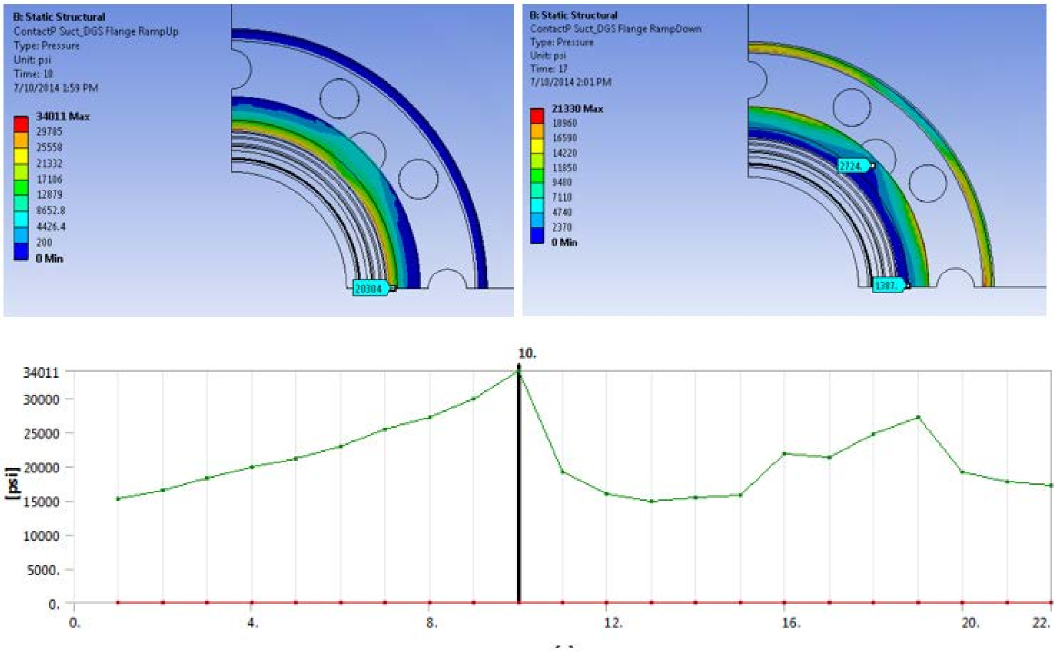

Figure 51: Inlet Plenum to Nozzle Casing Axial Face Contact Pressure – Start up and Shut Down

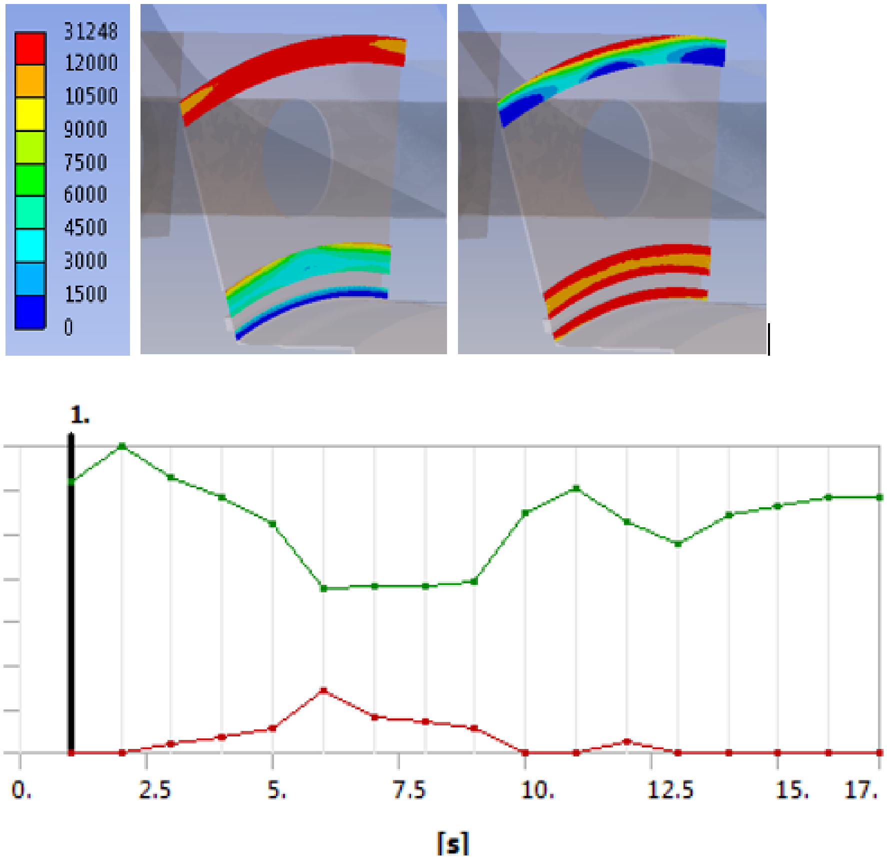

Figure 52: Nozzle Casing to Exit Plenum Axial Face Contact Pressure – Start up and Shut Down

Face contact is required to ensure there will be no leakage across the spring energized face seal. This provides a backup seal as well with a contact pressure around 2X greater than operating pressure. The outer axial face reduces the bending moment on the flanges, but can also see higher contact pressure which will lead to leakage through the bolts if the contact pressure is relieved on the inner face. Axial face contact pressure criteria is met with the 60 minutes start up and shut down times.

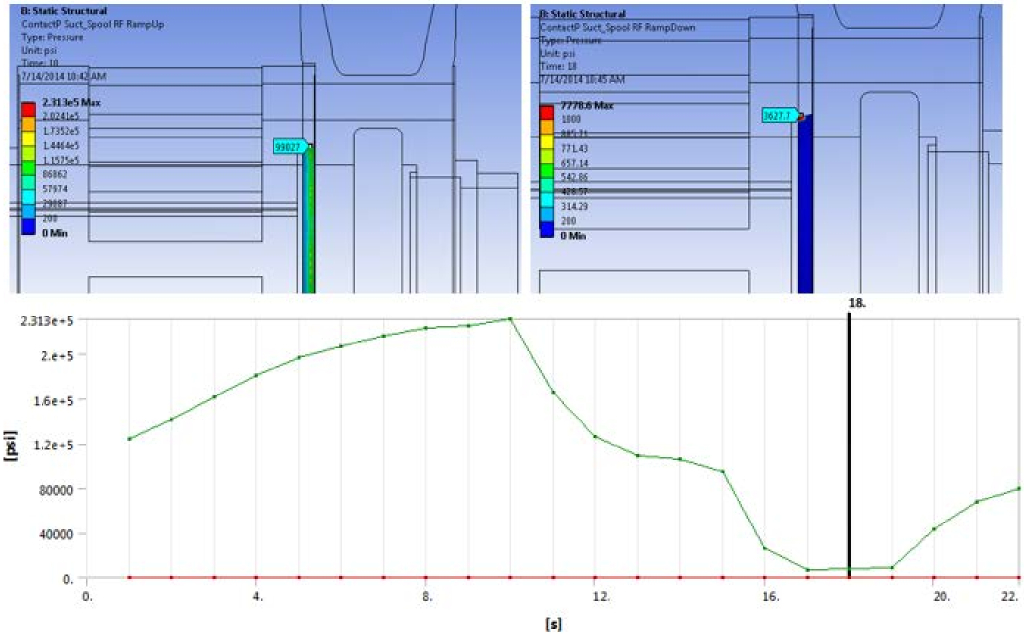

Figure 53: DGS Housing to Inlet Plenum Radial Contact Pressure - Start up and Shut Down

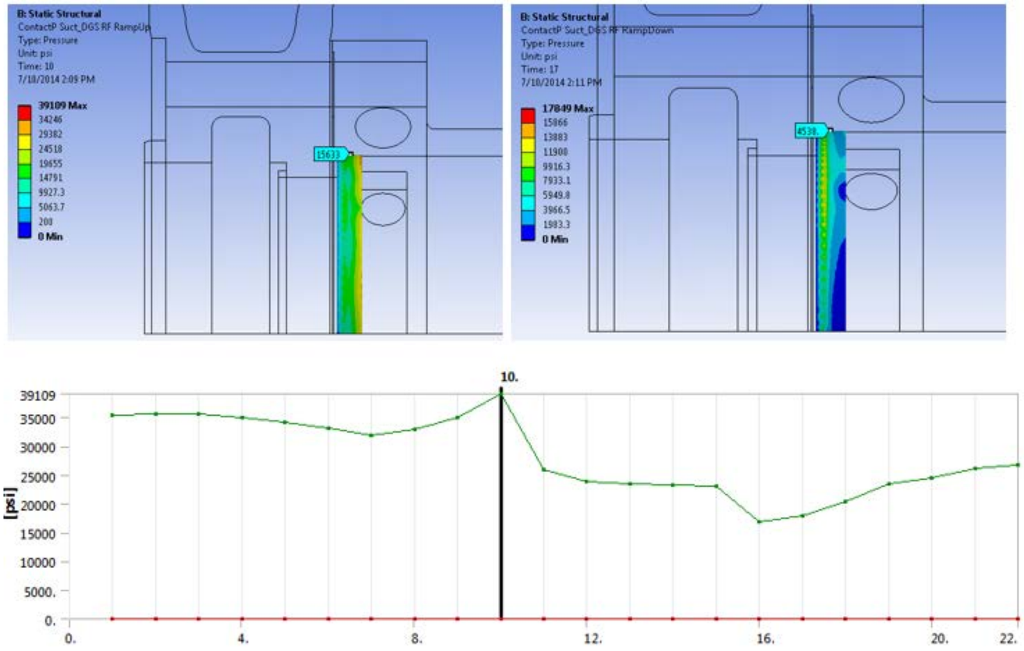

Figure 54: Inlet Plenum to Nozzle Casing Radial Contact Pressure – Start up and Shut Down

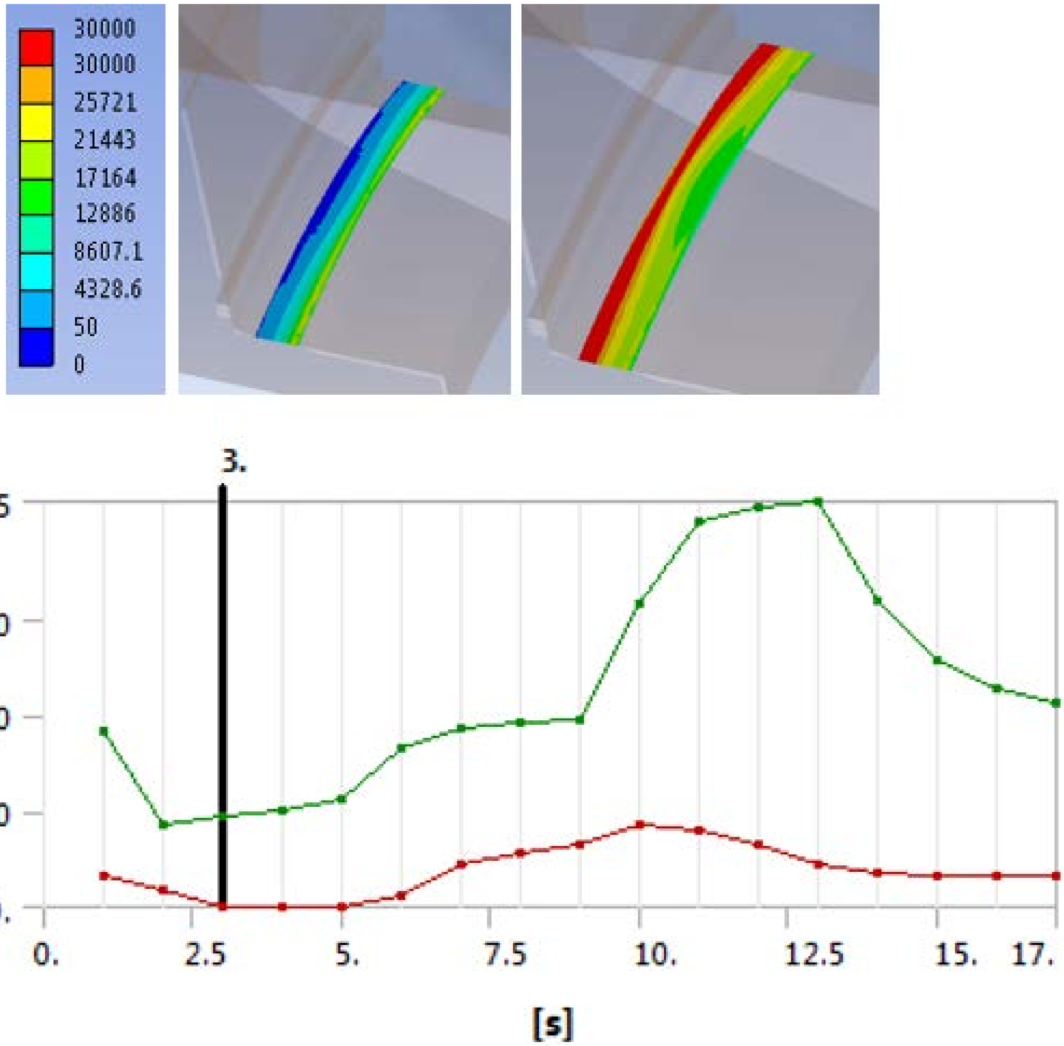

Figure 55: Nozzle Casing to Exit Plenum Radial Contact Pressure - Start up and Shut Down

For two of the joints, the max contact pressure remains relatively high, ensuring that the joint is always in contact. For the inlet plenum to dry gas seal housing, there is a point where the contact gets near zero but still in contact. This is due to the inlet plenum cooling down faster than the dry gas seal housing. This can be prevented by ensuring that no flow runs through the inlet, and it is allowed to cool down naturally. However, with dry gas seal flow still required to buffer the seals, this could lead to shock cooling of the dry gas seal housing leading to life limiting stresses. Radial contact pressure is met with the 60 minute start up and shut down times.

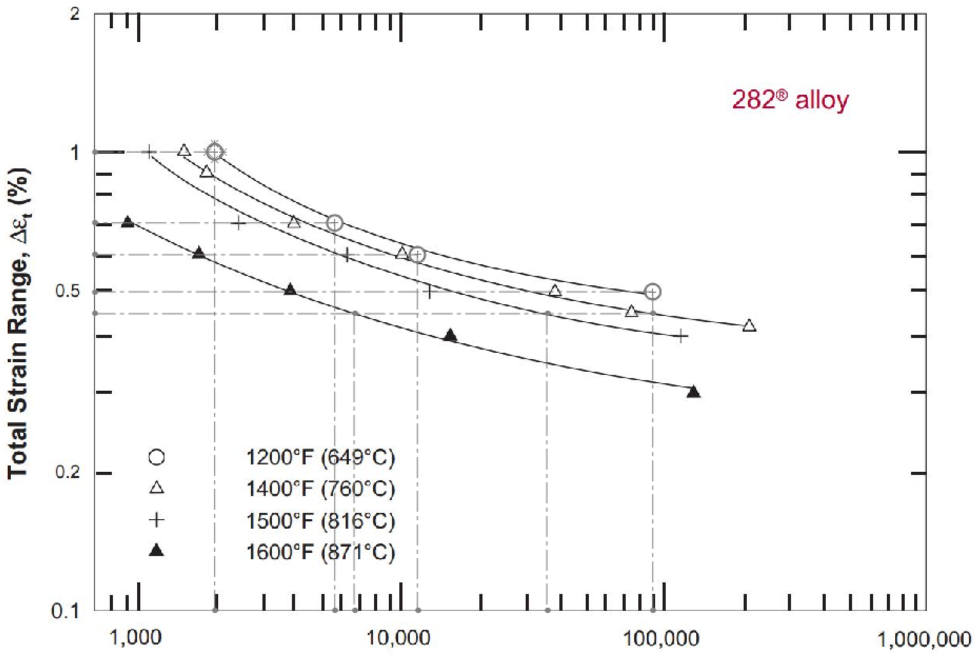

Figure 56: Haynes 282 Low Cycle Fatigue Data - Haynes International

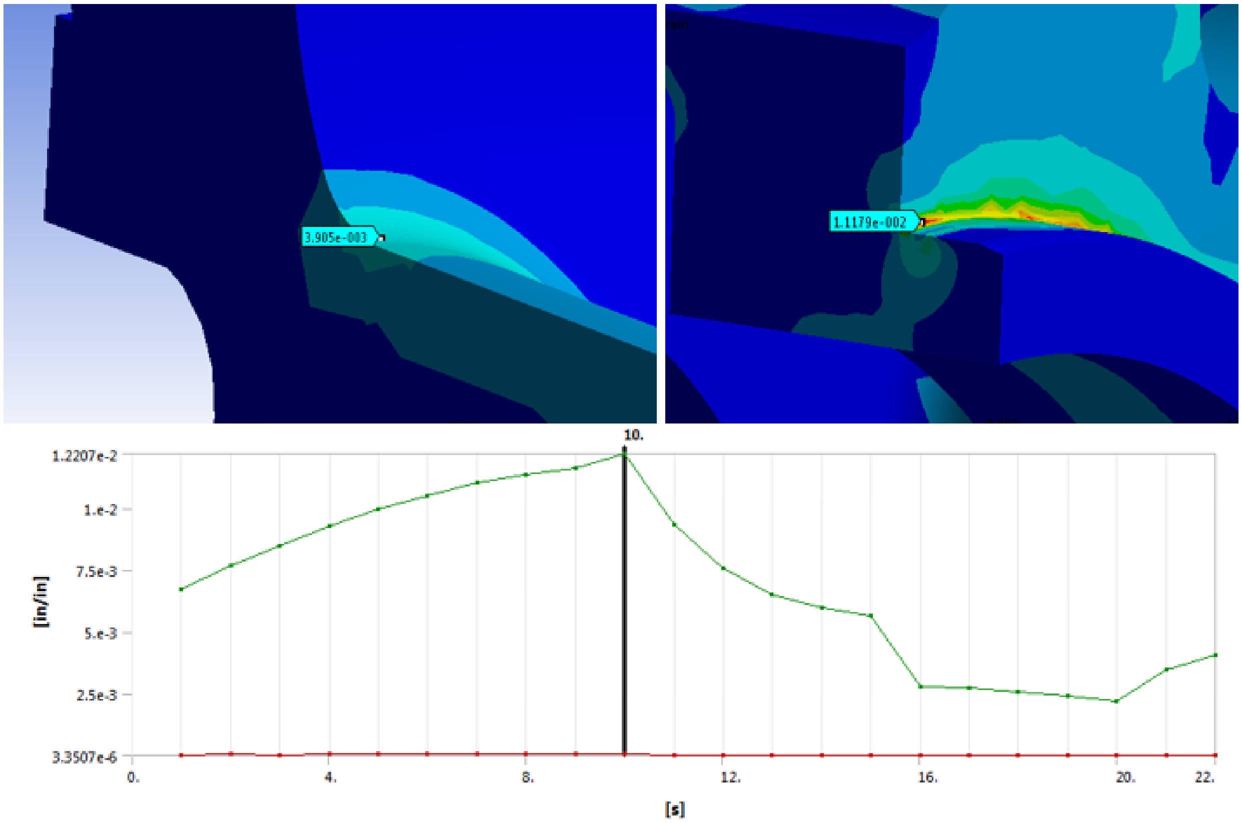

Figure 57: Inlet Plenum Peak Transient Thermal Stresses – Max Strain (green) & Min Strain (red)

The peak stress in the strut corresponds with a peak strain around 0.003 in/in which correlates to > 100,000 cycles. The peak stress in the pilot fit corresponds with a peak strain around 0.0095 in/in which correlates to 1,270 cycles. Because of this, the inlet plenum to nozzle casing joint was designed to be more flexible:

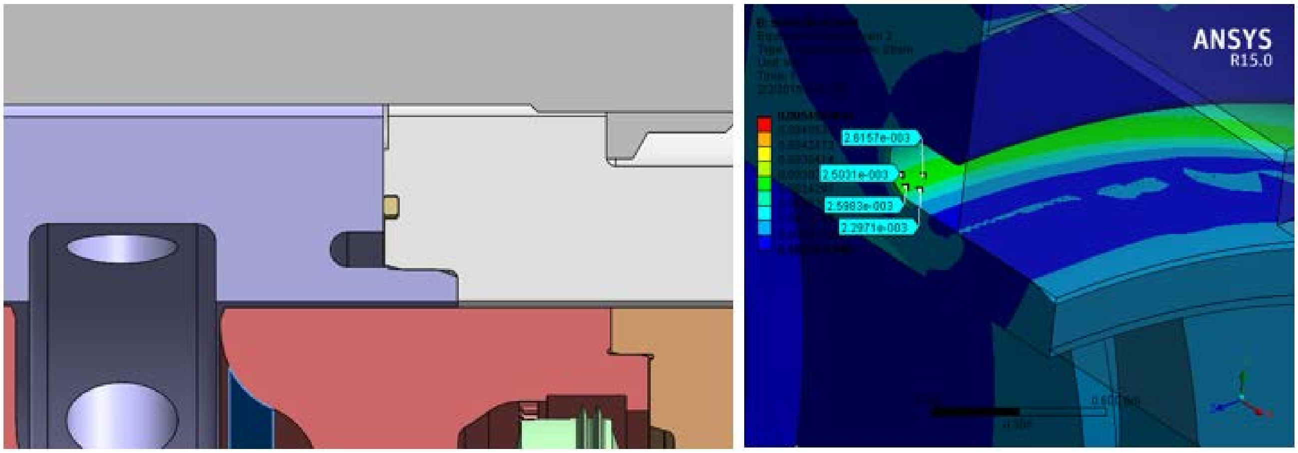

Figure 58: Updated Fit between Inlet Plenum and Nozzle Casing

Peak strain was reduced to less than 0.003 in/in which meets the limiting strain at the strut.

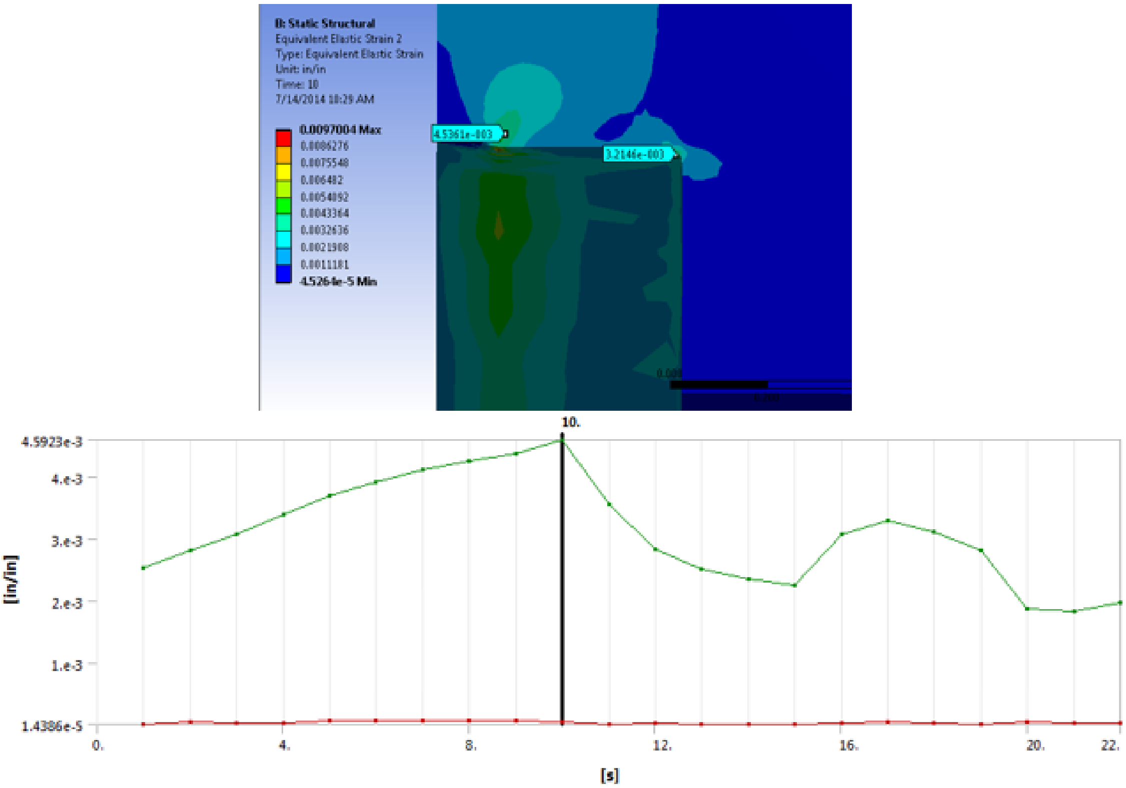

Figure 59: Nozzle Casing Peak Transient Thermal Stress

Peak strain is around 0.0025 in/in which leads to a fatigue life >100,000 cycles.

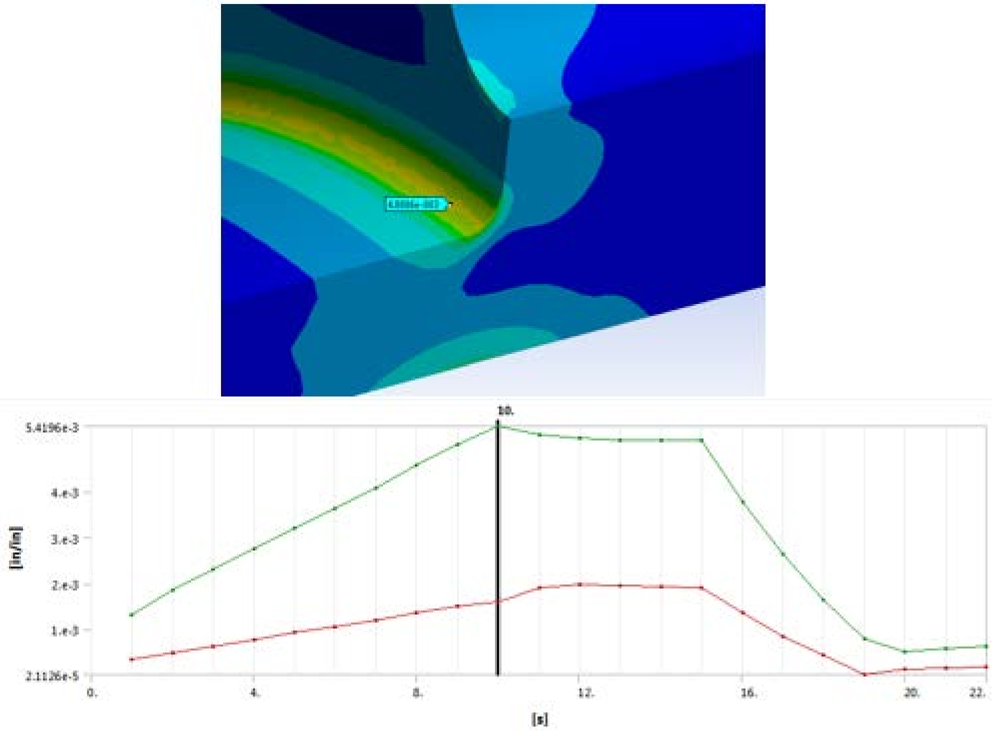

Figure 60: Dry Gas Seal Housing Peak Transient Thermal Strain

Peak strain is around 0.005 in/in which leads to a fatigue life around 20,000 cycles. Due to the location of this joint, it can be softened to reduce this stress. From a fatigue life stand point, this will be the limiting point of the case. All joints meet the 60 minute start up and 60 minute shut down times.

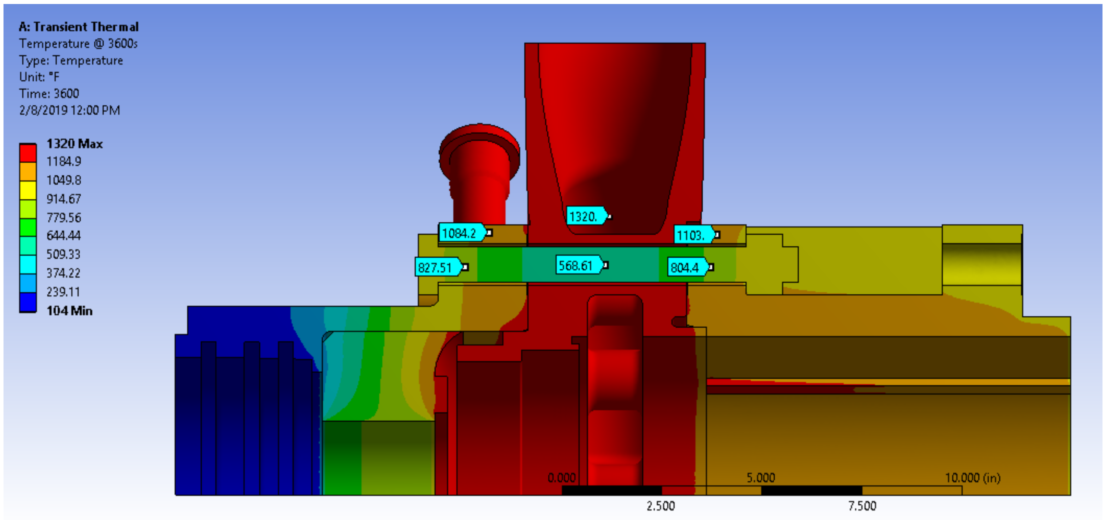

Figure 61: Inlet Bolt to Case Temperature Profile at 60 Minute Start up

At a 60 minute start up, the average bolt temperature is around 700°F with the average casing temperature around 1,200°F. This is about 350°F higher than desirable to prevent yielding of the bolts. By increasing the start up time to 90 minutes, the bolt would heat up to around 1,050 to 1,100°F and be within 150°F of the average case temperature as everything comes to a steady state condition.

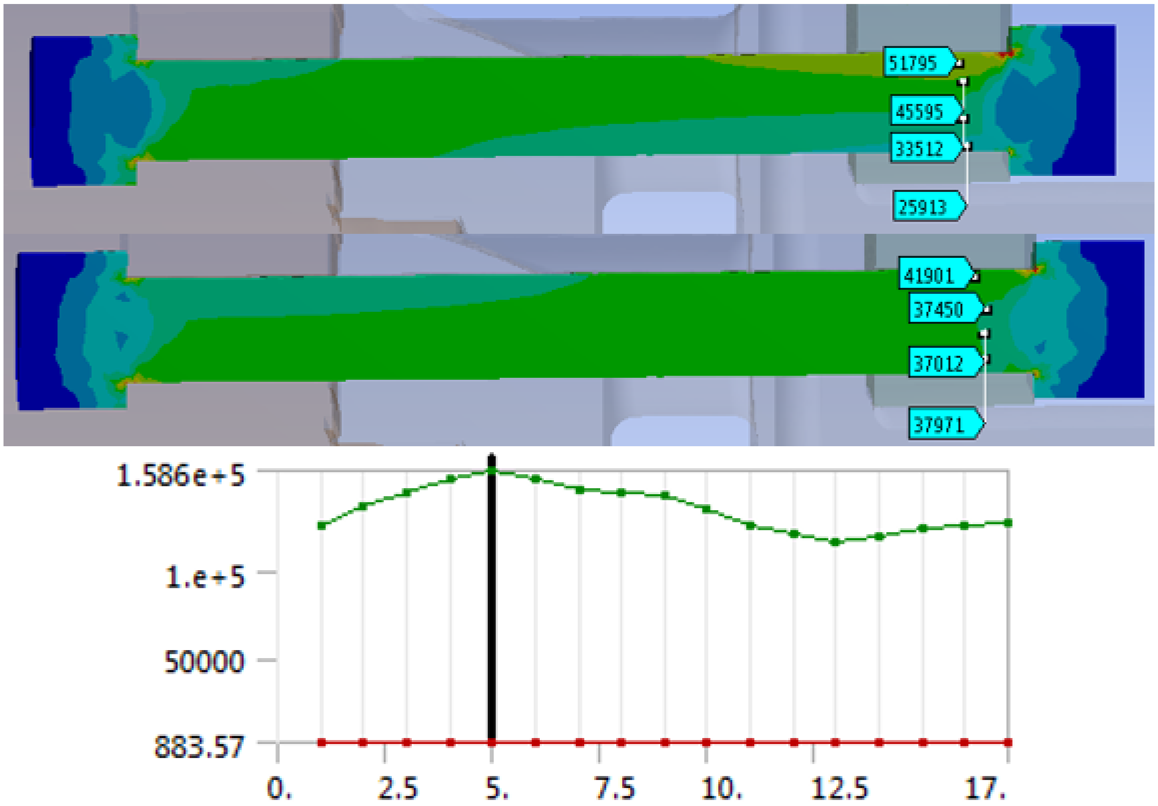

Figure 62: Exit Plenum Bolts - Peak Stresses – Max Stress (green) & Min Stress (red)

At 1,320°F, Nimonic 105 has a modulus of elasticity of 2.58e7 psi and a proof stress of 102,400 psi. This leads to a peak strain of 0.0039 in/in in the shank for the bolt. With the lower temperature, the exit plenum does not over stretch the bolts, however, the inlet bolts require a slower start up time. Increasing the start up and shut down times to 90 minutes kept the bolt below max strain.

With the case designed for pressure containment and fatigue life, it was important to look at the case bending modes to ensure that modes would either be above running speed or could be set at a lower frequency to ensure lower peak displacements in the case and stand.

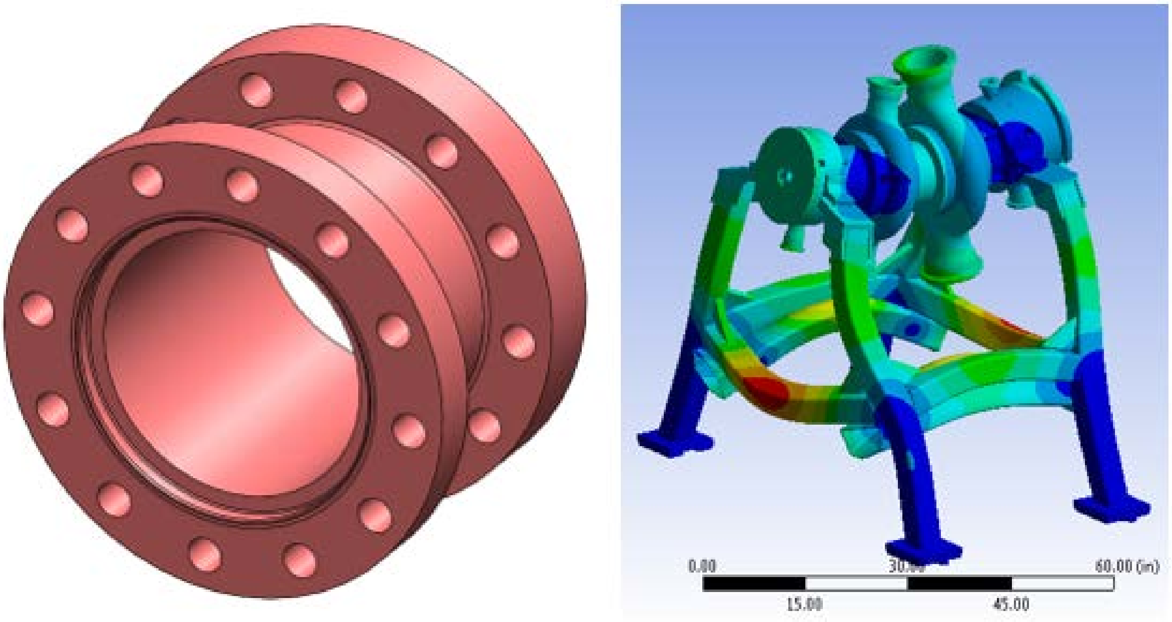

Figure 63: Initial Nozzle Case Design - Bending Mode at 25,950 cpm

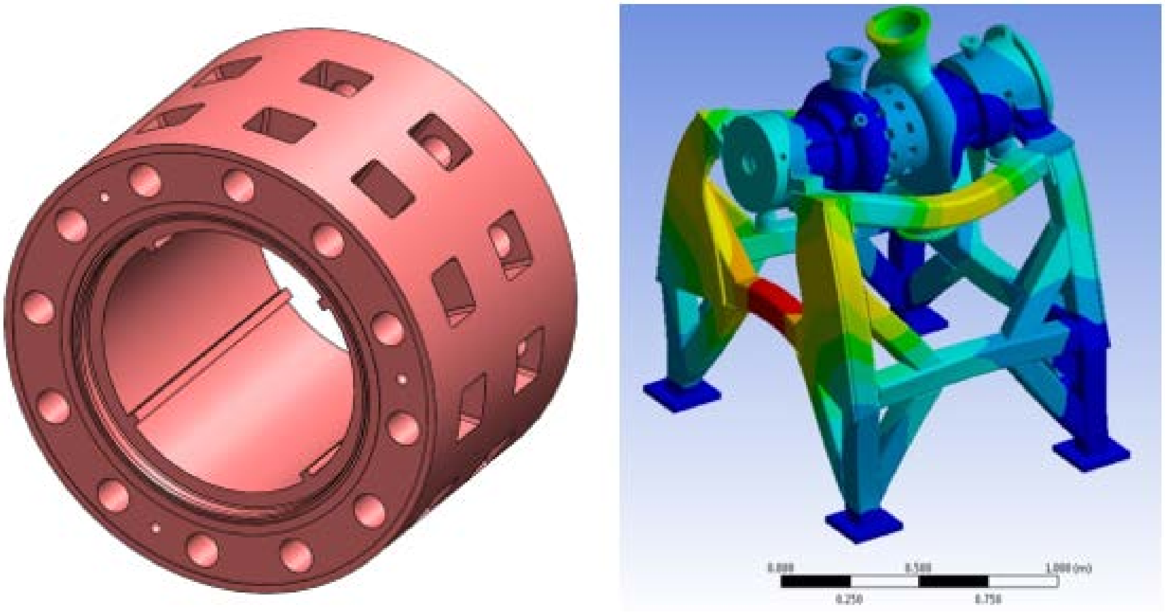

Figure 64: Nozzle Casing Design 2 - Bending Mode at 34,946 cpm

This updated nozzle casing stiffened the center portion of the case which is what was leading to the bending mode within 20% of operating speed (27,000 rpm). The goal was to increase the mode to 20% above max continuous speed which is 5% of operating (28,350 rpm). This puts the minimum mode at 34,020 rpm. This thicker nozzle casing lead to a slower heat up of the nozzle casing and increased thermal stresses in the inlet plenum. To correct that issue, the stiffness was maintained by removing mass and utilizing a ribbed design instead of a solid piece:

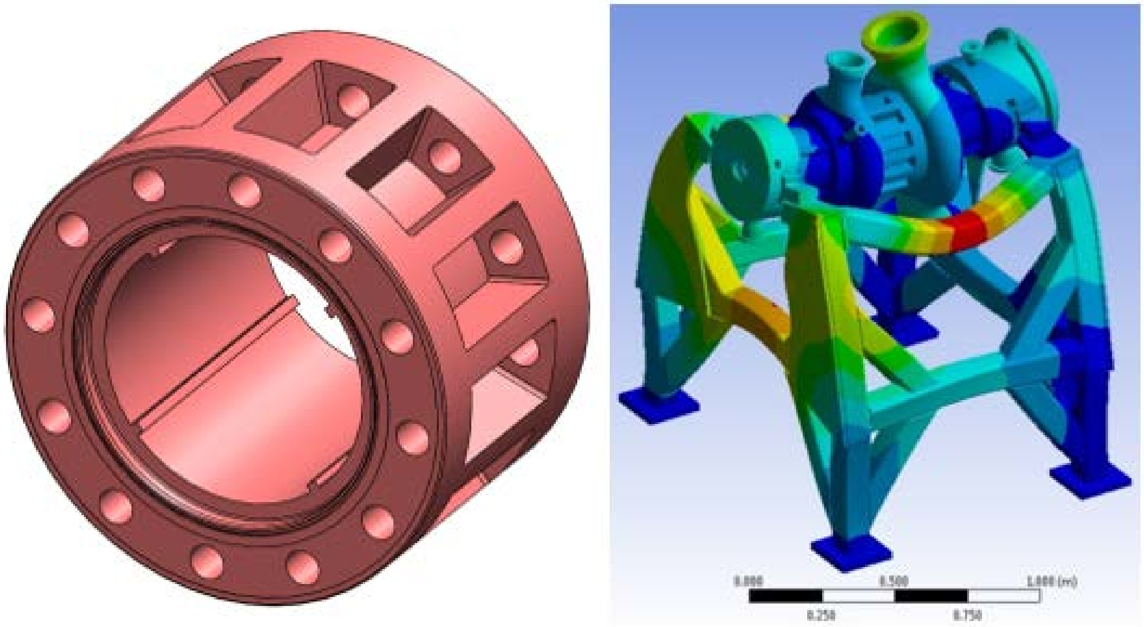

Figure 65: Final Nozzle Casing Design - Bending Mode at 34,813 cpm

The ribbed design kept the mode above the 20% margin and also allowed the nozzle casing to respond faster to temperature transients which kept peak stresses in the inlet plenum below 0.003 in/in.

The next component of concern were the stator nozzles. While stresses in the stator nozzles will be relatively low, it is important to check the contact stresses on the split faces and also peak strains on the 1st stage stator that pilots the inlet turn on to the main case:

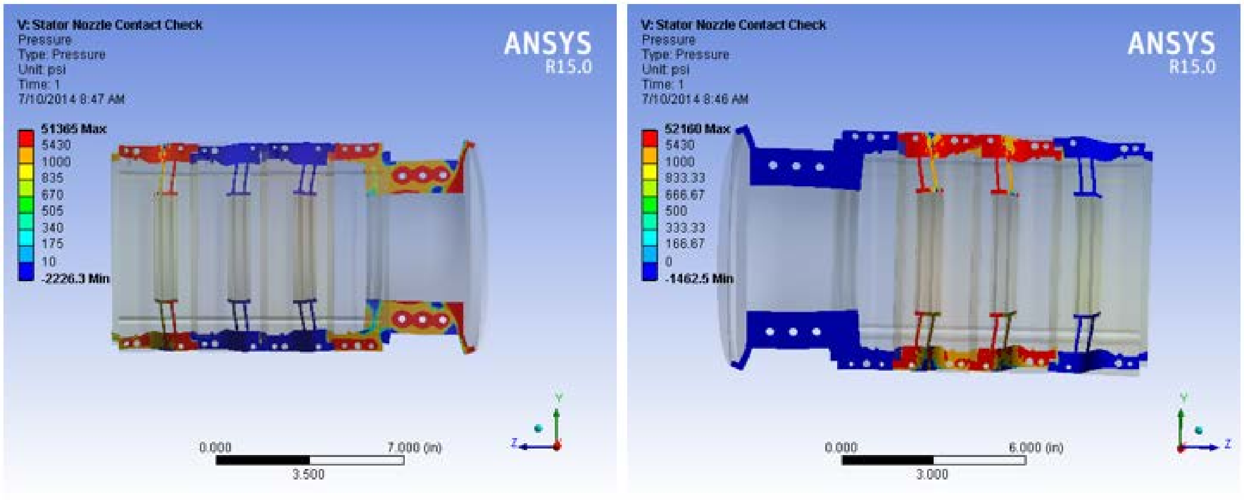

Figure 66: Stator Stack Contact Pressure

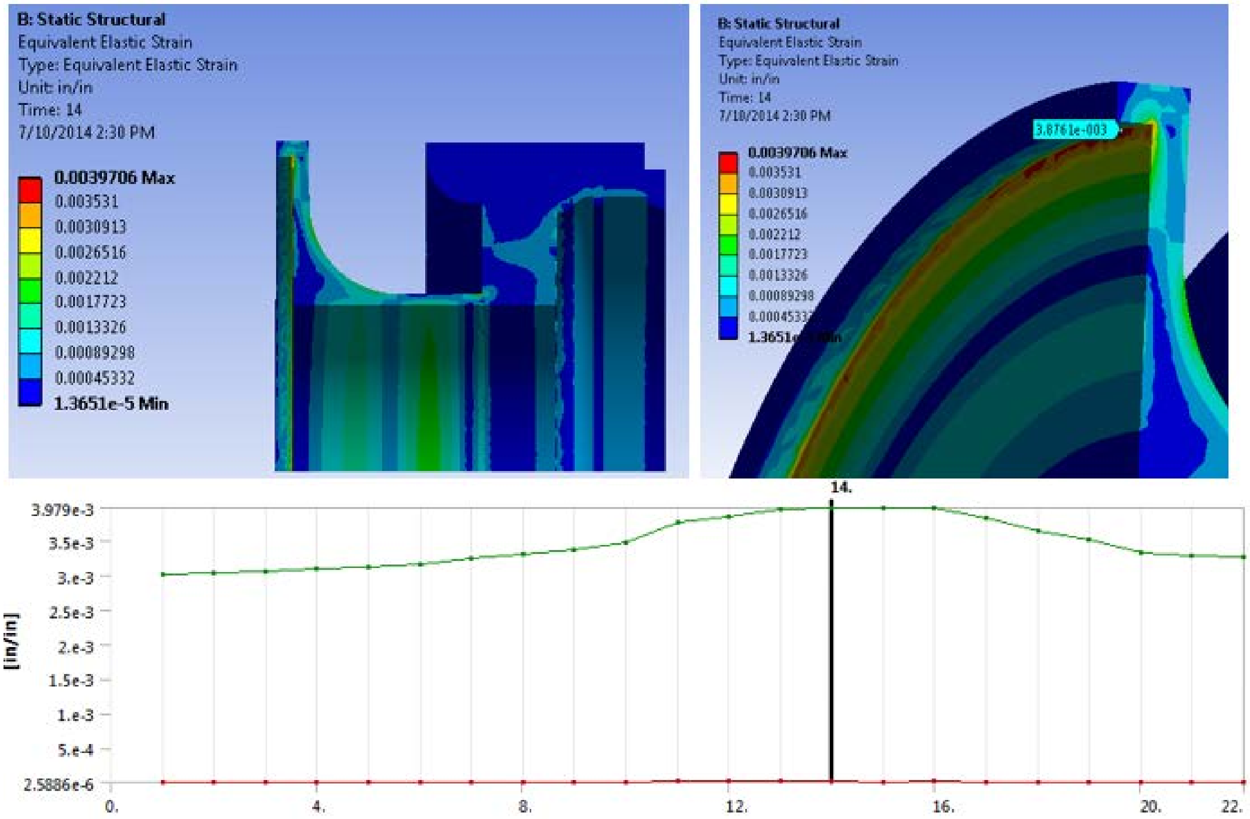

Figure 67: Peak Strain in Stator Nozzles – Max Strain (Green) & Min Strain (Red)

The contact model shows that the external pressure acting on the nozzles keeps the split faces in contact and will prevent leakage. Lower leakage leads to more flow and higher power through the turbine. In terms of fatigue life, the peak strain is at 0.0040 which yields a fatigue life > 100,000 cycles. Like the rest of the casing, the nozzles are made out of Haynes 282.

For the balance piston seal, it is important to look at three limiting features:

- Stress
- Radial deformation of the seal from pressure
    - Damping from the seal is influenced heavily by the taper in the seal due to machining or pressure difference across the seal
    - If the taper is predicted, it can be machined into the seal to be straight at nominal operating conditions
- High cycle fatigue of the support keys
    - Due to dynamic loading from the seal, the keys will be required to carry the load at 450 hz during the life of the rotor

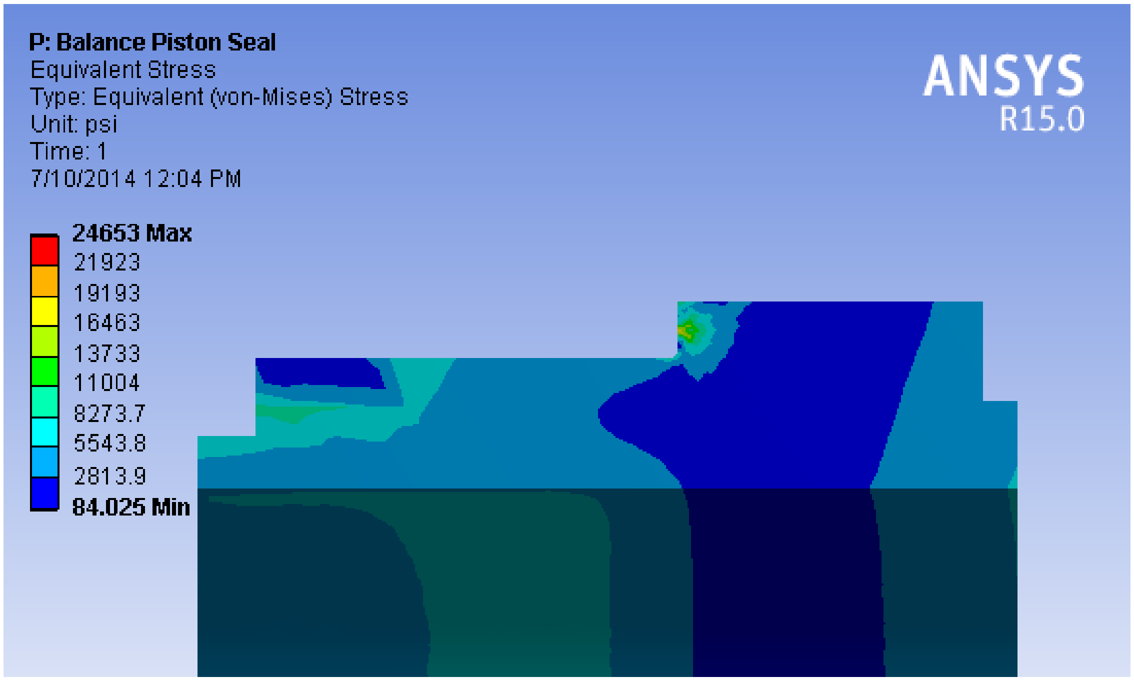

Figure 68: Balance Piston Peak Stresses

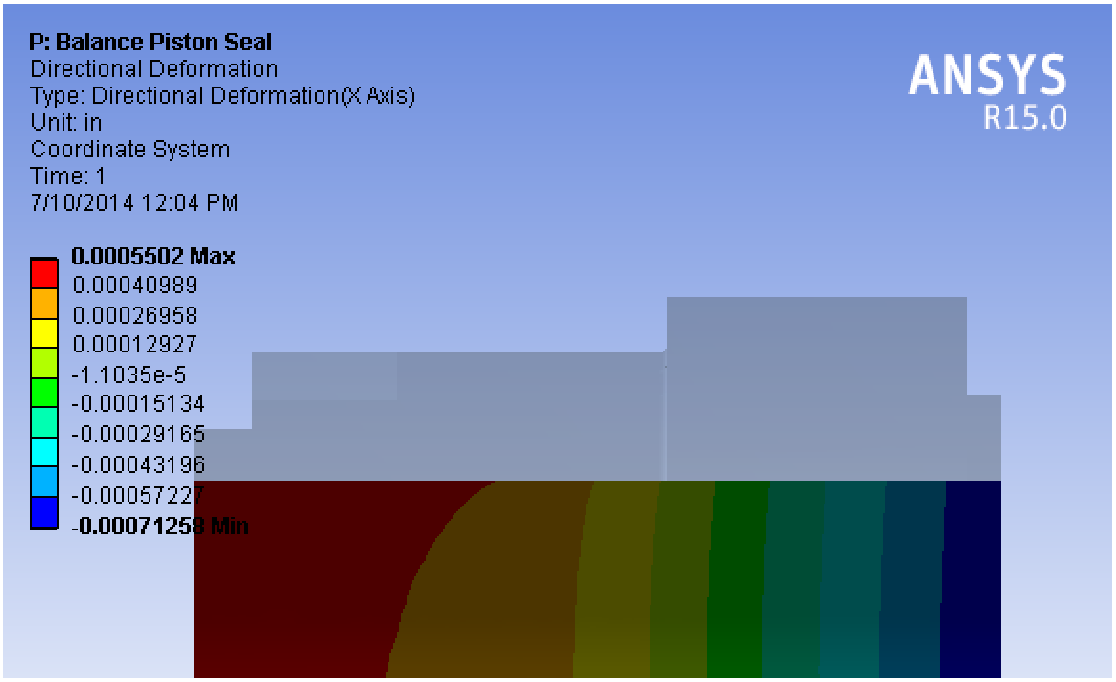

Figure 69: Balance Piston Radial Deformation

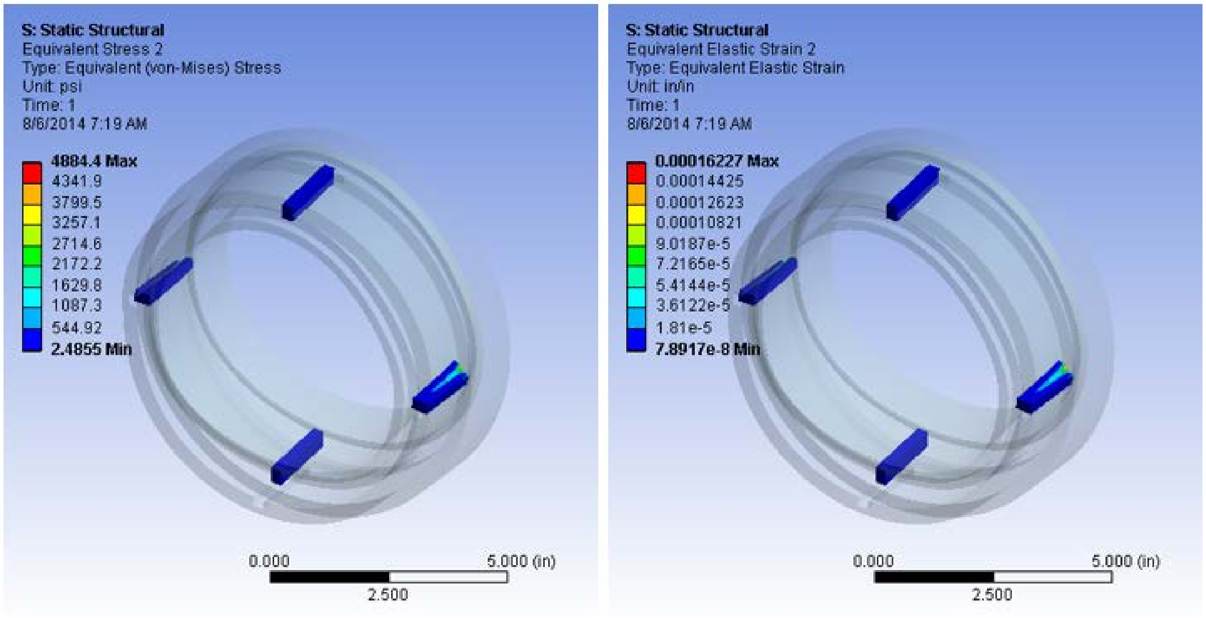

Figure 70: Balance Piston Peak Stress and Strain with 400 lbf Dynamic Load (2X Predicted)

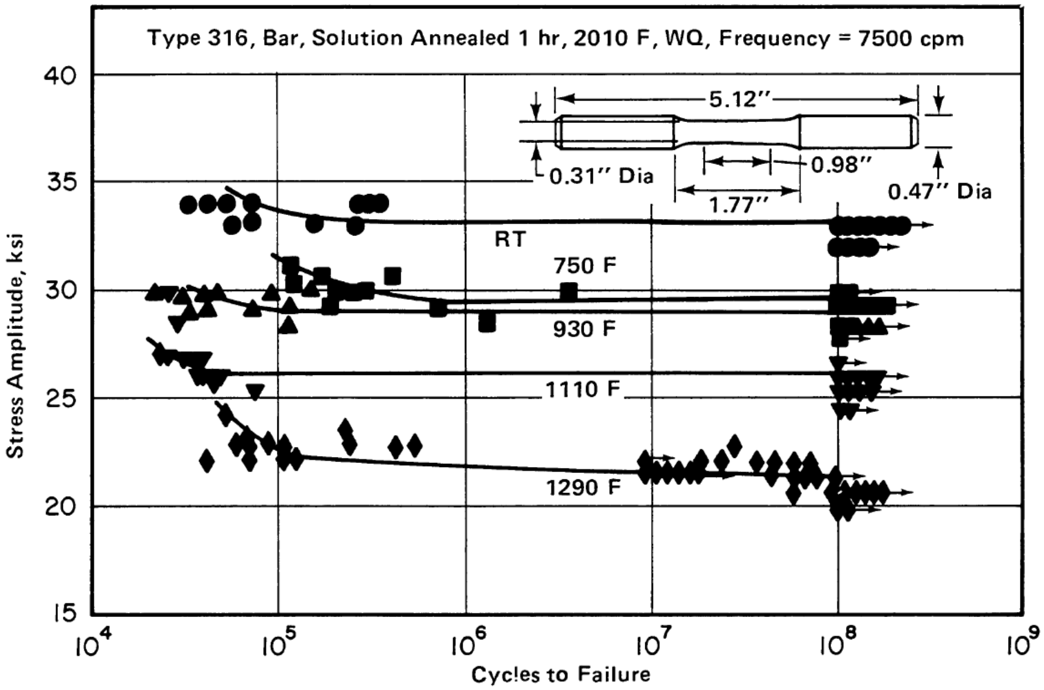

Figure 71: High Cycle Fatigue of 316 SS - Balance Piston Key Material (Aerospace Structures Metals Handbook, Edition 39:1)

At 1,290°F, the fatigue limit of 316 stainless is around 20 ksi. Peak stress in the keys from a dynamic 2x higher than predicted is 4.9 ksi. Based on these FEAs, the balance piston meets the stress requirements for shear and high cycle fatigue. The seal does deform into a taper of around 0.0012” at max pressure. This taper was machined into the seal along with increasing the diameter to ensure a radial clearance of 0.010” at operating conditions to match performance with rotordynamics.

For the thermal seal, the goal was to reduce stresses in the rotor by maintaining a linear thermal gradient across the seal between the dry gas seal and the balance piston. The thermal boundary conditions are shown in Figure 43.

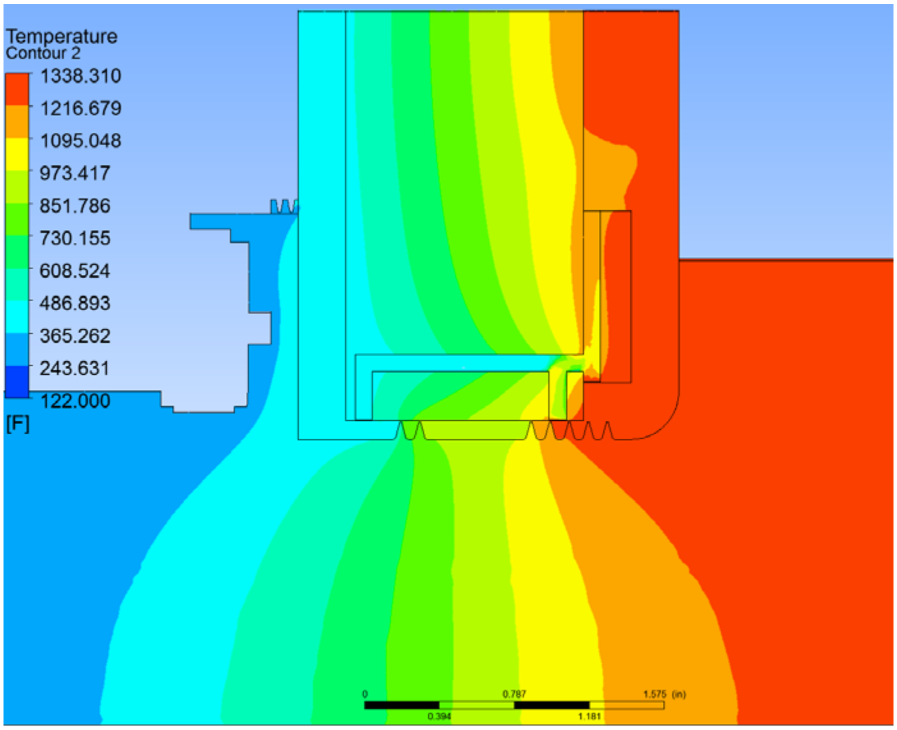

Figure 72: Thermal Seal Steady State Temperature Profile

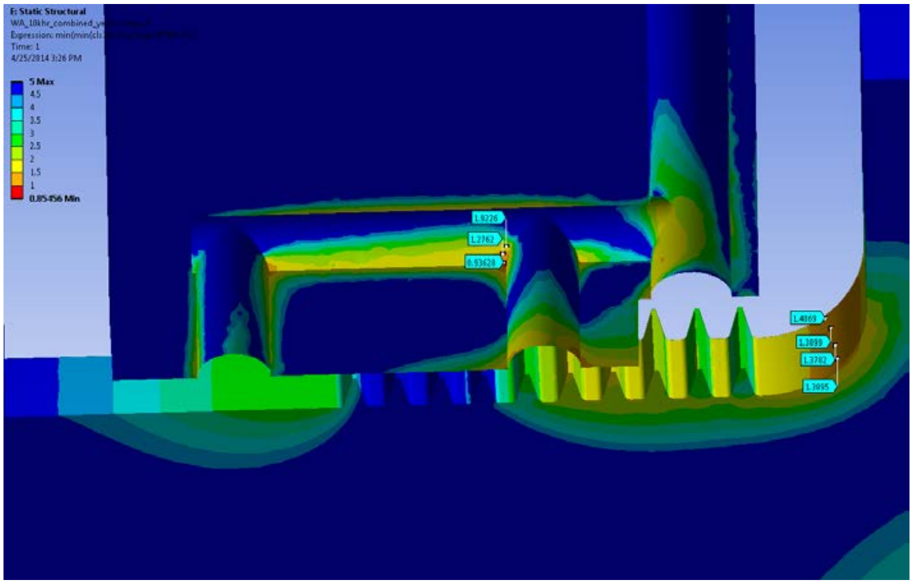

Figure 73: Steady State Safety Factor in Rotor based on Creep and Yield Properties

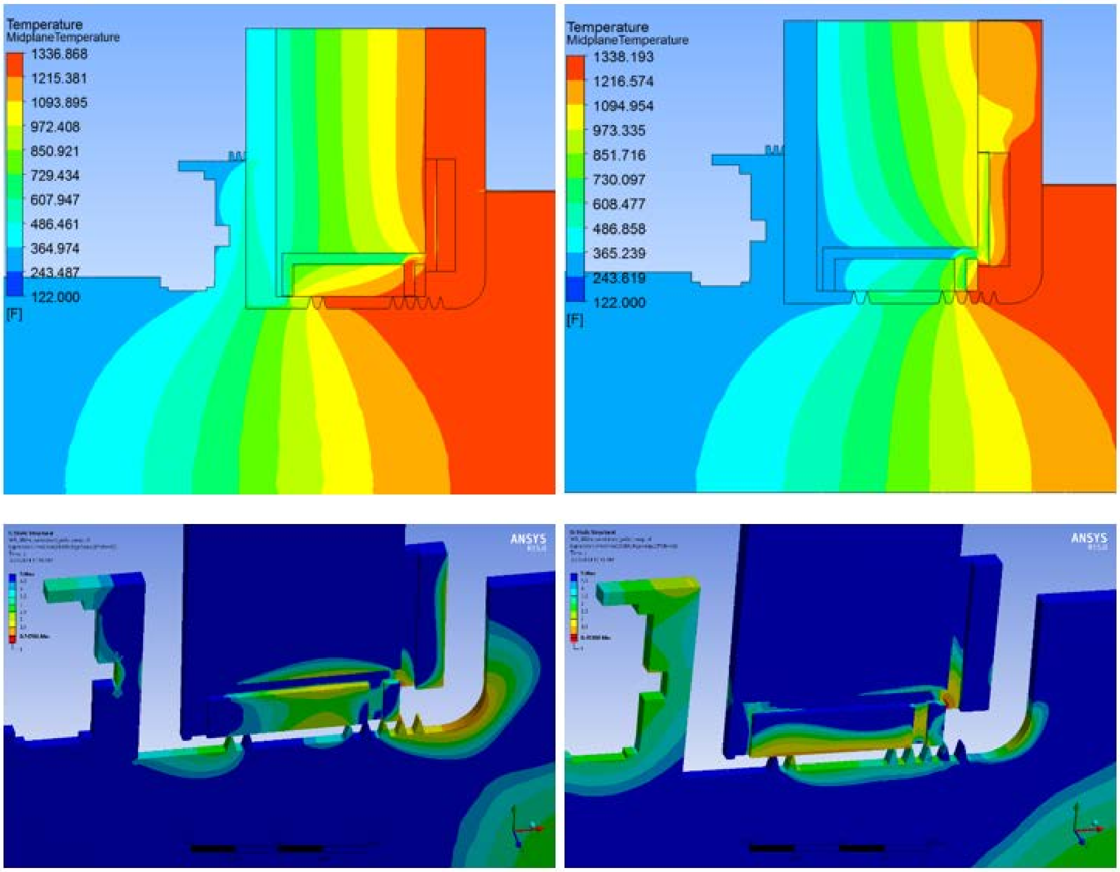

Figure 74: Thermal Seal Sensitivity Study - Increased Hot Flow (Left) and Increased Cold Flow (Right)

In the baseline and off design studies, the peak stresses in the rotor maintain a safety factor greater than 1. The worst case would be too much cold flow shooting across the seal, which would cool down the balance piston and lead to higher stresses in the fillet. Too much hot flow, and the thermal gradient is shortened leading to much higher thermal stresses across the rotor.

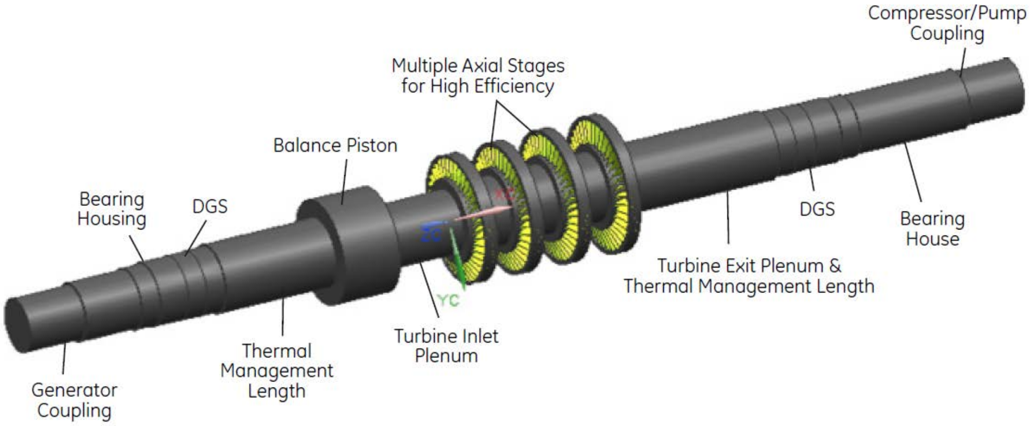

Figure 75: Final SunShot sCO_2 Turbine Rotor Design

Specific design details and metrics:

- Pressure containment and casing design in progress to industry standards per GE steam turbine design practice
- Lateral and torsional rotor-dynamics established per API and industry standards
- Rotor overspeed capability with 20% margin to all conditions anticipated in test loop
- Thrust bearing and balance piston design expected to meet API 617 standard for anticipated operating conditions in test loop
- Creep and low cycle fatigue life sufficient for 24,000 hours of operation and 1,000 starts
- Axial and radial clearances set to meet API 617 at all steady state and transient operating conditions
- Design of rotor and casing based on the current status is anticipated for continuous operation and product maintenance intervals greater than 24,000 hours or 1,000 starts
- Expander isentropic efficiency greater than 86% (actual 87%+) based on meanline analysis calibrated to GE aviation and power generation experience.

Task 1.3. Test Loop Design

Subtask 1.3.1 Define Operating Requirements for all Major Components of the Cycle

The operating conditions have been defined for all major components of the cycle and are summarized in Table 1, as well as in the P&ID. The pressure and temperature at the inlet and outlet of each component dictate the required materials of construction and define the density of CO_2 at that location. Based on the fluid density and the mass flow, the interconnecting piping can be sized to control the maximum flow velocity. The system which has been designed for construction and testing at SwRI has been sized based on a maximum flow velocity of 50 ft/s. This limit is based on past experience and is expected to maintain reasonable pressure losses between major components. Pipe diameter, thickness, material of construction, and the predicted flow velocity for each section are shown in Table 16.

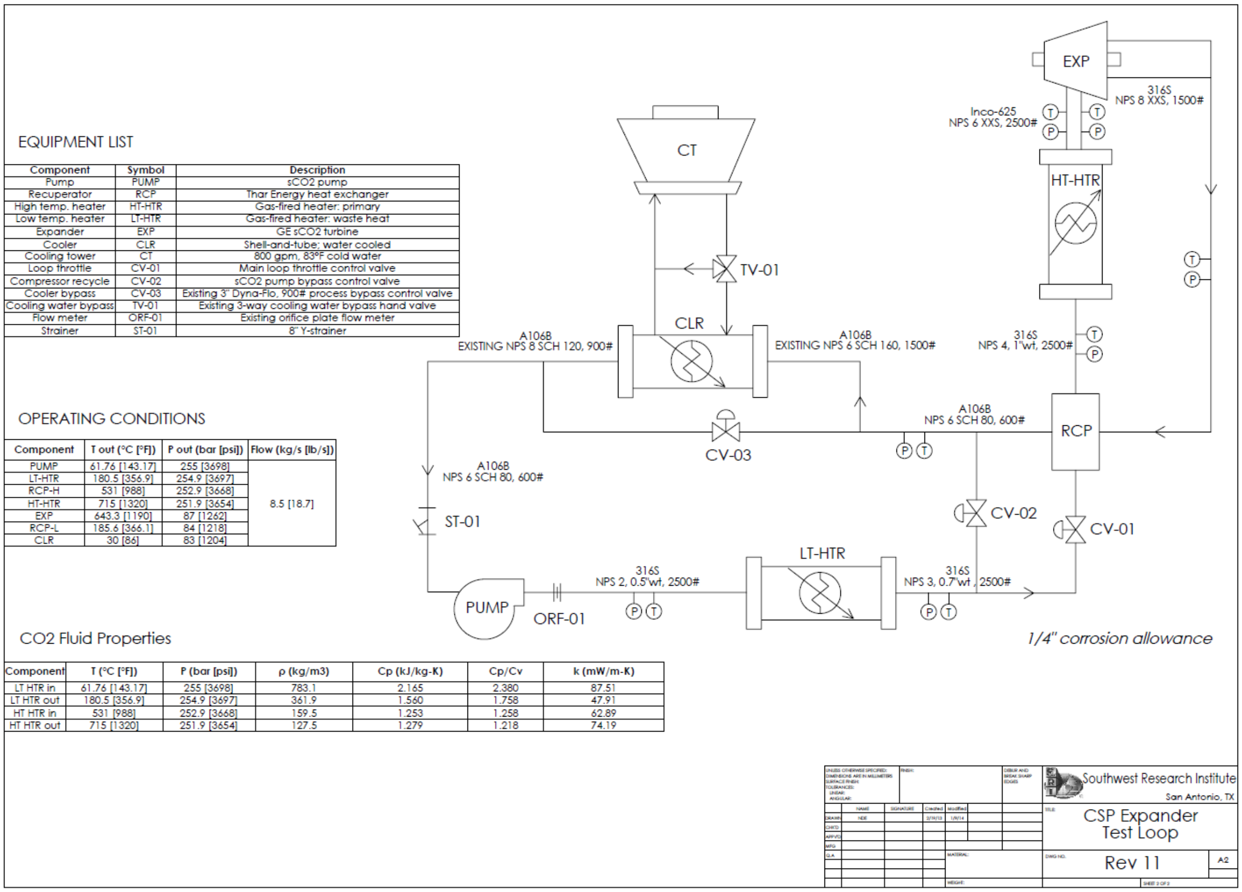

EQUIPMENT LIST

Component	Symbol	Description
Pump	PUMP	sCO2 pump
Recuperator	RCP	Thar Energy heat exchanger
High temp. heater	HT-HTR	Gas-fired heater: primary
Low temp. heater	LT-HTR	Gas-fired heater: waste heat
Expander	EXP	GE sCO2 turbine
Cooler	CLR	Shell-and-tube; water cooled
Cooling tower	CT	800 gpm, 83°F cold water
Loop throttle	CV-01	Main loop throttle control valve
Compressor recycle	CV-02	sCO2 pump bypass control valve
Cooler bypass	CV-03	Existing 3" Dyna-Flo, 900# process bypass control valve
Cooling water bypass	TV-01	Existing 3-way cooling water bypass hand valve
Flow meter	ORF-01	Existing orifice plate flow meter
Strainer	ST-01	8" Y-strainer

OPERATING CONDITIONS

Component	T out (°C [°F])	P out (bar [psi])	Flow (kg/s [lb/s])
PUMP	61.76 [143.17]	255 [3698]	8.5 [18.7]
LT-HTR	180.5 [356.9]	254.9 [3697]	
RCP-H	531 [988]	252.9 [3668]	
HT-HTR	715 [1320]	251.9 [3654]	
EXP	643.3 [1190]	87 [1262]	
RCP-L	185.6 [366.1]	84 [1218]	
CLR	30 [86]	83 [1204]	

CO2 Fluid Properties

Component	T (°C [°F])	P (bar [psi])	ρ (kg/m3)	Cp (kJ/kg-K)	Cp/Cv	k (mW/m-K)
LT HTR in	61.76 [143.17]	255 [3698]	783.1	2.165	2.380	87.51
LT HTR out	180.5 [356.9]	254.9 [3697]	361.9	1.560	1.758	47.91
HT HTR in	531 [988]	252.9 [3668]	159.5	1.253	1.258	62.89
HT HTR out	715 [1320]	251.9 [3654]	127.5	1.279	1.218	74.19

Figure 76: Test Loop Process and Instrumentation Diagram

Subtask 1.3.2. Design P&ID for Turbo-Expander Test Loop

The process and instrumentation diagram Figure 76 has been created and depicts the SwRI test configuration, process conditions, fluid properties, and equipment list. Additionally, process measurement locations are shown upstream and downstream of the recuperator and expander, which will allow quantification of their performance. Loop flow will be measured via an orifice flow meter downstream of the sCO_2 pump.

A steady-state flow model of the system was created using Stoner Pipeline Simulator (SPS). SPS is a transient and steady-state hydraulic simulator that calculates dynamic flow of single phase fluids and fluid handling machinery such as pumps and compressors based on an equation of state. The model was tested on CO_2 using the Benedict-Webb-Rubin-Staring (BWRS) equation of state and compared to values from NIST REFPROP to verify its performance at supercritical conditions.

Table 16: Pipe Specifications

Section	Temp. (°C)	Press (bar)	NPS (in)	Wall Thick. (in)	Schedule	Material	Predicted Velocity (ft/s)	ANSI Flange Class
Pump to LT heater	61.67	255	2	0.436	XXS	316s	31.10	2500#
LT heater to recup.	180.5	254.9	3	0.600	XXS	316s	28.74	2500#
Recup. to HT heater	531	252.9	4	0.674	XXS	316s	34.74	2500#
HT heater to exp.	715	251.9	6	0.864	XXS	Inco 625	18.00	2500#
Exp. to recup.	643.3	87	8	0.875	XXS	316s	23.55	1500#
Recup. to existing	185.6	84	6	0.432	80	A106B	15.68	600#
Existing to cooler	185.6	84	6	0.718	160	A106B	19.33	1500#
Cooler outlet	30	83	8	0.718	120	A106B	1.48	900#
Cooler to pump	30	83	6	0.432	80/XS	A106B	2.31	600#

The model was built using pipe and valve elements with the expander inlet and outlet conditions being achieved via a heat-exchanger and valve combination. The pump suction and discharge pressure, temperature, and flow were imposed via fixed boundary conditions. A schematic of the model is shown in Figure 77, and the resulting predicted density at each section is shown in Table 17. The conditions predicted by SPS agree well with the reference, where the greatest error is observed at the cooler outlet/pump inlet, where the CO_2 is at its coldest, lowest pressure state (nearest the critical point). This steady-state hydraulic model was used to verify flow velocities, pressure losses, and thermal exchange with the surrounding environment throughout the system. A dynamic simulation will facilitate simulations of normal startup and shutdown, as well as emergency shutdown procedures.

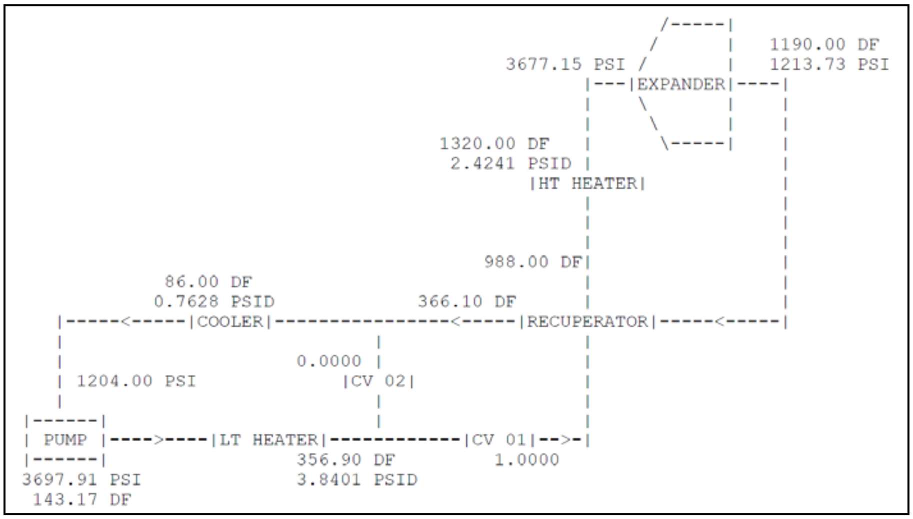

```
                                                            /-----|
                                                           /      |    1190.00 DF
                                             3677.15 PSI /        |    1213.73 PSI
                                                     |---|EXPANDER|----|
                                                     |    \       |    |
                                                     |     \      |    |
                                       1320.00 DF    |      \-----|    |
                                        2.4241 PSID  |                 |
                                                |HT HEATER|            |
                                                     |                 |
                                                     |                 |
                                                     |                 |
                                            988.00 DF|                 |
             86.00 DF                                |                 |
            0.7628 PSID              366.10 DF       |                 |
   |-----<-----|COOLER|------------------<-----|RECUPERATOR|-----<-----|
   |                             |                   |
   |                     0.0000 |                   |
   | 1204.00 PSI              |CV 02|                |
   |                             |                   |
|------|                         |                   |
| PUMP |---->----|LT HEATER|--------------|CV 01|-->-|
|------|                  356.90 DF         1.0000
3697.91 PSI               3.8401 PSID
 143.17 DF
```

Figure 77: Stoner Pipeline Simulator Model Schematic

Table 17: Comparison of CO_2 Density - Stoner Pipeline Simulator and REFPROP

Device	P (psia)	T (°F)	Density [lb/ft3]		Error
			Stoner	REFPROP	
Pump out	3697.91	143.17	49.387	48.883	1.03%
LT-HTR out	3690.28	356.90	22.9	22.554	1.53%
RCP 1 out	3681.14	988.00	10.306	9.9871	3.19%
HT-HTR out	3678.02	1320.00	8.259	8.0043	3.18%
EXP out	1213.73	1190.00	3.014	2.9711	1.44%
RCP 2 out	1205.08	366.10	6.621	6.5232	1.50%
CLR out	1204.00	86.00	47.988	44.789	7.14%

Subtask 1.3.3. Design Test Loop Layout and Identify Integration into Existing Infrastructure

A 3-D solid model was created incorporating the existing facility (SwRI Building 278, Turbomachinery Research Facility) and existing piping. The expander test rig is located adjacent to a centrifugal compressor skid which utilizes piping designed for testing CO_2 compression technologies. Most of the major components including the heater, recuperator, and expander are placed in close proximity to one another inside the lab. Sitting the expander near the heater is important, since it is necessary to minimize the lengths of the hottest sections of piping. This reduced material costs of high temperature components and helped manage thermal stresses. The pump is placed outside the lab in between the process cooler and the heater. The heater exhaust is vented through the building wall via ducting to an exhaust stack which directs the hot combustion products up and away from any occupied areas. The heater shown in the figures below represents a design produced by Thar employing a blower, combustion chamber, and a large number of heat exchanger tubes similar to the technology used in the recuperator. The high temperature stage is placed closer to the combustor and the low temperature stage uses downstream waste heat. A similar concept is being proposed by Brayton Energy. The facility configuration is shown in Figure 78 through Figure 81, and the piping sections are identified Table 18.

Table 18: Pipe Section Key

Pipe Section	Color
Pump to heater	Dark blue
LT heater to recuperator	Yellow
Recuperator to HT heater	Orange
HT heater to expander	Red
Expander to recuperator	Dark green
Recuperator to existing	Light green
Existing facility piping	White
Existing facility piping (unused)	Dark gray
Existing piping to pump	Light blue

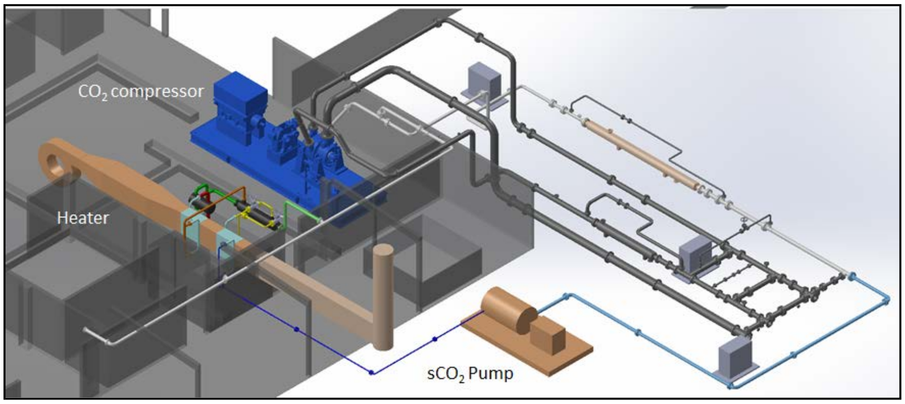

Figure 78: B278 – Turbomachinery Research Facility

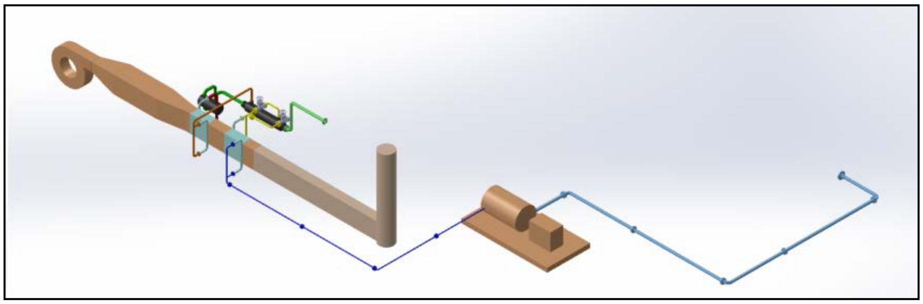

i

Figure 79: SunShot Expander Piping Only

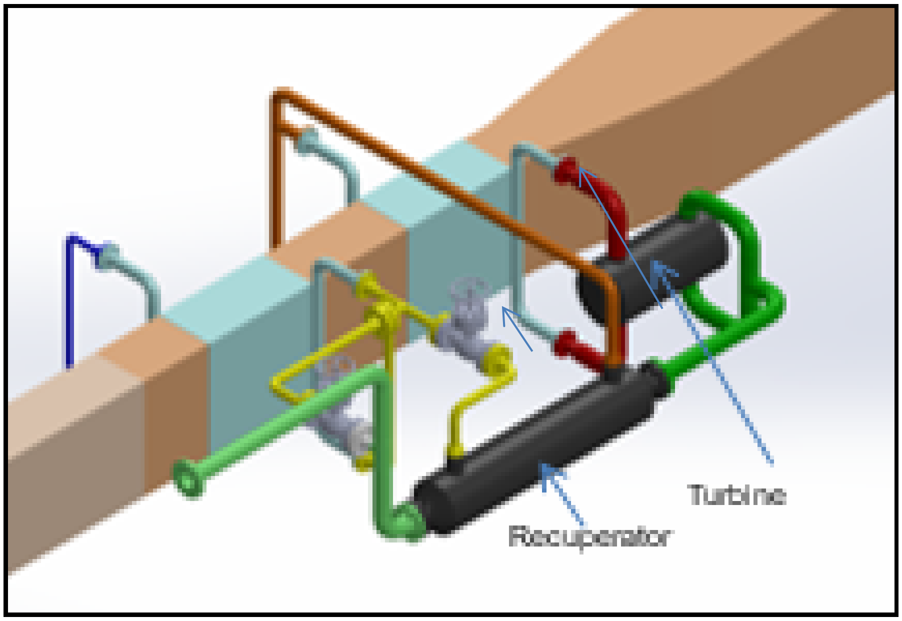

Figure 80: Expander Piping Detail

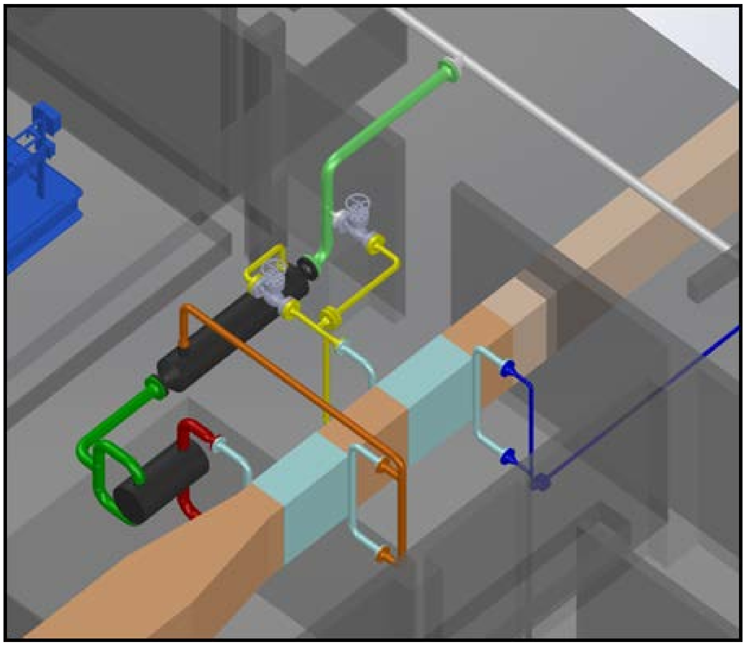

Figure 81: Expander Piping Detail with Facility

The roughly 600 kW of power produced by the 10 MWe turbine design while running at 10% of its design flow are absorbed by a custom engineered air dynamometer. This dyno consists of a single-stage centrifugal compressor impeller that is directly mounted to the drive-end of the turbine. The load absorbed by the dyno may be adjusted by varying both suction and discharge control valves. Power is measured by enthalpy rise across the stage times measured mass flow. Accuracy is expected to be within 1%. This concept is significantly less expensive than a gearbox/low speed generator and eliminates the need for a high temperature Turbine Trip Valve (TTV) because of potential unloading of the generator.

Heater Overview

Originally, the heater was going to be commercially procured, but no vendor quote fell within the project budget. The overall intent of the heater for the SunShot test loop is to increase the CO_2 temperature exiting the recuperator discharge to the required temperature for the turbine inlet while not exceeding 1 bar of CO_2 pressure drop. These operating conditions are outlined in Table 19.

Table 19: Heater Operating Conditions

	Recuperator Outlet/ Heater Inlet	Heater Outlet/ Turbine Inlet
Temperature	470°C	715°C
Pressure	251.9 bar	250.9 bar
Mass flow rate of CO_2	8.410 kg/s	8.410 kg/s

This was accomplished by using a natural-gas-fired heat exchanger consisting of a staggered array of tubes carrying the CO_2. This is illustrated in Figure 82.

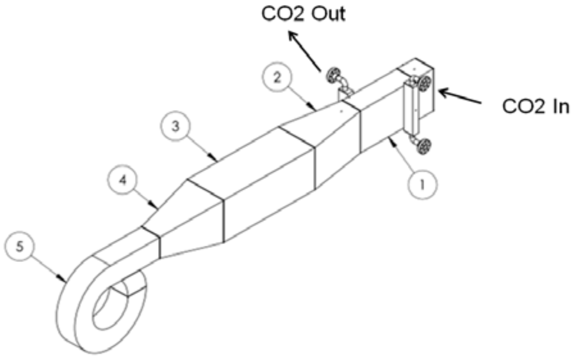

Figure 82: Diagram Showing Heater Components: 5) Blower, 4) Transition Piece, 3) Duct Section Containing the Natural Gas Burners, 2) Additional Transition Piece, and 1) Duct Surrounding the Staggered Tube Bundle. The CO_2 Entrance and Exits are Also Shown

In Figure 82, the CO_2 enters and exits the heater in the labeled locations. Between these locations, the CO_2 is distributed into multiple tubes which form a tube bundle. This bundle consists of tubes arranged in a staggered manner in order to increase the heat transfer between the combustion products on the outside of the tubes and the CO_2 flowing through the tubes.

A design optimization algorithm was developed at SwRI for the heat exchanger design to meet the design performance while minimizing cost. Inconel 740H was chosen as the target tube material, which was only recently approved for piping material but provides almost three times the creep strength at temperature compared to Inconel 625.

The optimization routine produced the design outlined in Table 20.

Table 20: Heat Exchanger Optimization Constraints

Variable	Range
ST/D	2.0
SL/D	2.351
Entrance Width	43.99 in
Number of Tubes	204
Firing Temperature	1200 K
Overall Heat Rate	35.5
Blower Flow Rate	18,775 CFM
Predicted Air DP	7.75 in-H2O
Predicted CO_2 DP	3.02 bar

The resultant 204 tubes are arranged in an alternating pattern with half of them staggered as shown in Figure 83

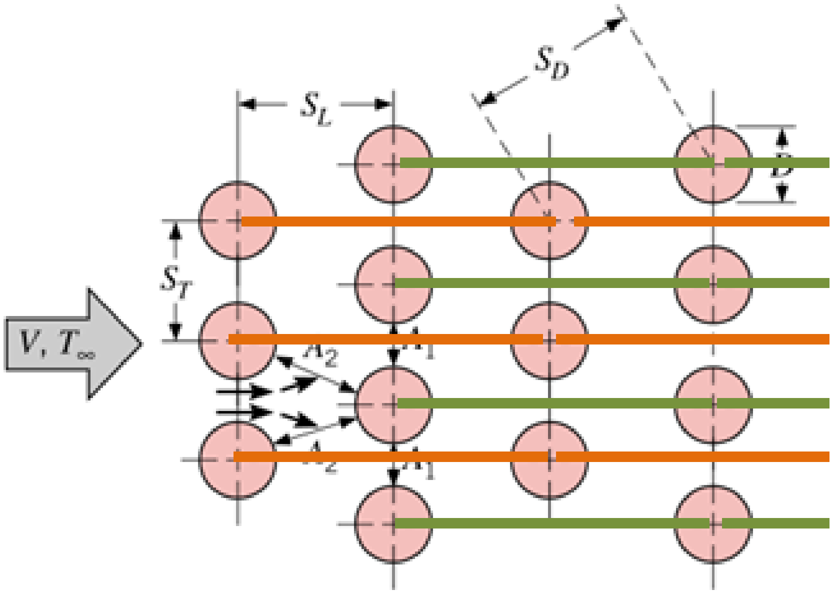

Figure 83: Heat Exchanger Tube Layout. Each Horizontal Row of Colored Connectors Represents a Single Tube. Different Colored Tubes Will be Fed from Different Headers.

This arrangement allows for the use of nearly identical tubes, all with in-plane bends. It also increases the bend radius to 2*SL. In Figure 83, the orange and green tubes (shown in Figure 84) are shown in blue and gray, the inlet headers are shown in blue and the outlet headers are shown in red.

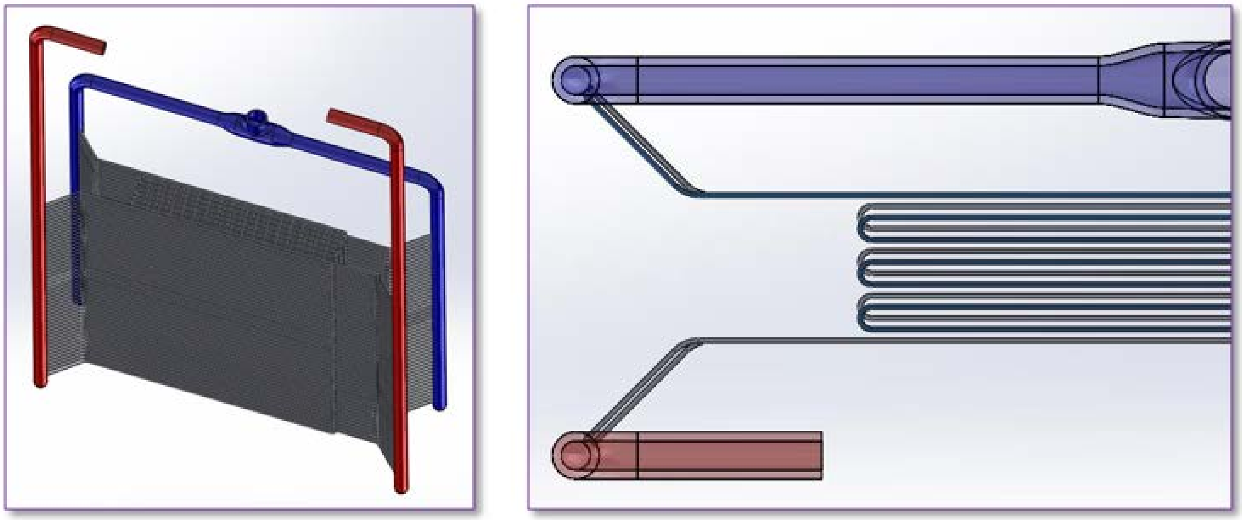

Figure 84: Top View of Heat Exchanger Tube Layout Showing Staggered Arrangement

To allow for increased weld spacing along the header pipes, the header connections are offset as shown in detail in Figure 85.

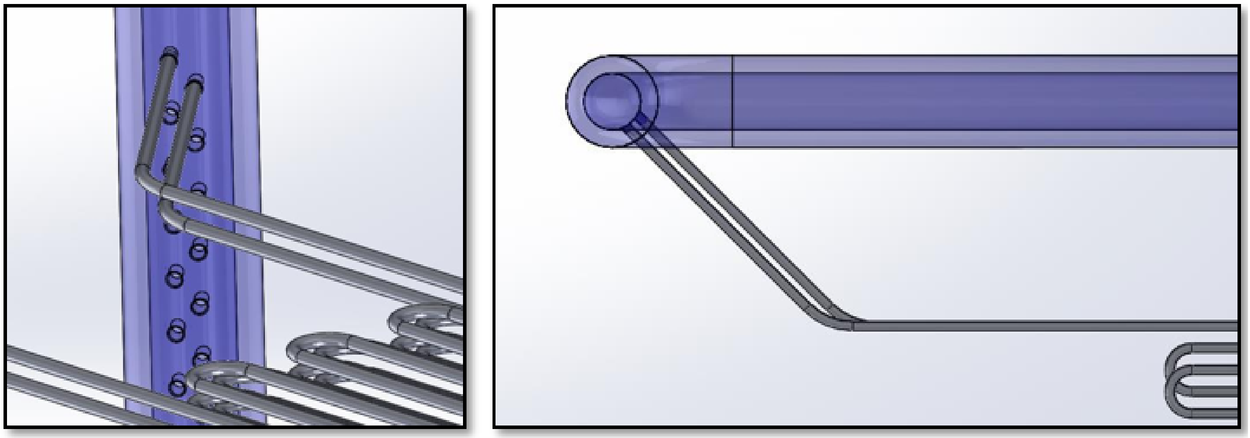

Figure 85: Detailed View of Tube to Header Connection

Once the fluid-thermal design was finalized, the majority of the progress made on the heater design consisted of creating specifications and drawings for the heat exchanger support structure, exhaust ducting, and other ancillary equipment. Figure 86 shows an overview of the location of the heat exchanger, burner/blower assembly (green) and exhaust ducting (gray) in relation to the SunShot turbine and recuperator.

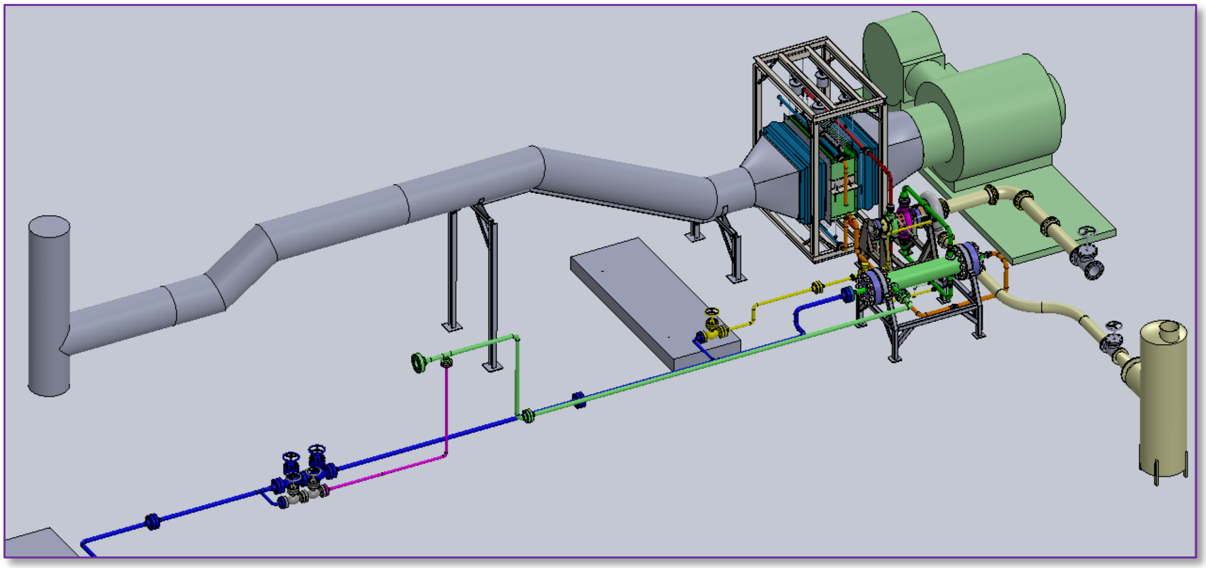

Figure 86: Overview of Burner/Blower, Heat Exchanger, and Exhaust Ducting in Relationship to the SunShot Turbine and Recuperator

Figure 87 shows a close-up view of the heat exchanger, including the associated support structure, spring can supports, expansion joints, etc. Note that in the actual installation, much of what appears to be exposed in Figure 87, such as the heat exchanger tubing and pipe headers, is insulated.

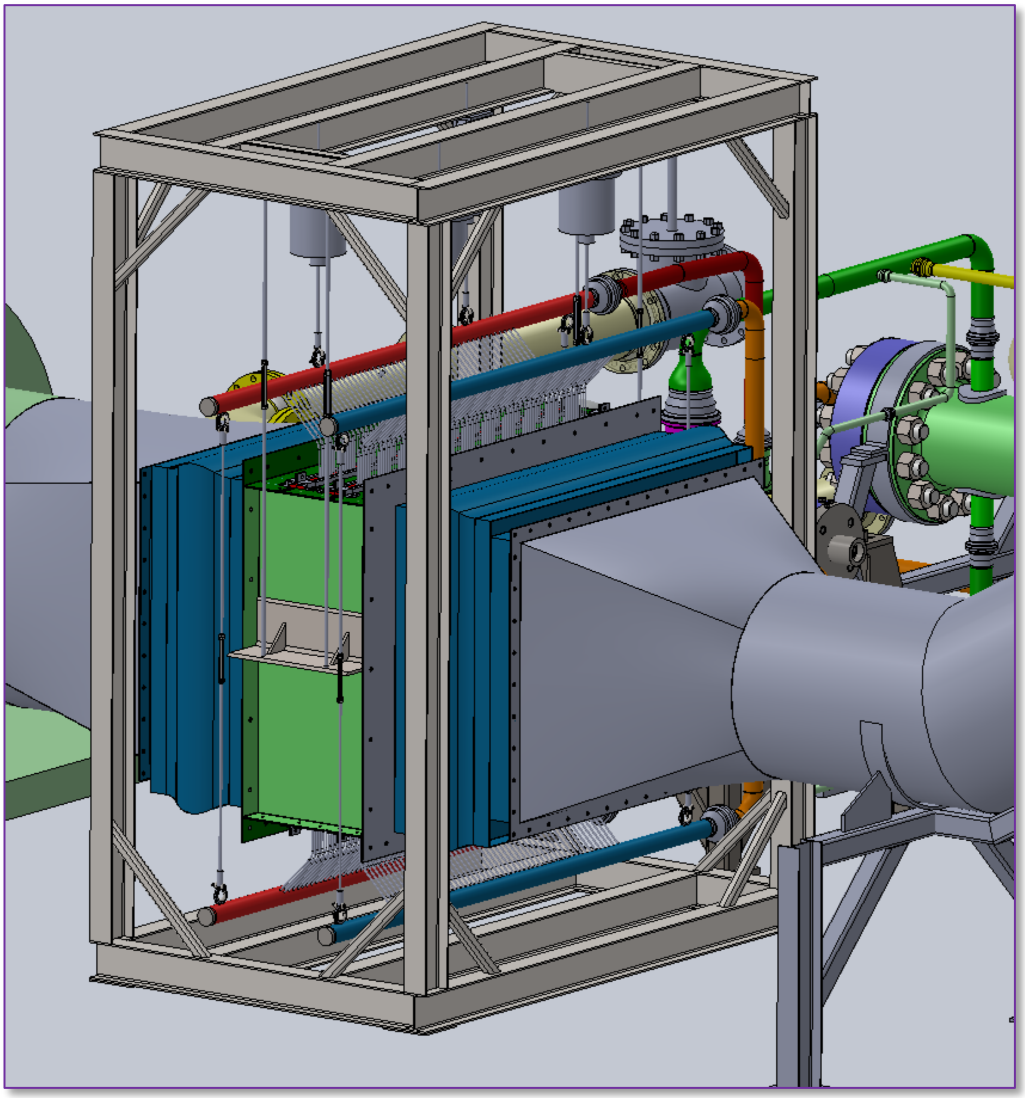

Figure 87: Close-up of the Heat Exchanger with the Associated Support Structure, Spring Can Supports, Expansion Joints, etc.

Phase 2. Component Fabrication and Test Loop Commissioning

Objectives for Phase 2 were the fabrication, installation, and commissioning of the sCO_2 turbo-expander, recuperator, and test loop.

Task 2.1. Heat Exchanger Fabrication

Fabricate the 5-MWt recuperator.

- Milestone: Delivery of 5-MWt compact recuperator and performance qualification testing to demonstrate that performance specifications are met.
- Completion target metrics:
    - Test unit size 50-kW scale up 100:1 for Phase 3.
    - Capacity (% of design) < Design goal is minimum of 80% of 35 MW/m3 (i.e., 27 MW/m3). (Note: This only affects the size of the heat exchanger and not the amount of heat transferred. If a pressure containment envelope is used for prototype testing, the demonstrated power capacity may be lower.)
    - Pressure drop (% of design) < 1.5 times of bench-scale performance
    - Cost (% of design) < Goal is not more than 1.5 times $50/kW (i.e., no more than $75/kW)

The recuperator heat exchanger design was evaluated over the course of a number of design review meetings. The evaluation included mechanical, thermal, and flow distribution analyses. In addition, ASME and TEMA code calculations were reviewed for the recuperator shell, tube-sheet, seals, and clamps.

The recuperator shell and flanges were designed to meet ASME Section VIII, Division 1, where the pressure vessel is designed/rated to the highest pressure and highest temperature that is seen anywhere within the heat exchanger shell and piping connections. Figure 88 shows a model of the shell design. The shell (flanges and vessel body) is made of 316H stainless steel and is rated to the design conditions of 567°C @ 280 bar (1,053°F @ 4,116 psi). Also the pipe, pipe connections, all threads, and nuts are made of 316H stainless steel.

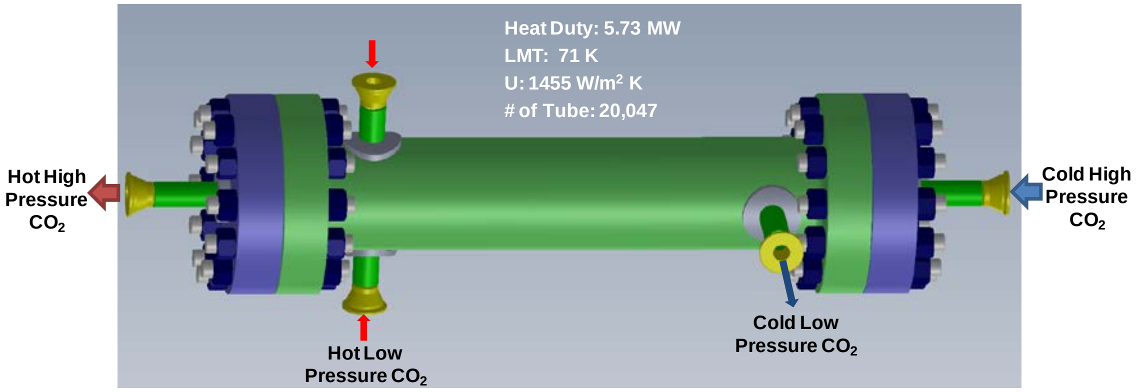

Low Pressure CO_2 (Hour-Glass)
- **9.910 kg/s**
- **T_{IN} = 567°C (1053°F)**
- **T_{OUT} = 80°C (175°F)**
- **P_{IN} = 86 Bar (1247 psi)**
- **ΔP = 1.5 Bar (22.4 psi)**

High Pressure CO_2 (Tubes)
- **8.347 kg/s**
- **T_{IN} = 29°C (85°F)**
- **T_{OUT} = 470°C (878°F)**
- **P_{IN} = 255 Bar (3698 psi)**
- **ΔP = 0.8 Bar (11.7 psi)**

Figure 88: Recuperator HX Configuration

The delta pressure across the HX was designed to meet the milestone of being less than 1.5 times the bench-scale performance. The capacity of the 20,000 micro-tube tube bundle is calculated at 89 MW/m3, exceeding the design goal of 35 MW/m3.

The pressure vessel fabrication has been completed. The pressure vessel fabrication has passed the hydro test and received an ASME stamp, as shown in Figure 89. The design process of the 5 MWt recuperator continued throughout the program as the test stand requirements became more defined through the Failure Mode and Effects Analysis. Some examples included 1) increasing the design temperature and pressure to enhance safety, 2) incorporating an anti-rotation key into the floating tube sheet, 3) adjusting the design to improve gas by-pass prevention and 4) increasing the design temperature for the floating tube-sheet dynamic seal.

Figure 89: SunShot Recuperator Pressure Vessel with ASME Stamp

The tube bundle assembly was completed. This included positioning the microtubes and separated sheets into the tube-sheets, bundle sleeve, and braze fixture. Vacuum brazing was used to bond the microtubes to the tube-sheets.

Several problems were observed in the vacuum brazing of the tube bundle. Some problems were related to the scaling of the braze fixture from a 1,000 microtube tube bundle to a 20,000 microtube bundle. Several lessons were learned from this effort.

QA/QC tests were performed on the 20,000 microtube bundle to assure the integrity of the braze bond between the microtube and the tube-sheet. The QA/QC process identified a number of sub-standard brazes requiring microtube repair or plugging.

In an ideal world, time would have been allowed to rebuild the microtube bundle taking into account lessons learned. With this option off the table, the cost and time to repair the microtube was weighted against the cost and time of ordering a backup commercial printed circuit heat exchanger (PCHE).

Other factors in the decision making included new market considerations. Learning from the advance recuperator program, DOE Project DE- FE0026273, indicated that industrial customer's preference was for larger size tubing. They saw small diameter passages as a maintenance issue. The smaller the passage diameter, the greater the potential for flow restrictions from corrosion and/or small particle contamination.

Additionally, while industrial customers desired the floating tube sheet from the perspective that it would accommodate thermal stress, they were unwilling to pay for the additional costs associated with this feature. The stresses on the floating tube sheet, at design conditions, required the tubing and tube-sheets to be made of Inconel 625, along with precision machining costs to enable a floating tube-sheet with minimal seal leakages.

A last consideration regarded the advancements in commercial PCHE heat exchangers. PCHE manufacturers can use lower cost 316 stainless steel to temperatures of 650°C based on ASME code cases 2621-1 and 2437-1. This enables a commercially available product to be readily designed and fabricated to meet the needs for the Sunshot test stand.

Given the above considerations, the decision was made to purchase a 316 stainless steel PCHE to serve as the recuperator for the Sunshot test stand versus continuing the repair process of the microtube recuperator. Thar continued efforts to develop improved manufacturing techniques to assure good tube to tube-sheet bonding and to improve recuperator performance/price metrics. [7, 8]

Vacuum Process Engineering (VPE) Recuperator Procurement

An alternative recuperator was ordered from VPE based on project considerations listed above. This replacement, diffusion-bonded, micro-channel recuperator was completed and delivered to SwRI in April 2017. The recuperator passed leak and hydro testing. Figure 90 shows the VPE recuperator on the stand in the SwRI Turbomachinery Research Facility. VPE was able to meet the design requirements for this application.

Figure 90: VPE Recuperator on the Stand in the SwRI Laboratory

Figure 91 shows the piping connections for the VPE recuperator. The placement of the recuperator was determined by the final placement of the turbine. After the assembly of the turbine casings, the field welds between the heater and the turbine were confirmed and modified as needed. Once the turbine location was finalized, the recuperator location was set, and the pipe connections between the loop and the recuperator were completed.

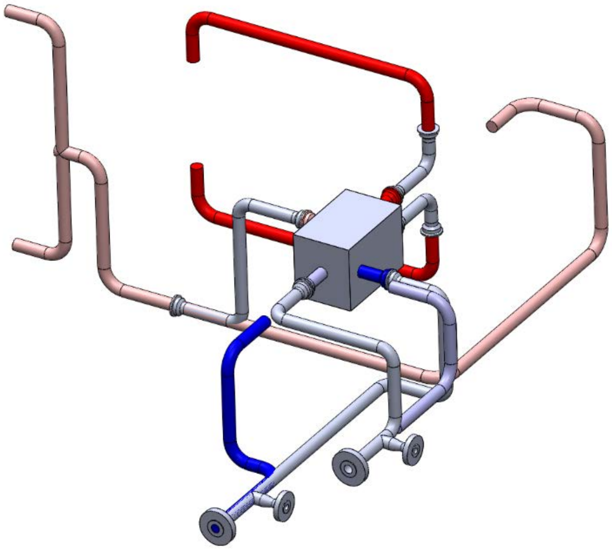

Figure 91: Updated Piping for VPE Recuperator

The colored piping shows the existing lines for the Thar micro tube heat exchanger. The gray lines show where changes needed to be made and piping was added to communicate the VPE recuperator with the existing loop.

The VPE recuperator is a cross-flow design, while the Thar recuperator design was counter-flow. Because of the fundamental design differences and significant dimensional differences between the designs, the pipe connections had to be modified significantly. The pipe needed to make the modifications has been fabricated and installed.

Task 2.2. Turbomachinery Fabrication

During Q1/2015, the expander went through a detailed design review. Corner reliefs, proper chamfer sizes for O-ring and rabbet fits, and proper clearances were finalized as shown in Figure 92. Also, the assembly and disassembly procedures were determined. Drawings were updated to reflect these changes and reviewed internally before being sent out for quotation.

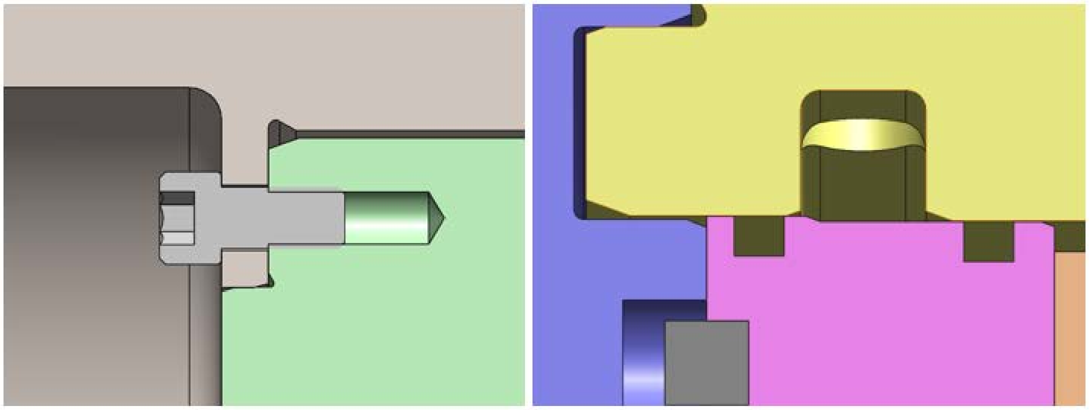

Figure 92: Turbine Detailed Design Features (Buffer Seal - Left, Dry Gas Seal Assembly - Right)

The bearing housings, including radial and axial bearings, were reviewed in conjunction with the bearing supplier to ensure that the bearing cavities were designed to their standards. This included radial interference, axial clearances, and proper relief and chamfers. Flow paths were also updated for the new reduced airfoils. Design drawings were sent out for an updated quote.

By the end of Q1/2015, ‘Quotation Only’ drawings had been sent out for pricing and lead time determination. For most of the parts, multiple vendors responded; however, some parts (e.g., rotor, stage-1 nozzle, Haynes 282 material) had to be single sourced due to the lack of companies willing to quote or the lack of suppliers for the material. The castings were quoted by Flowserve and MetalTek only, since they are the only two companies with licenses to cast Haynes 282.

During Q2/2015, the focus was placed on manufacturing, quotes, and schedule. The only design changes were based on instrumentation and accommodating changes based on hardware. These included bearings and dry gas seals. At the time, there were two options for dry gas seals, John Crane and Flowserve. The original design was based on the John Crane seal, but a slight modification to the housing would be required if Flowserve was chosen. As for the bearings, drawings had been submitted by Bearings Plus, but housing design could not be finalized until squeeze film damper testing was completed to determine if a standard O-ring or integral design would be used.

Also during Q2/2015, official drawings were sent out for all of the high-temperature components. This included the rotor, stators, castings, and balance piston seal. Purchase orders were placed for all of the above, and they were manufactured. The stator nozzles were sourced to two different companies to keep on schedule.

During Q3/2015, there were minor design updates, based on instrumentation requirements, in various parts in the expander. Tapered-seal Swageloks were chosen for all high-temperature fittings. Grayloc connections were finalized, and the dyno wheel went through one more design iteration to ensure that all stress and rotor dynamic requirements are met. Allowances for wiring to the various bearings and all proximity probes were implemented.

By the end of Q3/2015, quotes had been obtained for all major components, and POs had been placed for all long-lead-time items. This included bolts, castings, stators, and rotor. The last components to be ordered were some low-temperature stator parts, mainly the housing and dyno components.

During Q4/2015, the process of purchasing hardware continued. The main design updates were involved in finalizing the dyno weight, replacing all aluminum and titanium parts with stainless steel in the dry gas seal, and reducing weight on the coupling end to meet our rotordynamics requirements. The other change was in the balance piston diameter. To correct pressure balance, the piston diameter was reduced to 5.50” and the hole pattern seal was also modified. The second seal was ordered and did not cause a delay in the expander being assembled.

At this point, all major parts were on order. Parts and materials that have been received include:

1. 17830.01-130, 131, and 302 – Coupling dummy and housing. Rev. C was complete but modifications were made in-house to reduce weight to meet rotordynamic requirements.

Figure 93: Coupling Dummy and Housing

2. 17830.01-500 – Operating Stand

Figure 94: Operating Stand

3. 17830.01-223 – Exit Plenum Backing Ring

Figure 95: Exit Plenum Backing Ring

4. 17830.01-212-214 – Stator Nozzle - Trial Cutting

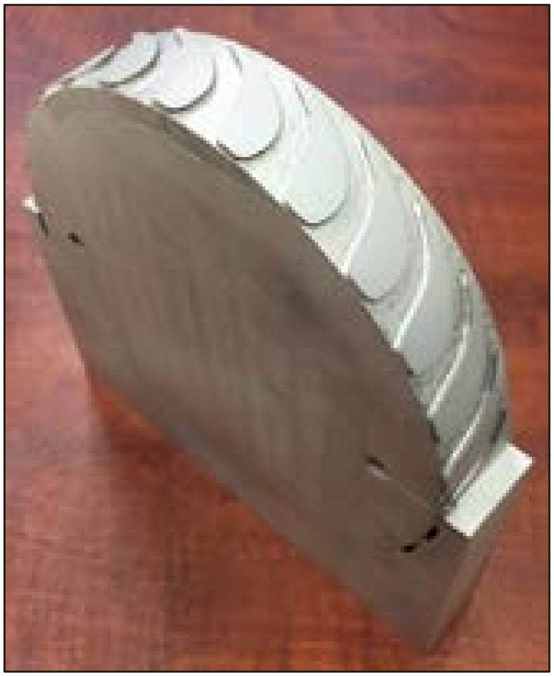

Figure 96: Stator Nozzle

5. 17830.01-231 – Balance Piston Seal (New one was made to match new Balance Piston Diameter)

Figure 97: Balance Piston Seal

6. 17830.01-121 – Thrust Collar – This part was shipped to Metalex, so they could finish machining the rotor based on the thrust collar tapered face and also, final grinding of the faces at the same time as the rest of the rotor.

7. 17830.01-121 – Air Dyno wheel has been machined and was delivered in December 2015.

Figure 98: Air Dyno

8. 17830.01-101-R – CSP Rotor – All EDM work and machining was done. The thrust collar needs were fitted and final ground. The rotor was progressively balanced by first balancing the shaft, and then progressively adding the thrust disk and dyno wheel.

Figure 99: CSP Rotor

9. 17830.01-200, 210, 220, & 230 – All Haynes 282 housings were cast and went through heat treat and final inspection. However, the exit plenum had significant quality issues and was recast four times due to core and cracking issues. There was a delay of about three to four weeks in material delivery from Haynes. That, along with casting issues, caused the schedule to slip several months. Flowserve shipped the castings to Atlantic Precision on December 22, 2015. X-ray inspections were made and approved by Flowserve.

Figure 100: Cast Housings

Figure 101 shows the Haynes 282 cast dry gas seal housing and nozzle housing. After finish machining, significant porosity and cracking were observed on the surface that was not revealed by x-ray inspection. These issues is discussed in detail later in this report.

Figure 101: Haynes 282 Cast Housings

10. Casings Nuts and Bolts. The Nimonic 105 bolts were manufactured by MS Aerospace on schedule. They were delivered in January 2016. The main challenge was forging the head on the Nimonic 105 bolts, since it was a new material for them to work with. Once this was successfully done, the rest of the machining was standard.

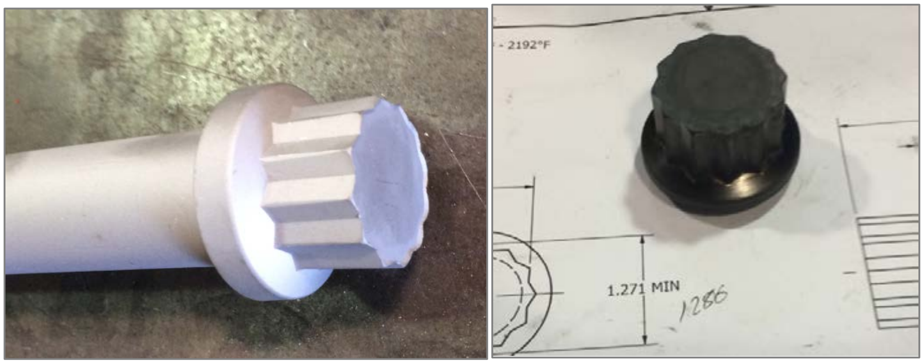

Figure 102: **Casing Nuts and Bolts**

11. 17830.01-211 – Stator 1 Nozzle is in process at Metalex. There was a slip in schedule due to EDM trials of the nozzle being more complicated. The EDM path is not as straight forward as the rotor. But the nozzles were delivered in Q1/2016.

Figure 103: **Stator 1 Nozzle**

12. 17830.01-212 – Stator 2 Nozzle – EDM was performed at EDM Laboratories. There was a slip in schedule due to the EDM of the Haynes 282 being more difficult than anticipated. They wanted to ensure that they had the process down fully to make sure that there would be no errors in the EDM of the actual parts. The process was developed on this first part and was much more streamlined on the other two nozzles.

Figure 104: **Stator 2 Nozzle**

13. Bearing housings are complete.

Figure 105: Bearing Housings

Exit Plenum Redesign

In May 2016, during the manufacturing of the Haynes 282 castings, the exit plenum was not able to be poured successfully. After multiple attempts in changing the gates and supports, it was determined that the casting could not be manufactured before the Flow Serve Foundry in Dayton, Ohio would close down. In order to save schedule and the project, another casting vendor with experience in stainless steel, Griffin Industries, was approached to see if they could deliver a CF8M version of the casting. Due to the lower strength of the material, the exit plenum was redesigned to meet the design stresses:

Figure 106: Haynes 282 Casting (Left) vs. CF8M Casting (Right)

To make up for the lower stress, the wall thickness was increased from ½” to 1.5”. In addition, the struts were thickened, and the nozzles leading out of the plenum were reduced as much as possible. Since the plenum was originally designed for the full flow loop, 104.5 kg/s, the smaller flow areas were acceptable for the 10.45 kg/s flow late of the SunShot loop.

Due to its availability, a cast version of 316 SS (CF8M) was chosen for the replacement exit plenum. The allowable stress of Haynes 282 is 26 ksi, and the 10,000 hr allowable stress for CF8M is 8.4 ksi. As already mentioned, the walls were thickened along with the struts to reduce stresses in the plenum.

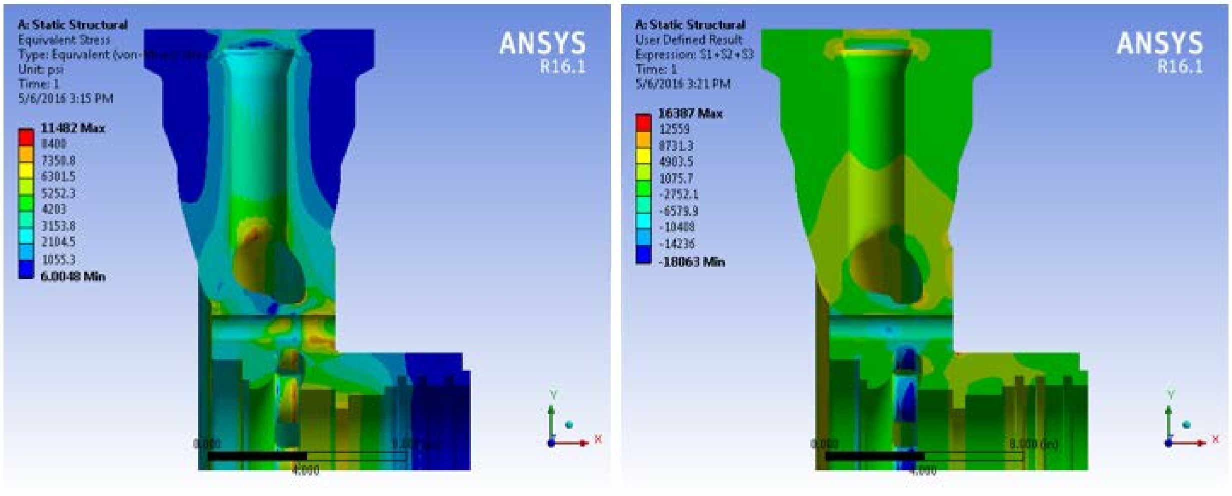

Figure 107: Redesigned Exit Plenum FEA Results - Von Mises (Right) and Sum of Principles (Left)

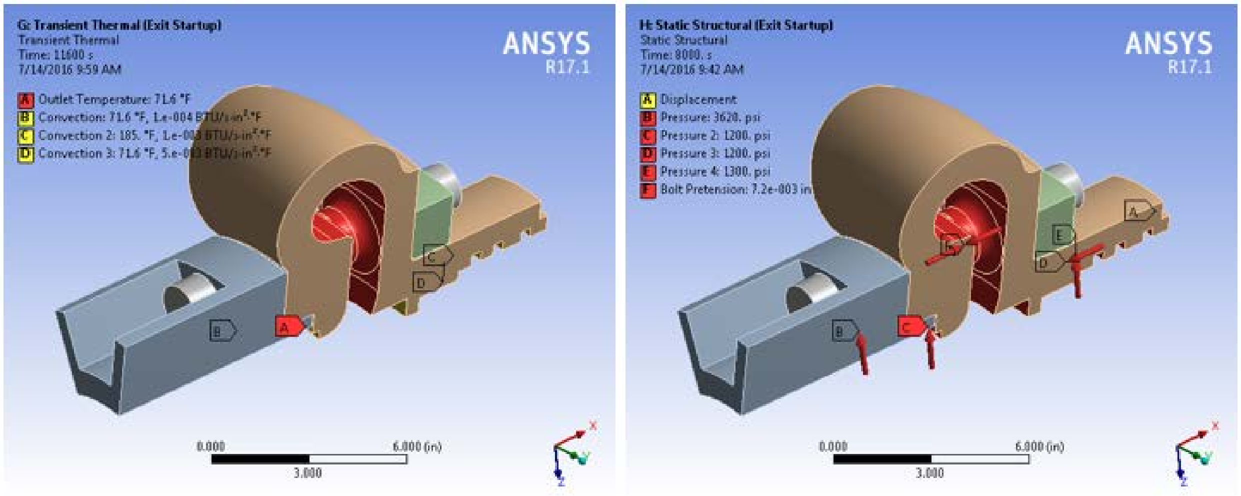

Figure 108: Boundary Conditions for Low Cycle Fatigue Analysis

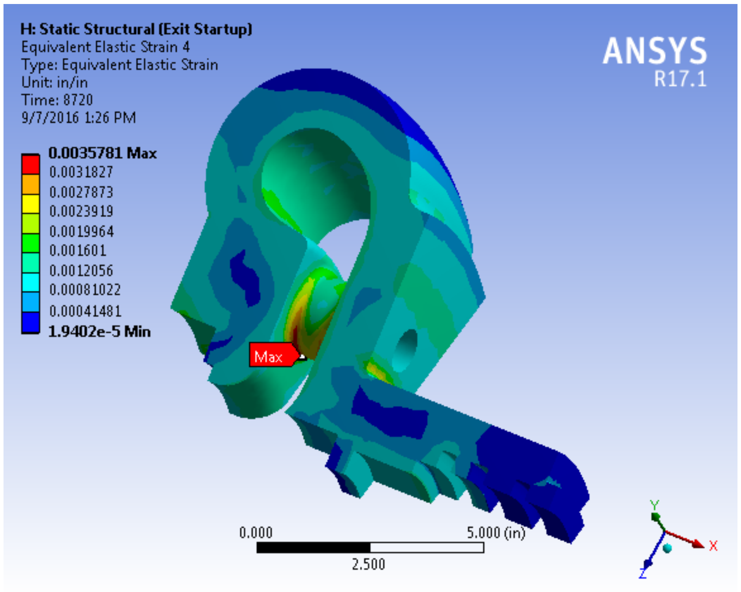

Figure 109: Peak Transient Strain for Redesigned Plenum

Peak strain of 0.0035in/in leads a fatigue life of around >10,000 cycles based on the following data. Total strain including plastic deformation < 1% which still yields > 1,000 cycles.

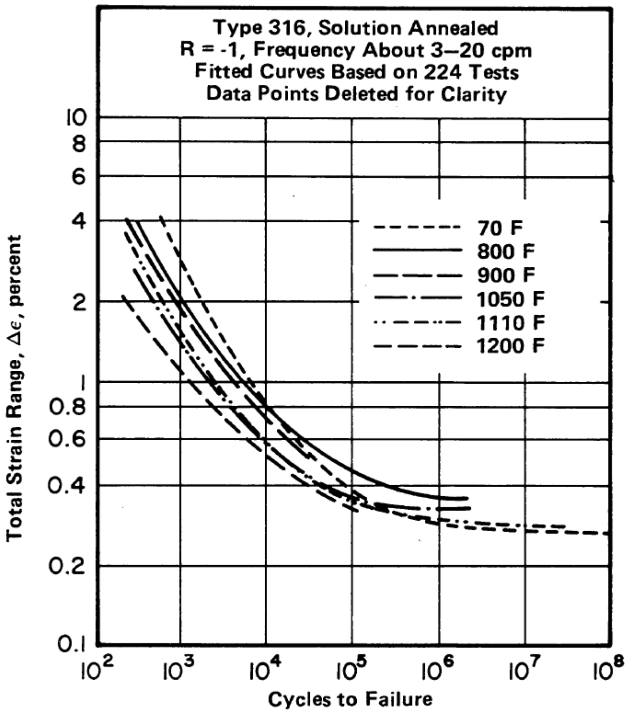

FIGURE 3.055. LONG-TIME LOW-CYCLE AXIAL FATIGUE BEHAVIOR IN AIR AT ROOM AND ELEVATED TEMPERATURES (99)

Figure 110: Low Cycle Fatigue for 316 SS (Aerospace Metals Handbook)

To account for the difference in thermal expansion, about 50% more for the CF8M, bolt yielding during start up and case to case alignment needed to be accounted for. For alignment, axial keys were implanted that maintain circumferential and radial alignment but allow the exit and the nozzle casing to grow separately from thermal expansion:

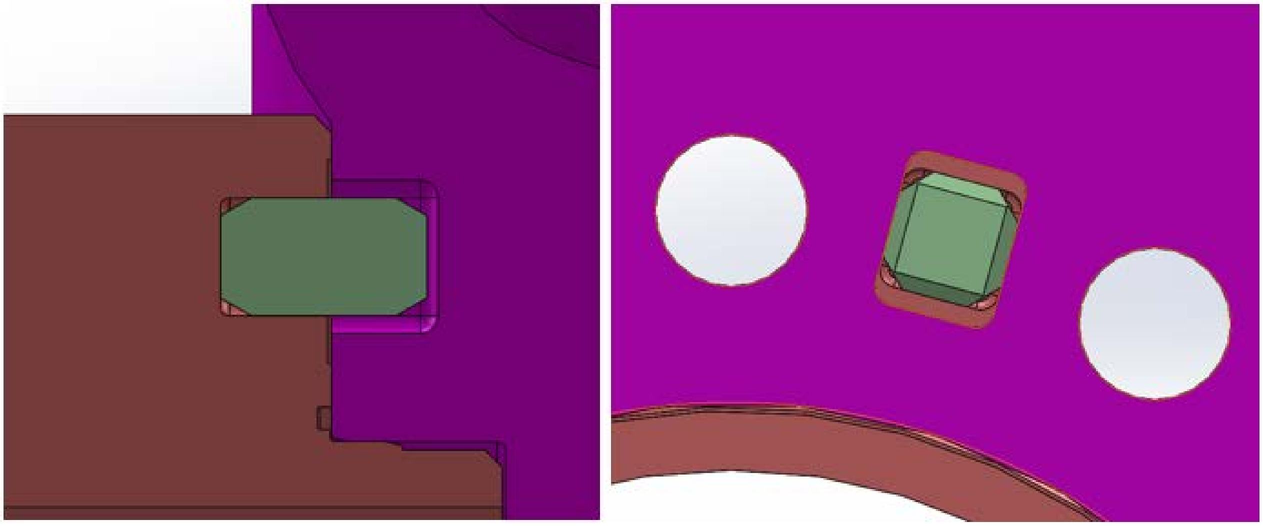

Figure 111: Axial Keys for CF8M Exit Plenum

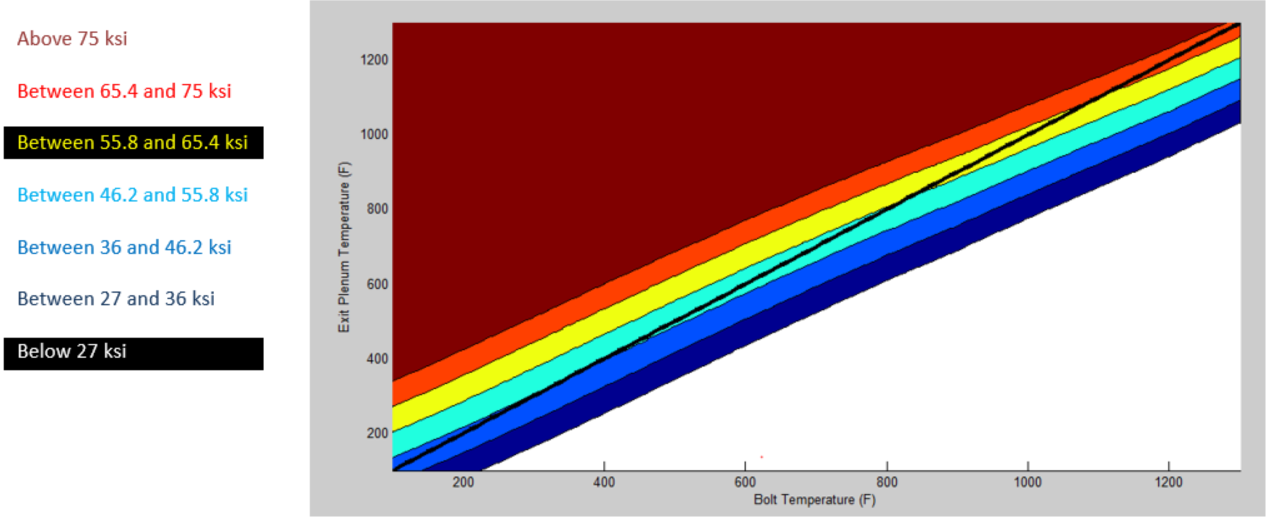

Figure 112: Bolted Joint Analysis with CF8M Exit Plenum

In Figure 112, white indicates a bolt pre-load below the minimum required loading (1.1X Pressure load) and dark red indicates reaching stresses in the bolts greater than 90% of yield. With an initial preload of 1.6X pressure load, the bolt and case could have seen a difference in temperature of around 150°F before yielding and containment could have been an issue. This is close to the same maximum temperature difference on the inlet during start up and shut down transients. The CF8M plenum was delivered in October 2016, around the same time as the other Haynes 282 fully machined parts so that hydro testing could begin.

The milestones reached during the hydro testing of the assemblies were:

- Establishing bolt torque procedures and gaining experience with the HiTorc pump. Also, verifying bolt stretch based on torque to quantify required torque to meet preload.
- Trial fitting and procedures for assembling the interference fits on the casing. Establishing temperatures to heat up the parts (~300°F for an hour) to make everything fit together easily. Use of anti-seize and dry ice on male fits.
- The inlet plenum and the nozzle casing reached 4,000 psi before sealing issues were encountered.

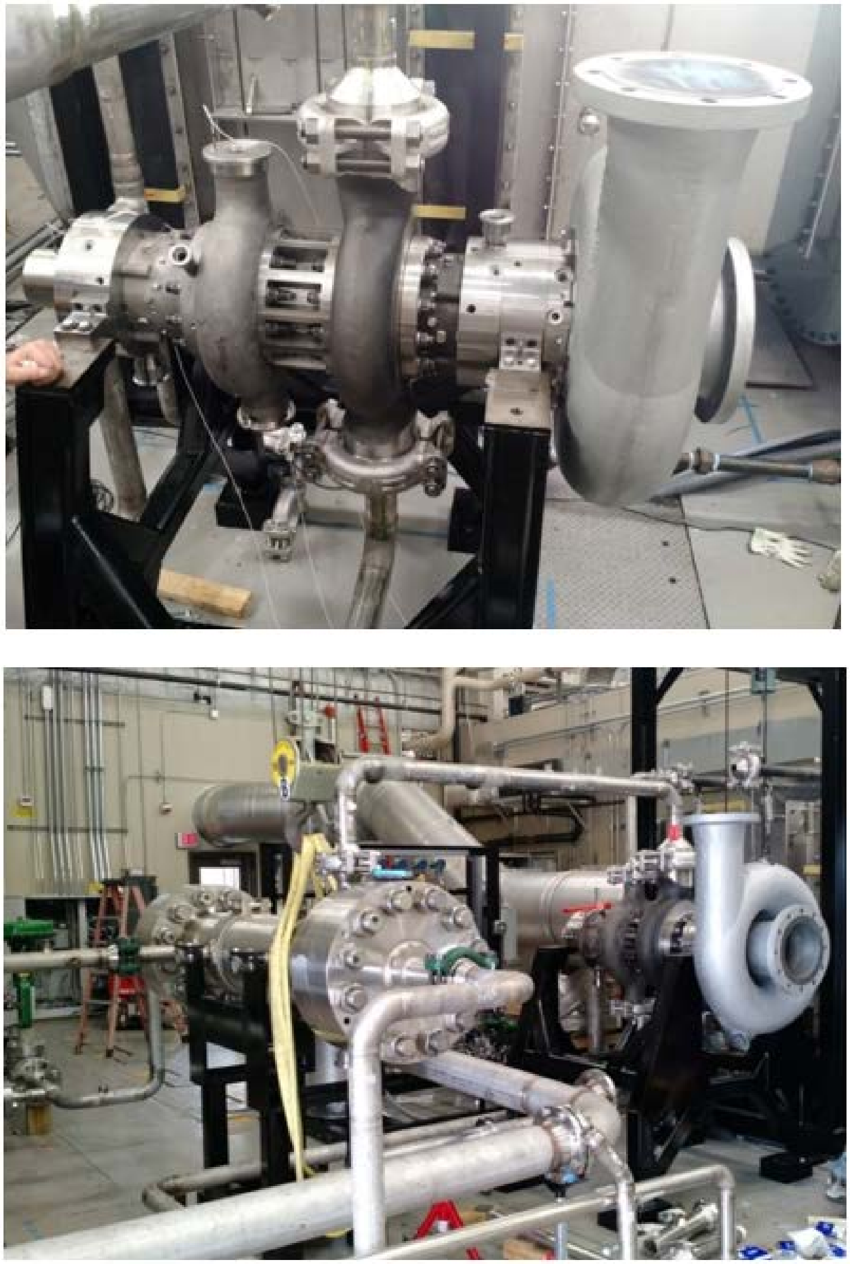

Figure 113: Assembled Turbine Casing on Operating Stand

With the turbine assembled, field welds were completed for the rest of the high-temperature piping. This included balance lines, piping to the recuperator, and piping from the heater. This allowed for the development of weld procedures for all of the Inconel 625 and 740 piping.

During the hydro test, some major issues were discovered. For the low-pressure test, it was determined that the sealing surface on the exit plenum was not flat enough and was preventing a good seal between the nozzle casing and the exit plenum. This led to the exit plenum being sent out to have the surface machined down and cleaned up to improve sealing. The plan was to hydro test this part on its own to make sure that it was a sound casting. This one was tested to 4,000 psi.

For the high-pressure hydro test, the pressure suddenly dropped at 4,000 psi, well short of the final hydro test pressure of 9,000 psi. After inspection, it was discovered that there was porosity in one of the struts, leading to a leak path to the cavity behind the bolts. All bolts were designed to a lower sealing diameter, so any pressure in this cavity would create excessive loads on the joint and caused it to open up:

Figure 114: Leak Path in Inlet Plenum Strut

Through further inspection of the Haynes 282 castings, numerous cracks and porosity issues were deemed a concern, and the possibility of weld repair on all of them was brought up to Arc Applications, the company that did welding on a Haynes 282 casting under DE-FE0000234 – “Materials for Advanced Ultra-supercritical Steam Turbines.” With their experience and expertise in complicated weldment, they deemed these castings as unrepairable. Any work could have produced more cracks and issues, and there would have been no proof that the part would be safe for these high pressure and temperature applications.

The casings were sectioned using waterjet techniques in order to preserve the metallurgy. Numerous cracks and porosity can be seen in Figure 115 indicating cracking and porosity much worse than originally thought. A set of these samples was delivered to EPRI, who performed a full metallurgical analysis, which is documented in Appendix A.

Figure 115: Metallurgical Samples from Haynes 282 Castings

Fabricated Casing - With the exit plenum already replaced with a CF8M casting, the other three Haynes 282 castings were scrapped and a weldment out of solution-annealed Inconel 625 developed. Due to lead-time concerns, other castings were avoided, and CF8M would not have met the strength requirements of the higher-pressure and higher-temperature components. Therefore, a fabricated approach was taken, making the casing components from Inconel 625 forgings.

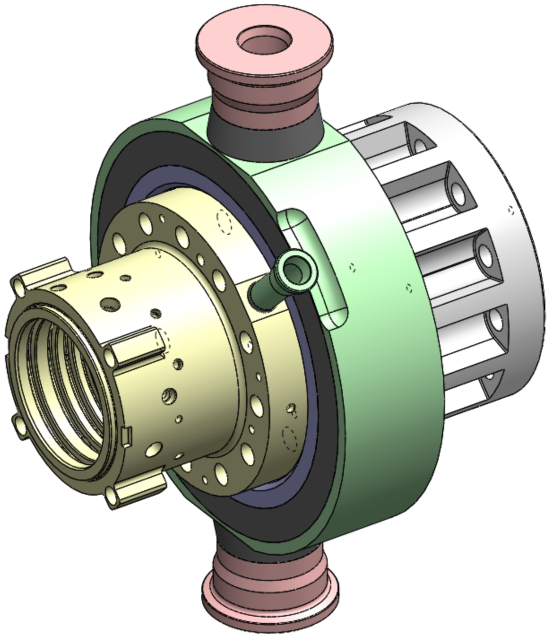

Figure 116: Inconel 625 Weldment Models of Replaced Castings

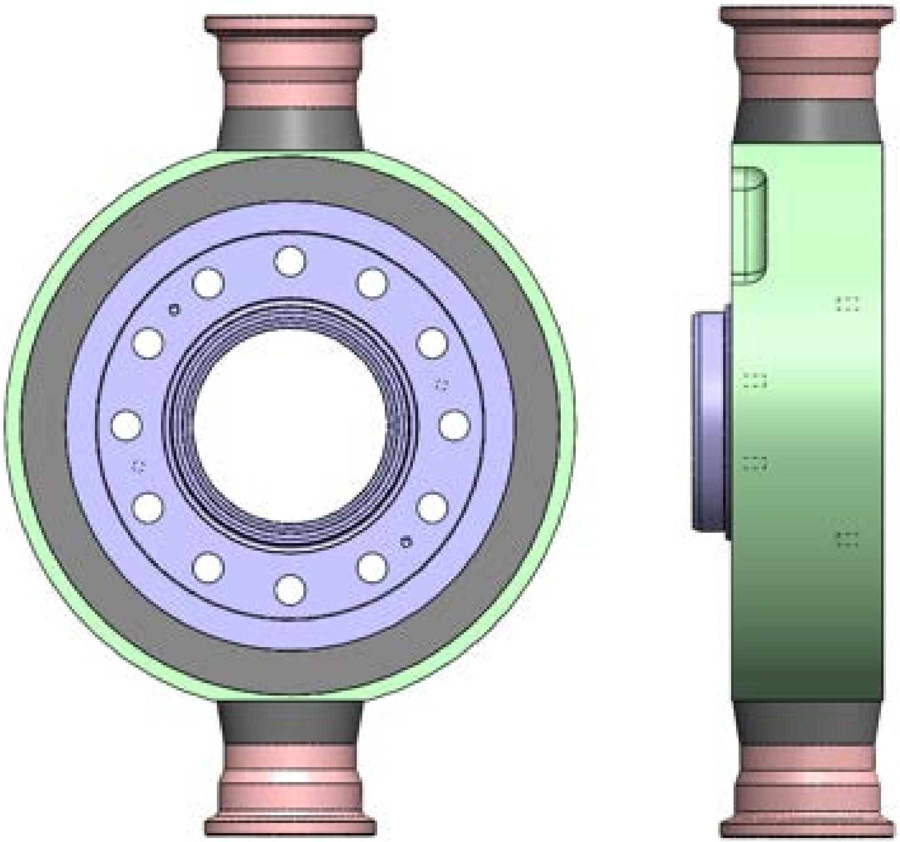

Figure 117: Inlet Plenum - 17830.01-200

To summarize, the inlet plenum (17830.01-200) was made out of four parts and four major welds.

Parts:

1. Center ring (blue) – Custom Inconel 625 forging
2. Outer ring (green) – Custom Inconel 625 forging
3. 2X Grayloc Hubs (red) – 6” Inconel 625 bar stock

Welds:

1. Center ring to outer ring, 1.5” single J-Prep full penetration weld with a 45° angle for access – 2X
2. Grayloc hubs to outer rings, ¾” single J-Prep full penetration weld with a 45° angle for access – 2X

Due to the lower allowable stress on the Inconel 625, the internal features had to be redesigned to decrease the stresses from pressure. This was done by reducing the flow area, which is allowable for the 1-MW test, since the original part was designed for the full mass flow. Due to everything now being machined, it also has allowed for simpler methods of machining to reduce cost and lead time. This part is designed to meet ASME Section VIII, Division 2 requirements for up to 10,000 hours of life.

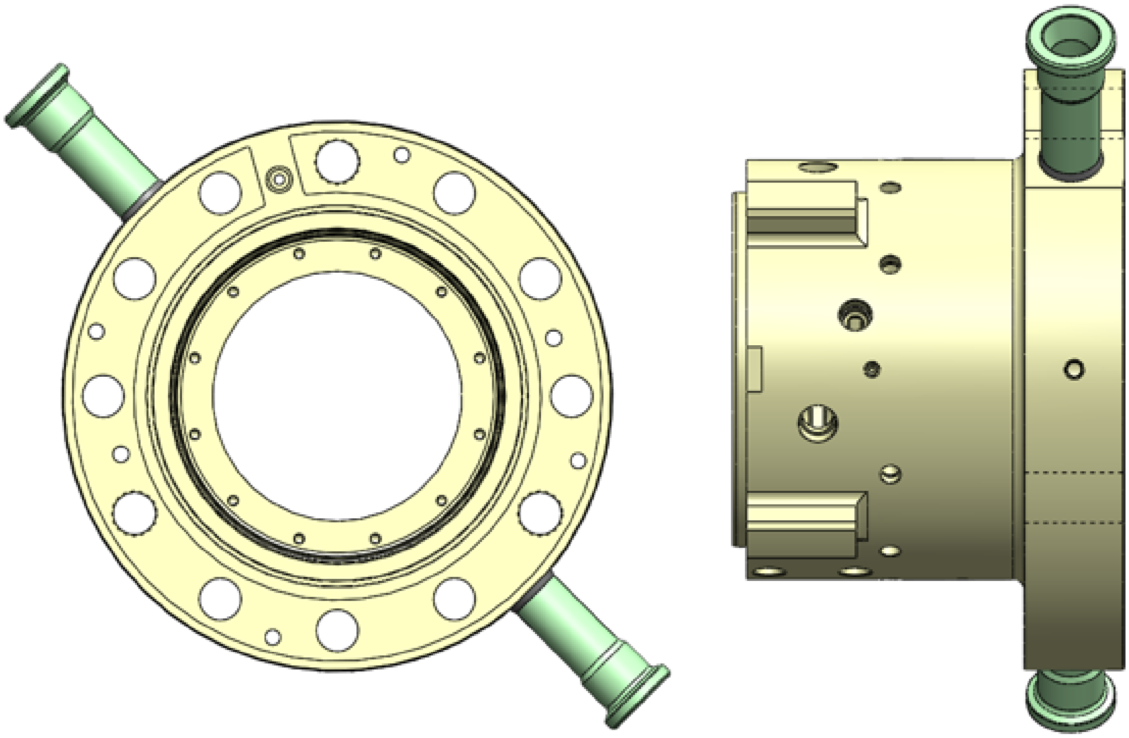

Figure 118: Dry Gas Seal Housing - 17830.01-230

The dry gas seal housing was designed to be made out of three parts with two welds:

Parts:

1. Main Casing (yellow) – Custom Inco 625 forging
2. 2X Grayloc nozzles (green) – 2" Inco 625 bar stock

Welds:

1. Grayloc Hubs to main casing. ¼" fillet full penetration weld with 45 degree angle for access – 2X

No major design changes were made to this part due to extra wall thickness already existing from the previous design due to modal and thermal issues. This part is designed to meet ASME Section VIII, Division 2 up to 10,000 hours of life. The main changes were slight modifications for ease of machining.

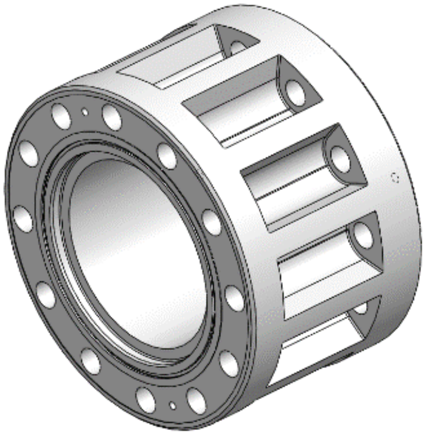

Figure 119: Nozzle Casing - 17830.01-210

The nozzle casing was made from a single piece, as originally planned, except that it now has a different shape for the bolt sections to help with ease of machining. This feature reduces lead time and cost by allowing use of a much larger ball-end mill.

All of these parts are made from annealed Inconel 625. This allowed for easier welding and machining. After welding, all the parts were heat treated to meet ASTM B446 Grade 2 – Solution annealed. They then were final machined on all critical alignment and sealing faces.

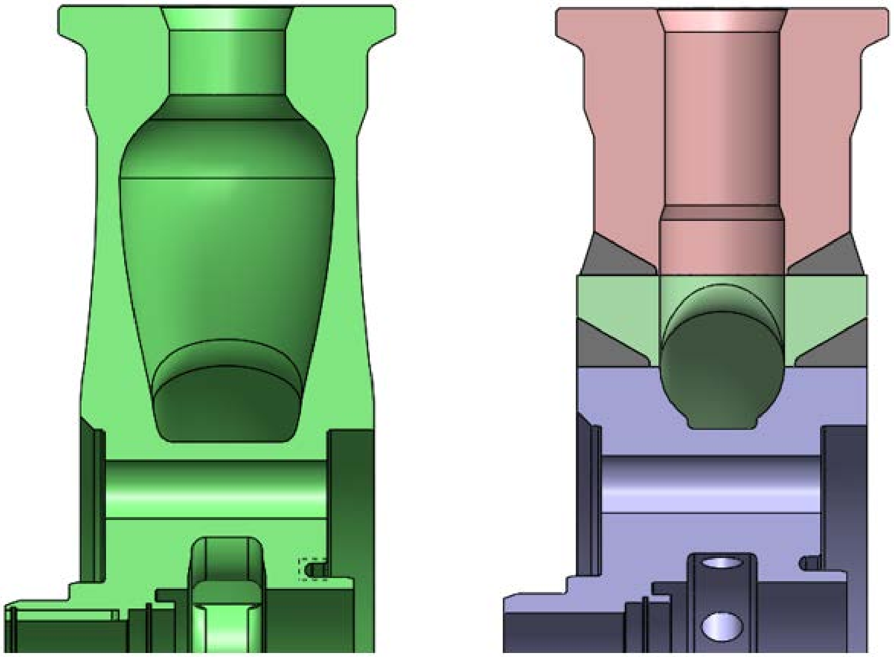

Figure 120: Haynes 282 Inlet Plenum (Left) Compared to INCO 625 Inlet Plenum (Right)

To manufacture the internal cavities, the plenum was divided into 4 total parts. Two nozzles, outer ring, and inner ring. The flow paths were reduced due to the lower mass flow of the SunShot loop. Instead of circular struts, and radial flow path was modified to 12 radial holes. This was cheaper and easier to manufacture and also provided more material to reduce the stresses from the pressure load on the part. For the dry gas seal housing and the nozzle casing, the design was kept the same due to limited space:

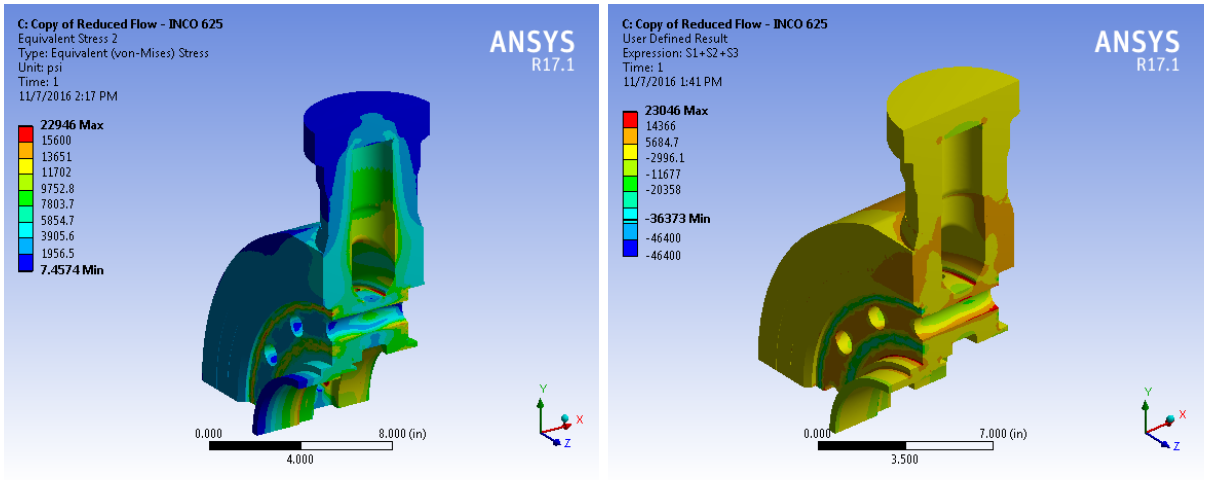

Figure 121: Static FEA Results for Fabricated INCO 625 Inlet Plenum - Von Mises (Left) vs. Sum of Principles (Right)

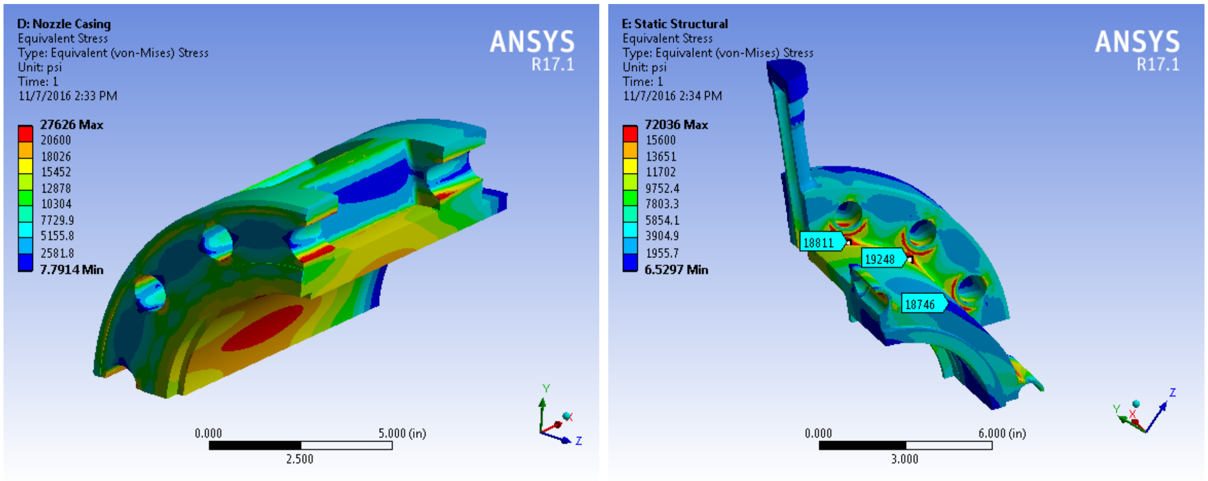

Figure 122: FEA of INCO 625 Nozzle Casing and Dry Gas Seal Housing

Peak membrane stress in the inlet plenum was < 15.6 ksi, peak membrane in the nozzle casing was 17.5 ksi, and peak membrane in the nozzle casing is 7.9 ksi. Inlet plenum and dry gas seal housing both meet the required 15.6 ksi at 715°C for 10,000 hr design stress. The nozzle casing meets 10,000 hr design stress 700°C but can only see around 1,000 hours at 715°C at full pressure.

Table 21: INCO 625 Material Properties vs. Design Life (Special Metals and ASME Data)

All Stress Units in ksi								
Design Life	**100,000 hr**		**10,000 hr**		**1,000 hr**		**100 hr**	
Design Temp	**700°C**	**715°C**	**700°C**	**715°C**	**700°C**	**715°C**	**700°C**	**715°C**
Tensile	99.2	96.2	99.2	96.2	99.2	96.2	99.2	96.2
Yield Strength	37.9	38.5	37.9	38.5	37.9	38.5	37.9	38.5
Creep Rate	14.3	12.1	20.5	16.3	29.0	22.7	39.2	33.7
Creep Rupture	18.7	16.7	26.1	23.3	35.4	31.2	46.5	41.0
Allowable	**12.5**	**11.2**	**17.5**	**15.6**	**23.7**	**20.9**	**25.3**	**25.7**

It is important to note that due to the lower material stresses, the INCO 625 parts were not designed to meet the same design life as Haynes 282, which was designed for 20,000 hours of operation. To match the design stress, the design life of the parts was reduced to 1,000 hours at max operating temperature. At max temperature, the design life was around 25% lower than Haynes 282. The inlet plenum was redesigned with thicker walls to accommodate this. The DGS housing and Nozzle casing had significant margin, so they did not have to be redesigned. These parts were forged at a nearby vendor and then machined and welded at SwRI. Due to available forgings grades of INCO 625, the parts were post weld heat treated from an annealed condition to a solution annealed condition to allow for better high temperature creep properties. These parts were delivered in 14 weeks from drawing release in May 2017. The casings were then assembled, passed hydro testing, and were then installed on the turbine stand so that field welding could be completed.

Table 22: Manufacturing Setback and Recovery Summary

Part/s	Recovery Plan	Delivery Time
Turbine Exit Plenum – Haynes 282	Redesign exit plenum to be manufactured out of cast stainless steel (CF8M)	Design – 4 weeks Manufacturing – 16 weeks
Recuperator – Thar	Order PCHE from VPE	VPE Design – 4 weeks VPE Delivery – 14 weeks
Turbine Inlet Plenum, Nozzle Casing, and Dry Gas Seal Housing	Redesign all parts to be made from INCO 625 forgings. Reduce part life based on creep rupture	Design – 4 weeks Manufacturing – 14 weeks

The nozzle casing and dry gas seal housing were then finish machined at the SwRI Main Machine Shop, truing up all critical faces and diameters. The inlet plenum was finish machined at an outside shop that could swing the part with the nozzles welded on. Figure 123 shows the parts during final machining.

Figure 123: Photos of Turbine Casing Components during Final Machining

Below were steps performed for the casings before final assembly:

1. Grind keys and fit the balance piston to the inlet plenum. Trial fit keys between nozzle casing and exit plenum.
2. Assemble the low-temperature hydro build.
3. This ensures proper alignment and fits between all of the new casings.
    - 3.1. Install the low-pressure hydro assembly onto the turbine stand and field fit the remaining pipe joints.
4. All of the joints connecting to the turbine, recuperator, and heater were field tacked in place and then hydro tested separately before being installed with the full turbine assembly.
5. Perform the low-pressure hydro test on the turbine casing while the pipe joints were being welded and tested.
6. Configure the assembly for the high-pressure hydro test on the inlet plenum and nozzle casing.
7. Complete the final assembly of the turbine with all internal components.

SwRI fabricated and assembled the complete turbo-machinery package, including skid, ancillary systems, and control system using in-house machine shops and contractors as necessary, as shown in Figure 127. The rest of the turbine parts were received, which included all of the casing components (inlet plenum, exit plenum, nozzle casing, and dry gas seal housing). With all of the parts in-house, an initial assembly was completed of both the high-pressure and low-pressure hydro test.

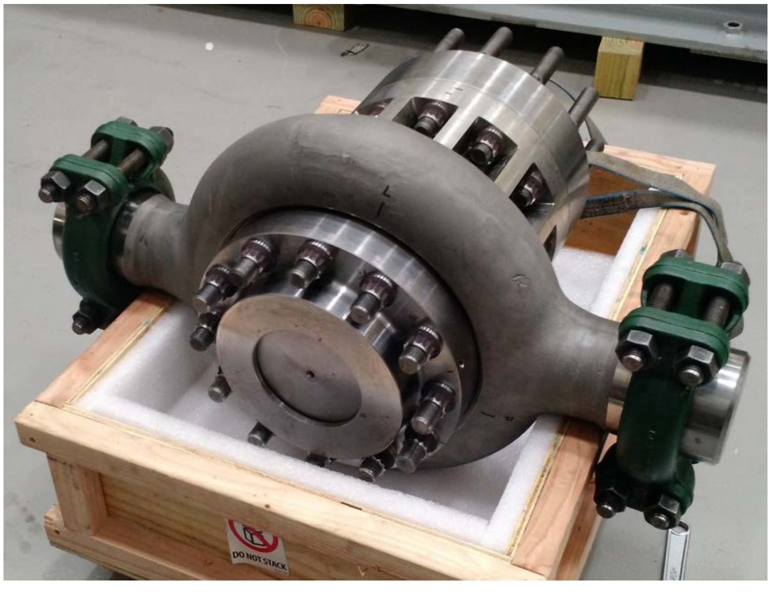

Figure 124: Assembly for High-Pressure Hydro Test (9,000 psi)

Once the hydro testing was completed for all high-pressure piping and casings. The rebuilt turbine casing passed low pressure and high-pressure hydro test. All field welds were completed at SwRI, and the SwRI weld shop passed a weld procedure to successfully weld INCO 740. All field welds passed 100% RT inspection and all required hydro testing. Once all of the piping was fitted up, the turbine was disassembled, cleaned out, and prepared for final assembly with all internal components. The turbine was then assembled with the rotor, bearings, stator nozzles, dry gas seals, and all other internal turbine components. The turbine went together successfully, and there was proper alignment for the critical spacing on the thrust bearings and also the concentricity of the journal bearings. Below are some photos from the assembly, as shown in Figure 125 through Figure 127.

With the turbine completed, the focus has shifted to final connecting of all the piping and instrumentation. It involves routing of all the dry gas seal lines, buffer air, and oil for the bearings. Once these were installed and completed, testing of the buffer air and dry gas seals was performed. After that, oil was slowly introduced into the system to ensure proper drainage, and that oil was not creeping into the dry gas seals. After air and oil systems were tested successfully, instrumentation was confirmed, and the turbine was slowly rolled around 1,000 rpm to test the rest of the system. For this test, the dyno wheel was not attached.

Figure 125: Turbine Assembly Showing Thrust Bearing Installation

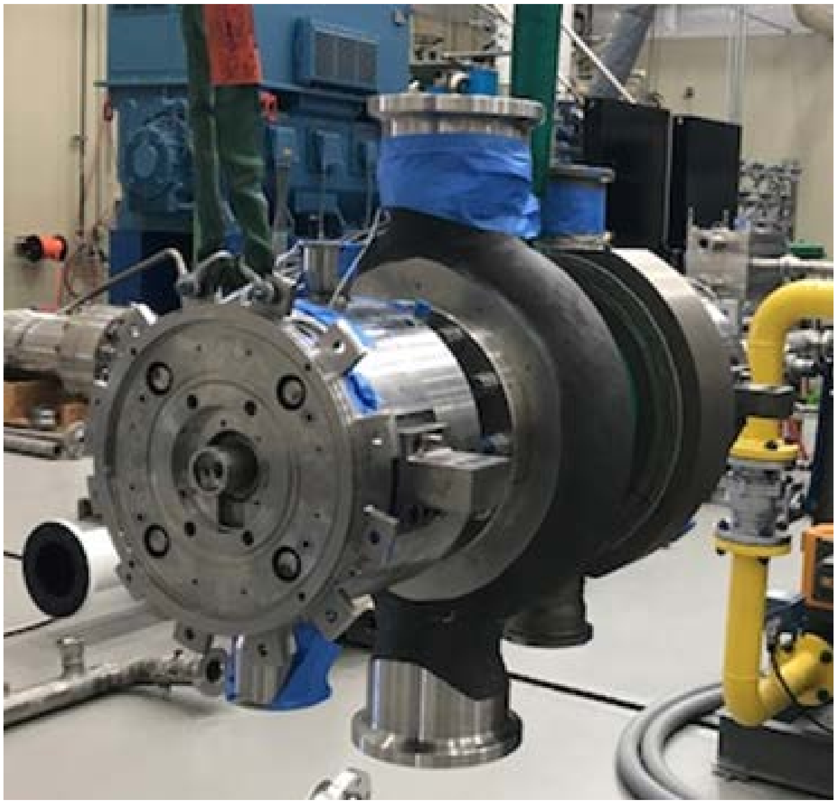

Figure 126: Fully Assembled Turbine

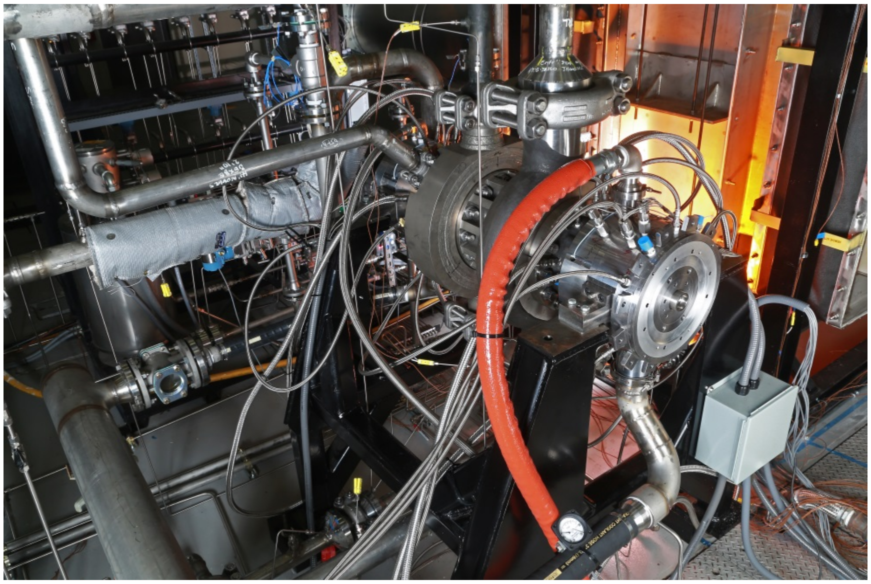

Figure 127: Assembled Turbine Casing on Operating Stand

With the turbine assembled, field welds were completed for the rest of the high-temperature piping. This included balance lines, piping to the recuperator, and piping from the heater and all instrumentation

Task 2.3. Test Loop Construction

Primary Heater Overview

Figure 128 shows the completed heater heat exchanger using Inconel 740H tubing material. The tubing penetrations through the outer shell can be seen as well. The primary heater system includes 2.5 MWt, Inconel 740H, primary heater heat exchanger and an 11.7MWt Natural Gas/Burner/Blower System. It should be noted that this is the first primary heater heat exchanger to be fabricated and tested using 740H.

Figure 128: Heater Heat Exchanger

Figure 129: Gas Fired Primary Heater Installation

Figure 129 shows photos of the gas-fired heater installation. The heat exchanger passed all leak and hydro testing. The exhaust ducting is routed outside the high bay and through the roof. The heater was commissioned in December 2016 and fired to 1000°F, as shown in Figure 130. Higher temperatures were possible once CO_2 was flowing through the heat exchanger tubes. Dayco representatives were brought on-site to tune the burners.

Figure 130: Commissioning Test of Primary Heater

Test Loop Fabrication

All of the piping is in place, and the field joints have been completed including the Inconel 740 piping that connects the heater to the turbine expander. Figure 131 shows the currently installed piping inside the high bay laboratory. The piping includes the connections from the pump (located outside the high bay) to the recuperator, from the recuperator to the heater, and from the recuperator back out of the high bay to the loop in the yard outside. The connections that are not installed are from the heater to the turbine and from the turbine to the recuperator.

Figure 131: SunShot Piping in the High Bay of Building 278

Figure 132 shows the piping that connects the pump to the loop and the recuperator. This piping is complete and fully installed.

Figure 132: SunShot Piping Connecting the Pump to the Loop

Phase 3. Performance Testing

Task 3.1 Performance Testing

During commissioning, the only issue discovered was in operation of the fill pump. Due to an over current trip, the fill pump would have issues operating consistently above 50% operating speed. Rather than keep resetting the fill pump VFD, the pump was run at 50% speed and monitored more closely to make sure that it was on when needed. During operating, the fill pump would only be needed to replace lost mass in the loop due to losses from dry gas seals and various leaks.

Early in December 2017, testing began with filling of the entire loop. This included an initial leak check of the turbine section, and purging air out of the loop. During this initial filling, dry ice formation in the dry gas seals became an issue in both the pump and the turbine. While filling the pump loop on a colder day at around 1100 psi, the flow rate through the dry gas seal vents increased drastically. The thought was that dry ice formed between the seal faces or in the downstream vents and caused the axial faces to open up and vent the entire loop. These seals would eventually seat themselves at around 600-650 psi.

To prevent this from happening, the pump dry gas seal supply system was modified so that they could be supplied with heated CO_2 (> 180°F) from the dry gas seal panel for the turbine. By doing this, in order to ensure that there was enough heater capacity, the pump loop and turbine section were filled separately. The fill procedure was modified as such:

1. Prime the fill pump
2. Fill pump loop with vapor and purge. Repeat 3 times.
3. Fill pump loop through main fill line and pump dry gas seals. Control flow through seals and dry gas seal heater to ensure seals are supplied with 180°F or greater CO_2
4. Once pump loop reaches 1100 psi, turn on chiller and outside cooling tower
5. Once pump loop reaches 1250-1300 psi, start pump and slowly ramp up
    5.1. 500 rpm → 1000 → 2500 (being throttling) → 3566 rpm
    5.2. Once pump is building head, the pump discharge will supply the pump dry gas seals. Rotation helps keep the seals warm
6. Begin filling and purging the turbine section of the loop through the dry gas seals only
    6.1. If more mass flow is needed, mixing valve can also be used to fill
7. Once turbine section is equal to pump suction, open isolation valves to equalize the loop

This proved to ensure successful and repeatable starting up of the pump loop without dry gas seals venting. However, once the pump loop was up the full pressure on the discharge, it became the dry gas seal supply source for the turbine. This flow was dropping from 3500 psi to atmosphere at the start of the turbine loop fill. Initial pressure drop was taken across the panel regulator, the flow would then heat up through the heater and then drop in pressure across the control valves. With Joule-Thompson cooling, all the heat from the heater was lost, and the turbine seals were not being supplied with warm flow. To correct this, control valves were rearranged so that flow through the heater was at the same pressure as the turbine loop to prevent additional cooling across supply valves:

Figure 133: Reconfigured Dry Gas Seal Panel with Control Valve upstream of the Heater

This reconfiguration of the dry gas seal panel proved to be successful over the remainder of turbine testing. Ideally, both supplies would have their own control valve, but by having the main flow controlled by one valve and the other two controlled by a pinched hand valve and a control valve, the controller was able to balance flow between the two sides.

Below summarizes the overall testing and achievements on each day.

1) December 21, 2017
    - First time turbine spun on its own power
    - Achieved 8,000 rpm at 2,300 psi (159 bar). Spun turbine for 2 hours.
    - Failed dry gas seal due to dry ice formation in seal vents
2) March 1, 2018
    - Repaired seal installed and turbine rebuilt
    - Achieved 14,000 rpm at 2,500 psi (172 bar) and 300°F (149°C). Spun turbine for 2.5 hours
    - Normal shutdown
3) March 8, 2018
    - Achieved 20,500 rpm at 2,700 psi (186 bar) and 1050°F (550°C)

   - Had heater controller issues that led to fluctuating temperature and multiple heater and turbine trips.
   - 4 total trips and 4 total start ups during this day of testing
   - Turbine spun for a total of 7.5 hours.
   - Normal shutdown
4) March 20, 2018
   - Achieved 24,300 rpm at 3,060 psi (211 bar) and 1060°F (571°C)
   - Switched to manual control of heater by setting the gas output instead of relying on the controller to set a temperature
   - Dry gas seal failed on inlet side due to speed and temperature and vented the loop
   - Turbine spun for 2.5 hours

Since the Sunshot program funds were depleted, the team kicked off the testing phase of the FOCUS program which retrofitted the thermal seal with a novel design to improve the temperature gradients through this section. The rotor also required modification to implement this design, so repairs from the dry gas seal failure were made at the same time which consisted of applying a tungsten-carbide coating to both bearing journal locations and cleaning up some other diameters. New journal bearings were procured along with a new dry gas seal (other seal was cleaned and re-used).

5) December 6, 2018
   Turbine repaired and rebuilt with FOCUS thermal seal and modified dry gas seals
   - Achieved 18,500 rpm at 2,400 psi (166 bar) and 1080°F (582°C)
   - Discovered bearing clearance was too tight on one side and bearing temperatures were too high.
   - Controlled shutdown so that bearing could be removed and repaired
   - Turbine spun for 5.5 hours
6) December 13, 2018
   - Achieved 24,600 rpm at 3,200 psi (221 bar) and 1070°F (577°C)
   - Heater tripped due to low air supply. Blower had been turned down to minimum speed to get more heat with less fuel
   - Turbine spun for 3.5 hours
7) December 18, 2018
   - Achieved 18,000 rpm at 2,200 psi (152 bar) and 1320°F (715°C)
   - Reached design temperature at lower mass flow to look at temperature profiles and hold steady for longer duration. Keep bearing temperatures low. Heater tripped after 6 hours of steady hold at max temperature
   - Turbine spun for 9.5 hours
8) December 20, 2018
   - Achieved 27,000 rpm at 3,500 psi (241 bar) and 1100°F (593°C)
   - A settings at maximum power: Max pump speed, recycle valve closed, turbine valve wide-open, heater at maximum heat rate, natural gas supply at minimum allowable pressure
   - Reached design speed. Attempted controlled shutdown but heater tripped.
   - Turbine spun for a total of 4.5 hours

The temperature, speed, and pressure goals were reached for the turbine but not simultaneously due to limitations of the natural gas supply to the heater. The team believes that the turbine was sufficiently exercised and demonstrated robust mechanical and rotordynamic behavior throughout the test program.

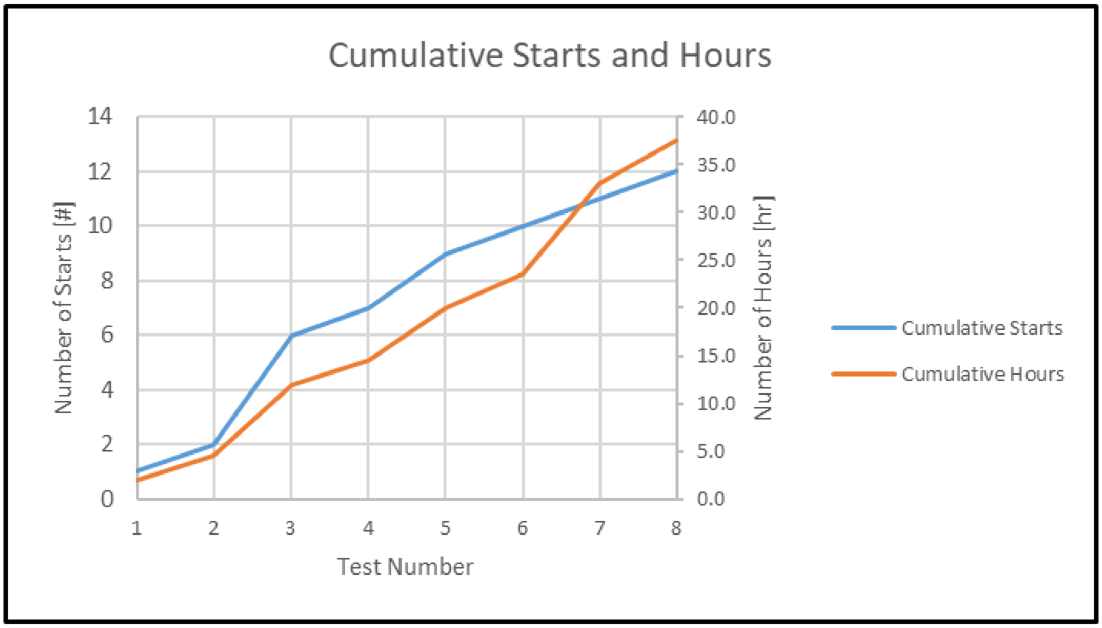

Figure 134: SunShot Test Summary - Total Starts and Hours of Operation

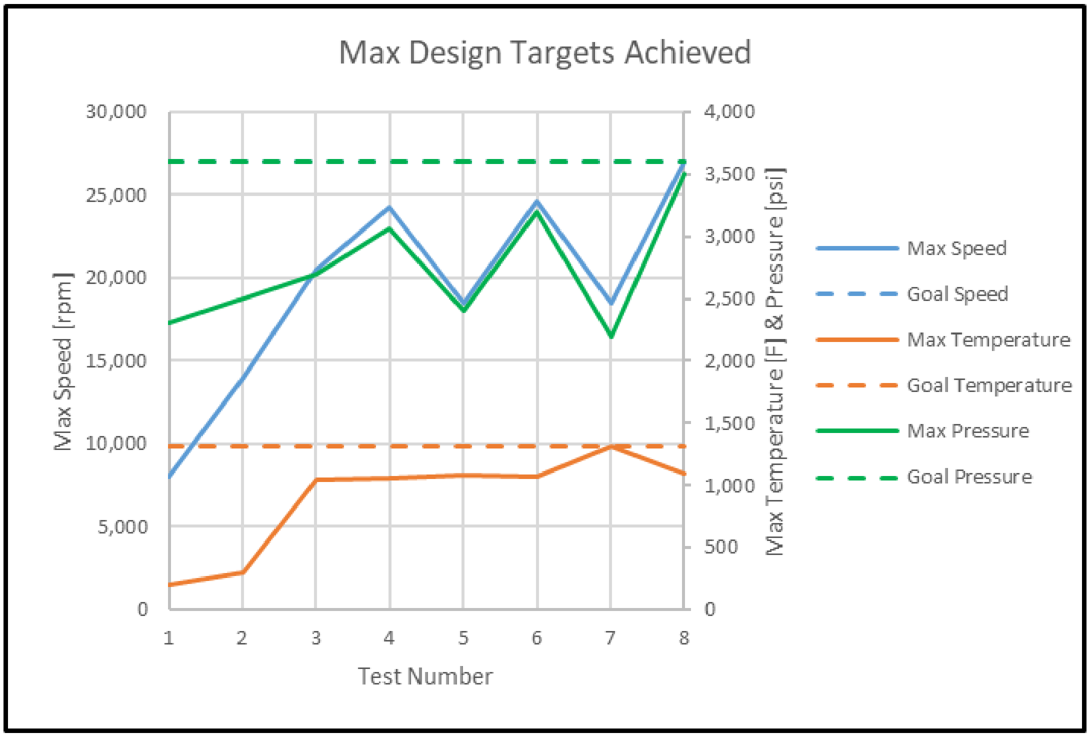

Figure 135: Design Goals Reached During Testing

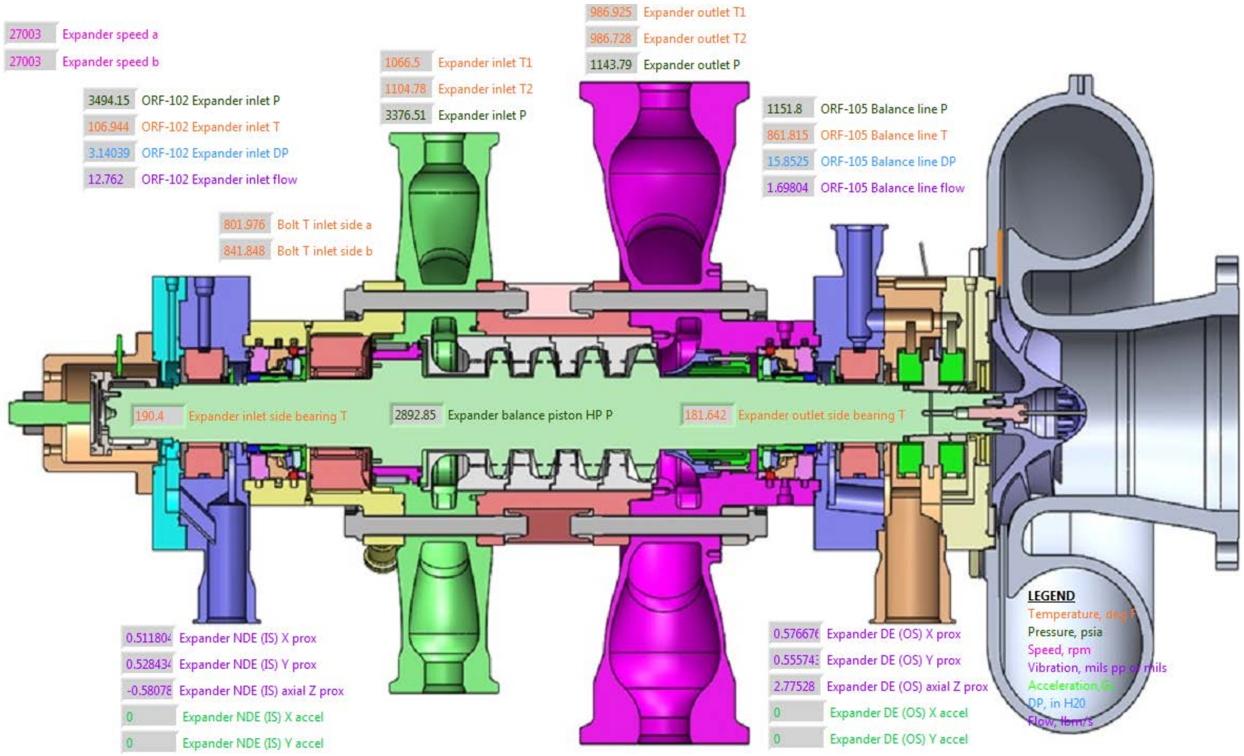
27003 Expander speed a
27003 Expander speed b
3494.15 ORF-102 Expander inlet P
106.944 ORF-102 Expander inlet T
3.14039 ORF-102 Expander inlet DP
12.762 ORF-102 Expander inlet flow
801.976 Bolt T inlet side a
841.848 Bolt T inlet side b
1066.5 Expander inlet T1
1104.78 Expander inlet T2
3376.51 Expander inlet P
986.925 Expander outlet T1
986.728 Expander outlet T2
1143.79 Expander outlet P
1151.8 ORF-105 Balance line P
861.815 ORF-105 Balance line T
15.8525 ORF-105 Balance line DP
1.69804 ORF-105 Balance line flow
190.4 Expander inlet side bearing T
2892.85 Expander balance piston HP P
181.642 Expander outlet side bearing T
0.51180 Expander NDE (IS) X prox
0.52843 Expander NDE (IS) Y prox
-0.58078 Expander NDE (IS) axial Z prox
0 Expander NDE (IS) X accel
0 Expander NDE (IS) Y accel
0.57667 Expander DE (OS) X prox
0.55574 Expander DE (OS) Y prox
2.77528 Expander DE (OS) axial Z prox
0 Expander DE (OS) X accel
0 Expander DE (OS) Y accel

Figure 136: Operating Screen at 27,000 rpm

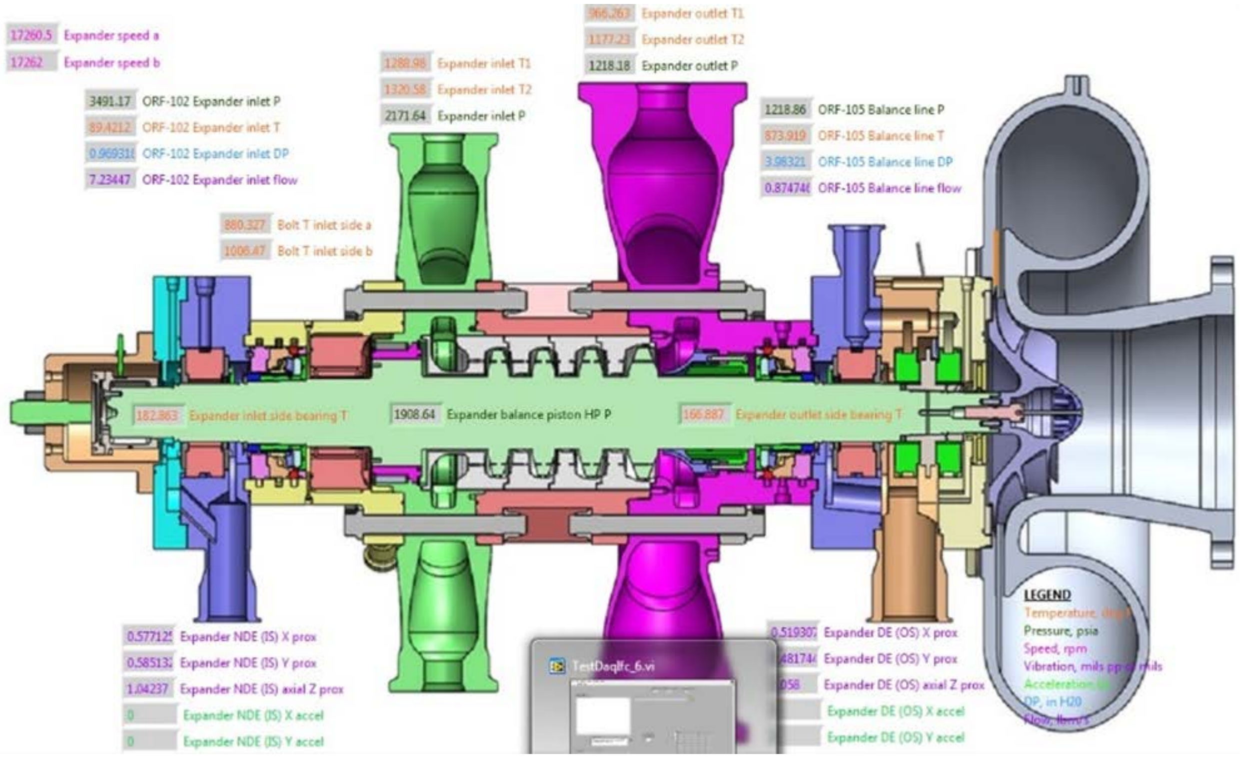
17260.5 Expander speed a
17262 Expander speed b
3491.17 ORF-102 Expander inlet P
89.4212 ORF-102 Expander inlet T
0.96931 ORF-102 Expander inlet DP
7.23447 ORF-102 Expander inlet flow
880.327 Bolt T inlet side a
1006.47 Bolt T inlet side b
1288.98 Expander inlet T1
1320.58 Expander inlet T2
2171.64 Expander inlet P
966.263 Expander outlet T1
1177.23 Expander outlet T2
1218.18 Expander outlet P
1218.86 ORF-105 Balance line P
873.919 ORF-105 Balance line T
3.98321 ORF-105 Balance line DP
0.87474 ORF-105 Balance line flow
182.863 Expander inlet side bearing T
1908.64 Expander balance piston HP P
166.887 Expander outlet side bearing T
0.57712 Expander NDE (IS) X prox
0.58513 Expander NDE (IS) Y prox
1.04237 Expander NDE (IS) axial Z prox
0 Expander NDE (IS) X accel
0 Expander NDE (IS) Y accel
0.51930 Expander DE (OS) X prox
48174 Expander DE (OS) Y prox
058 Expander DE (OS) axial Z prox
Expander DE (OS) X accel
Expander DE (OS) Y accel

Figure 137: Operating Screen at 1,320°F

Key areas of performance that were reviewed in detail:

- Recuperator effectiveness and pressure drop
    - PCHE was looked at for future projects, and it was good to understand their performance based on prediction
- Heater effectiveness
- Turbine performance
    - With no dyno wheel needed during testing, all power was consumed by bearings and windage
    - These power losses were seen in a full scale machine and can be used to predict parasitic losses
- Thermal seal performance
    - Thermal management was a key are of concern
    - Compare both seal designs to determine optimal designs for future applications
- Balance piston leakage
    - Balance pistons are required for thrust balance and rotor damping
    - Leakage is a direct hit to turbine performance
    - Comparing prediction to test data will help with future designs
- Loop transient performance
    - Understanding transients are critical in studying the overall performance of a loop
    - Start up and shut down scenarios can affect the design life of various components
- Rotor performance
    - Peak vibrations during start up and shutdown
    - Peak vibrations when running through modes
    - Stability at max speeds and temperatures
- Dry Gas Seal performance
    - Temperature control on thermal seal
- Bearing Performance
    - Journal temperature
    - Thrust bearing temperatures to monitor thrust balance

Recuperator Performance

The following figure shows the temperatures throughout the day when 1,320°F was reached at turbine inlet. This shows how the temperatures changed throughout the day as the turbine was warmed up to max operating conditions.

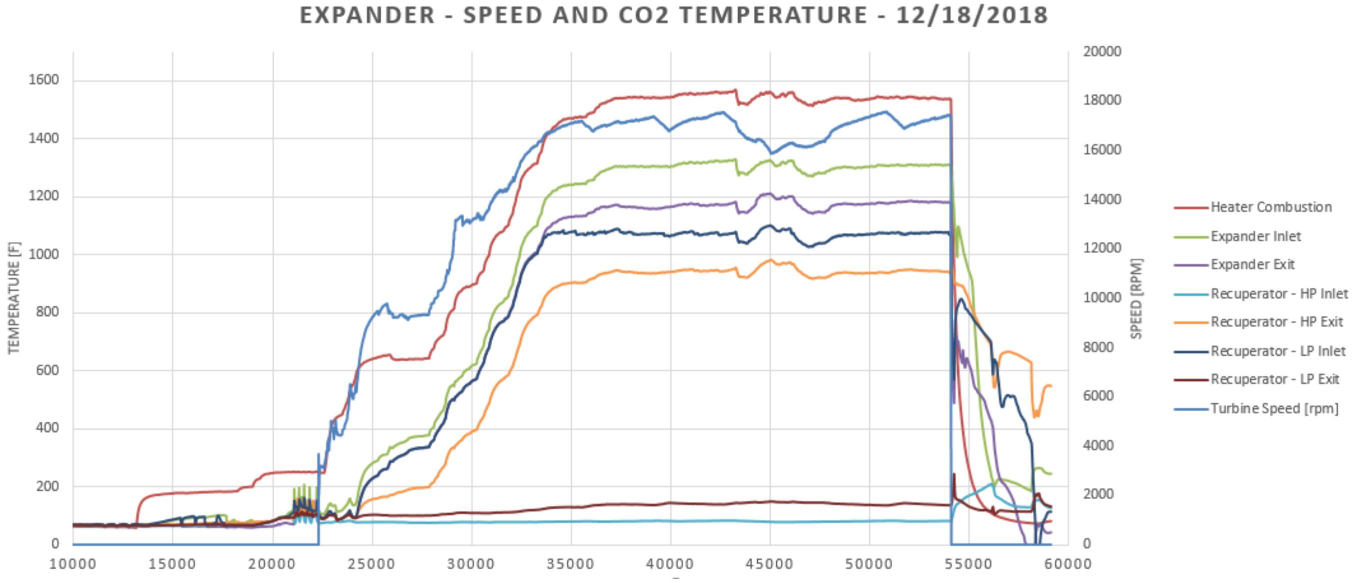

Figure 138: Recuperator CO_2 Temperatures during Max Temperature Testing

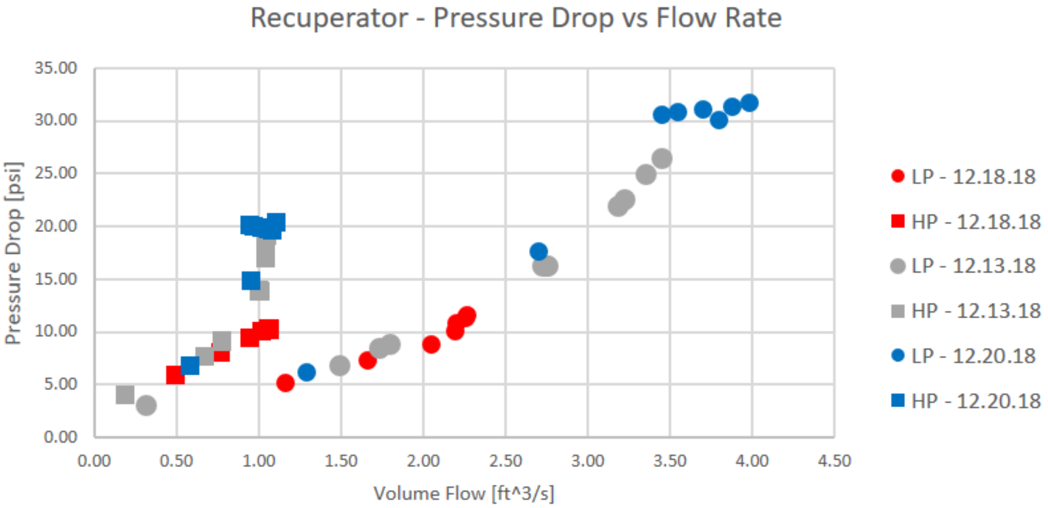

Figure 139: Recuperator Performance - Pressure Drop vs. Flow Rate

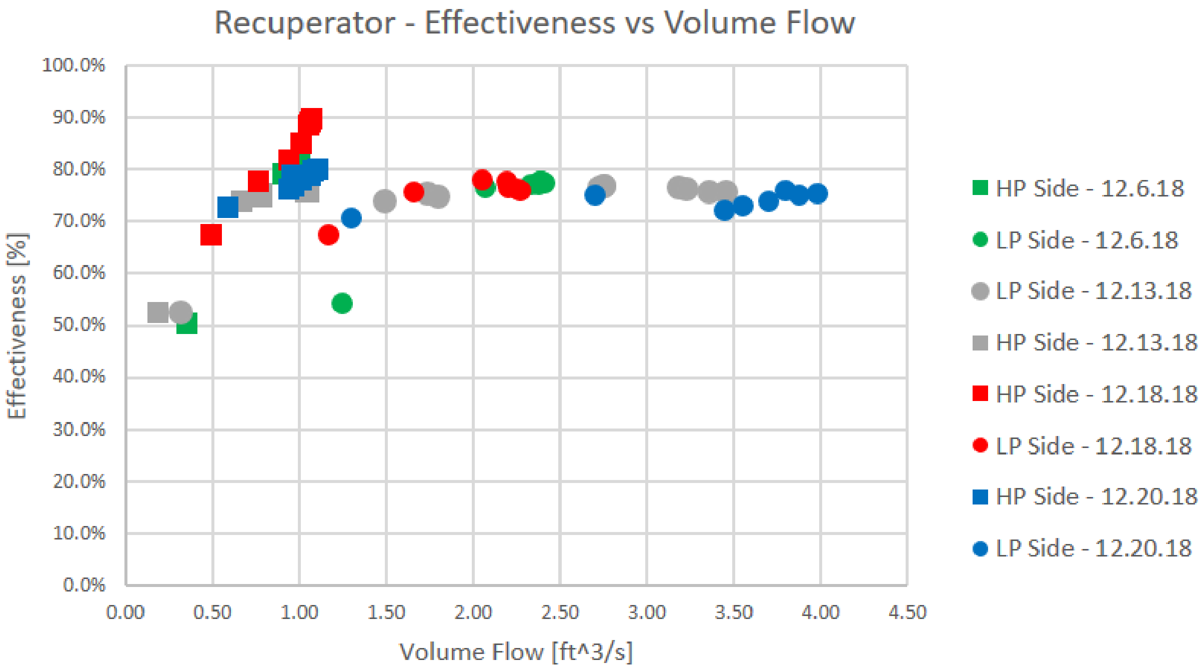

Figure 140: Recuperator Performance - Effectiveness vs. Volume Flow

Figure 139 and Figure 140 break down the key performance metrics of the recuperator, which pressure drop and effectiveness. The dates are noted so that the various days can be looked at based on what goals were achieved that day. Of note, the max temperature was achieved on December 18, 2018, and the max speed and pressure were achieved on December 20, 2018. This was the highest flow rate and closest to the overall design. One of the key aspects to note is that the performance did not change throughout the various days. Even at the highest temperature, this shows that there was no short term degradation in performance due to fouling or corrosion in the 316 SS recuperator.

Table 23: March 20, 2018, Test Data Compared to Design Data

	Test	Design	
Recuperator HP Pressure	2,655.6	3,698.0	**psi**
Recuperator LP Pressure	1,230.7	1,247.0	**psi**
Recuperator HP In Temp	91.9	85.0	**F**
Recuperator HP Ex Temp	753.7	877.4	**F**
Recuperator LP In Temp	969.5	1,053.0	**F**
Recuperator LP Ex Temp	131.0	176.7	**F**
HP h1	113.45	107.96	**Btu/lbm**
HP h2	367.34	400.50	**Btu/lbm**
LP h1	434.17	458.16	**Btu/lbm**
LP h2	189.13	209.23	**Btu/lbm**
HP h2 ideal	430.37	453.07	**Btu/lbm**
LP h2 ideal	127.50	118.99	**Btu/lbm**
hmax HP	316.92	345.11	**Btu/lbm**
hmax LP	306.67	339.17	**Btu/lbm**
hmax	316.92	345.11	**Btu/lbm**
Effectiveness	80.11%	84.77%	**%**

HP: high pressure section of recuperator; LP: low pressure section of recuperator; h1: enthalpy in; h2: enthalpy out

At design conditions, the recuperator was predicted to see an effectiveness around 85%. This matches relatively well with the HP side data from December 18, 2018, at the highest temperature data points. Those seemed to be trending upward as volume flow increases which would mean that an effectiveness greater than 90% would be expected at design conditions, which is 5% greater than predicted.

Heater Performance

The heater heat exchanger was designed for minimum size and cost while meeting the heat input requirements, not necessarily for highest efficiency. It represents the highest temperature sCO_2 heat exchanger ever tested and the first to use Inconel 740H. Overall, it performed well and met the project requirements.

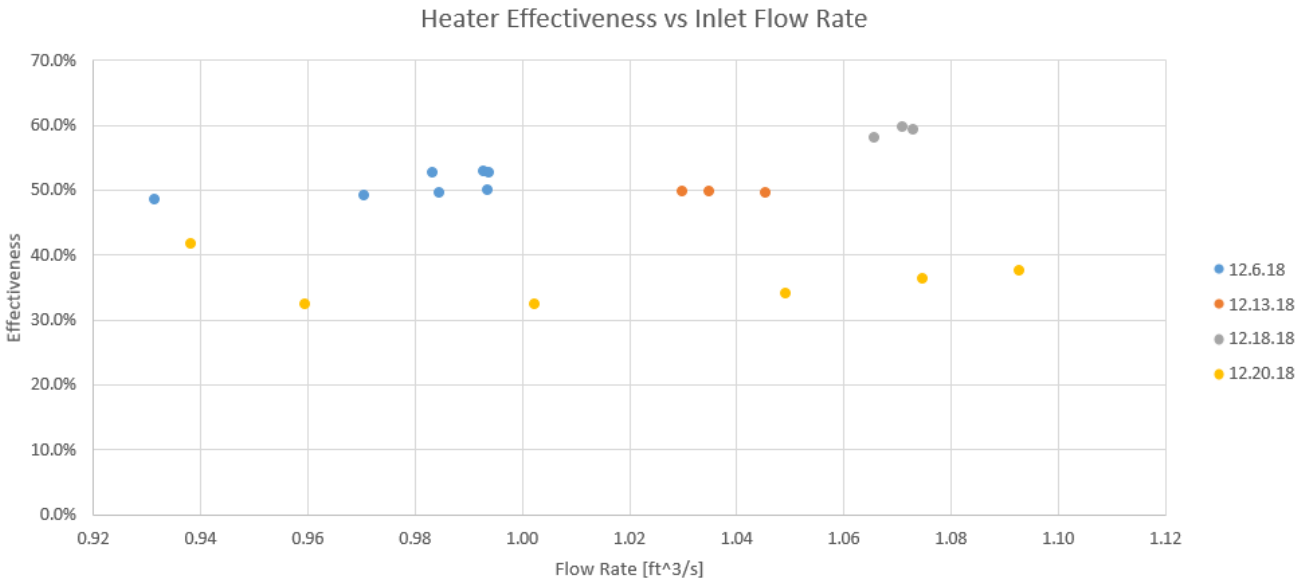

Figure 141: Heater Effectiveness vs. Turbine Inlet Flow Rate

Similar to the recuperator, flow rate was used to compare heater effectiveness throughout the testing. On the first three days of testing, the heater effectiveness seemed to trend upward with flow rate, but there was a drop off between the December 18, 2018 and the December 20, 2018 data. This was further investigated as to what caused this drop. Due to the need to accommodate bend allowance at the ends, several gaps in the tube bundle were filled with insulation to prevent flow bypassing the bundle. If this insulation blew out at the max temperatures, this would cause a clear drop in performance. Since the tube externals saw the highest heater temperature of 1,750°F, it was important to investigate if any oxide layers formed on the outside of the tubes that could lower the heat transfer between the air side and the CO_2.

Figure 142: Heater Bundle with Insulation Installed in Gaps

Turbine Performance

Since all of the turbine power was consumed by parasitic losses in the dry gas seals, bearings, and windage in the shaft, the dyno wheel and loop were never installed for this test. During operation, this was determined to not be needed, since to reach max speed, the heater was pushed to its limits, and to reach max temperature, the mass flow and speed were much lower. To measure performance, the enthalpy drop is calculated across the turbine based on the following measurements:

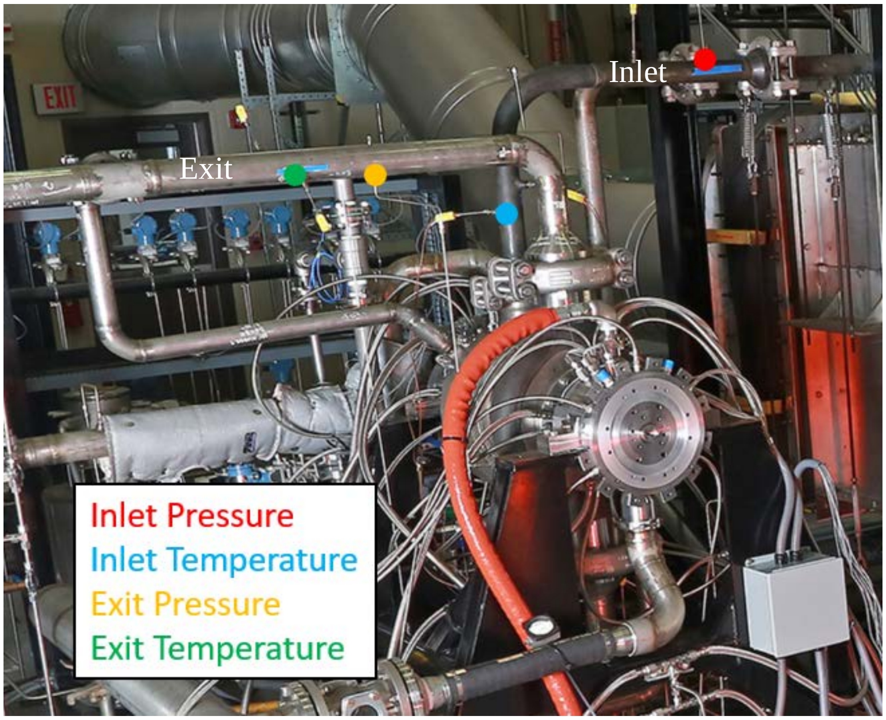

Figure 143: Turbine Pressure and Temperature Measurement Locations for Performance Calculations (Note: Colored Dots Correspond to Legend Color)

Pressure measurements were made using pressure taps routed to 0-4,000 psi Rosemount transducers on the inlet and 0-2,000 psi transducers on the exit, which were mounted to the dry gas seal panel. Temperature measurements were made using thermowells in the piping with K-type thermocouples routed to the micronet controllers and a temperature scanner. Pressures were taken at a single location, and temperatures were taken at four locations on both the inlet and exit. All piping and clamp connections were insulated during operation. For the turbine, the nozzle case was insulated but the inlet and exit plenums were not.

In terms of mass flow, an orifice plate upstream of the turbine throttle valve was used to measure total mass flow going into the hot section of the loop. In terms of what was going through the turbine, a few streams had to be removed. This included the dry gas seal supply flow and the balance piston flow that was being taken from the stage 1 nozzle exit. Both inlet and exit dry gas seal flows were measured using orifice meters on the dry gas seal panel. Balance piston mass flow was measured using an orifice meter integral to one of the clamp connections on a single balance line. Balance piston flow is doubled from this calculation to account for the two pipes leaving the turbine and connecting to exit piping. It is important to note that balance piston flow also includes around 95%+ of the dry gas seal supply flow on the inlet side. Based on all of these measurements, the mass flow, enthalpy in, and enthalpy out are calculated with the use of REFPROP CO_2 properties and power is calculated at steady state points during operation.

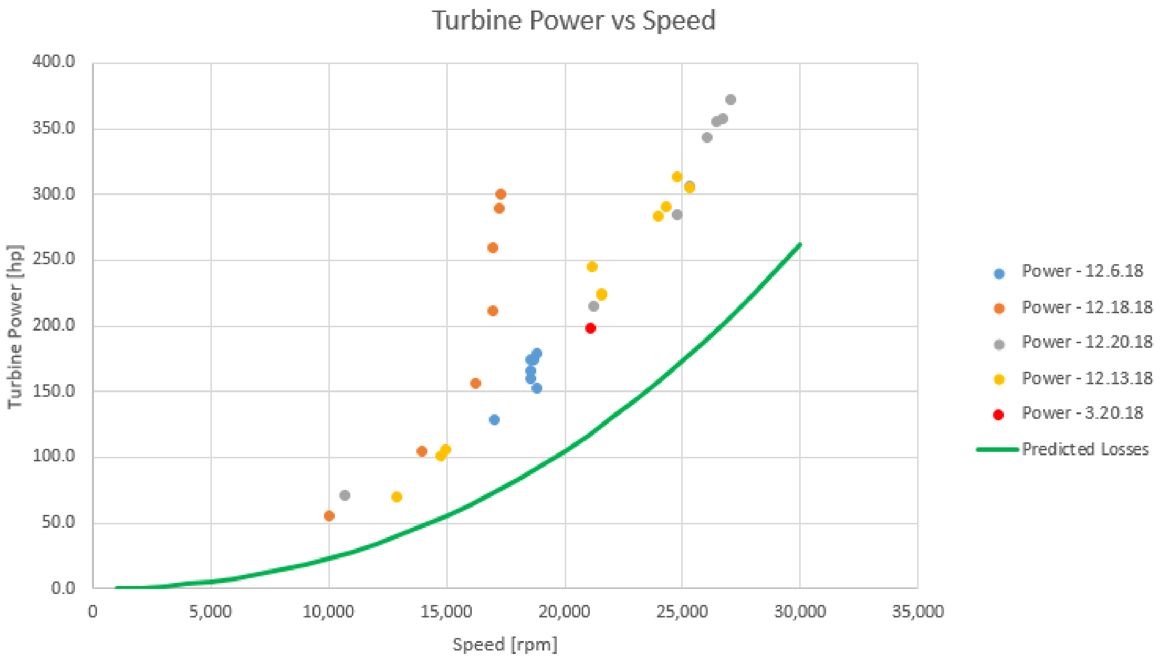

Figure 144: Turbine Power vs. Speed

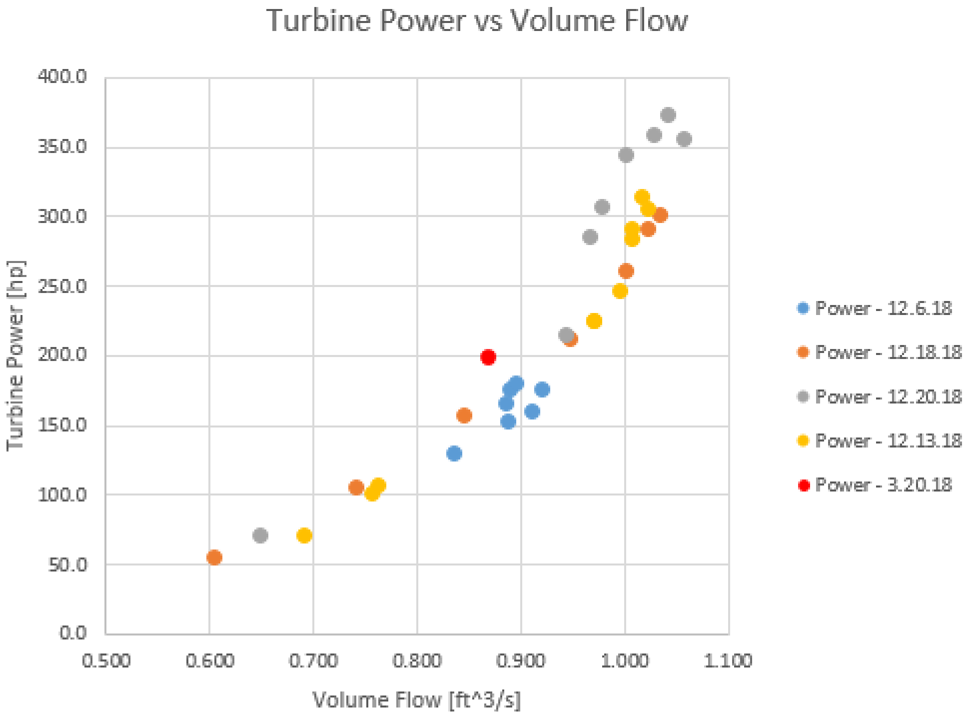

Figure 145: Turbine Power vs. Volume Flow

Prior to spinning the turbine, the only predicted losses were friction in the journal and thrust bearings and windage losses in the dry gas seals. For the bearings, the predictions were based on the viscosity of the oil and operation at the design conditions of 27,000 rpm. For lower speeds, the bearing consumed power was based on a speed squared relationship. At full speed, total bearing power consumption was estimated to be 148.12 hp. For windage losses in the dry gas seals, the losses were based on a speed cubed relationship. From John Crane predictions, at 27,000 rpm each seal would consume 29.07 hp. The predicted loss line (green) as shown in Figure 144 is based on bearing and dry gas seal power consumption at 27,000 rpm with the squared and cubed relationship, respectively. The difference between the two lines would have been additional parasitic losses or errors in the predictions and measurements.

Since this was a mechanical test of a full 10 MWe rotor and case, any measurements of parasitic losses will be useful for developing performance models for future loops and designs. These kind of losses will be worse for high speed machines due to the relation of bearing and windage losses with speed.

Figure 145 shows that turbine power does follow a consistent trend based on volume flow, even throughout the five different days of testing. However, based on speed, the trend is as expected, except for December 18, 2018 data, when the highest temperatures were reached. Being that losses should be based on a relationship to speed, this could indicate that either temperature effects also lead to an increase in windage or that higher temperatures lead to higher thermal losses in our system that affect the accuracy of the calculation. Since the plenums are not insulated, higher losses would be expected.

Thermal Seal Performance

One of the major design challenges in the SunShot turbine was the thermal gradient zone between the hot turbine inlet and the cold dry gas seals. With a turbine inlet temperature of 1320°F, this thermal gradient would be above 200°F/in. This large thermal gradient will lead to high thermal stresses in the rotor that have to be managed. More importantly, fast thermal gradients near the balance piston will lead to high stresses in the balance piston fillet, which is one of the highest stresses regions on the entire rotor. The goal of the thermal seal is to maintain a linear thermal gradient from dry gas seal to balance piston to help maintain acceptable stresses in the rotor. Two difference thermal seals were designed, one that was originally designed under the SunShot project and a redesigned seal under the Focus project that utilized a thermal barrier coating (TBC) on the rotor.

The only difference between the SunShot turbine test and the FOCUS turbine test was the thermal seal on the inlet side of the turbine and the addition of a thermal barrier coating (TBC) on the rotor adjacent to the thermal seal, which minimizes the heat transfer into the rotor:

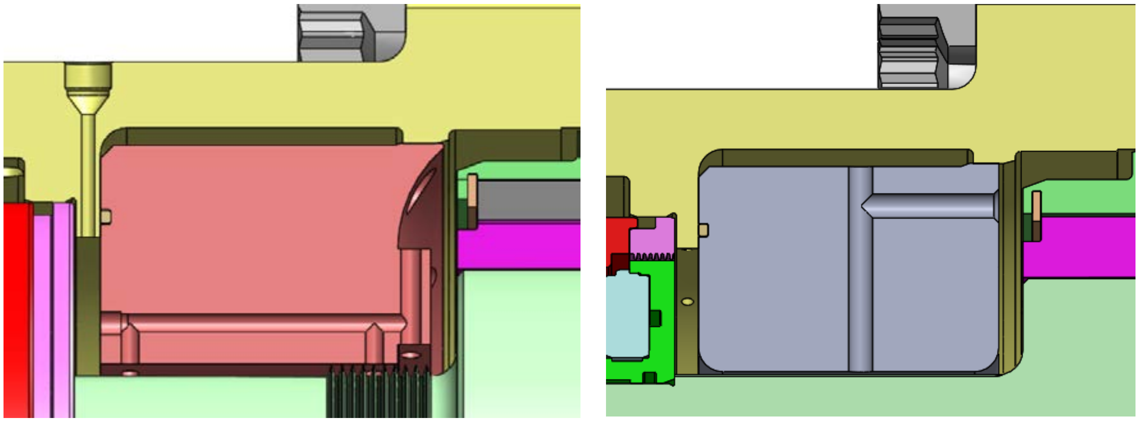

Figure 146: Cross Section of SunShot Thermal Seal (Left) vs. FOCUS Thermal Seal (Right)

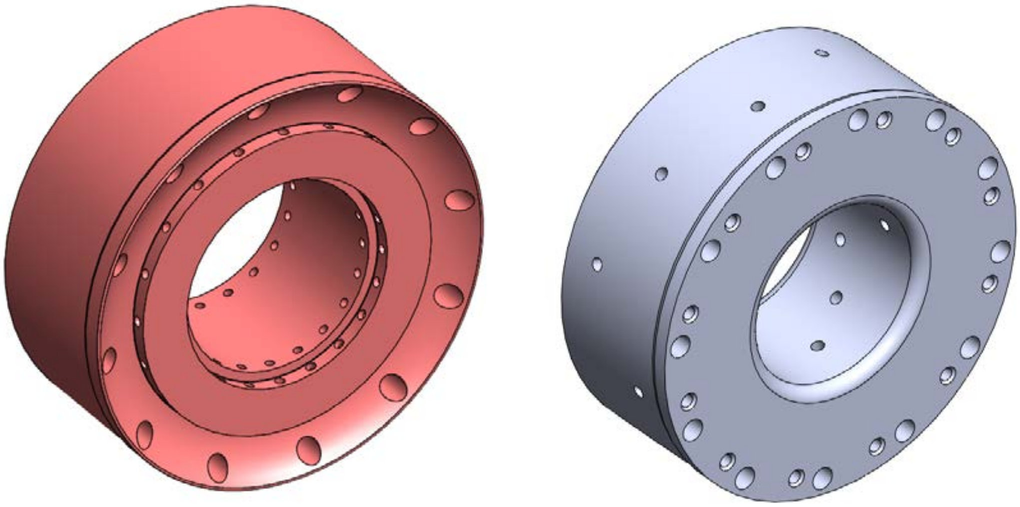

Figure 147: Iso view of SunShot Thermal Seal (Left) vs. FOCUS Thermal Seal (Right)

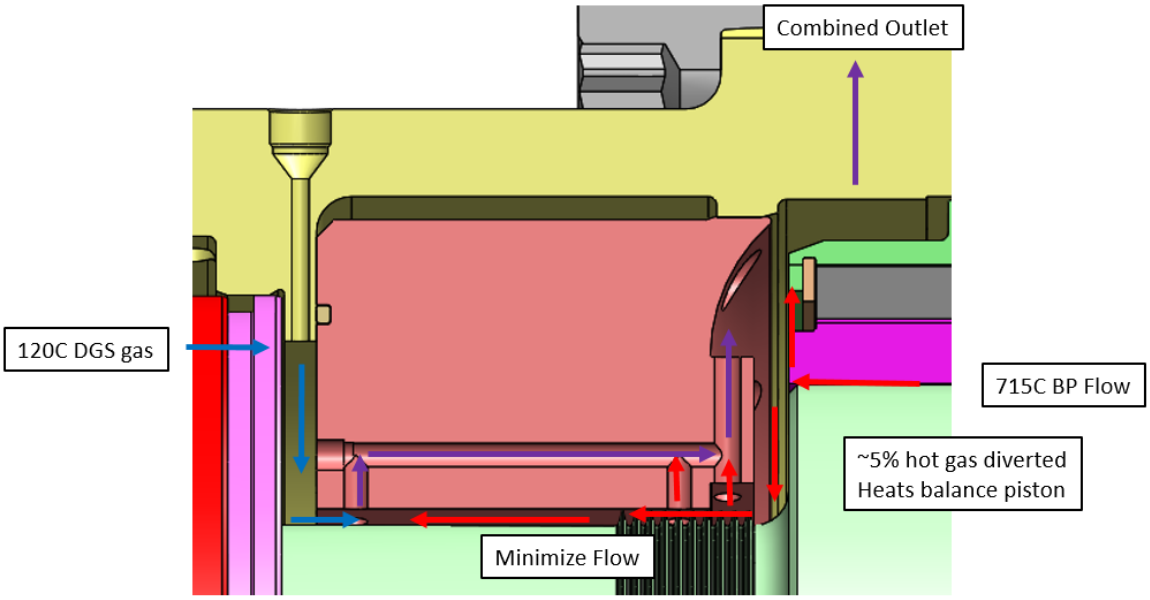

Figure 148: SunShot Thermal Seal Cold and Hot Flow Path

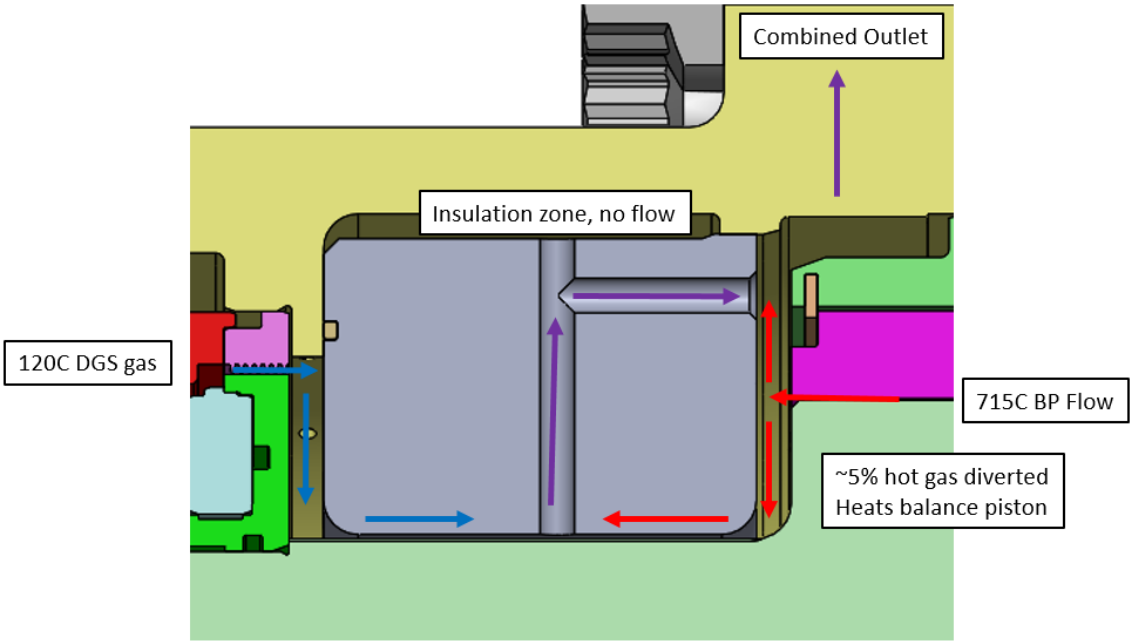

Figure 149: FOCUS Thermal Seal Cold and Hot Flow Path

The main difference between the two seals are shown in Figure 146 through Figure 149. The goal of both seals was to minimize flow between the seal and the rotor. By restricting this flow, only hot flow should go across the balance piston, keeping it hot and reducing peak stresses in the rotor. The various holes in the seal would allow for mixing of the flow. The SunShot design utilized a labyrinth configuration with mixing holes at each end of the seal. The SunShot design has a uniform flow path, patterned 20X around the seal. By preventing flow across the seal, the rotor would maintain a linear gradient. Instead of labyrinth teeth, the FOCUS design used a narrow annular passage to control the percentage of flow from the balance piston and allowed for mixing through twelve passages at three axial locations shown in Figure 150. The FOCUS seal also had a thermal barrier coating on the rotor to limit the temperature gradient.

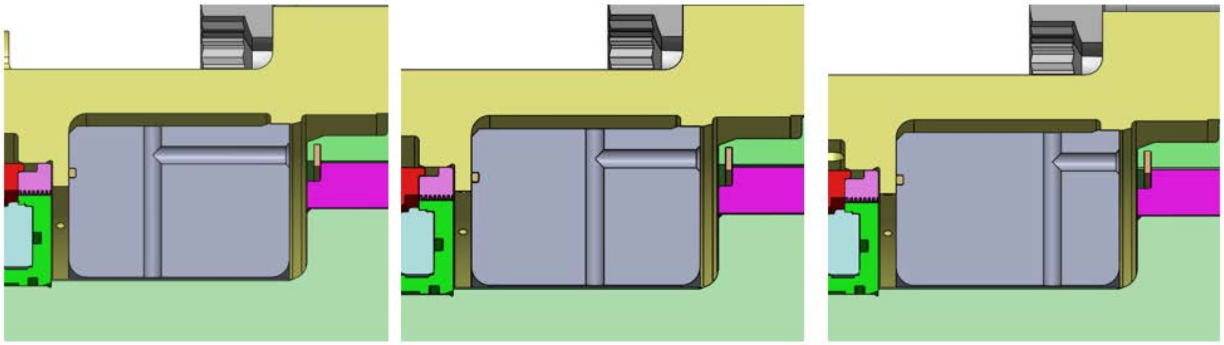

Figure 150: Axial Locations for FOCUS Thermal Seal Mixing Holes

To check performance of the seal, temperature measurements were made at five different axial locations shown in Figure 151. Temperature locations are the same between both seal configurations:

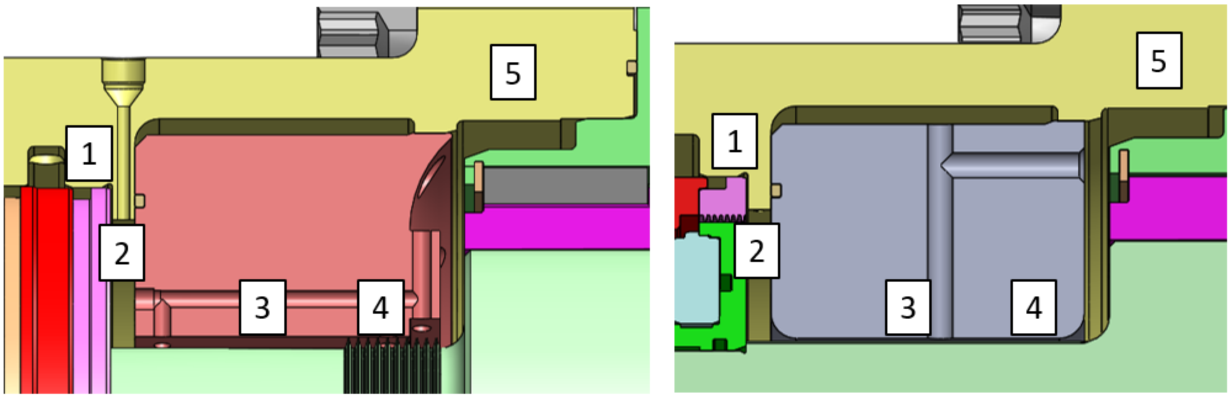

Figure 151: Temperature Measurement Locations – SunShot (Right) vs. FOCUS Left)

1. Metal temperature above the polymer seal on the dry gas seal; two total thermocouples. This thermocouple would verify case temperatures right above this seal to ensure that it never got above 350°F, which would damage the seal.
2. Fluid temperature between dry gas seal and thermal seal; 3 total thermocouples. This one looked at the flow coming out of the dry gas seal to ensure that it was not approaching the 350°F design limit. Windage will affect the temperature of this flow. As the flow reached 300°F, dry gas seal flow was increased to cool this cavity more.

3. Metal temperature mid-span of the thermal seal; three total thermocouples. This measurement monitored the mid-span of the seal to help monitor the temperature profile.
4. Metal temperature inboard of the thermal seal; three total thermocouples. This measurement monitored the hot side of the seal to help monitor the temperature profile.
5. Fluid temperature in the insulated balance piston flow outboard of the turbine; one thermocouple. This temperature was used on an orifice meter to measure balance piston flow. It would also show the mixed hot and cooling flow from the dry gas seal and the balance piston.

Data to compare the thermal seal performance was taken on two different days, March 20, 2018, with the SunShot seal and December 13, 2018, with the FOCUS seal. The long time in between the tests was due to a dry gas seal failure on March 20, 2018, that led to an eight-month delay in repairing and rebuilding the turbine and some of its components. In order to ensure the comparison would be valid, certain parameters were adjusted to be close:

Table 24: Operating Parameter Comparison

Parameter	SunShot	FOCUS
Turbine Speed [rpm]	21,080	21,536
Turbine Inlet Temperature [F]	1,051	1,066
Dry Gas Seal Flow [lbm/s]	0.131	0.130
Dry Gas Seal Inlet Temperature [F]	119	108

An overall comparison of the temperatures throughout the turbine is shown in Figure 152. A description of all of the temperature measurements is shown in Table 25. Temperature measurements were tracked through a temperature scanner and National Instruments compact data acquisition system. Most temperatures were through the scanner only and just tracked. Other critical temperatures including turbine inlet, bearing temperatures, and dry gas seal temperatures were monitored through a Woodward micronet control system and were tied to alarms and trips. Thermocouple accuracies are shown in Table 26:

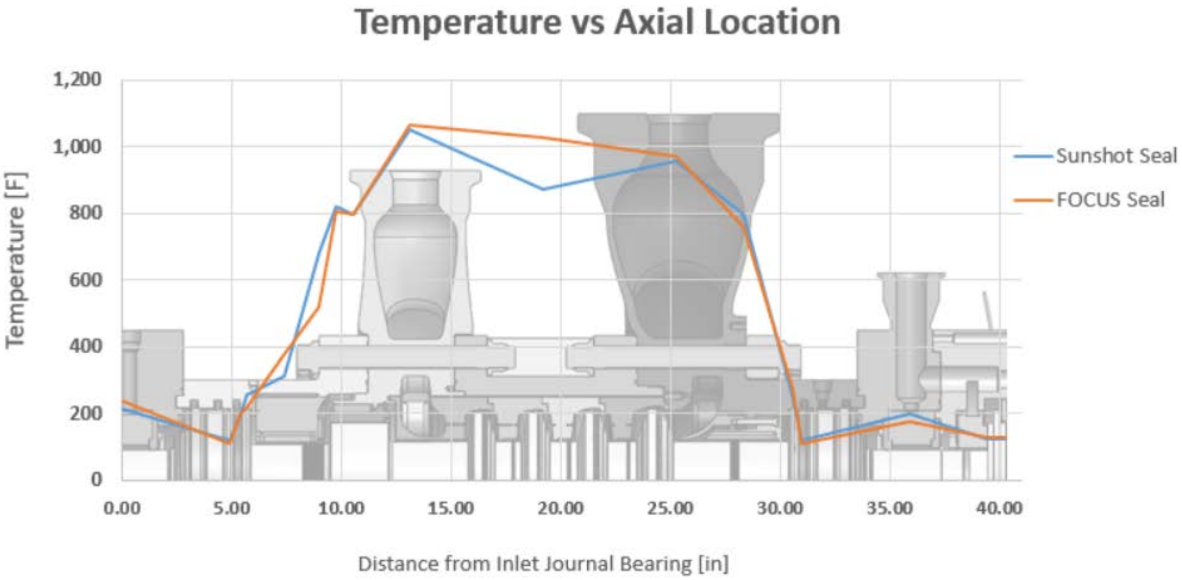

Figure 152: Turbine Temperature Profile - SunShot vs. FOCUS

Besides the thermal seal which will be looked at more closely in Figure 153, the main difference was in the middle of the turbine around the spool piece that housed the turbine nozzles. This was due to the spool piece being insulated during the FOCUS testing and not during the SunShot testing. Looking more closely at the thermal seal, the gradient difference can be seen between the two and also how it compares to an ideal linear thermal gradient across the rotor:

Table 25: Case Temperature Measurement Breakdown

Temperature Measurement	Axial Location [in]	Type of Measurement
Journal Bearing - Inlet Side	0.00	RTD – Pad
DGS Supply – Inlet Side	4.92	TC – T Type – Fluid in Supply Tubing
DGS Metal – Inlet Side	5.37	TC – T Type – Thermowell
Thermal Seal – Outboard	5.71	TC – K Type – Fluid
Thermal Seal – Midspan	7.39	TC – K Type - Thermowell
Thermal Seal - Inboard	8.96	TC – K Type - Thermowell
Balance Piston Flow	9.76	TC – K Type – Fluid in External Piping
Inlet Case	10.52	TC – K Type – External Metal
Inlet Flow	13.14	TC – K Type – Thermowell in Inlet Pipe
Spool Piece	19.21	TC – K Type – External Metal
Exit Flow	25.22	TC – K Type – Thermowell in Exit Pipe
Exit Case	28.31	TC – K Type – External Metal
DGS Metal – Exit Side	30.52	RTD - Thermowell

Temperature Measurement	Axial Location [in]	Type of Measurement
DGS Supply – Exit Side	30.98	TC – T Type – Fluid in Supply Tubing
Journal Bearing – Exit Side	35.89	RTD – Pad
Thrust Bearing – Inboard	39.38	RTD – Pad
Thrust Bearing - Outboard	40.26	RTD – Pad

Table 26: Thermocouple Ranges and Errors

Thermocouple Type	Temperature Range	Standard Limits of Error
K	-328°F to 2282°F	Greater of 2.2°C or 0.75%
T	-418°F to 662°F	Greater of 1.7°C or 0.50%
RTD – Class C	-50°C to 260°C	+/- (0.15 +0.002*t)

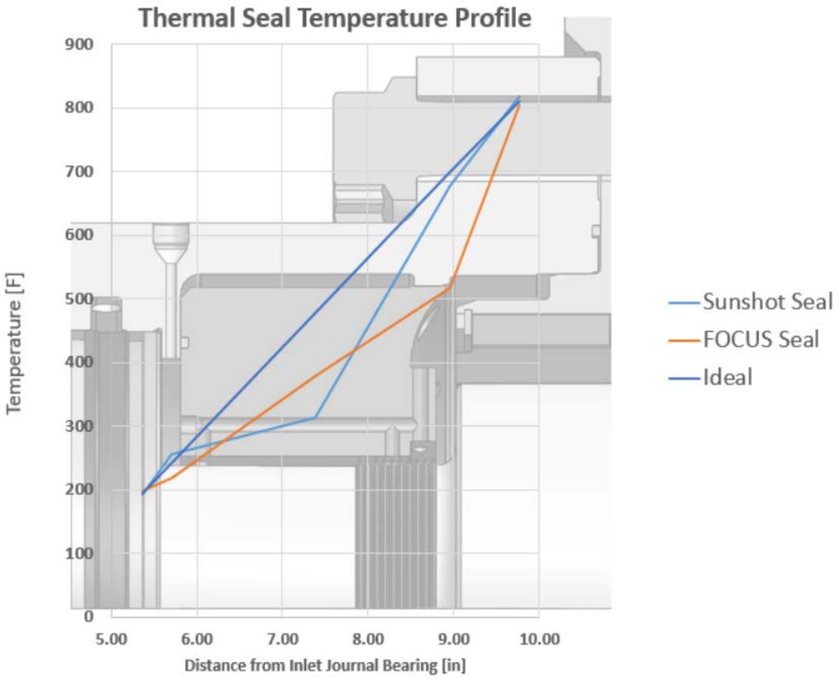

Figure 153: Thermal Seal Comparison

Neither seal achieves the perfect thermal gradient, but they both achieve a nice linear gradient over a section of the thermal seal. The SunShot seal sees a very small gradient between the outboard thermal seal measurement and the midspan measurement, and then it achieves a linear gradient from midspan to balance piston mixed flow. The FOCUS seal achieves a slower linear gradient across the seal and then a sharper gradient between the inboard end of the seal and the mixed balance piston flow. Ideally, the flow at the inboard end of the seal would want to be closer to the balance piston mixed flow, since this would lower the peak stresses on the fillet of the balance piston.

- SunShot Seal
    - Positive: Less thermal gradient between inboard end of thermal seal and balance piston flow. This shows that it allowed for better mixing between the two flows near the balance piston
    - Negative: Not enough flow mixing on the outboard end of the seal leading to a sharper thermal gradient between midspan and inboard of the thermal seal
- FOCUS Seal
    - Positive: Linear thermal gradient across the thermal seal. This can also be seen in Figure 154 at the higher speeds and temperatures. This shows that the seal achieved good flow mixing across the seal with the multiple axial hole locations
    - Negative: Sharp thermal gradient between inboard end of the seal and the balance flow. This shows that not enough of the hot flow was mixing with the cool flow to warm the flow near the balance piston more.

While 1,320°F inlet temperature and 27,000 rpm were not achieved with the SunShot seal in the turbine, Figure 154 shows the performance of the FOCUS seal and these max conditions. There are similar linear gradients across the seal, but a sharp gradient between the seal and the balance piston flow. The hole size in the seal would need to increase to allow for more cold and hot flow mixing across the seal. Maintaining the various axial locations is important in keeping the linear gradient across the seal.

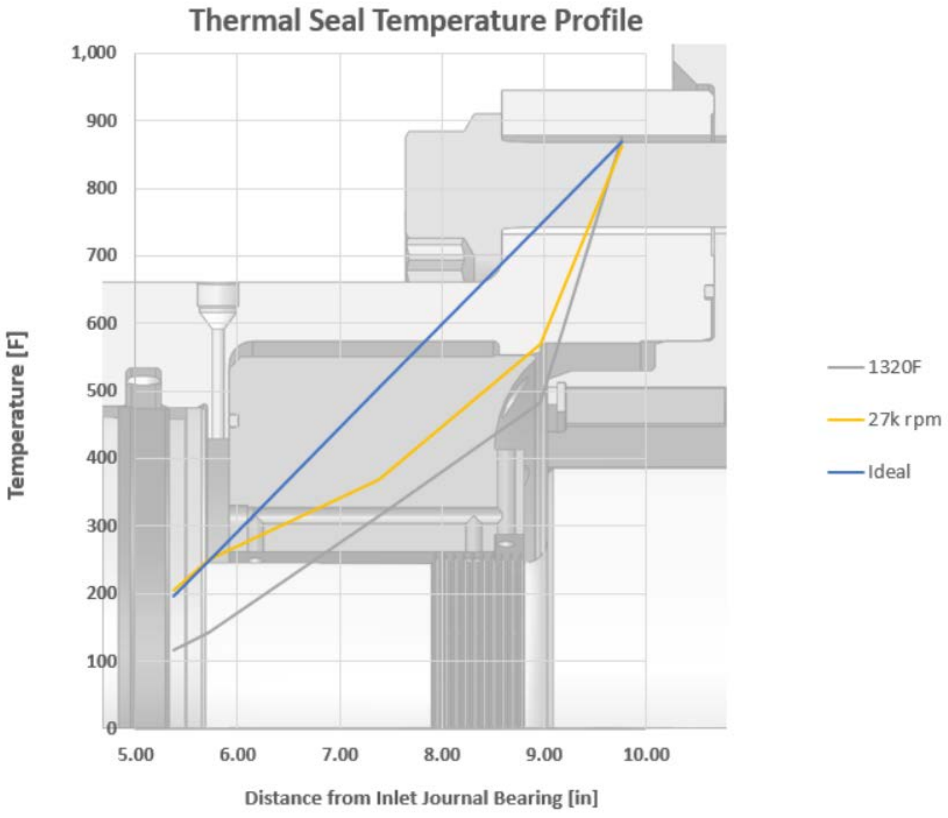

Figure 154: FOCUS Thermal Seal Performance at Full Temperature and at Full Speed

Balance Piston

Another key feature of this design, as mentioned in the detailed design and rotordynamics section, is the balance piston seal. A balance piston is required in a straight through machine to maintain thrust balance. The seal can be chosen based on how much damping is needed to satisfy rotordynamic design requirements. For this machine, a hole pattern seal was chosen which provides significantly more damping than a labyrinth seal. When comparing the two, a labyrinth seal will not only be easier to machine and manufacture, but it also can lead to lower leakage, since the clearances can be tighter with the use of abradable stators; however, tooth-on-rotor labyrinth seal designs are not typically used at these high pressures. With a hole pattern seal and these temperatures, it is preferred to maintain a larger gap to ensure there is no rubbing of the rotor and stator with both being high temperature nickel alloys. Because of this, a nominal gap at design of 0.010" was chosen.

This leakage is a direct loss to the performance of the turbine due to the leakage flow bypassing all of the rotor blades and being taken from stage 1 stator nozzle exit flow. Because of this, it is important to know how much mass flow is going across the balance piston seal and also how it compares to predictions that can be used for future designs. Just like the turbine performance, since this feature along with the bearings and dry gas seals are all important, it is important to know what kind of performance hit will be seen on the turbine.

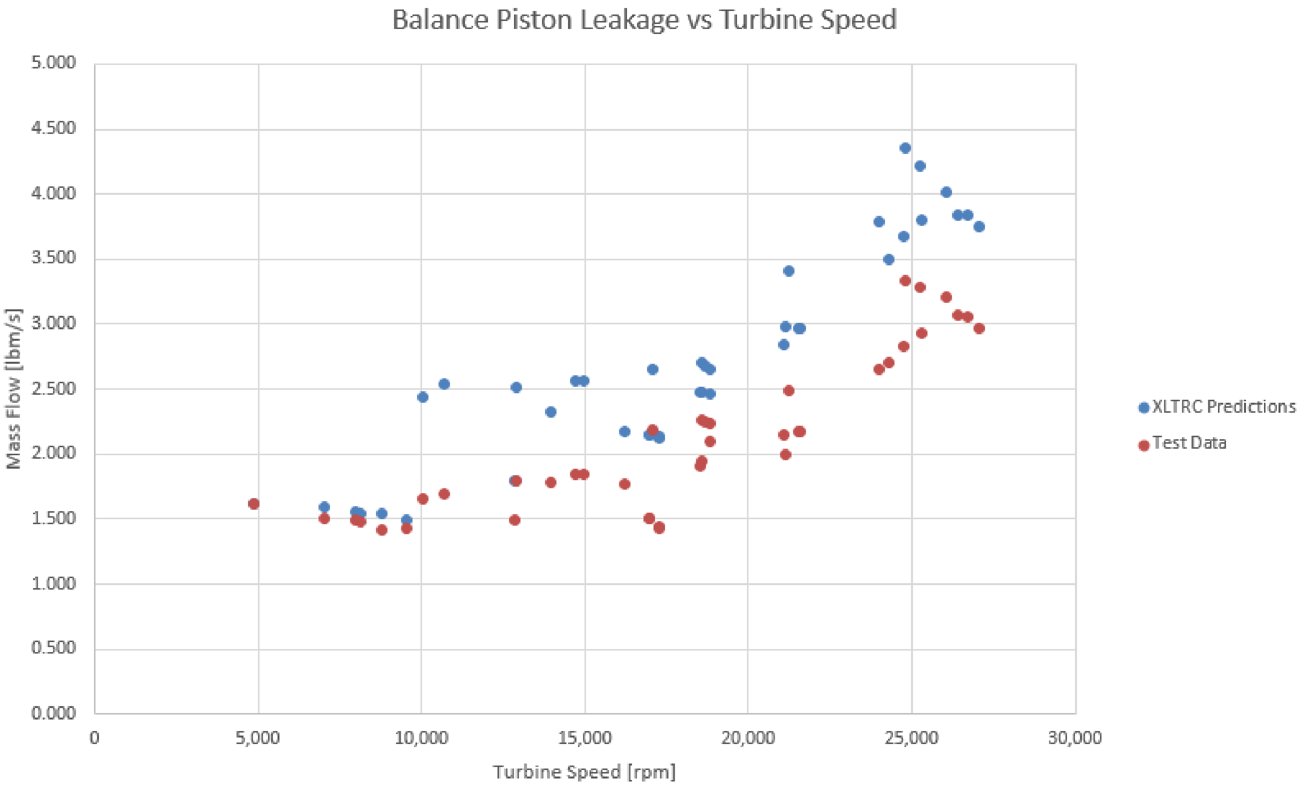

Figure 155: Balance Piston Leakage vs. Turbine Speed

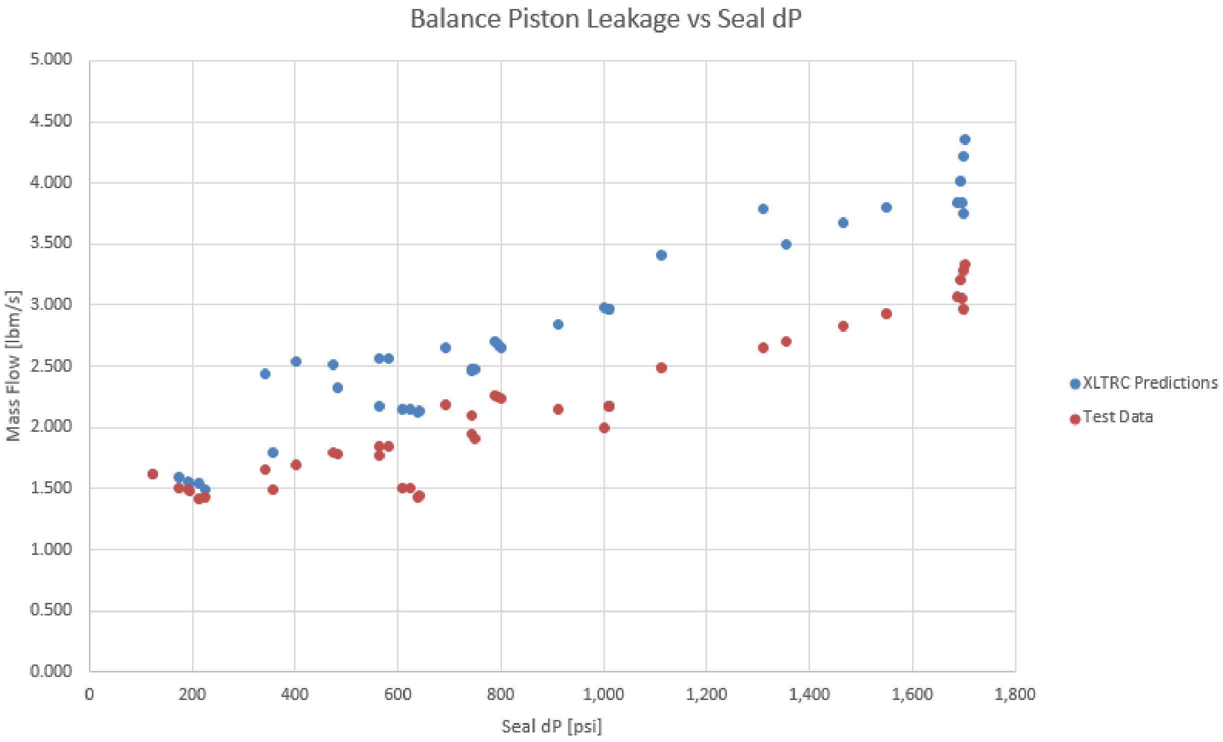

Figure 156: Balance Piston Leakage vs. Pressure Difference across Seal

What can be seen in the data is that at lower speeds and lower pressure differentials across the seal, the code and test data match very close. Above 10,000 rpm and 400 psi dP, the predictions are around 40% higher than test data. Based on previous experience, the predictions are usually within around 15% of test data, but these pressures and speeds are beyond experience with other machines and applications using CO_2. At higher speeds and pressures, a few things are happening that will affect the leakage across the seal. Without knowing the temperature of the balance piston or the balance piston seal, it is impossible to know the thermal growth between the two and how the clearance has changed. It is assumed to be equal in temperature for the prediction calculations. Higher speeds also lead to higher windage and friction which can lead to more heat being generated and either cause the rotor to close the gap or the seal to grow more increasing the gap. Speed also leads to centrifugal growth of the rotor which is accounted for in these calculations.

In terms of pressure differential, this affects the taper of the seal and the clearance at the smallest gap on the exit side. A taper was machined into the seal to account for this. This does provide some error in the calculation and it will need to be investigated further to find out other sources of error between the actual machine and the predictions to see if they can match closer than 30%. But the overall predictions are reasonable and on the conservative side.

Transient Performance

When operating a new loop, understanding how the loop performs during start ups and shut downs is critical in determining design conditions and safe operation, especially during rapid and emergency shut down or fast start ups. With sCO_2, there are large changes in density throughout all of the operating conditions in the loop. This can lead to sudden changes in temperature and pressure that will need to be accounted for when designing the fatigue life of various components.

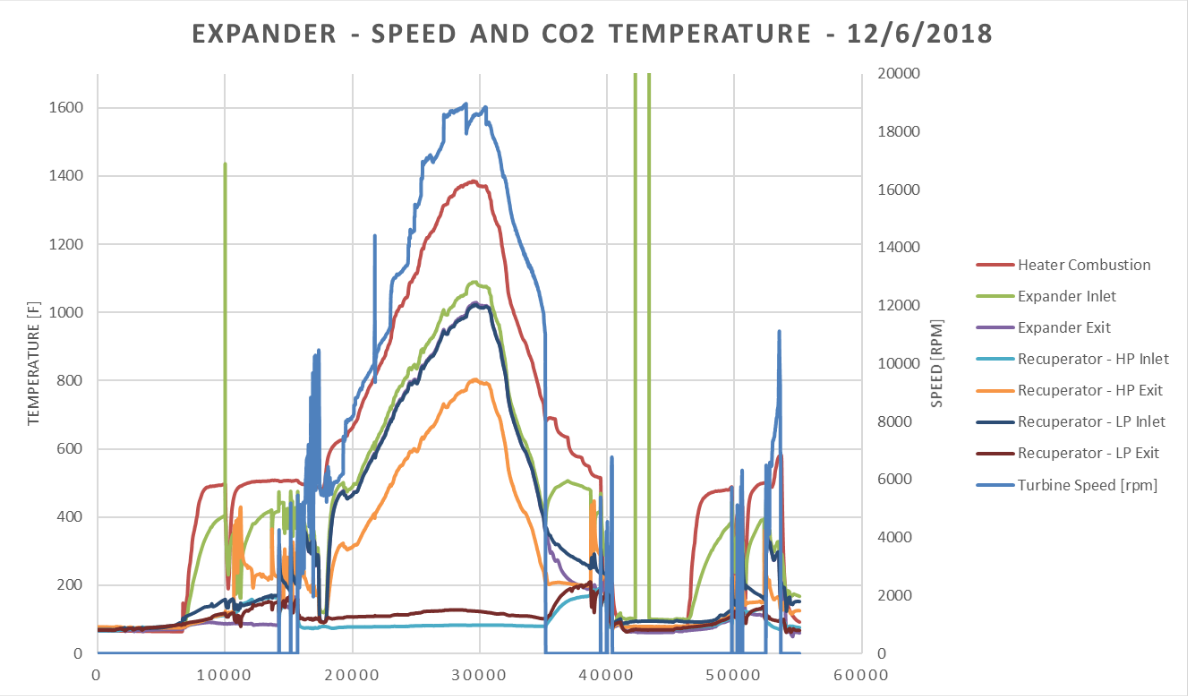

Figure 157: Loop Temperatures - Normal Start Up and Shut Down

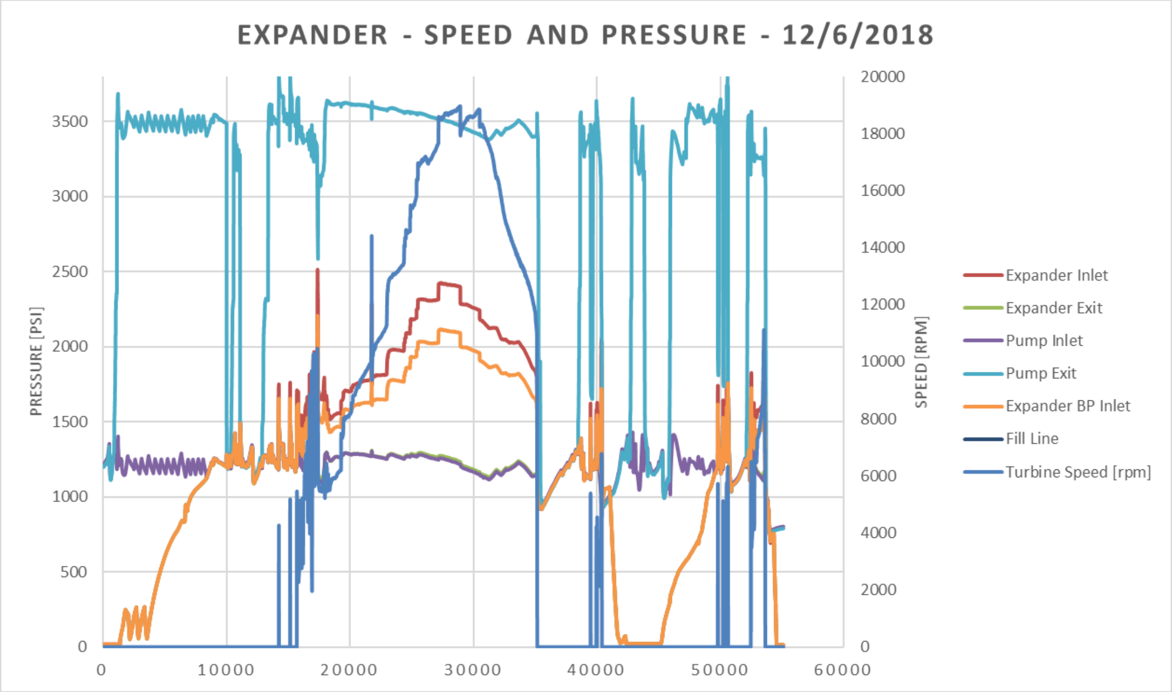

Figure 158: Loop Pressures - Normal Start Up and Shut Down

With a controlled start up and shut down, the procedure is very similar, just performed in reverse. The hot section of the loop is warmed up with low mass flow as everything is heat soaked. Once everything is up to desired temperature, the mass flow is increased along with heater combustion temperature to increase speed while maintaining the same temperature. For a shut down, the heater combustion temperature is reduced as mass flow is reduced to slow down the turbine, and then the heater combustion temperature is slowly reduced to allow for everything to be cooled down at a steady and controlled rate. This reduces thermal transient stresses on all of the components. Based on this experience, it shows that a controlled start up and shut down can be performed; however, it was emergency trips and shut downs that were observed the most.

Many of the emergency shut down transients were seen during a heater trip. A heater trip leads to an emergency shut down of the system. This is due to the heater having to run through a purge cycle, the loop quickly coming to a settle out pressure that was lower than operating, and heat loss in the system. The following transient plots show what happens when a heater trips:

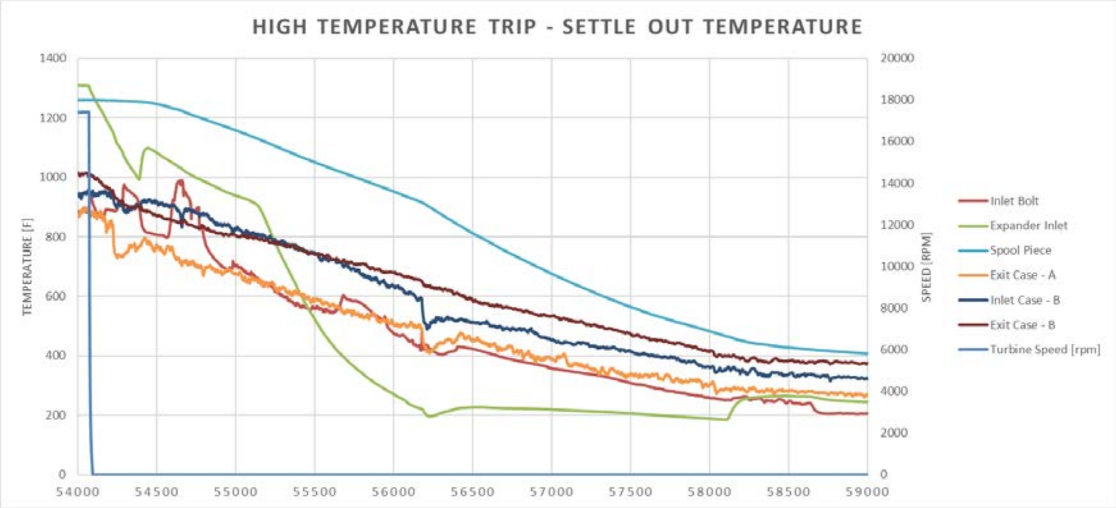

Figure 159: Loop Settle out Temperature - High Temperature Trip

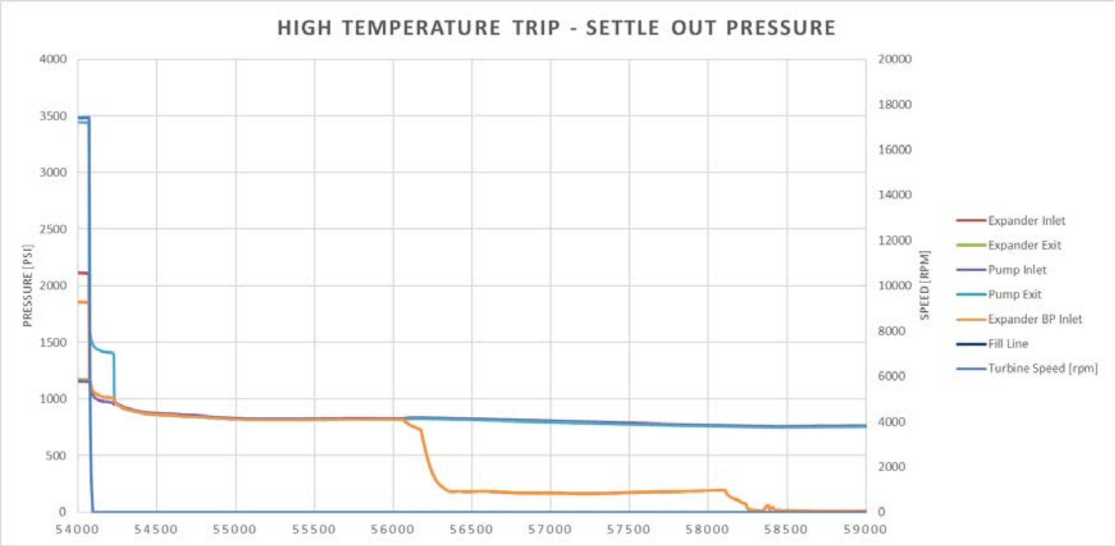

Figure 160: Loop Settle out Pressure - High Temperature Trip

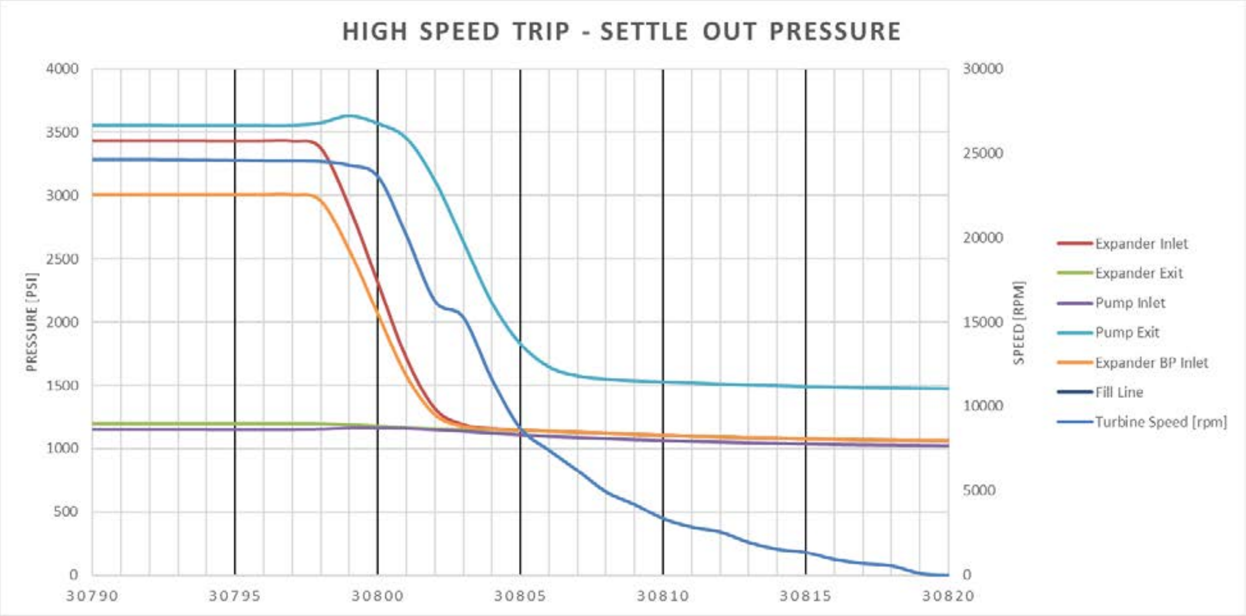

Figure 161: Loop Settle out Pressure - High Pressure Trip

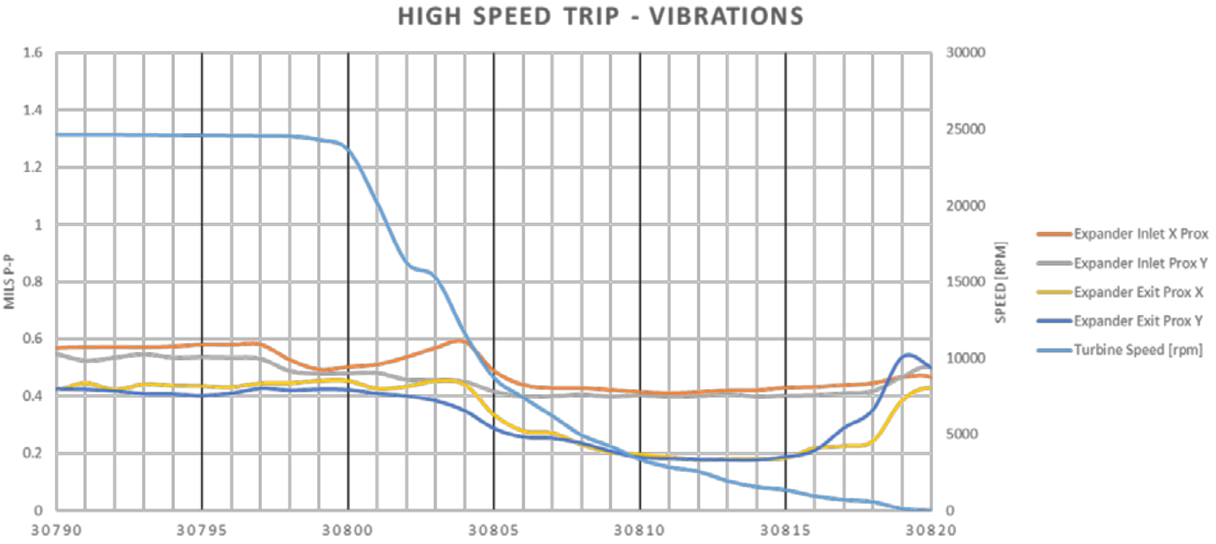

Figure 162: Rotor Vibrations - High Pressure Trip

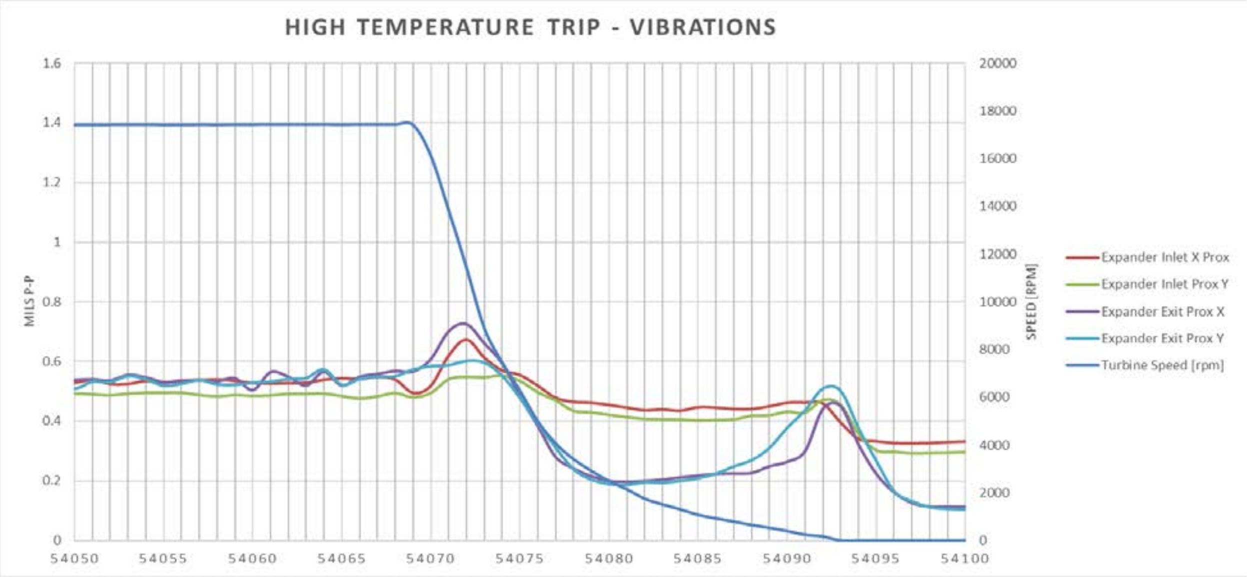

Figure 163: Rotor Vibrations - High Temperature Trip

The heater trips that were experienced were caused by two things, low air supply to the heater and low gas supply. A heater trip would lead to two immediate signals, closing of the turbine throttle valve and opening of the pump recycle valve. The turbine throttle valve is immediately closed to prevent cold flow running through the hot section of the loop, and the recycle valve is opened so that the pump cannot dead head. These trips would lead to full shutdowns of the system due to not being able to recover when at elevated temperatures. This is due to the heater going through a purge cycle and the pump loop having to be brought up to pressure due to mass that was vented out as the heater temperature was increased.

It is important to note three things that occur after a trip:

- Loop pressure settles out in around 6 seconds. For the case of this loop, the settle out pressure from a max temperature trip is around 950 psi which is at the minimum suction pressure of the pump at high speeds
- The turbine rotor will coast down in around 20 seconds
- CO_2 temperatures settle out in around 30 – 40 minutes
    - Seen in the expander inlet temperature which is a thermowell in the flow
- Metal temperature reach near room temperature in around 60 minutes
    - This only applies to the case that is not insulated
    - There were no metal temperatures of insulated pipe or the recuperator
- Rotor vibrations only increase slightly during a trip

One of the concerns when designing the loop was the settle out pressure. This was predicted to be around 1,650 psi and was used as the design pressure of the low pressure side of the loop and also the dry gas seals in the turbine. With a nominal pressure of 1,200 psi, this does not affect the design significantly and it is good to have some design margin. This can especially be seen as the pump is turned on and when heat is added to the loop. As the pump starts spinning, flow begins to circulate through the pump chiller, and there is a sudden drop in suction pressure. This is why it is good to start the pump with around 1,300-1,350 psi, so that suction pressure stays above 1,100 psi. This is mainly an issue on warmer days, when the pump suction needs to drop to 50-55°F to be at design conditions. As temperature drops, suction pressure also drops, and more mass is needed in the loop to get suction pressure back to 1,200 psi or higher. When the flow starts to run through the heater and the temperature in the loop increases, suction pressure will also increase quickly. This is due to all the warm flow between recuperator inlet and outside loop cooler warming up. In order to maintain suction pressure, mass is vented every so often as everything warms up. Before venting, pressures could spike up to 1,400+ psi quickly.

Settle out pressure becomes a concern if the low side pressure has to be doubled in order to accommodate for it. This leads to much thicker walls and stiffer pipes which can lead to longer runs. It is important to accurately calculate settle out pressure and not be too aggressive or too conservative being that is will have a negative impact in both directions.

Rotor Performance

For rotor performance, rotordynamics were the main concern since the operating speed and fluid density were at the edge of GE and SwRI's experience. To provide enough damping, integral squeeze film diaphragms were manufactured in the bearing, hole pattern seals with swirl brakes, and labyrinth seals with swirl brakes were implanted to reduced peak vibrations, even when running through modes. At 27,000 rpm, the rotor was operating between the 3rd and 4th mode. The 4th mode, the 2nd bending mode, is the one of highest concern. The design was FOCUSed on ensuring that mode was at least 20% above max continuous speed of 28,350 rpm.

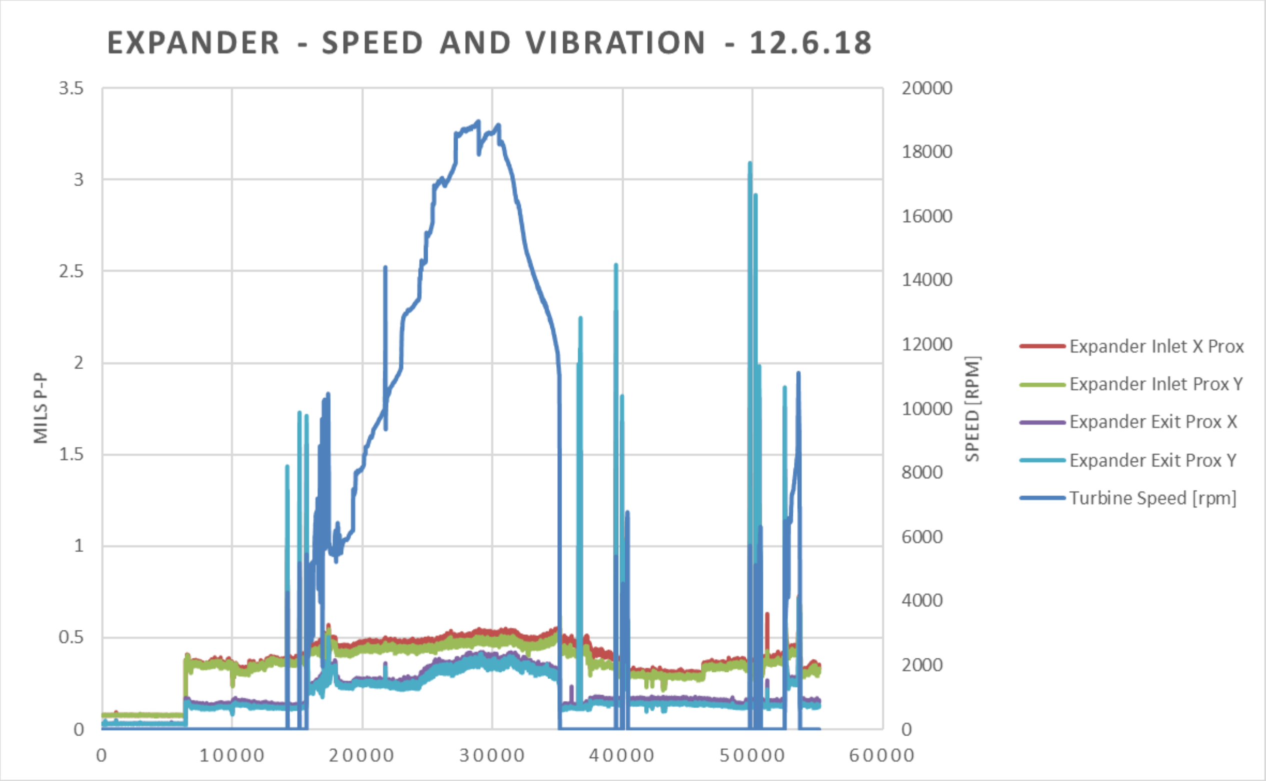

Figure 164: Speed and Vibration Plot - 12.6.18

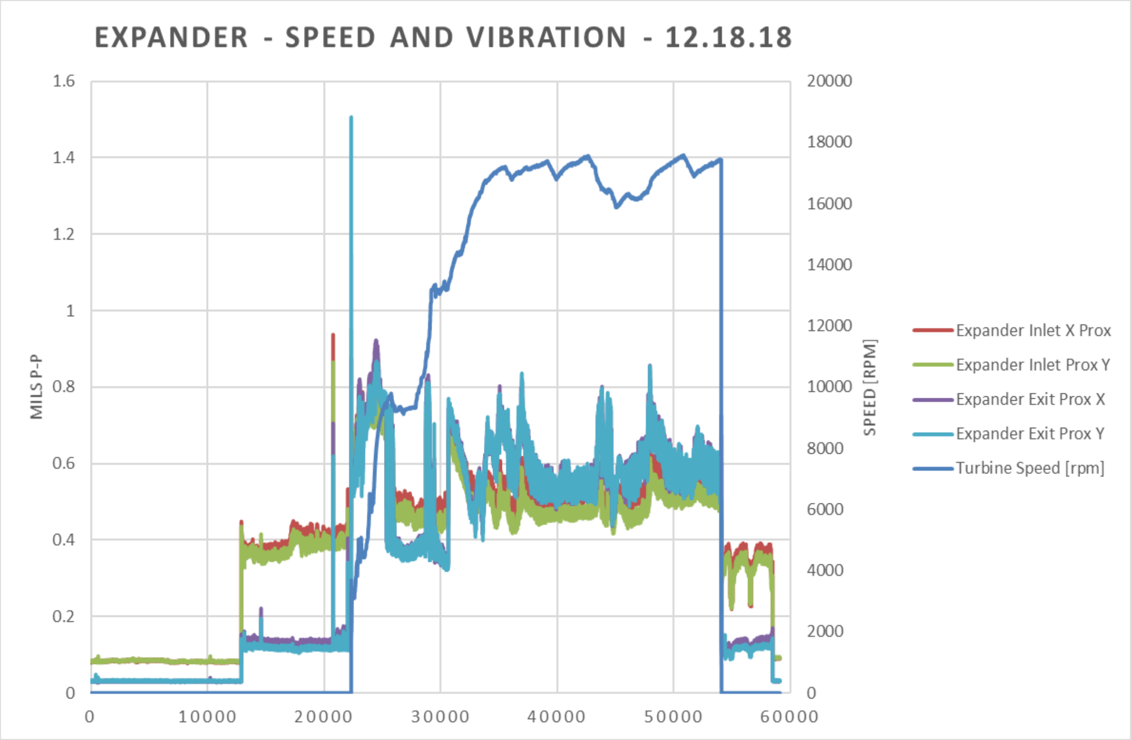

Figure 165: Speed and Vibration Plot - 12.18.18 (Max Temperature Test)

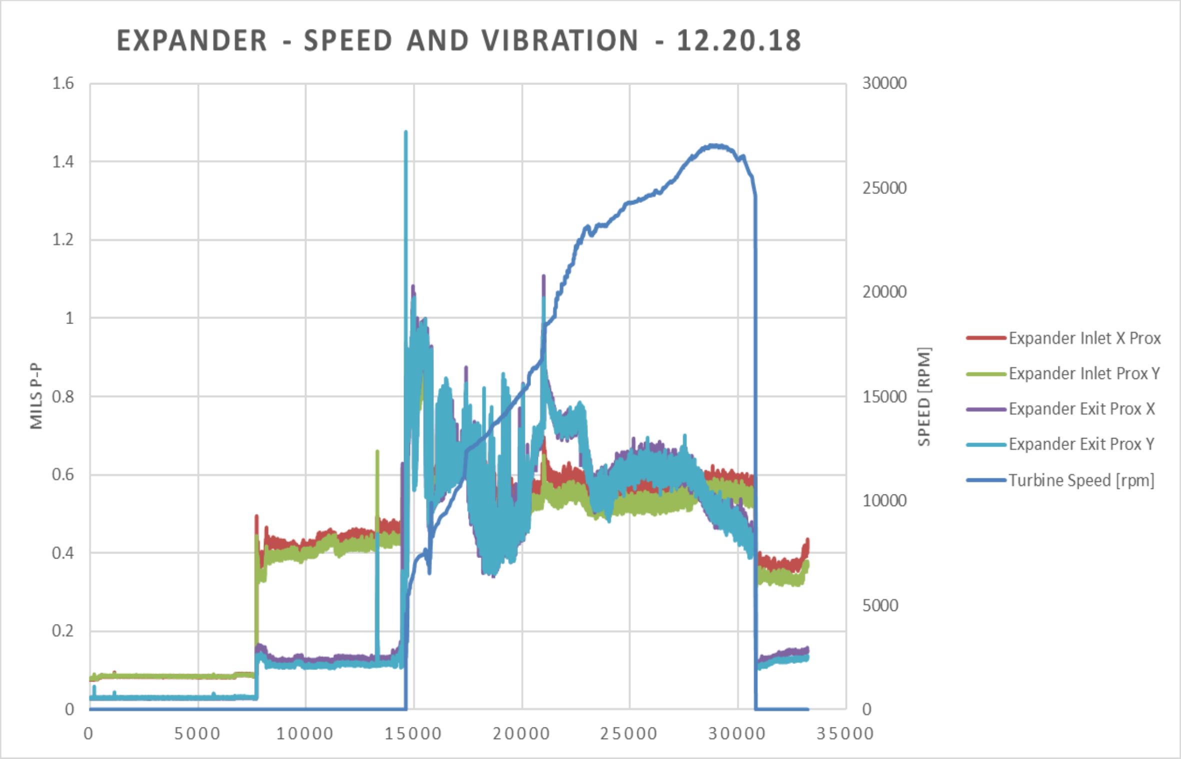

Figure 166: Speed and Vibration Plot - 12.20.18 (Max Speed Test)

From the three days of testing shown after the turbine was rebuilt, it can be seen that most of the vibrations throughout the testing were hovering at less than 0.5 mils p-p. There was a slight increase in vibration on the exit bearing between December 6, 2018 and December 18, 2018. This was due to the bearing diameter being increased by 0.001" to reduce operating temperatures which will be discussed further in the bearing performance section.

The highest peaks were during turbine start ups. This was due to a thermal bow in the rotor while the loop was being warmed up. To keep the case warm, the heater was turned on to help provide a convective heating loop. However, this resulted in the rotor being hotter on one side leading to a thermal bow. In order to get rid of this bow, the turbine had to be broken free and slow rolled (<5,000 rpm) to keep vibrations low while also making sure that the rotor remained spinning. On 12.6.2018, this process was practiced and was better implanted on the last two days of testing. At around 10,000 and 18,000 rpm, other modes were seen, but the peak vibration still stayed below 1 mil p-p. Overall, the rotor performance while speeding up, was far below limits and operated at low vibrations at the maximum operating conditions (Figure 167) as well as during a trip (Figure 168).

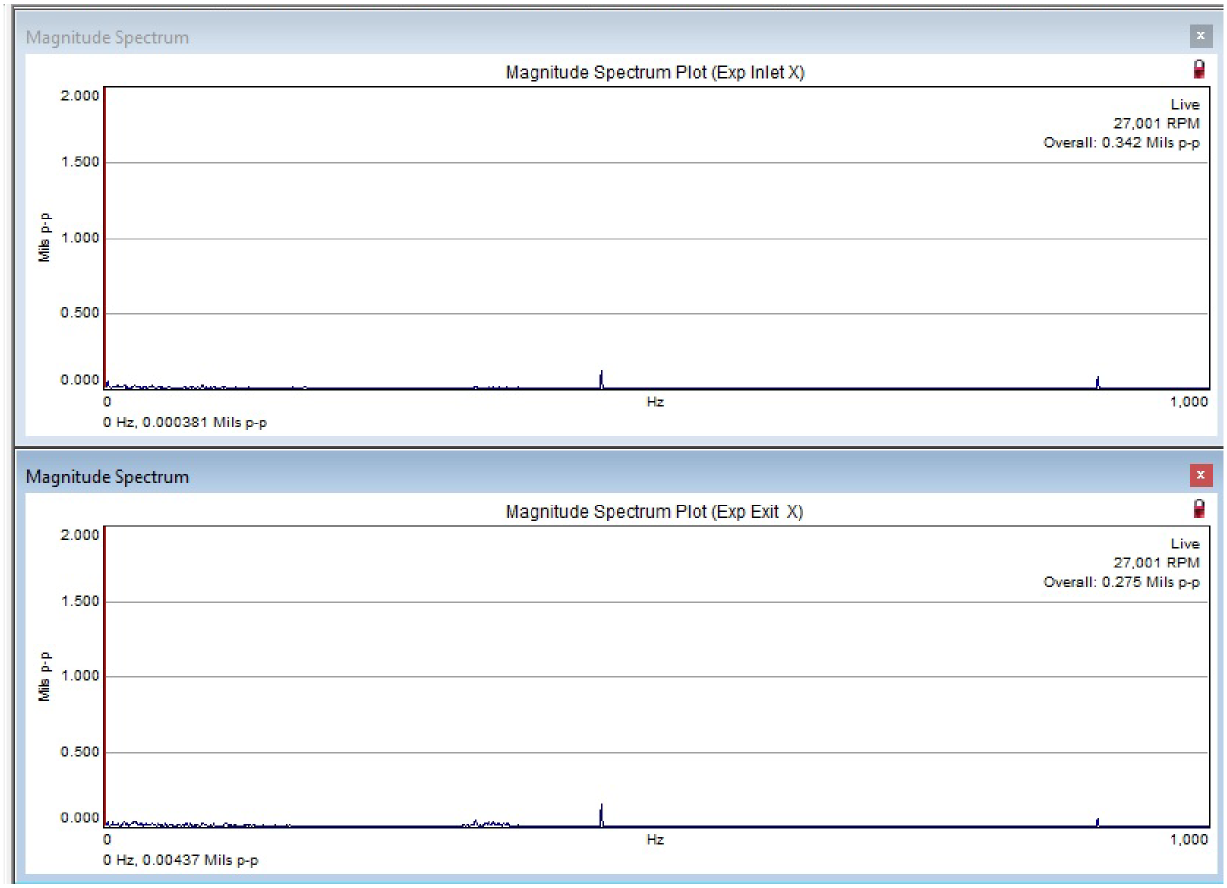

Figure 167: Bearing Spectrum Plot - 27,000 rpm

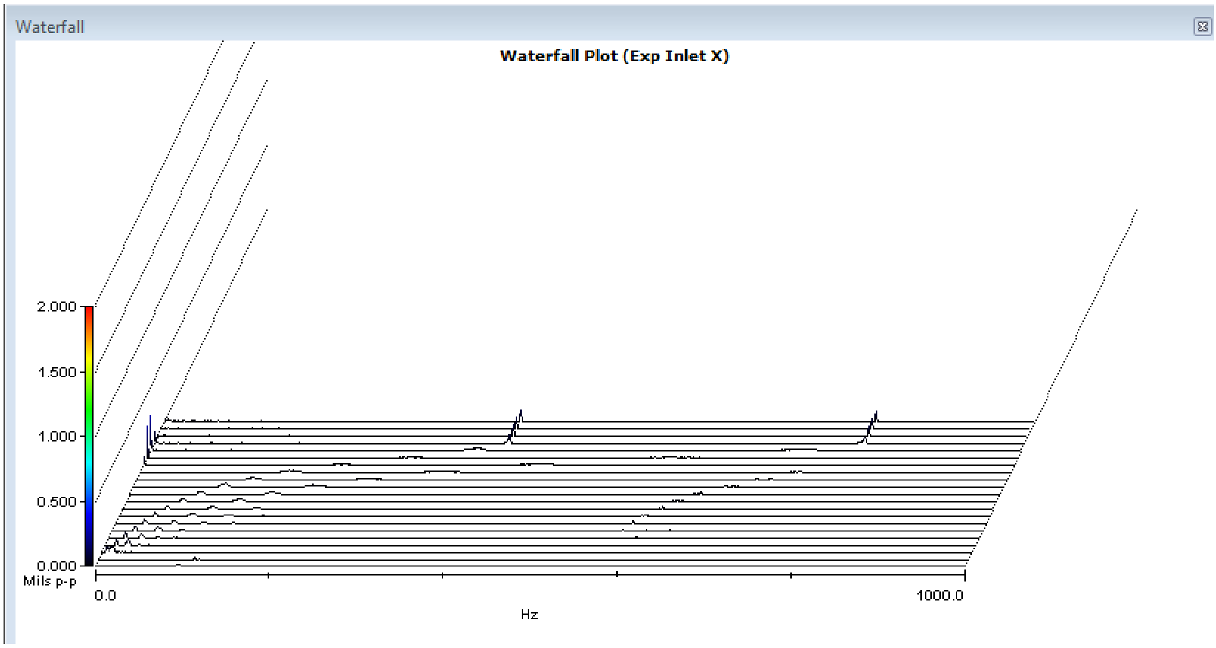

Figure 168: Waterfall Plot - Trip at 24,500 rpm

Dry Gas Seal (DGS) Performance

During the first few months of testing, one of the biggest issues was in dealing with DGS on the pump and also on the turbine. The pump seals are manufactured by EagleBurgmann and use a diamond face coating technology on their axial sealing faces. The turbine seals are manufactured by John Crane and use a carbon ring mated to a silicon carbide primary ring. One of the key issues mentioned previously, is that dry ice can form in CO_2 when there are large pressure drops to atmosphere, which occur across these axial faces. It is not fully understood what can happen, but dry ice can cause the seals to ratchet open which leads to venting the loop, or it can clog up vents that will also lead to venting.

One of the solutions for both of these seals, and it was mentioned previously, is to supply the seals with warm CO_2 flow, especially when they are not spinning. Spinning will help generate heat and will also prevent CO_2 from forming between the seal faces. At this point, all of the seal failures had occurred during low temperature operation, and catastrophic failures were prevented. The pump seals would eventually reseat themselves and then work well. One of the turbine seals initially had an internal static seal failure, which required it to be removed from the turbine and returned to the manufacturer for repair.

During high speed and high temperature operation on the March 20, 2018 test, there was a seal failure at 24,500 rpm, 3,200 psi, and 1,050°F turbine inlet. As speed was increased, temperatures near the DGS would also increase, and more supply flow was required to keep the cavity cool. At this point, an alarm went off in the control system that temperatures near the DGS had increased above the alarm point. By the time it was caught, the seal temperatures had increased by 400-500°F in a matter of seconds, and the loop began venting through the seals, signifying a failed seal.

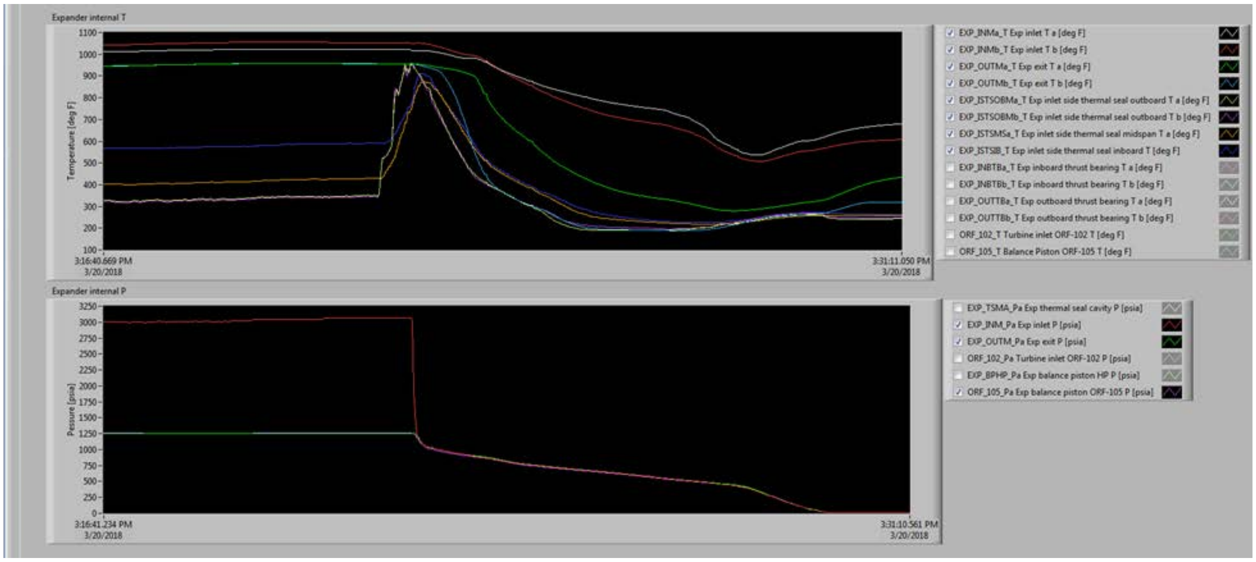

Figure 169: Dry Gas Seal Temperature Increase

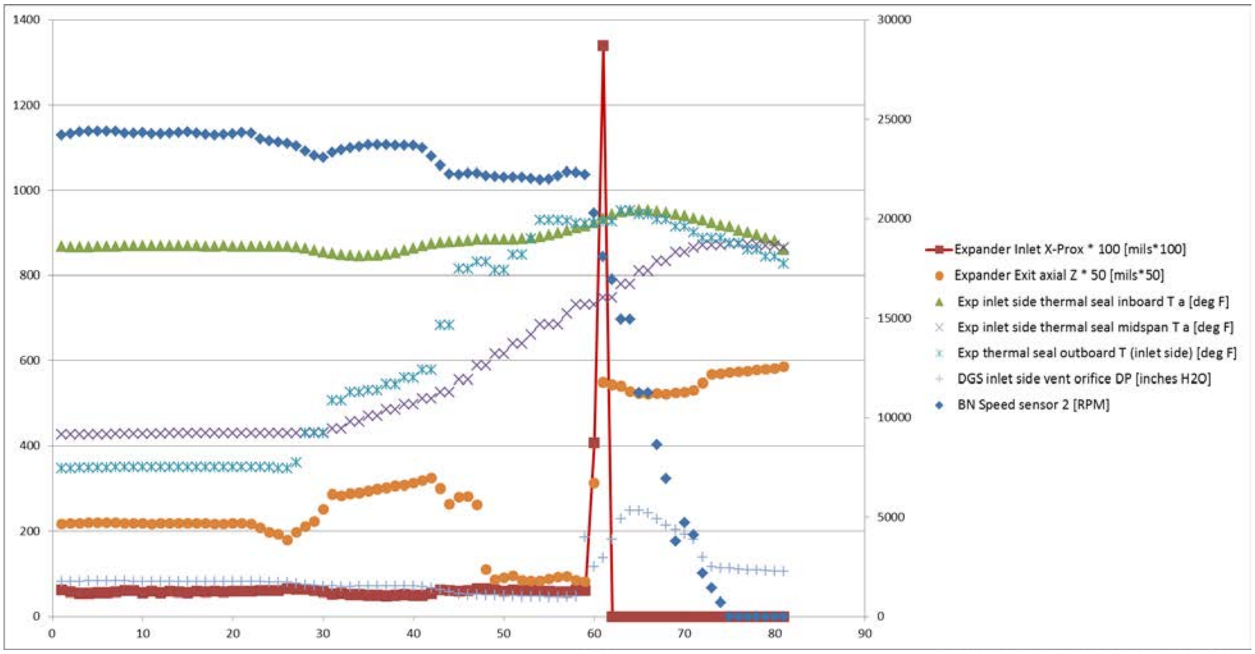

Figure 170: Temperature Plots during DGS Failure (x-Axis is Time (sec))

The sudden rise in temperature indicates that buffer supply flow was lost, which meant the flow was now going through the seal cartridge and not through the labyrinth seals into the process flow. When the seal failed, the silicon carbide primary seal ring broke apart, creating a large unbalance in the turbine and tripping the entire system. Figure 171 shows the large synchronous vibration right as the seal failed:

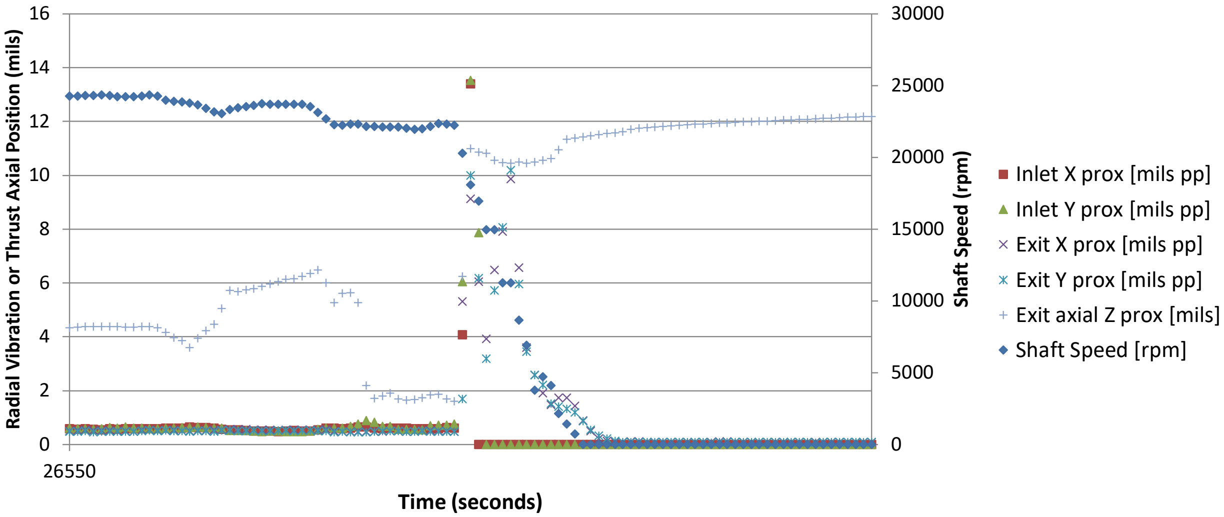

Figure 171: Vibration Data during DGS Failure (x-Axis is Time (sec))

After a failure of this magnitude, an entire tear down was required for the turbine. This would be necessary to see what damage occurred during the failure. The main components of concern were both DGSs, the rotor, and all the bearings. All components would be inspected during tear down.

The DGS failure occurred on the inlet side of the turbine (Step 1 for disassembly). Previous DGS failure occurred on the exit side (Step 2 for disassembly). During that repair, the DGS was able to be removed while it was on the stand which prevented the need for disconnecting all the connections to the turbine.

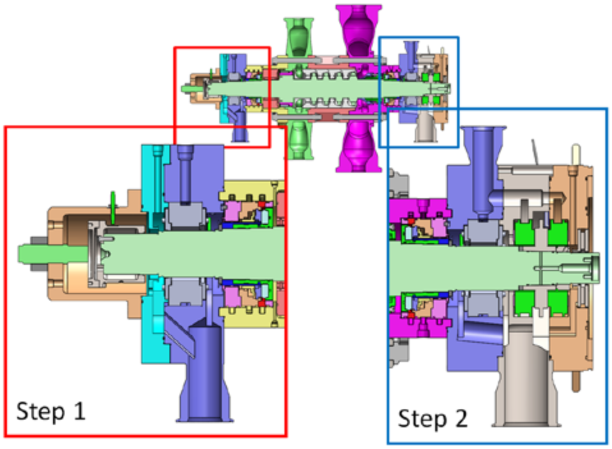

Figure 172: Teardown Order of Turbine

Step 1 of the tear down involves removing all the proximity probes and end cap first. This exposes the dummy coupling that is used from key phasors and relative thermal growth measurements.

Figure 173: End Cap and Dummy Coupling Removal

The main thing to notice in these images is some of the debris in the middle right image and also on the back face of the dummy coupling on the bottom left image. This cavity should be filled with clean lubricating oil and buffer air. This indicates there was something that came through the oil flow and went out into this area.

Figure 174: Bearing Housing and Bearing Removal

Seen here are lots of debris and signs of damage from hot flow through the bearing cavity. Plastic connectors are disintegrated, and the Resistance Temperature Detector (RTD) casings are burnt. There is damage to the shaft from a rub with the end seal of the bearing along with the Babbitt of the bearing being completely worn away. This means the shaft would have to be machined and coated to get the proper diameter for the bearing. The bearing were also inspected and eventually replaced.

Figure 175: Inlet Side DGS Removal

The most significant items to note on these images are the failed Si-C ring shown on the middle right image and the rubbed away labyrinth seal on the middle left image. The other images show signs of debris and damage from the hot flow. The top left image shows that no flow paths were opened inboard of the seal to indicate that the flow went through the cartridge, not around. From this, it appears there was a labyrinth seal rub. With this rub, heat would have been generated that would slow down the turbine and also cause the seal to grow radially due to the generated heat causing a run-away condition. The heat due to the laby rub would conduct through the sleeve closing the internal clearance between the seal ring and sleeve. The Si-C ring underwent a brittle fracture, leading to hot flow through the seal and consequential bearing damage. The entire seal and bearing would need to be replaced.

Figure 176: Exit Side Bearing and DGS Removal

It was determined that the failure was caused by a tight labyrinth seal clearance at the buffer seal for the DGS to process flow. To correct this, the labyrinth seals were opened up by 0.010” on the diameter to allow for a nominal operating gap of 0.005→0.006”. In addition, cooling flow was increased to maintain temperatures of less than 250°F, so that any increase in temperature would be seen and could be controlled before it ramped up too quickly.

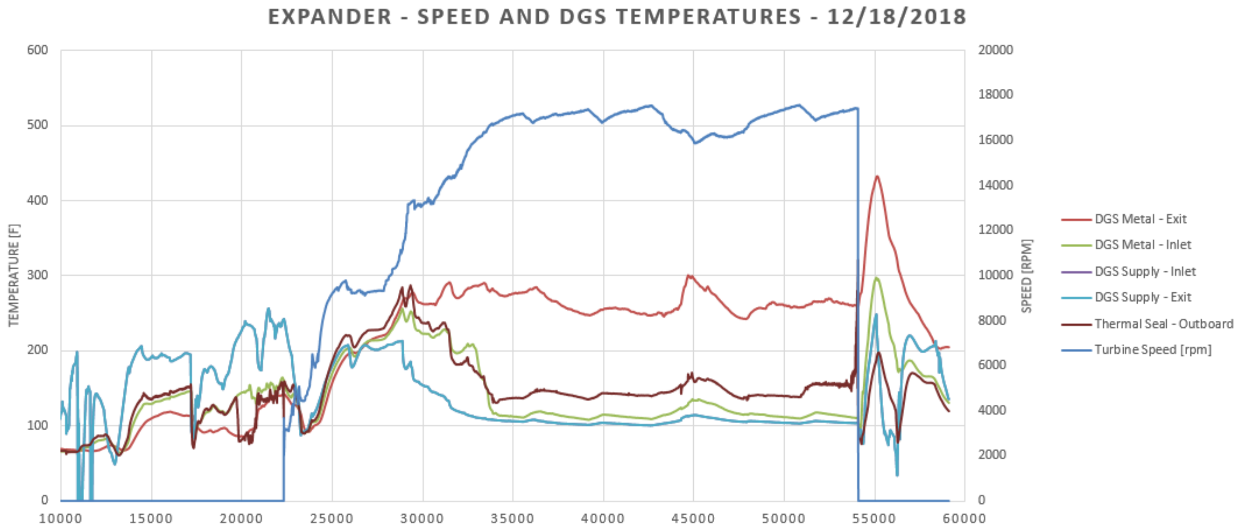

Figure 177: DGS Temperatures - 12.18.18 (Max Temperature Test) (x-Axis is Time (sec))

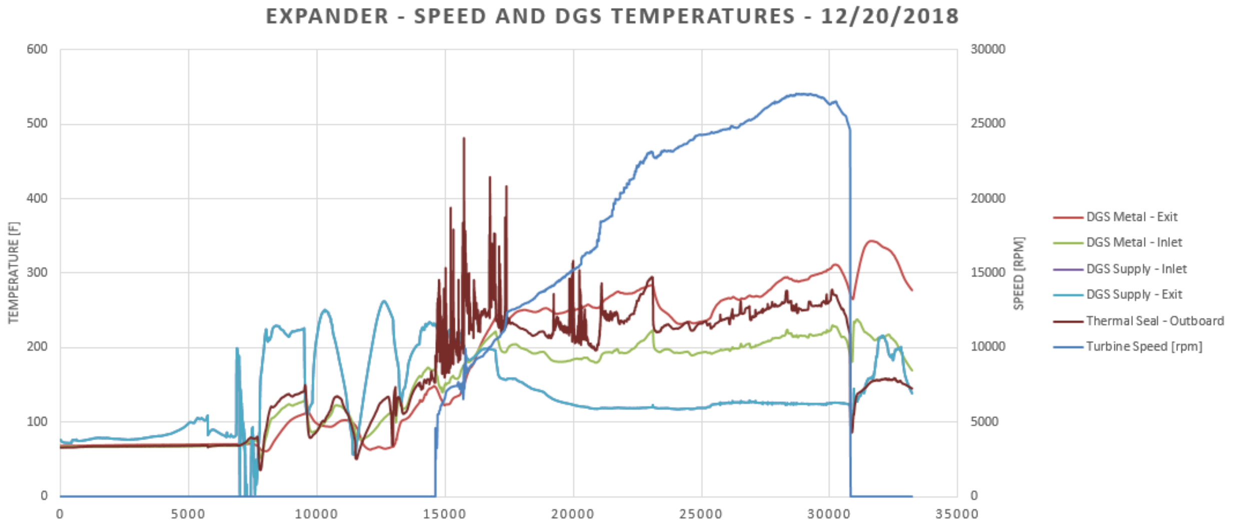

Figure 178: DGS Temperatures - 12.20.18 (Max Speed Test) (x-Axis is Time (sec))

During the testing after the seal repair, the seals performed as desired. Temperatures were kept at around 250°F as necessary, but did approach 300°F as speeds and temperatures increased. Increased flow rates led to cooler supply flows. In order to prevent dry ice formation, the supply temperature was kept above 100°F, taking heating across the seal into account. Vents were monitored to ensure they were not cooling down compared to supply flow.

Bearing Performance

Outside of rotordynamic performance as already discussed, the bearing temperatures were monitored due to the high surface speeds that the pads would see. RTDs were installed and monitored on the journal bearing pads and the thrust bearing pads. The maximum desirable temperature was 225°F on both sets of bearing, but for thrust bearings it was important to look at the difference between the two to ensure that one was not running hotter than the other, indicating that thrust was not balanced. The test data consistently showed small differences between the inboard and outboard thrust bearing indicating good axial thrust balance for the turbine.

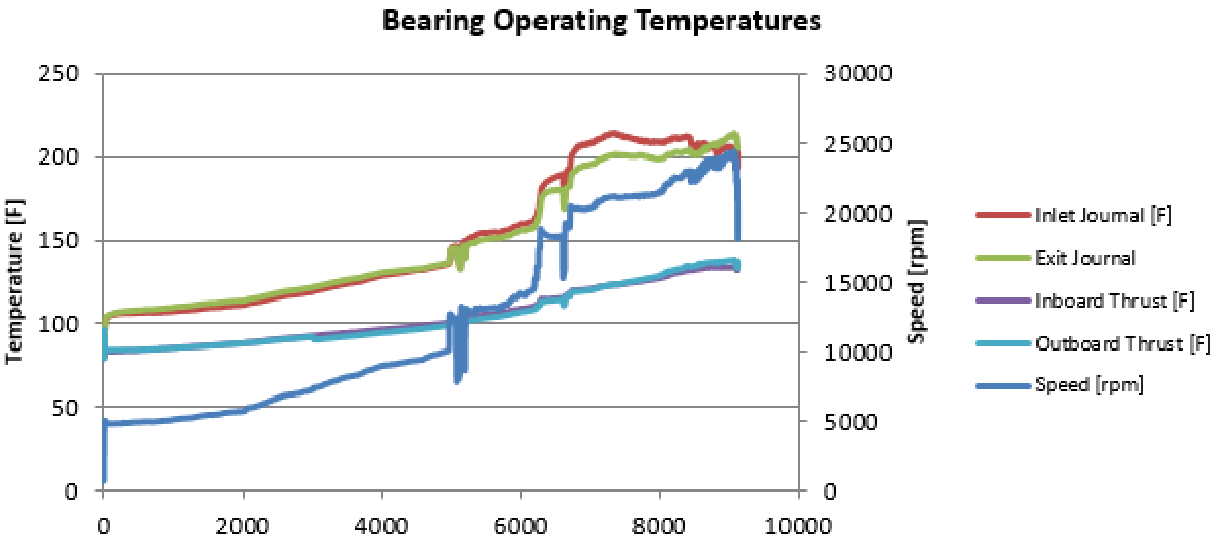

Figure 179: Bearing Temperatures - 3.20.18 (x-Axis is Time (sec))

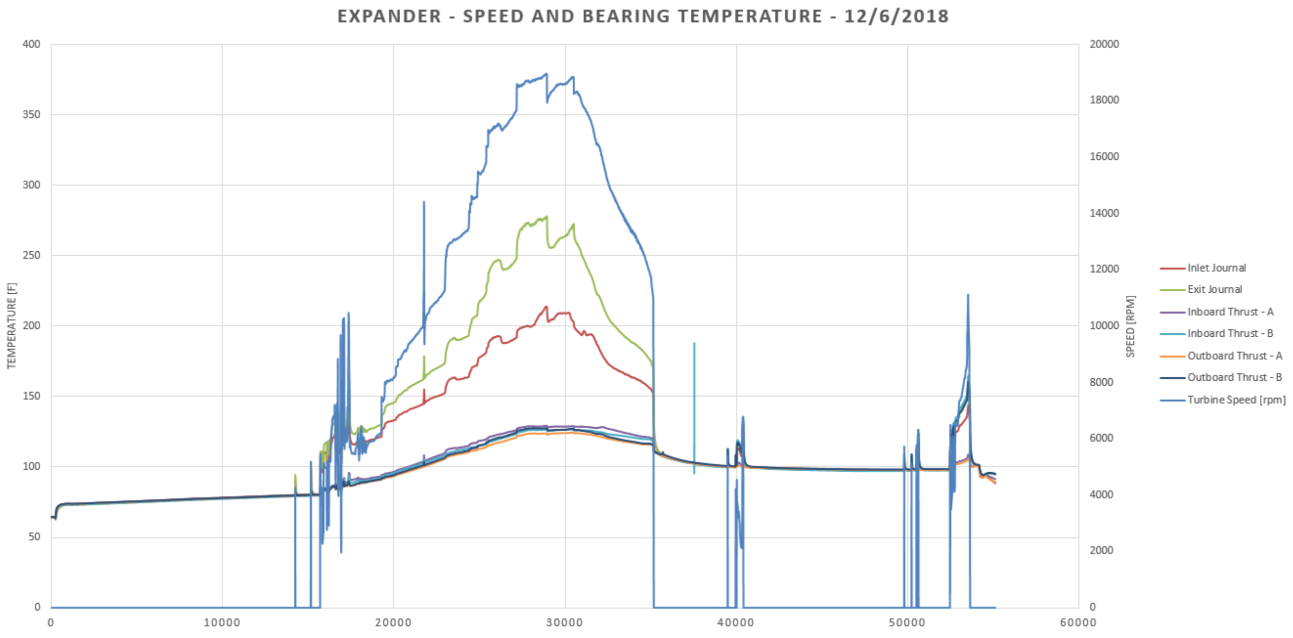

Figure 180: Bearing Temperatures - 12.6.18 (x-Axis is Time (sec))

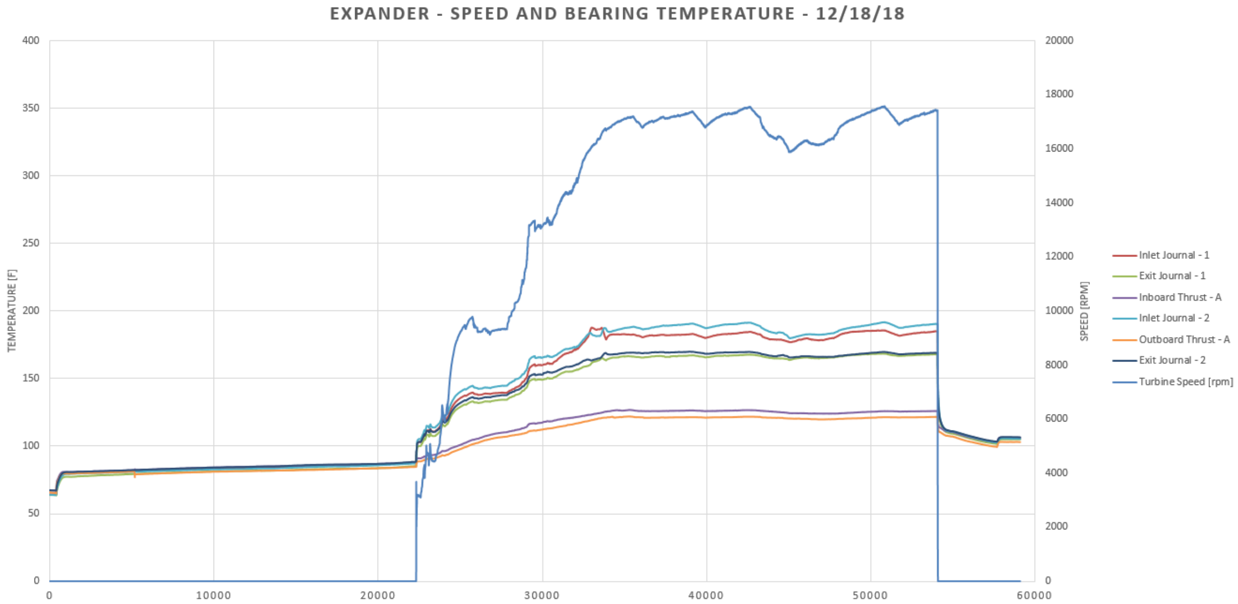

Figure 181: Bearing Temperatures - 12.18.18 (x-Axis is Time (sec))

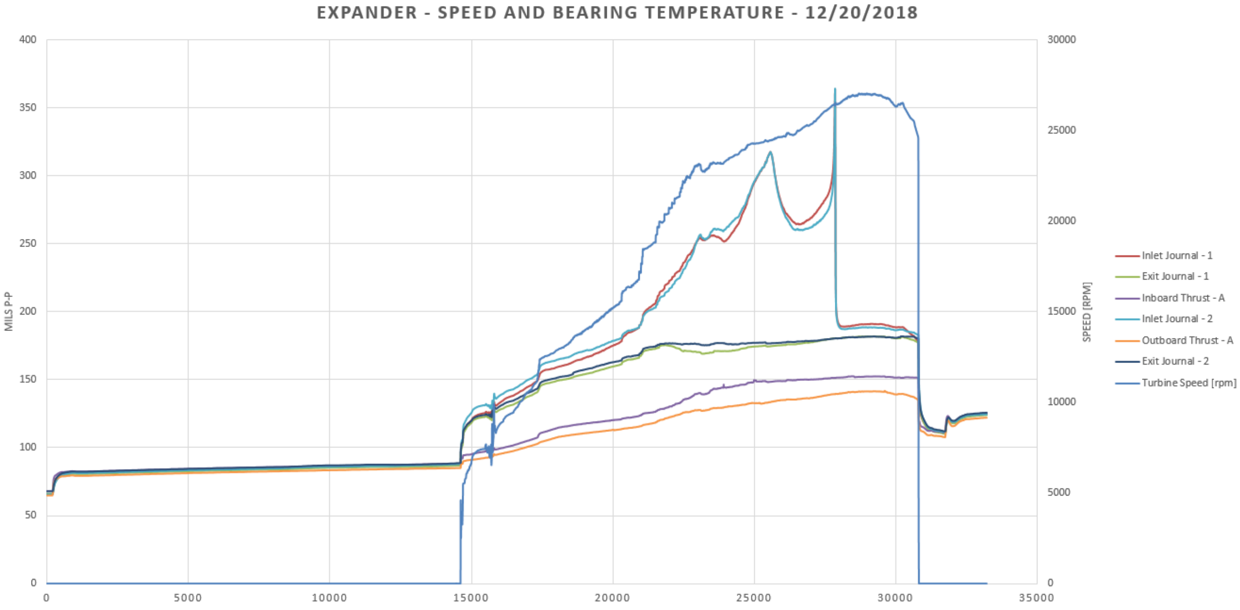

Figure 182: Bearing Temperature - 12.20.18 (x-Axis is Time (sec))

During 12.6.2018 testing, it was noticed that the exit journal bearing was reaching temperatures above 250°F. This was determined to be due to bearing clearances being tighter with the replacement bearings than previous testing. The March 20, 2018 data shows that temperatures were around 220°F at 24,000 rpm, but the new temperatures were at 250°F at 18,000 rpm. After reviewing inspection data, both the bearing and the shaft were at the max material condition, meaning the tightest operating clearance from tolerance. The inlet side was operating at 0.0005" larger clearance than the exit side. It was at this point that the turbine was brought down so that the bearing could be removed, and the clearance would be opened up prior to the next round of testing. Thrust bearing temperatures were low and equal, showing that thrust was balanced.

For testing on December 18, 2018, with the exit bearing opened up, the bearing temperatures on the exit journal reached a max of 190°F, at the equivalent speed, which was much lower than before. However, as speed was ramped up, the inlet journal bearing temperature was starting to increase rapidly with speed. During operation, the temperature initially peaked around 300°F, but then dropped. But as speed was further increased, it suddenly peaked to around 350°F, but dropped down to 190°F and stayed steady. This matched the pad temperature of the exit side, and no high vibrations were seen during the sudden temperature increase. The inlet side bearing will need to be inspected during shutdown, to see if there was any damage from high temperatures. Clearly, contact occurred between the journal and pad opening up the clearance

For the original bearings, the shaft diameter was sized at 2.9995/3.0000", and bearings were tolerance at 3.0040/3.0045". The corrected bearing diameter was increased to 3.0050/3.0055", while the shaft will remain the same. Future turbine builds like STEP will use these larger clearances.

Task 3.2. Thermo-Economic Cycle Analysis and Commercial Product Evaluation

Updated Commercialization Summary (2019)

The turbine package achieves 87% isentropic conversion efficiency and component selection was done within this project to design the overall power block meeting 46.2% thermal conversion efficiency. A roadmap to achieve +50% thermal conversion efficiency based on testing to be performed within this program is presented. Also, the impact other development program currently in progress and in development is presented in detail. The turbomachinery design completed in this phase of the project is a stepping stone towards achieving the Sunshot goals of 6 c/kWh. And to compete favorably with PV without the need of thermal energy storage. The heliostat cost must be reduced to $75/m2, the receiver must be reduced to $110/kWt, and the power block must cost $775/kWe installed at 50% efficiency. These targets are consistent with the Sunshot component program goals and the power block targets were shown to be achievable in the commercialization addendum.

Disclaimer

This commercialization addendum was produced under the Sunshot sCO_2 Turboexpander component development project (DE-EE0005804). It contains forward-looking projections about future cost and performance targets for advanced technology still under research and development. Projections are not intended to imply commitments by GE or its partners. Near-term uncertainties for component development programs in terms of efficiency predictions can typically be +/- 3%, without testing.

Installation Size

The fundamental design philosophy for this product is factory-built modules that are road-shippable and can be installed on top of a solar tower. This is made possible by the high power density of sCO_2 turbomachinery. The benefit of this design philosophy is that it can reduce site installation costs and EPC soft costs. Cost benefits for this approach are estimated from data for similar tower installations by GE Wind.

The constraints due to various packaging modalities are shown in Table 27. The lowest cost packaging system is ISO containers, but these have the most limiting width and weight constraints. The backup option is to transport custom skids via 13-axle trailers commonly used to transport Wind nacelles. US logistics cost for wind nacelles as a function of distance are shown in Figure 183. To be conservative, it is currently assumed that all modules use this cost curve. Further cost reductions are possible if ISO container packaging is possible. Preliminary packaging estimates for the various power block modules are shown in Table 27. It appears feasible for the turbomachinery module and the 2020 heat exchanger module (based on Thar technology) to be packaged and shipped via ISO containers. The generator package and the 2015 heat exchanger module, which may have to rely on existing heat exchanger technologies, will likely require permitted transport similar to Wind nacelles.

Table 27: Packaging Constraints & Estimates

Modality	**L (in)**	**W (in)**	**H (in)**	**Wt (lb)**
ISO 20'	240	96	114	63000
ISO 40'	480	96	114	67000
13-axle Wind Trailer	472	169	169	200000
2015 Product	**L (in)**	**W (in)**	**H (in)**	**Wt (lb)**
Turbomachine	240	96	114	29573
Generator	186	133	112	56416
Heat Exchanger	400	96	114	222364
2020 Product	**L (in)**	**W (in)**	**H (in)**	**Wt (lb)**
Turbomachine	240	96	114	27126
Generator	186	133	112	56416
Heat Exchanger	240	96	114	21994

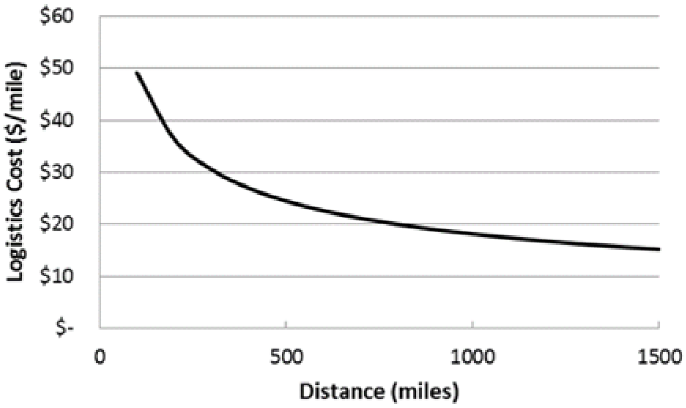

Figure 183: US Wind Nacelle Logistics Costs. 13-axle Trucks with 69 Ton Weight Limit

The impact of total project size (farm size) on the installation cost is shown in Figure 184. Due to fixed crane setup costs and labor mobilization costs, there is a high economic penalty for single-module projects. Economics improve significantly beyond at least four modules (40MWe net project output), with diminishing returns beyond 10 modules (100MWe net project). This study assumes 100MW project size.

The maximum module size is limited by the generator. The world's biggest portable crane, currently used attached to a ship to assemble off shore wind turbines is limited to the capacity of a 50MW generator. This then sets the maximum power block size at 50MW. The tower weight capacity can handle multiple power blocks as the pure weight load of a CSP tower is significantly less than the bending moments for a wind turbine that a wind tower must withstand. Therefore, the power blocks modules can range in size from 10-50MW. Care must be taken to make sure that only a few power block modules are designed. For example, a 10, 25, and 50MW; otherwise, the economies of scale for the structured design process is lost.

For a 100MW CSP plant, two 50MW power blocks would be appropriate for a 2x50MW configuration. For a 130MW CSP plant, one could use two 50MW power blocks and three 10MW power blocks.

For a land-based CSP power block, potentially used to accommodate land based thermal storage, there is no limit to the power block size; however, it could still remain economically feasible to stay within the tower mounted power block configuration in order to gain the advantages of economy of scale.

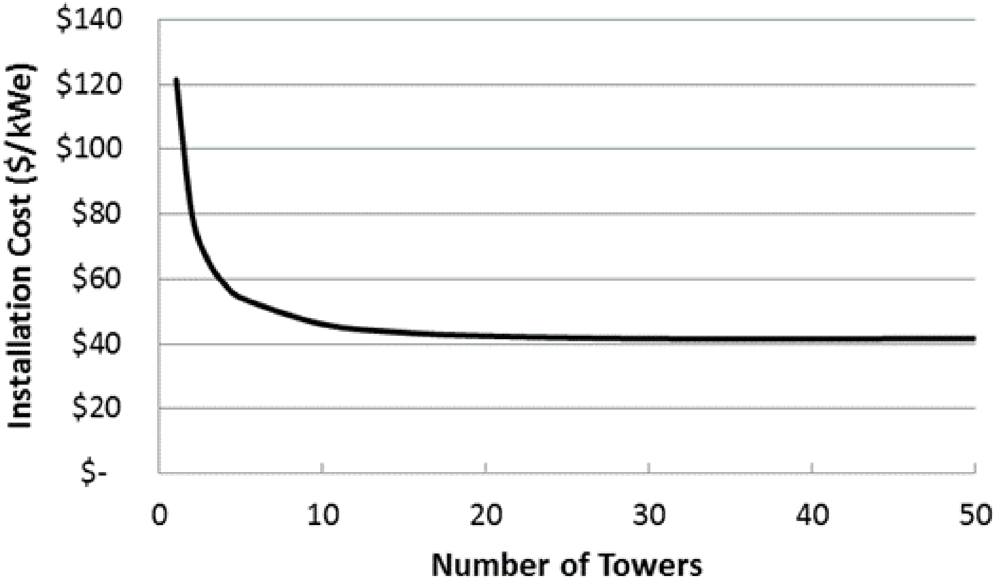

Figure 184: Estimated Power Block & Receiver Installation Costs. Includes Tower and Foundation

Capacity Factor

The impact of solar multiple on the capacity factor, capital cost, and LCOE is shown in Figure 185. Solar multiple is defined relative to a design DNI of 950 W/m2. The 2015 initial product is shown as a solid line and assumes component parameters given in Revision History

The 2020 product is shown as a dashed line. Capacity factor and LCOE continue to improve even with a solar multiple as high as 1.7, which is the nominal value selected for this analysis in 2020 to a value of 32%. A solar multiple of 1.4 has been chosen for the 2015 product in order to limit the initial capital cost for these early demonstration projects.

The impact of a hypothetical Thermal Energy Storage (TES) technology on the capital cost and LCOE is shown as a red dashed line in Figure 186. The TES technology is assumed to have no impact on the power block design and efficiency, meaning that it must operate between 715°C and 515°C. A total TES system cost of $15/kWht, plus an additional 18.7% EPC soft cost are assumed. The solar multiple remains unchanged. The addition of four hours of thermal energy storage can increase the capacity factor to 42.4%, estimated from an hourly simulation.

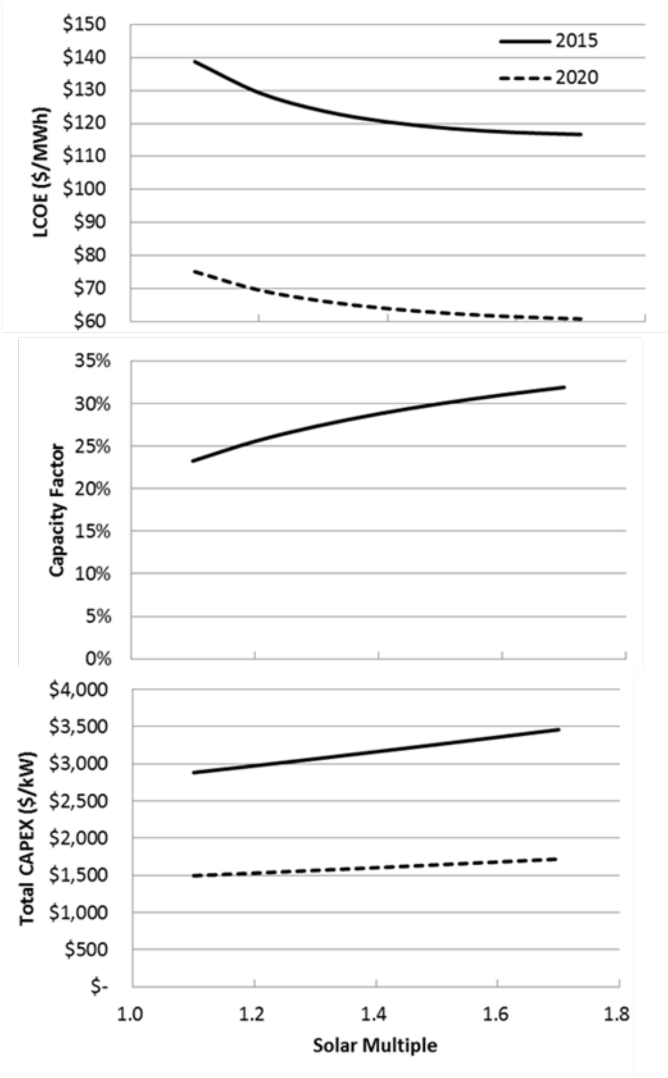

Figure 185: Effect of Solar Multiple on Real LCOE, Capacity Factor, and Capital Cost.

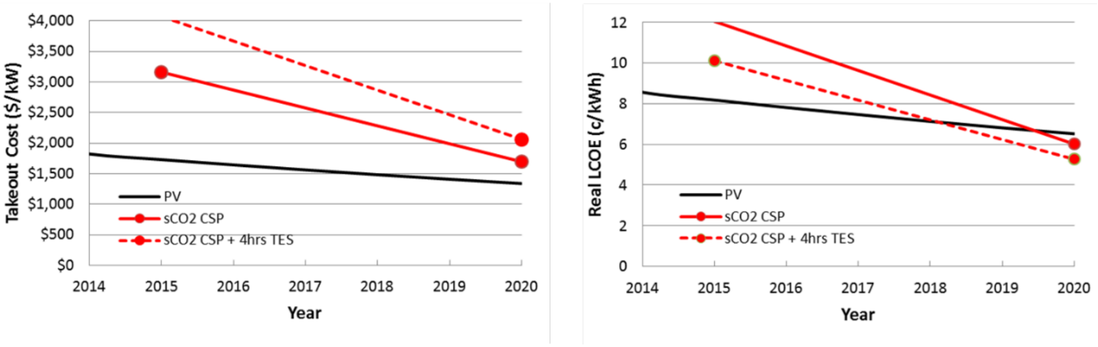

Figure 186: Cost and LCOE Projections in the Envisioned Market. PV Costs are on a DC Basis, CSP Costs are on an AC Basis

Component Cost & Performance Targets

The thermodynamic heat and mass balance assumed for the 2015 product is shown in Figure 187. This results in a net design point power cycle thermal efficiency of 46.0%. Power block component trade studies have been conducted, evaluating the performance impact as well as the break-even cost (additional cost which leads to no net change in LCOE) allowable for that change. Results are shown in Figure 188. Preliminary cost estimates of these trades indicate that the items colored in red will cost more than the allowance, will result in an increase in LCOE, and are not recommended. Trades colored in blue have the potential to cost less than the allowance, can lower LCOE, and should be investigated further. The net impact of these beneficial trades on the 2020 product net cycle efficiency is shown in Figure 189. From this analysis, it appears that there is a path to the 50% efficiency target in 2020 that also results in a net reduction in LCOE. The thermodynamic heat and mass balance assumed for the 2020 product is shown in Figure 190.

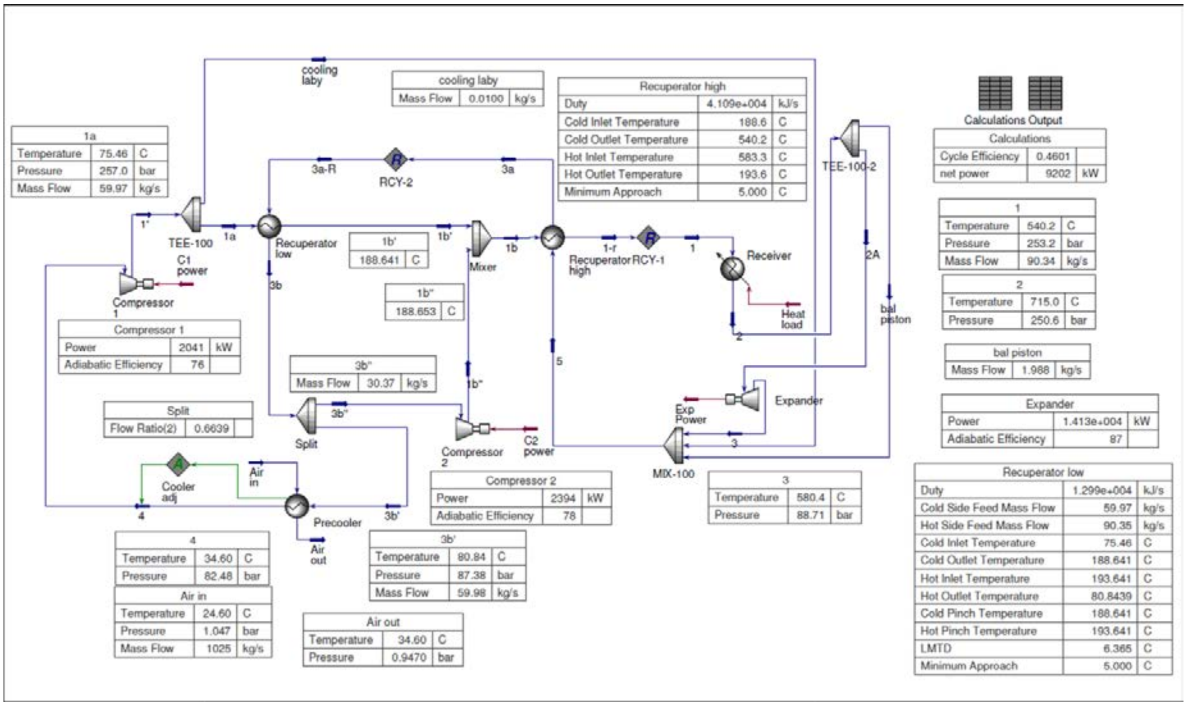

cooling laby		
Mass Flow	0.0100	kg/s

Recuperator high		
Duty	4.109e+004	kJ/s
Cold Inlet Temperature	188.6	C
Cold Outlet Temperature	540.2	C
Hot Inlet Temperature	583.3	C
Hot Outlet Temperature	193.6	C
Minimum Approach	5.000	C

Calculations		
Cycle Efficiency	0.4601	
net power	9202	kW

1a		
Temperature	75.46	C
Pressure	257.0	bar
Mass Flow	59.97	kg/s

1b'	
188.641	C

1b"	
188.653	C

Compressor 1		
Power	2041	kW
Adiabatic Efficiency	76	

3b"		
Mass Flow	30.37	kg/s

Split		
Flow Ratio(2)	0.6639	

1		
Temperature	540.2	C
Pressure	253.2	bar
Mass Flow	90.34	kg/s

2		
Temperature	715.0	C
Pressure	250.6	bar

bal piston		
Mass Flow	1.988	kg/s

Expander		
Power	1.413e+004	kW
Adiabatic Efficiency	87	

Compressor 2		
Power	2394	kW
Adiabatic Efficiency	78	

3		
Temperature	580.4	C
Pressure	88.71	bar

Recuperator low		
Duty	1.299e+004	kJ/s
Cold Side Feed Mass Flow	59.97	kg/s
Hot Side Feed Mass Flow	90.35	kg/s
Cold Inlet Temperature	75.46	C
Cold Outlet Temperature	188.641	C
Hot Inlet Temperature	193.641	C
Hot Outlet Temperature	80.8439	C
Cold Pinch Temperature	188.641	C
Hot Pinch Temperature	193.641	C
LMTD	6.365	C
Minimum Approach	5.000	C

4		
Temperature	34.60	C
Pressure	82.48	bar

3b'		
Temperature	80.84	C
Pressure	87.38	bar
Mass Flow	59.98	kg/s

Air in		
Temperature	24.60	C
Pressure	1.047	bar
Mass Flow	1025	kg/s

Air out		
Temperature	34.60	C
Pressure	0.9470	bar

Figure 187: 2015 Power Cycle Heat & Mass Balance

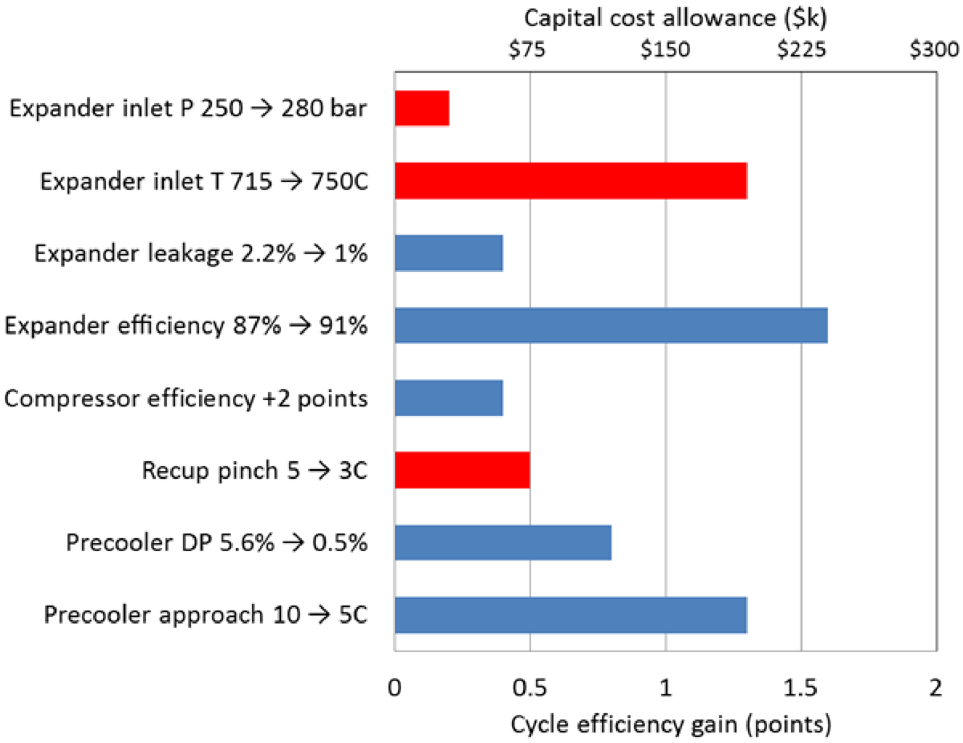

Figure 188: Component Trade Studies. Blue Bars are Recommended Trades

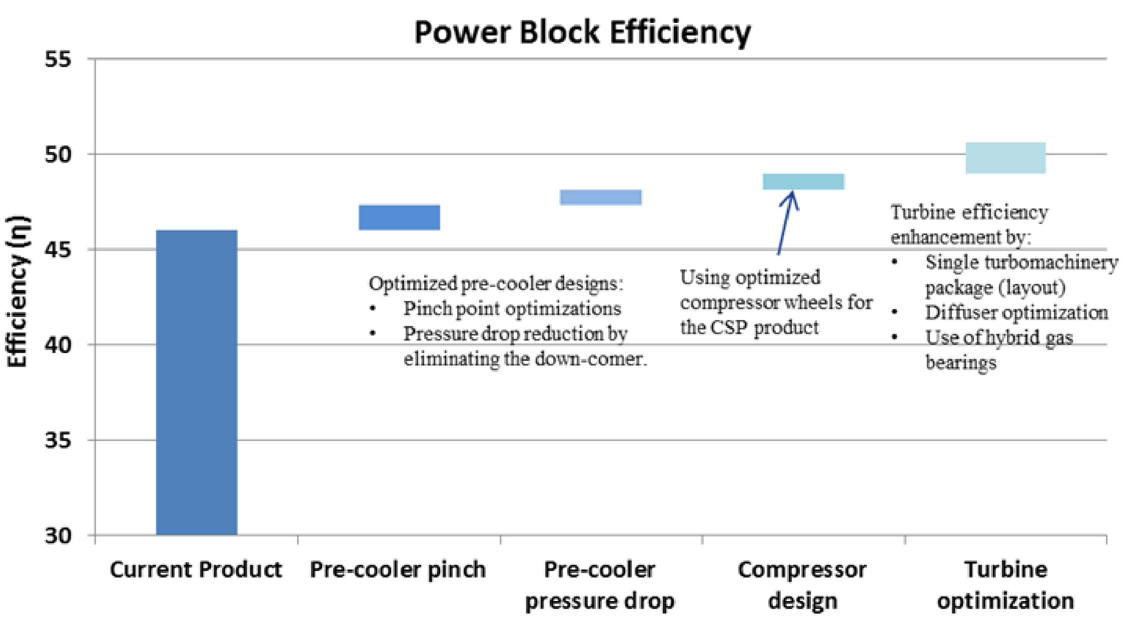

Figure 189: Efficiency Roadmap to 50% by 2020

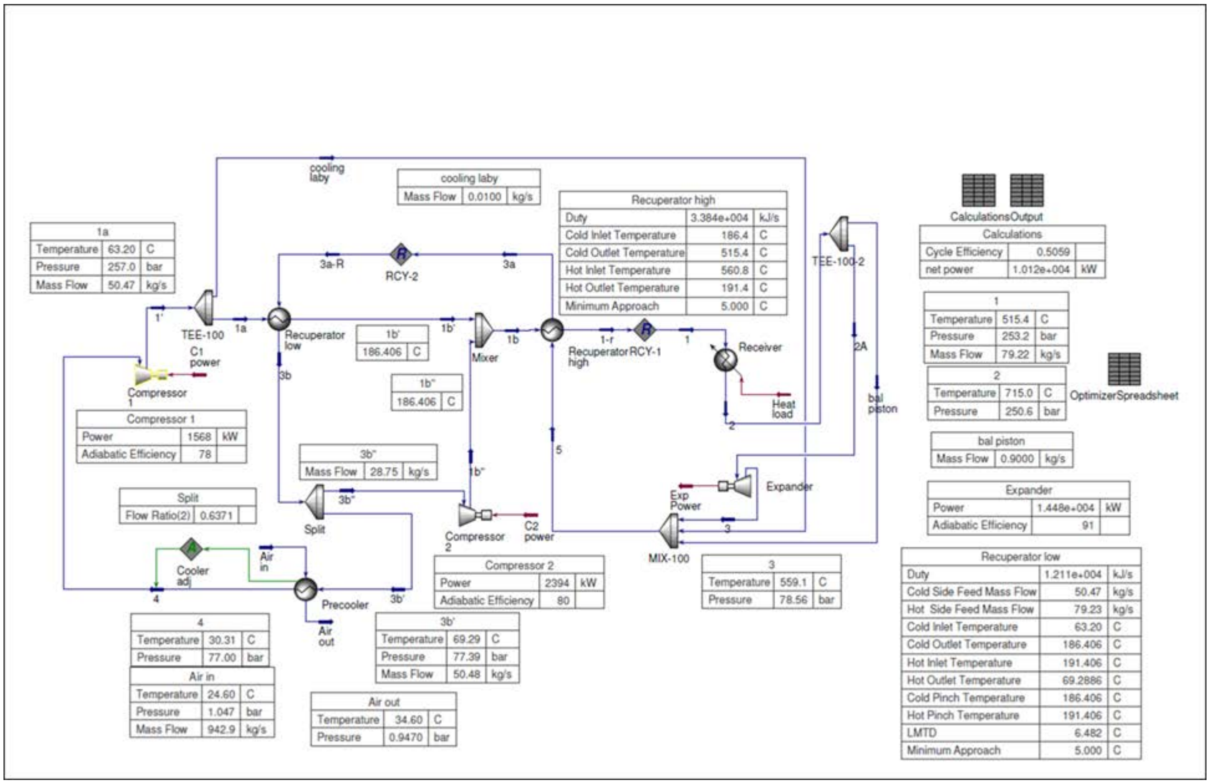

1a		
Temperature	63.20	C
Pressure	257.0	bar
Mass Flow	50.47	kg/s

cooling laby		
Mass Flow	0.0100	kg/s

Recuperator high		
Duty	3.384e+004	kJ/s
Cold Inlet Temperature	186.4	C
Cold Outlet Temperature	515.4	C
Hot Inlet Temperature	560.8	C
Hot Outlet Temperature	191.4	C
Minimum Approach	5.000	C

Calculations		
Cycle Efficiency	0.5059	
net power	1.012e+004	kW

1b'	
186.406	C

1b"	
186.406	C

1		
Temperature	515.4	C
Pressure	253.2	bar
Mass Flow	79.22	kg/s

2		
Temperature	715.0	C
Pressure	250.6	bar

Compressor 1		
Power	1568	kW
Adiabatic Efficiency	78	

3b"		
Mass Flow	28.75	kg/s

bal piston		
Mass Flow	0.9000	kg/s

Split		
Flow Ratio(2)	0.6371	

Expander		
Power	1.448e+004	kW
Adiabatic Efficiency	91	

Compressor 2		
Power	2394	kW
Adiabatic Efficiency	80	

3		
Temperature	559.1	C
Pressure	78.56	bar

Recuperator low		
Duty	1.211e+004	kJ/s
Cold Side Feed Mass Flow	50.47	kg/s
Hot Side Feed Mass Flow	79.23	kg/s
Cold Inlet Temperature	63.20	C
Cold Outlet Temperature	186.406	C
Hot Inlet Temperature	191.406	C
Hot Outlet Temperature	69.2886	C
Cold Pinch Temperature	186.406	C
Hot Pinch Temperature	191.406	C
LMTD	6.482	C
Minimum Approach	5.000	C

4		
Temperature	30.31	C
Pressure	77.00	bar

3b'		
Temperature	69.29	C
Pressure	77.39	bar
Mass Flow	50.48	kg/s

Air in		
Temperature	24.60	C
Pressure	1.047	bar
Mass Flow	942.9	kg/s

Air out		
Temperature	34.60	C
Pressure	0.9470	bar

Figure 190: 2020 Power Cycle Heat & Mass Balance

The overall component cost parameters required for the 2015 and 2020 product are shown in Table 28. Per the SunShot Vision Study, heliostat equipment cost is expected to decrease from \$165/m2 to \$75/m2. Receiver cost is expected to decrease from \$180/kWt to \$110/kWt. A preliminary bottoms-up cost estimate of the power block shows that its cost could potentially decrease from \$1270/kWe to \$775/kWe. It is important to note that the EPC soft costs for the power block have already been included in the power block cost estimate because of the modular design. A waterfall chart showing this cost reduction is given in Figure 191. A final summary of the 2015 and 2020 system design is given in Table 29.

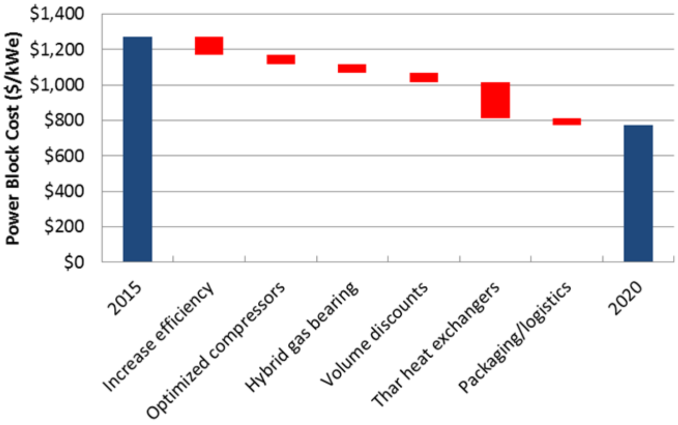

Figure 191: Cost Waterfall from 2015 to 2020

Table 28: Component Cost Parameters

		2015	2020
Land prep	*\$/m2*	\$20	\$10
Heliostat cost	*\$/m2*	\$165	\$75
Receiver cost	*\$/kWt*	\$180	\$110
Power block cost	*\$/kWe*	\$1,270	\$775
EPC soft cost (heliostat & receiver)	*%*	29.4%	18.7%
EPC soft cost (power block)	*%*	incl	incl
Owner's cost	*%*	6%	6%

Table 29: Overall Product Summary

		2015	2020
Net Module Output	*MWe*	9.2	10.0
Power block efficiency	*%*	46%	50%
Solar Multiple	-	1.4	1.7
Tower Height	*m*	90	120
Solar field reflective area	*m2*	44192	52118
Take-out cost	*\$/kWe*	\$3,160	\$1,700
Capacity Factor	*%*	28.8%	31.9%
Real LCOE	*c/kWh*	12.0	6.0

The commercialization update for SunShot, at the end of 2018, allows one to establish a “2018” turbine that can incorporate the learnings of not only the current Shout program but also those from the related sCO_2 Power block programs. Two programs that have contributed directly to performance and/or cost updates are DE-EE-0007109, referred to in this document as “Apollo” and DE-FE-002979, referred to in this document as “STEP”. The 2018 turbine was still considered a first unit; however, the programs referenced in conjunction with the original SunShot commercialization study allow an “nth” cost future unit to be developed. This unit is considered a 2023 unit and represents the inclusion of advanced technology as well as economies of scale in production or structured units.

The revised mass and flow balances for the 2018 and 2023 turbines are shown in Figure 192 and Figure 193.

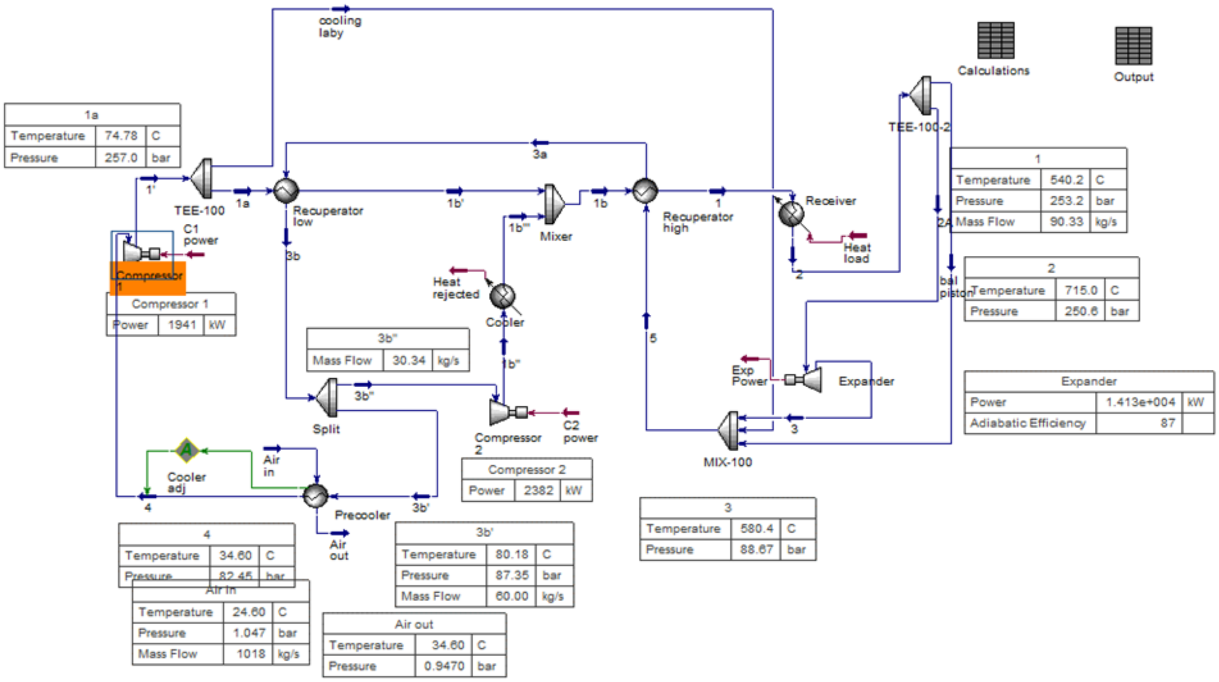

Figure 192: 2018 Power Cycle Heat & Mass Balance

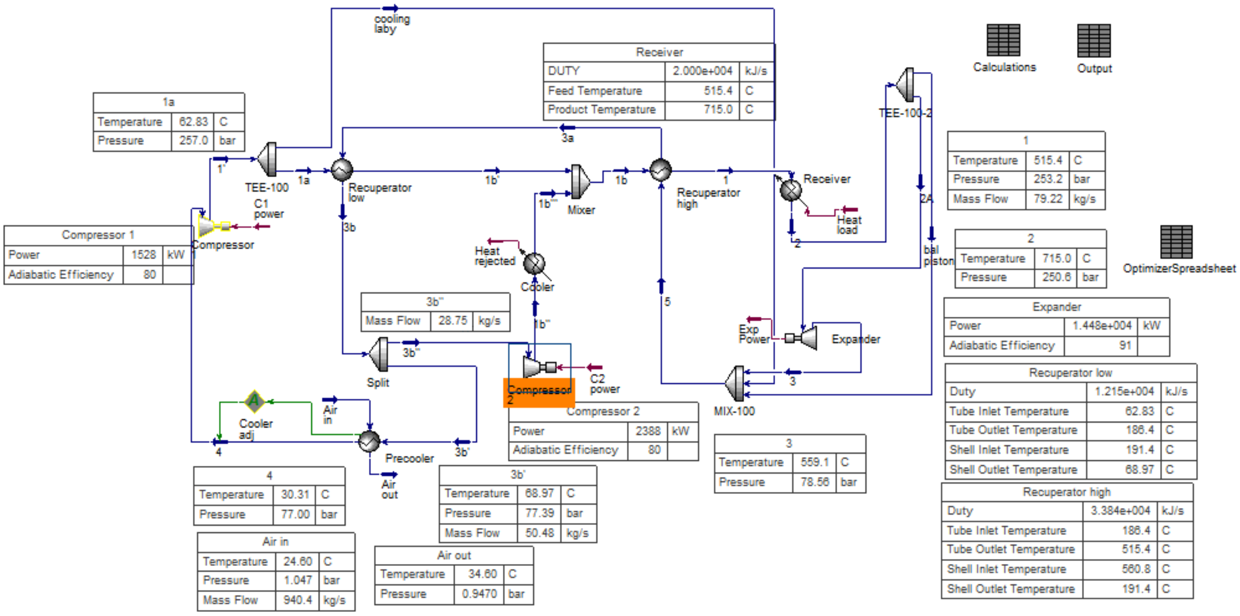

Figure 193: 2023 Power Cycle Heat & Mass Balance

The learnings from the Apollo and STEP programs are summarized in Table 30. Note: only the compressor has an efficiency increase in the current program scope due to the efforts of the Apollo program. The turbine design for STEP has the same efficiency target as the initial SunShot (87%) and therefore, the original SunShot advanced turbine design (91%) is retained for the 2023 unit. Similarly, the heat exchangers are adjusted by cost only, and the heat exchanger performance for the 2018 unit is the same as the initial 2015 SunShot unit; similarly, the 2023 unit is the same as the 2020 unit. The changes are summarized in Table 30.

Table 30: Product Summary Changes with SunShot Update

		2015	2018	2020	2023
Net Module Output	*MWe*	9.2	9.4	10.0	10.0
Power block efficiency	*%*	46%	46.6%	50.6%	50.8%
Power-block cost	*$/kWe*	$1260	$1680	$760	$1090

One can easily see that there is a small efficiency improvement for the 2018 and 2023 turbines; however, the power block costs have exceeded the initial SunShot estimate, and although the 2023 turbine shows a decrease in power block cost, it does not meet the desired target from the initial 2020 SunShot estimate.

A high-level summary of the changes that have led to these numbers is presented:

- Compression system: From the Apollo program, the compressor efficiency is predicted to increase to 80% for both the main and recompressor. In addition, the compressor cost has decreased significantly, exceeding the Apollo program targets. The actual efficiency will be validated in the test phase of the program. The cost estimates have high certainty as the hardware has been manufactured. Compression changes were in the positive direction.
- Turboexpander: The turboexpander cost is based on actual SunShot turbine costs scaled to a full 10MWe turbine, incorporating any design changes undertaken for the STEP 10MWe. The turboexpander has shown a small increase in cost, mostly due to the Ni based super-alloys required at these high temperatures, as those alloys have increased in price recently, due to raw Ni and other alloying element cost increases because of the large increase in use of those elements in batteries.
- Heat Exchangers: The cost for the heat exchangers has increased significantly from the time of the initial SunShot estimation to current data. The current data is taken from the STEP program which has very similar conditions, but it scaled to the CSP cycle based on a $\$/kW_{th}$ ratio. The 2023 turbine incorporates a significant potential cost saving based on economies of scale as well as technology increases. However, it is limited to a 40% reduction as many of these potential cost reductions are unproven at this time.
- Turbine stop/control valve: This is an additional very significant cost increase from initial SunShot estimates. A significant cost addition is due to the required high temperature H282 casing. The 2023 power block represents a 1/3 cost reduction to estimate the reduction in cost of the H282 as it takes advantage of economies of scale as well as proposed material cost reduction programs. The 1/3 limit as with the heat exchangers is limited as many of the potential cost reductions are unproven at this time. To understand the valve cost increase better, shows the trends in valve cost with temperature. This cost increase is attributed to the

advanced alloys required as temperatures increase. The two lower valve costs are based on current steam turbine valves costs of equivalent size.

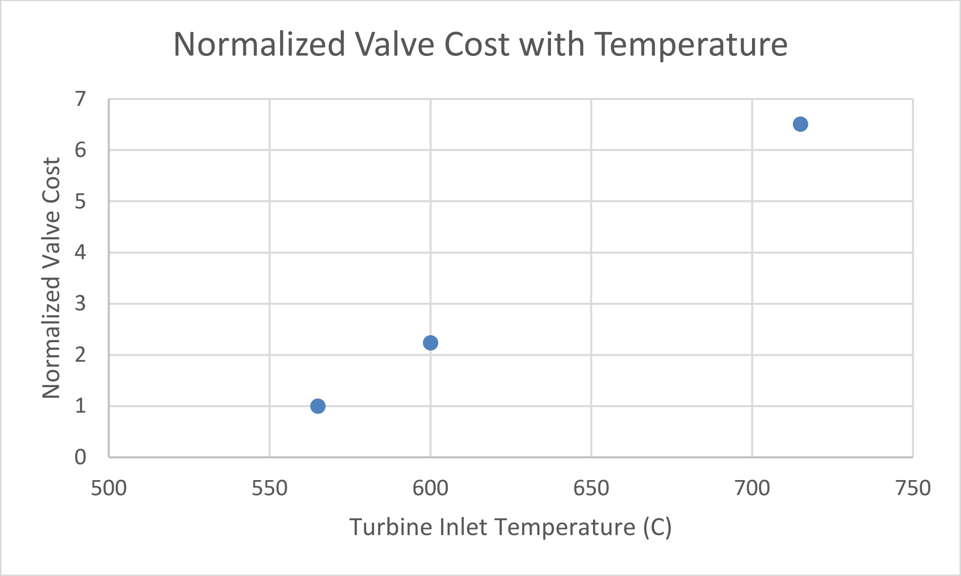

Figure 194: Normalized Valve Cost with Temperature

Table 31 provides more granularity on the cost roll-up, comparing the initial Sunshot values (2015, 2020) to the revised values based on the lessons learned (2018, 2023).

Table 31: Power Block Cost Breakdown by Major Component

Component	Metric	2015	2018	2020	2023
Compressor	Efficiency	76%/78%	80%/80%	80%/80%	80%/80%
	Cost ($/kWe)	250	171	175	154
Turbine	Cost ($/kWe)	248	250	166	180
Control Valve	Cost ($/kWe)	54	200	135	25
HTR	Cost ($/kWth)	50	61	25	38
LTR	Cost ($/kWth)	50	139	25	86
Process Cooler	Cost ($/kWth)	63	51	50	42

Revision History

Revision 1:

The information in this addendum includes the following changes and revisions to the information previously presented to DOE in the Continuation Report (Moore) and the Continuation presentation presented to DOE on 2/5/2014. Many of these changes have been made to be consistent with the 2015 and 2020 component parameters in Table 29 of the DOE SunShot Vision Study (DOE). The remaining changes have been made due to additional refinements to the estimation of capacity factor, presented under Component Cost & Performance Targets, and component costing described in Revision History.

- 2020 Solar Multiple increased from 1.4 to 1.7
- 2020 Tower Height increased from 90m to 120m
- 2020 Receiver cost reduced from $150/kWt to $110/kWt
- 2015 Solar Field Land Preparation Costs increased from $0 to $20/m2
- 2020 Solar Field Land Preparation Costs increased from $0 to $10/m2
- Power Block EPC Soft Cost reduced from 29.4% to 0%
- 2015 Fixed O&M increased from $75 to $65/kW/yr
- 2020 Fixed O&M decreased from $60 to $40/kW/yr
- Power Block & Receiver availability decreased from 100% to 99.3%
- Power output annual degradation increased from 0% to 0.1%/yr
- 2015 Power Block cost increased from $1200 to $1270/kW
- 2020 Power Block cost decreased from $840 to $775/kW
- Figure 42 in the Continuation Report is replaced with Figure 195 in this Addendum.

Revision 2:

The information in this addendum was updated in Phase 3 to satisfy the SunShot SOPO requesting a commercialization update. The update was focused on incorporating two volumes of data:

1. Further study of the appropriate power block size in section 4: Installation size, incorporates a mobile crane study leveraging wind tower erection data to limit the tower mounted Power Block size to 50MW modules.
2. Incorporation of additional data on cost and performance from the SunShot testing program as well as any applicable data from related sCO_2 Power block programs: DE-EE0007109, DE-EE0006345, DE-FE0024007, DE-FE0031617, DE-AR0000467, DE-FE0002979

Lessons Learned

One of the most important aspects of developing this loop was that it would allow for some larger scale experience in designing, manufacturing, and running an sCO_2 power cycle. With any new concept or process gas, there are many unknowns. Throughout this project, it was well documented what features, controls, and experience could be utilized for future sCO_2 applications. This includes any test loop utilizing sCO_2, larger pilot or full scale plants, and even general rules of thumb when designing and manufacturing similar components that were used in this loop.

Component Control Systems

- The main heater utilized a Proportional Integral Derivative (PID) controller to set an airside temperature. Based on a downstream thermocouple, the PID controller experienced instabilities and would cycle the gas output level oscillating around the airside set point.
  - Problem: The controller was not properly tuned (despite efforts by the manufacturer on-site) for higher temperatures and would not settle on the set point leading to large temperature fluctuations (~100°F). This caused the turbine to fluctuate speed and also lead to low gas supply trips as the controller would try to cycle the temperature down. A heater trip would cause a full system trip that would take hours to recover from.
  - SunShot Solution: Routed the controller to the control room and manually set the gas supply valve. This allowed for more stable control for the current test and allowed for proper steady state performance data of the entire loop.
  - Future Solution: A feedback controller will be required for future testing since the ability to set an airside temperature is critical in order to control the speed of the turbine. It was difficult to try to change the temperature quickly with the manual controller and required small steps to see how the loop responded. In order to ensure the feedback controller works properly, it is important to properly tune it at desired operating temperatures to ensure the control will allow it to settle at a set temperature.
- The dry gas seal heater also had a PID controller that was tied to a thermocouple at the dry gas seal supply to the turbine.
  - Problem: While trying to maintain a set temperature, the heater core would overshoot its trip limit and trip the heater. The only way to reset the heater was through a manual reset after the core had dropped below its trip point. This could lead to cold dry gas seal flow entering the turbine and to eventual dry ice formation, which could damage the seals. It was hard for the heater controller to maintain temperature during filling because of the large property changes of CO_2 as the loop was coming up to pressure
  - SunShot Solution: Instead of controlling the temperature going into the turbine, the heater core temperature was manually set, and the control valves from the seal panel were used to control the seal supply temperature. By increasing or decreasing the flow, the temperature would drop or increase. At full operating conditions, the heater could keep up with the seal supply flow that was required and had no issues in tripping on core temperatures

  - Future Solution: Being able to control the heater core temperature from the control room will be ideal. This along with using control valves on the seal supply to set the temperature will allow for easier control.

- Main heater tripping proved to be one of the biggest challenges in the entire loop. If the heater tripped, the turbine throttle valve would be closed, and the turbine section would have to be vented to prevent any shock cooling from dry gas seal buffer flow.
  - Problem: The heater would trip itself on two events: low gas supply and low air supply. Either of these trips would lead to an emergency shut down of the loop.
  - SunShot Solution: Removed an excess regulator between gas supply and heater to allow for increased supply pressure. Blower speed was lowered to minimum to allow for increase in temperature but blower speed was increased by 5 Hz to allow for more air supply.
  - Future Solution: Ensure proper sizing of blower speed and gas supply network to maintain more margin to gas pressure trip limits.

Dry Gas Seals

- In order to prevent the formation of dry ice when dropping from above 850 psi to atmosphere, CO_2 must be at an elevated temperature based on pressure. A target enthalpy around 190 btu/lbm will ensure that the liquid dome (and then solid ice line) is not crossed when dropping in pressure. This requires heaters upstream of the turbine, pump, or compressor seal supply flow.
  - Problem: The formation of dry ice can lead to clogging of vents, ratcheting open of seal faces, and eventually seal failure. This can cause permanent damage to the seals or lead to issues when filling up a loop with uncontrolled venting. For the case of the GE pump, flow venting through the seals did not cause catastrophic failure. In the case for the turbine, the dry gas seal panel provides buffer flow. If that is lost, high temperature flow will run through the seal and damage many internal seal components and anything outboard of the seal.
  - SunShot Solution: Ensure that there is a heater on the seal supply panels. This was already designed into the turbine dry gas seal panel, but was not included on the pump panel (OEM did not think it was necessary). In order to fill properly, the pump seal gas supply was run through the heater first and then supplied the pump, until the pump was brought up to speed and eventually fed its own seals. Rotation of the seals helped generate more heat to keep from forming dry ice.
  - Future Solution: Ensure that all dry gas seals are supplied with warm CO_2 especially during any filling or static hold. At a static hold, the seal supply flow will not be as high, but heaters need to be sized properly so that all seals can be supplied properly, especially when transitioning through the liquid phase (600-800 psi).
- Properly sizing of the dry gas seal heater is critical in ensuring that all seals can be supplied with warm flow during each stage of operation. At full operating conditions, turbines will require a majority of the flow to properly cool the cavity while lower temperature components will mainly require flow to properly buffer the seals. It is important

to look at all operating points since the effectiveness of the heater will change based on the CO_2 properties.

  - Problem: At off design conditions, mainly when the CO_2 would turn into a liquid (600-800 psi, ambient temperature), the heater was not able to provide enough heat input into the seal supply flow. This would lead to low supply temperatures and a higher potential for the formation of dry ice in the seals.
  - SunShot Solution: In order to get through the liquid phase, supply flows were decreased significantly to allow for more temperature gain with the same heat input until the flow turns back to a gas.
  - Future Solution: Properly size the heaters for worst case operating conditions. In this case, the worst heat transfer conditions would need to be considered. This would most likely be during filling or a static hold when all seals could require significant flow.

- Heater placement is also important. This focuses around the pressure of the flow in the heater versus pressure of the flow entering the turbine. When seals are supplied from the pump or compressor, the supply flow is at a much higher pressure than the turbine is seeing.
  - Problem: The dry gas seal panel will have a regulator and PSV to ensure that flow entering the heater is below its design point. This flow will then have to take another pressure drop before entering the turbine. With isenthalpic expansion, Joule Thomson cooling occurs, since CO_2 has real gas properties, and the temperature of the flow will be colder than expected.
  - SunShot Solution: In order to drop the pressure before the heater without having to adjust the manual regulator, a control valve was moved from downstream to upstream of the heater. This control valve was replaced with a hand valve that was pinched to allow for separate flow control of the dry gas seals. This control valve was then used to drop the pressure after the panel regulator and ensure that any pressure drop across the other valves is minimal.
  - Future Solution: Utilize three control valves for future DGS panels or use the two control valves and one hand valve configuration from SunShot to ensure proper flow control. A controlled panel regulator could also replace the control valve upstream of the heater.
- It is important to know the manufactured and operating clearances of all internal seals, especially for the process side inside the dry gas seal.
  - Problem: At full operating conditions, the rotating portion of the dry gas seal will experience the most centrifugal growth, and its highest temperatures due to convection from the turbine flow and also windage in the cavities. Because of this, the rotating seal will grow more than the stationary portion leading to smaller labyrinth seal clearances. Heat conducting up from the shaft aggravates this situation. This can eventually lead to a rub and a catastrophic seal failure.
  - SunShot Solution: In order to reach full speed, the dry gas seal's buffer labyrinth seals were opened up radially to ensure that the operating clearance was sufficient.

  - Future Solution: This larger clearance should be applied to any seals operating at high speeds near higher temperatures to prevent rubs and component damage. After this was implemented, no dry gas seal failures were observed.

Bearing Operating Clearances

- Operating clearances for the journal bearings are critical for overall bearing performance. They will control stiffness, damping, stability, temperature, and load capacity.
  - Problem: Due to tight clearances at the low end due to tolerances, bearing pad temperatures were higher than expected. This prevented going up to higher operating speeds.
  - SunShot Solution: Bearing diameters were opened up from 3.0040/3.0045” to 3.0050/3.0055”. This extra mil on the diameter dropped the bearing temperature from 275°F at 24,000 rpm to 190°F at 27,000 rpm. Vibrations increased by < 0.25mils, which was far below trip limits.
  - Future Solution: For high speed machines, larger clearances will be used to significantly reduce pad temperatures and allow for higher speed operation.

Loop Performance

- Some of the most important knowledge gained in operating this loop was the experience during loop transients, mainly during shut downs and startups for this particular testing. In order to properly operate a power cycle, it is important to understand how to bring the loop up to speed.
  - Problem: Once the loop was pressurized, and the turbine was ready to spin, the heater would be turned on, and flow would be introduced to the turbine loop. If the mass flow was too high initially, any heat in the turbine and heater would be removed, no recuperation would occur, and the turbine speed could not be increased.
  - SunShot Solution: To bring the turbine up to speed, the mass flow was kept at a minimum to break the turbine free. Then the heater temperature was increased to allow the loop to properly heat soak. Once a desired temperature was reached, mass flow and heater temperature were increased together, to bring the turbine up to speed.
  - Future Solution: Startup controllers will need to be programmed to allow for proper heat soaking of the loop before a turbine can be brought up to full speed when connecting to the grid. This will lead to longer cold startup times, but a balance can be configured when going from partial to full loads.
- In addition to startup performance, shut down transients also were observed. Emergency transients were seen during every heater trip. Emergency shut downs of this nature will lead to high thermal stresses in high temperature components which will need to be accounted for in the design process.
  - Problem: With a heater trip and no more heat input into the system, cold CO_2 would immediately run through the loop and cold shock the heater, piping, turbine, and recuperator. This kind of shock cooling can lead to fatigue life limits of components.

    - SunShot Solution: Heater trips were tied directly to turbine throttle valve closing and pump recycle valve opening. This stopped any flow going through the hot section of the loop and allowed for the pump to keep spinning without dead heading it.
    - Future Solution: For test components, designing for emergency shut downs is critical, since they could happen more often than planned. Ensuring that control systems work properly when a heater trips is important in reducing these thermal stresses on critical components.
- During startup of the loop, it is important to understand how pressures can fluctuate and how to account for the large changes in fluid density.
    - Problem: When starting the pump up, once flow starts running through coolers and chillers, that flow will cool down fast, increasing the density of the fluid and decreasing the pressure in the loop. If the pressure drops too low, it could reach the minimum pressure of the pump, leading to a trip, and having to restart the process. When starting up the turbine, once flow starts going through the heater, loop temperature will increase, lowering the density and increasing the pressure. This can lead to high pressure trips in the exhaust side of the loop.
    - SunShot Solution: In order to prevent excess venting and extra filling of the loop, the pump would be started at a higher pressure (e.g. 1400 psi) that allowed it to stay above minimum pressure once everything cooled down. Opposite for the turbine, the loop pressure would be lower than designed (e.g. 1100 psi) so that once everything was warmed up, the pressure would not go above design limits. Also, the hot section near the turbine was filled through the DGS system with warm CO_2 while the main loop was filled with ambient temperature CO_2 helping the loop achieve the proper amount of mass.
    - Future Solution: It is important to understand these changes in density, pressure, and temperature to prevent excess venting and extra fill time. A system to manage the CO_2 will help in maintaining turbine speeds and pressures while going through various transients. The inventory management system in STEP will help maintain the proper amount of mass in the loop for different operating conditions. Also, since compressors are being used instead of a pump, no minimum start-up pressure exists so the loop can start flowing at much lower pressures minimizing these pressure transients.

Project Schedule

Figure 195 shows the schedule for the Phase 3 turbine and loop assembly and test. The project tasks including manufacturing and test were completed per this schedule. Furthermore, the project was completed within the original DOE budget with no additional funds being requested.

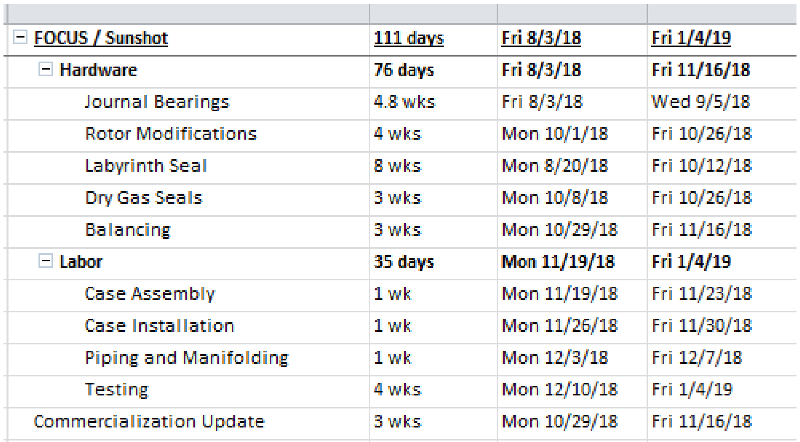

FOCUS / Sunshot	**111 days**	**Fri 8/3/18**	**Fri 1/4/19**
Hardware	**76 days**	**Fri 8/3/18**	**Fri 11/16/18**
Journal Bearings	4.8 wks	Fri 8/3/18	Wed 9/5/18
Rotor Modifications	4 wks	Mon 10/1/18	Fri 10/26/18
Labyrinth Seal	8 wks	Mon 8/20/18	Fri 10/12/18
Dry Gas Seals	3 wks	Mon 10/8/18	Fri 10/26/18
Balancing	3 wks	Mon 10/29/18	Fri 11/16/18
Labor	**35 days**	**Mon 11/19/18**	**Fri 1/4/19**
Case Assembly	1 wk	Mon 11/19/18	Fri 11/23/18
Case Installation	1 wk	Mon 11/26/18	Fri 11/30/18
Piping and Manifolding	1 wk	Mon 12/3/18	Fri 12/7/18
Testing	4 wks	Mon 12/10/18	Fri 1/4/19
Commercialization Update	3 wks	Mon 10/29/18	Fri 11/16/18

Figure 195: Manufacturing and Test Schedule

Works Cited

1. Moore, J, "Phase 1 Continuation Report," Development of a High Efficiency Hot Gas Turbo-expander and Low Cost Heat Exchangers for Optimized CSP Supercritical CO_2 Operation, DE-EE0005804, 2014
2. DOE, SunShot Vision Study, 2012
3. Lazard, Levelized Cost of Energy Analysis Version 5.0, 2011
4. SEIA, Solar Market Insight, 2013
5. DE-EE-0007109 “Compression System Design and Testing for sCO_2 CSP Operation” DoE Concentrating Solar Power Advanced Projects Offering Low LCoE Opportunities (APOLLO) Award
6. DE-FE-0002979 "Supercritical Transformational Electric Power (STEP)"
7. Portnoff, M., Chordia, L., sCO_2 Brayton Power Cycle Test Loop - Operations Reviews, The 6th International Symposium-Supercritical CO_2 Power Cycles, March 28, 2018, Pittsburgh, PA
8. Portnoff, M., Chordia, L., Development of Modular, Low-Cost, High-Temperature Recuperators for the sCO_2 Power Cycles – Project Update, 2018 University Turbine Systems Research Project Review Meeting, October 31, 2018, Daytona Beach, Florida

Addendum A – EPRI Metallurgical Analysis of H282 Turbine Case Castings

Daniel Purdy
Sr. Technical Leader
EPRI, Materials & Repair

April 25, 2018

Introduction

Higher temperature applications, specifically in concentrated solar, require new alloys for long term performance and stability. SWRI opted to examine the effectiveness of a nickel-based superalloy Haynes 282 in its cast form following recommendations out of the DOE-funded AUSC turbine project. Unfortunately, casting defects plagued this examination resulting in refabricating the components of interest in lower-complexity alloys.

Materials

EPRI received two cut segments from the cast exit plenum and nozzle casing. Figure 196 details the approximate location of the segments on the larger casting. The castings were produced at Flowserve (Dayton, Ohio). Flowserve had been involved as a supplier in the previous work (through the DOE consortium), and had worked with specifically 282 previously.

Figure 196: Approximate Locations of Material Received from the Exit Plenum (Left) and Nozzle Casing (Right)

Evaluation

The samples were found to be too dirty even after extensive cleaning for significant SEM analysis. Optical microscopy techniques were more than sufficient to evaluate the samples and provide evidence as to the nature of the casting defects.

Exit Plenum

The damage in the exit plenum appeared to be limited to hot tears on the extrados of locations of complex, changing geometry. The hot tear appeared as a crack that extended very nearly through-wall (wall thickness is approx. 1 cm in this area). The crack's jagged appearance and location are strong indicators of its cause: while thickness transitions cool, zones that are still hot are pulled away from each other by different cooling (contraction) rates in the component. Figure 197 through Figure 199 provide a look at the crack features. Significant oxidation was noted on internal features, and well into the grain structure indicating a solid but extremely hot structure.

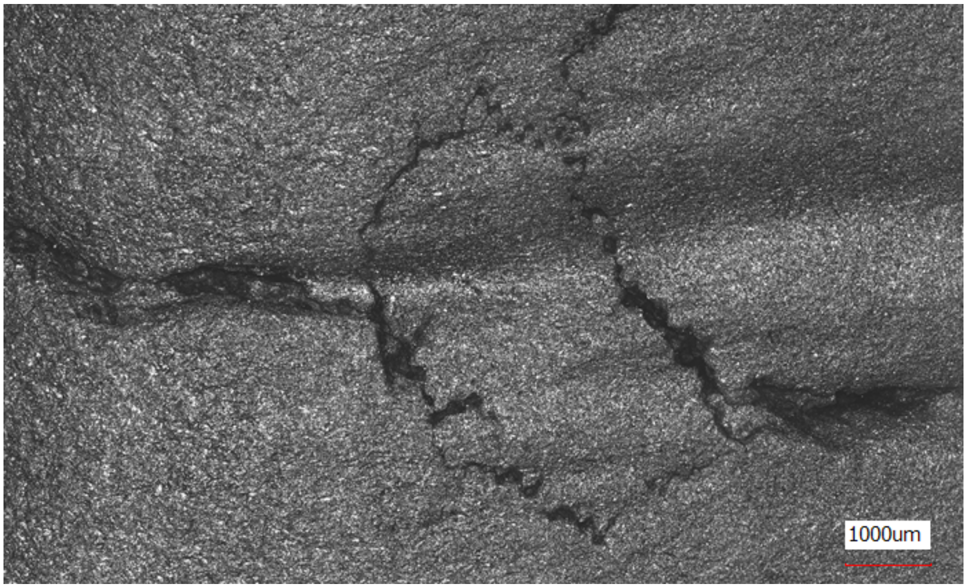

Figure 197: Confocal Laser Micrograph of a Segment of the Surface of the Hot Tear Observed in the Exit Plenum

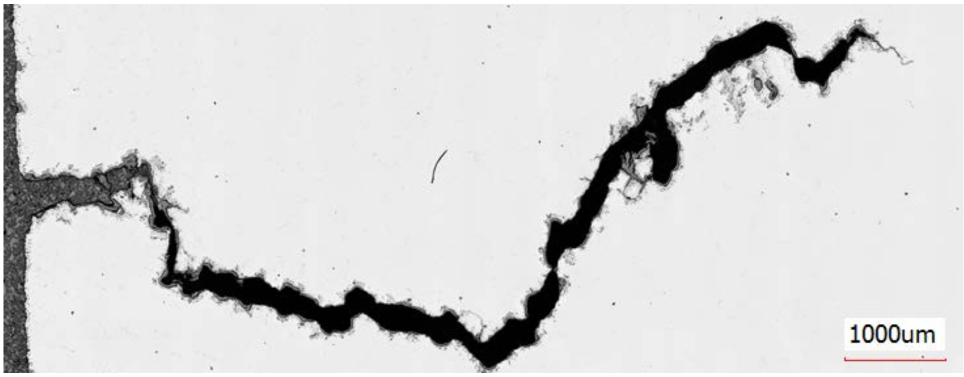

Figure 198: A Metallographic Cross Section Through the Crack in the Exit Plenum Showing over 11 mm of Crack Length in this Region

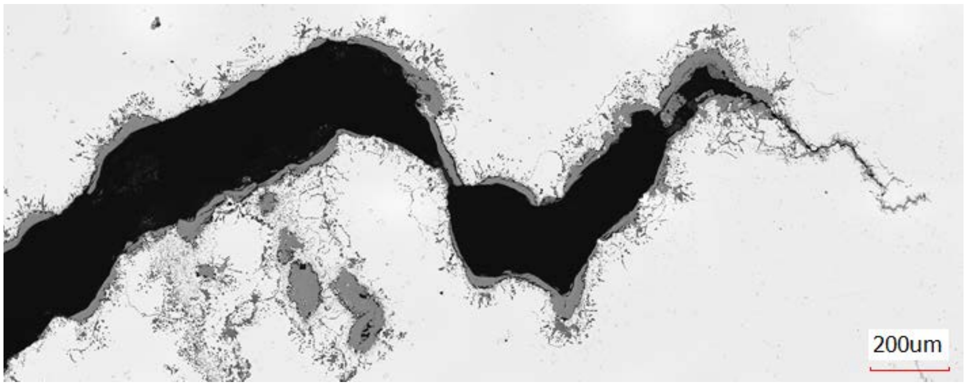

Figure 199: High Magnification Laser Microscopy Image of the Tip of the Hot Tear Crack. Note the Extensive Oxidation and Penetration of Oxide Deep into the Microstructure Indicating Very High Temperatures at the Time of Exposure.

Nozzle Casing

The casting defects observed in the nozzle casing were consistent with shrinkage porosity. At low magnification, dendrite growth was easily observed leaving a discontinuous and tortuous surface morphology. Shrinkage is caused by a lack of material flow to the area as it cools and shrinks. This leaves a void volume as material solidifies which can lead to porosity similar to that observed in this part. Addressing this issue would require additional metal flow to this region (e.g. risers), or perhaps exothermic heating locally such that liquid metal can continue to flow into that region while is solidifies.

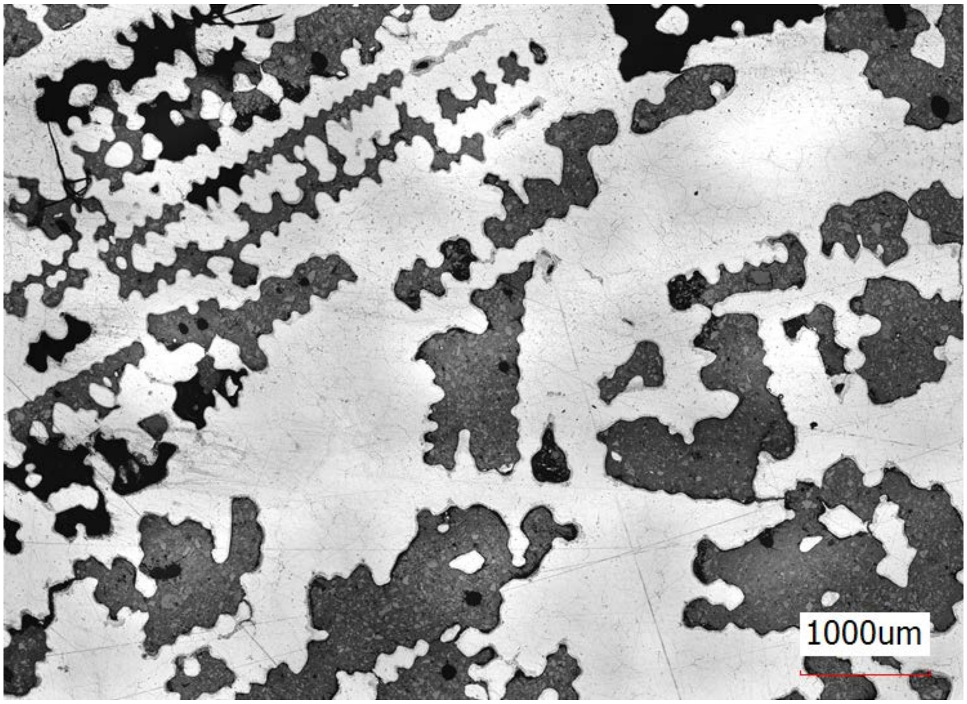

Figure 200: Micrograph of Polished Section from Nozzle Casing Casting Showing an Incomplete Microstructure of Dendritic Growth Characteristic of Shrinkage Porosity

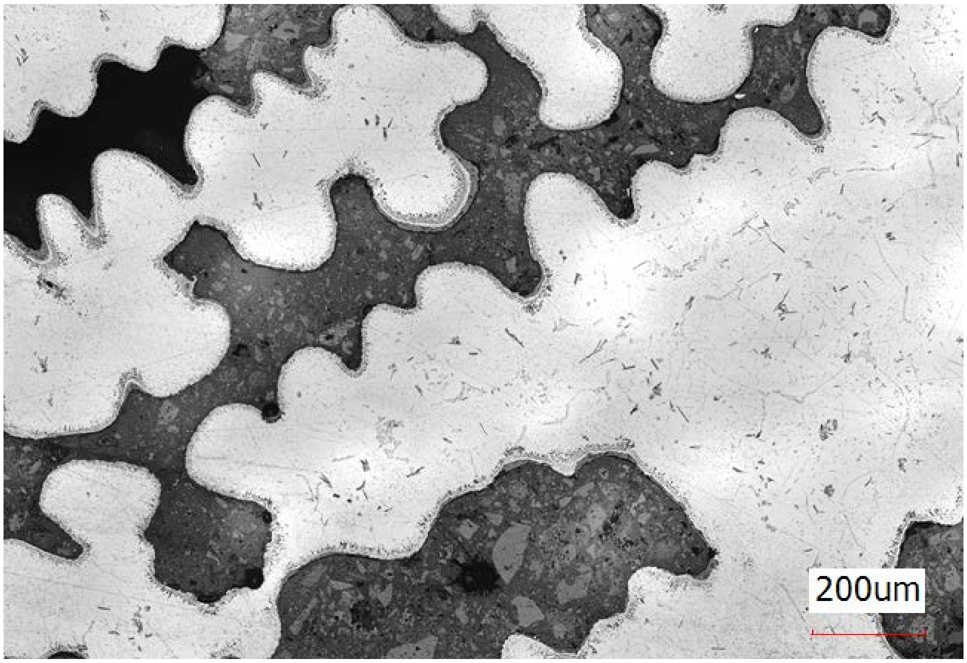

Figure 201: A Magnified Micrograph of the Same Region in Figure 200. Note the Presence of Oxidation in the Tips of the Secondary Dendrites

Discussion

The DOE funded AUSC Turbine project of 2005-2015 was able to successfully demonstrate large (17,000 lbs pour weight) castings of Haynes 282 on the first try. However, considerable engineering effort was used to plan for this casting given the expense of a nickel-based casting of this size. Further, the wall thickness in this work are substantially thicker than the ones in these SWRI concentrated solar designs. Thick and thin components offer very different challenges in a foundry; some alloys may perform better in one versus the other.

In the instance of hot tears, a local area is insufficiently strong during cooling to provide structural integrity. Cooling this area more rapidly (such as through in-wall chills) would strengthen it, but may lead to moving the hot tear to another location. Alternately, keeping the adjacent areas hotter longer may provide the needed duration for the torn location to strengthen relative to its contracting neighbors and maintain component integrity until a stress relief can be performed. Alternately, stiffening features can be built into the casting; these can be left on if the design permits or machined off.

Porosity is an indication that there is insufficient liquid metal in this region. EPRI was not provided the foundry method for this casting, but it would appear it the region provided in this sample was the top of the casting with risers feeding the center of the casting. Porosity was identified all along the OD of the nozzle casing in this corner region. This type of a casting defect can be addressed with additional risers providing liquid material the ability to flow throughout the top of the casting during solidification. Unfortunately, such an investment in casting design reduces the overall yield (part weight / pour weight), but it does increase success rate.